Title

Understanding the Role of Atomic and Nanoscale Structure in Fast-Charging Electrode Materials

Author

Robertson, Daniel

Publication Date

2023

Peer reviewed|Thesis/dissertation

UNIVERSITY OF CALIFORNIA

Los Angeles

Understanding the Role of Atomic and Nanoscale Structure in Fast-Charging Electrode Materials

A dissertation submitted in partial satisfaction of the requirements for the degree Doctor of Philosophy in Chemistry

by

Daniel Davies Robertson

2023

ABSTRACT OF THE DISSERTATION

Understanding the Role of Atomic and Nanoscale
Structure in Fast-Charging Electrode Materials

by

Daniel Davies Robertson
Doctor of Philosophy in Chemistry
University of California, Los Angeles, 2023
Professor Sarah H. Tolbert, Chair

Electrochemical energy storage devices with both high energy density and high power density are technologically necessary for the electrification of transportation and many other applications. This dissertation focuses on the development of fast-charging Li-ion batteries through a fundamental understanding of structural parameters that allow for fast and reversible redox reactions in electrode materials. Using solution-based routes, the atomic and nanoscale structure of electrode materials was controlled and connected to their electrochemical characteristics, including specific capacity, rate capability, and cycling longevity. Additionally, advanced *in operando* characterization techniques were employed to probe how materials' structure and properties evolve during cycling. Overall, these findings provide guiding principles for the design of fast-charging electrode materials going forward.

The first two sections focus on size-dependent phase transition behavior in MoO_2, a model tunnel structure anode (Chapters 2 and 3). Chapter 2 shows how the large first-order phase transition in bulk MoO_2 becomes systematically suppressed in a series of size controlled nanoarchitectures. The phase transition remains first-order, but shrinks dramatically, in intermediate-sized nanoporous MoO_2 and becomes entirely continuous solid-solution in smaller MoO_2 nanocrystals. Accordingly, the signatures of slowed charge storage from the bulk phase transition disappear in the nanomaterials. In chapter 3, we employ this suite of materials to show that this change phase transition behavior is key to the development of pseudocapacitive properties in nanoscale MoO_2 using electrochemical impedance spectroscopy. Chapters 4 and 5 characterize the charge storage properties of $V_9Mo_6O_{40}$, which transforms into a disordered rock salt structure during cycling. In chapter 4, the crystal structure of $V_9Mo_6O_{40}$ is shown to govern its transformation pathway and resulting morphology compared to a well-studied analog, V_2O_5, while chapter 5 highlights the role of optimized Li^+ diffusion distances to realize fast-charging using nanoporous $V_9Mo_6O_{40}$. Chapter 6 details the use of a newly developed technique to measure the insulating to conductive transition in two high rate anode materials, T-Nb_2O_5 and $Nb_{18}W_{16}O_{93}$. The rate of the increase in conductivity is shown to explain the difference in performance. Finally, Chapter 7 focuses on synthesis and characterization of $(W_{0.2}V_{0.8})_3O_7$, a unique V-based Wadsley-Roth shear structure that shows high rate capability.

This dissertation of Daniel Davies Robertson is approved.

Richard B. Kaner

Chong Liu

Bruce S. Dunn

Sarah H. Tolbert, Committee Chair

University of California, Los Angeles

2023

TABLE OF CONTENTS

LIST OF FIGURES

Chapter 2: Size-Dependent Suppression of Phase Transitions Leads to Fast-Charging in Nanoscale Li_xMoO_2

Chapter 6: Measuring electronic conduction in Nb-based high-rate anode materials *in situ*

Appendix A: Supporting Information for Chapter 2: Size-Dependent Suppression of Phase Transitions Leads to Fast-Charging in Li_xMoO_2

Appendix D: Supporting Information for Chapter 7: High Capacity Li^+ Storage Through Multielectron Redox in the Fast-Charging Wadsley-Roth Phase $(W_{0.2}V_{0.8})_3O_7$

LIST OF TABLES

Chapter 4: Electrochemically-Formed Disordered Rock Salt ω-$V_9Mo_6O_{40}$ as a Fast-Charging Li-Ion Electrode Material

Appendix A: Supporting Information for Chapter 2: Size-Dependent Suppression of Phase Transitions Leads to Fast-Charging in Li_xMoO_2

Appendix D: Supporting Information for Chapter 7: High Capacity Li^+ Storage Through Multielectron Redox in the Fast-Charging Wadsley-Roth Phase $(W_{0.2}V_{0.8})_3O_7$

ACKNOWLEDGEMENTS

Many people have helped me along the way as I completed this dissertation. I am deeply grateful for the support these individuals provided to me. First, I would like to acknowledge the members of the Tolbert lab for the pleasure of working with them for my Ph.D. I am especially grateful for my cohort, Charlene, Natalie, and Shreya, for their wonderful friendship throughout our journey together, and to the pseudocapacitor subgroup, Helen, David, Casey, Yiyi, Tori, and Grace, for the hours spent brainstorming and carrying out experiments. I would like to thank all of my many collaborators in the SCALAR EFRC, including Kira, Molleigh, Rebecca, Muna, Billal, Rodrigo, Sun, Nicholas, Yucheng, Jessi, David, Professor Ram Seshadri, Professor Anton Van der Ven, Professor Laurent Pilon, Professor Brent Melot, Professor Sri Narayan, and others. I am grateful to have been a part of an exciting research center and to have gotten the experience of working with so many different scientific perspectives in the process. I would like to thank the members of my doctoral committee, Professor Chong Liu, Professor Ric Kaner, and Professor Bruce Dunn. The time that they have invested into my future as a scientist and their guidance throughout my Ph.D. has been a key component to my success. I am blessed to have an incredible support system in my family. I am so thankful for my mom and dad, my brother and Angela, and my loving fiancé Max, for all of the support they have given me towards achieving my goals. Finally, I would like to thank my advisor, Sarah Tolbert, who has been a fabulous role model of a scientist throughout my time with her. As a mentor, Sarah gives so much of herself, and it shows in the quality of her mentorship, as she has been a tremendous catalyst for my personal and professional growth. I am so grateful to have her as an advisor and as a lifelong mentor going forward.

Previous Publication and Contributions of Co-Authors

Chapter 2 is the unpublished version of Daniel Robertson, Helen Cumberbatch, David Pe, Yiyi Yao, and Sarah H. Tolbert's manuscript titled "Size-Dependent Suppression of Phase Transitions Leads to Fast-Charging in Nanoscale Li_xMoO_2". I performed the synthesis, structural characterization, electrochemical testing, operando XRD, and data analysis, while Helen, David and Yiyi helped with operando XRD data collection. I wrote the manuscript while Helen, David, Yiyi, and Professor Tolbert helped edit. This manuscript has been submitted for publication and is under review.

Chapter 3 is the unpublished version of Daniel Robertson and Sarah H. Tolbert's manuscript titled "Analyzing How the Suppression of Phase Transitions Leads to Pseudocapacitive Properties in Li_xMoO_2 Using Electrochemical Impedance Spectroscopy". I performed the synthesis, structural characterization, electrochemical testing, operando XRD, and data analysis. I wrote the manuscript while Professor Tolbert helped edit. This manuscript will be submitted for publication shortly after this dissertation is filed.

Chapter 4 is the unpublished version of Daniel Robertson, Charlene Salamat, David Pe, Helen Cumberbatch, and Sarah H. Tolbert's manuscript titled "Electrochemically-Formed Disordered Rock Salt ω-$V_9Mo_6O_{40}$ as a Fast-Charging Li-Ion Electrode Material". I performed the synthesis, structural characterization, electrochemical testing, and data analysis. Charlene carried out X-ray photoelectron spectroscopy while David and Helen collected operando XRD data. I wrote the manuscript while Charlene, David, Helen, and Professor Tolbert helped edit. This manuscript will be submitted for publication shortly after this dissertation is filed.

Chapter 5 is the unpublished version of Daniel Robertson, David Pe, Helen Cumberbatch, Glareh Kashanchi and Sarah H. Tolbert's manuscript titled "Fast-charging Disordered Rock Salt

Li-Ion Electrodes from Nanoporous $V_9Mo_6O_{40}$". I performed the synthesis, structural characterization, electrochemical testing, and data analysis. David and Helen collected operando XRD data while Glareh carried out N_2 porosimetry. I wrote the manuscript while David, Helen, Glareh, and Professor Tolbert helped edit. This manuscript will be submitted for publication shortly after this dissertation is filed.

Chapter 6 is the unpublished version of Daniel Robertson, Shreya Patel, Helen Cumberbatch, Billal Zayat and Sarah H. Tolbert's manuscript titled "Measuring electronic conduction in Nb-based high-rate anode materials *in situ*". I performed the synthesis, structural characterization, electrochemical testing, and data analysis. Shreya carried out magnetometry measurements, Helen synthesized and tested bulk NWO, and Billal helped developed the testing protocol. I wrote the manuscript while Shreya, Helen, and Professor Tolbert helped edit. This manuscript will be submitted for publication shortly after this dissertation is filed.

Chapter 7 is the published version of Kira Wyckoff, Daniel Robertson, Molleigh Preefer, Samuel Teicher, Jadon Bienz, Linus Kautzsch, Thomas Mates, Joya Cooley, Sarah Tolbert, and Ram Seshadri's manuscript titled "High-Capacity Li^+ Storage through Multielectron Redox in the Fast-Charging Wadsley-Roth Phase $(W_{0.2}V_{0.8})_3O_7$". Kira synthesized the bulk WVO, lead electrochemical testing, and carried out structural characterization, while I synthesized the nano WVO, and assisted with electrochemical testing. Molleigh performed the operando XRD and Samuel did the DFT calculations. Jadon assisted Kira with her contributions. Kira wrote the manuscript while Molleigh, Samuel, Professor Tolbert, Professor Seshadri and I helped edit.

The research presented in this dissertation was directed by Professor Sarah H. Tolbert and was supported by: US Department of Energy, Office of Basic Energy Sciences under Award Number DE-SC0014213 and the Center for Synthetic Control Across Length-scales for Advancing

Rechargeables (SCALAR), an Energy Frontier Research Center funded by the U.S. Department of Energy, Office of Science, Basic Energy Sciences under Award # DE-SC0019381. I acknowledge support from a National Science Foundation Graduate Research Fellowship under award DGE-2034835 and the UCLA Graduate Division Dissertation Year Fellowship. Much of the diffraction data presented here was collected at the Stanford Synchrotron Radiation Lightsource, a national user facility operated by Stanford University on behalf of the U.S. Department of Energy, Office of Basic Science under contract DE-AC02-76SF00515 and the Advanced Photon Source, a U.S. Department of Energy (DOE) Office of Science User Facility operated for the DOE Office of Science by Argonne National Laboratory under Contract No. DE-AC02-06CH11357. For all transmission electron microscopy characterization, the authors acknowledge the use of instruments at the Electron Imaging Center for NanoMachines supported by NIH (1S10RR23057, 1S10OD018111 and 1U24GM116792), NSF (DBI-1338135) and CNSI at UCLA.

VITA

2018	B.A. in Chemistry, Physics, and the College of Integrative Sciences, *Wesleyan University*
2018	Phi Beta Kappa Honor Society
2018	Karl Van Dyke Prize for Excellence in Physics, *Wesleyan University*
2018	Wallace C. Pringle Prize for Research in Chemistry, *Wesleyan University*
2018	ACS Division of Inorganic Chemistry National Award for Undergraduate Research, *Honorable Mention*
2018	UCLA College of Letters & Sciences Alumni Merit Award
2019	UCLA Research Showcase Fellowship Award
2019	National Science Foundation Graduate Research Fellowship
2020	M.S. In Chemistry, *University of California, Los Angeles*
2021	Jim and Barbara Tsay Excellence in Second Year Research and Academics Award
2022	Ralph and Charlene Bauer Award for Research, Teaching and Service
2022	George Gregory Excellence in Research Award
2022	UCLA Dissertation Year Fellowship
2023	Trueblood Dissertation Award

PUBLICATIONS

1. Yao. Y.; Cumberbatch, H.; Robertson, D.D.; Chin, M.A.; Lamkin, R.; Tolbert, S.H.; On the Interplay between Size and Disorder in Suppressing Intercalation-Induced Phase transitions in Pseudocapacitive Nanostructured MoS_2. *Adv. Funct. Mater. In press*.

2. Patel, S.K.; Robertson, D.D.; Cheema, S.S.; Salahuddin, S.; Tolbert, S.H.; *In-situ* Measurement of Magnetoelectric Coupling in Composites of $CoFe_2O_4$ and $Hf_{0.5}Zr_{0.5}O_2$ with Residual Porosity. *Nano Lett.* **2023,** *23* (8)*,* 3267-3273.

3. Robertson, D.D.; Tolbert, S.H. A direct and clean route to MXenes. *Science* **2023**, *379* (6638), 1189-1190.

4. †Patel, S.K; †Karaba, C. T.; Robertson, D.D.; Chang, J.; Fitzell, K.; Salamat, C.Z.; Chang, J.P.; Tolbert, S.H. Increased Magnetic Coupling in Porous Nanocomposites of $CoFe_2O_4$ and $BiFeO_3$ with Residual Porosity for Switchable Magnetic Devices. *ACS Appl. Nano Mater.* **2023**. *6* (6) 4141-4150.

5. Baek, S.W.; Wyckoff, K.E.; Robertson, D.D.; Frajnkovic, M.; Zhou, Y.; Tolbert, S.H.; Seshadri, R.; Pilon, L.; Probing the effect of particle size in the heat generation of Wadsley-Roth shear phase $(W_{0.2}V_{0.8})O_7$ with *operando* calorimetry. *ACS Appl. Energy Mater.* **2023**. *6* (3), 1355-1357.

6. Cook, J.B.; Ko, J.S.; Lin, T.C.; Robertson, D.D.**;** Kim, H.-S.; Yan,Y.; Yao, Y. Dunn, B.S.; Tolbert, S.H. Ultrafast Sodium Intercalation Pseudocapacitance in MoS_2 Facilitated by Phase Transition Suppression. *ACS Appl. Energy Mater.* **2023**, *6* (1), 99-108.

7. Andrews, J.L.; McClure, E.T.; Jew, K.K.; Preefer, M.B.; Irshad, A.; Lertola, M.J.; Robertson, D.D.; Salamat, C.Z.; Brady, M.J.; Piper, L.F.J.; Tolbert, S.H; Nelson Weker, J.; Chmelka, B.F.; Dunn, B.S.; Narayan, S.R.; West, W.C.; Melot, B.C. Room Temperature Electrochemical Fluoride (De)Insertion into the Defect Pyrochlore $CsMnFeF_6$. *ACS Energy Lett.* **2022**, 7*,* 2340-

2348.

8. Yan, Y.; Chin, M.A.; Robertson, D.D.**;** Lesel, B.K.; Tolbert, S.H. Tuning the Porous Structure in PMMA-Templated Mesoporous MoO_2 for Pseudocapacitive Li-ion Electrodes. *J. Electrochem. Soc.* **2022***,* 169, 4, 040545.
9. †Wyckoff, K.E.; †Robertson, D.D.**;** Preefer, M.B.; Teicher, S.M.; Bienz, J.; Kautzsch, L.; Mates, T.E.; Cooley, J.A.; Tolbert, S.H.; Seshadri, R. High-Capacity Li^+ Storage through Multielectron Redox in the Fast-Charging Wadsley–Roth Phase $(W_{0.2}V0_{.8})_3O_7$. *Chem. Mater.* **2020**, *32* (21), 9415-9424.
10. Robertson, D. D.; Personick, M. L. Growing Nanoscale Model Surfaces to Enable Correlation of Catalytic Behavior Across Dissimilar Reaction Environments. *Chem. Mater.* **2019**, 31, 4, 1121-1141.
11. Stone, A. L.; King, M. E.; McDarby, S. P.; Robertson, D. D.; Personick, M. L. Synthetic Routes to Shaped AuPt Core-Shell Particles with Smooth Surfaces Based on Design Rules for Au Nanoparticle Growth. *Part. Part. Syst. Charact.* **2018**, *35*, 1700401.
12. Robertson, D. D.; King, M. E.; Personick, M. L. Concave Cubes as Experimental Models of Catalytic Active Sites for the Oxygen-Assisted Coupling of Alcohols by Dilute (Ag)Au Alloys. *Top. Catal.* **2018**, *61*, 348

† = authors contributed equally.

PRESENTATIONS

1. Robertson, D.D.; King, M.E.; Personick, M.L. *Shaped Nanoparticles as Experimental Models of Computationally Predicted Active Sites: (Ag)Au Concave Cubes for the Oxidative Coupling of Alcohols.* American Chemical Society, Spring National Meeting, **2018**, New Orleans, LA.
2. Robertson, D.D.; Yao, Y., Chin, M.; Lin, T.; Tolbert, S.H. *Operando X-ray diffraction gives insight into the origin of pseudocapacitance in nano-MoO_2.* American Chemical Society, Fall National Meeting, **2019**, San Diego, CA.
3. Robertson, D.D.; Yao, Y.; Dawson, A.D.; Agyeman-Budu, D.; Tolbert, S.H. *Understanding the order-to-disorder transition in the fast-charging Li-ion electrode material $V_9Mo_6O_{40}$.* American Chemical Society, Spring National Meeting, **2022**, San Diego, CA.

CHAPTER 1

Introduction

Electrochemical energy storage devices with both high energy density and high power density are technologically necessary for the electrification of transportation and many other applications.[1-4] Insertion-based Li-ion batteries, which rely on redox reactions in which Li^+ is reversibly inserted into a host material, are the current standard for high capacity fast-charging devices.[3] With decades of research, these electrodes have shown dramatic improvements in performance, but still possess limits on their achievable capacities at high rates, especially in thick electrodes used for commercial cells.[5] At high cycling rates, the solid-state diffusion of Li^+, the transport of electrons, and the need for phase transformations during (de)lithiation can all slow charge storage.[6-9] These challenges can be mitigated through control over material structure. Nanoscale architecture can provide short distances for diffusion of Li^+ in the electrode and alter the mechanisms for phase transformations during cycling.[10-15] In combination, strategic design of atomic-scale crystal structure can provide faster Li^+ diffusion and electron transport throughout the host material.[16-18] Further improvements in power density beyond the current state-of-the-art Li-ion batteries will require a fundamental understanding of these parameters, which is the goal of this dissertation.

Chapters 2 and 3 focus on size-dependent phase transition behavior in MoO_2, a model tunnel structure insertion host. MoO_2 has shown promise as a potential anode material since the 1970s, but has recently received greater interest due to its significantly improved performance when nanostructured.[19,20] We demonstrate clearly that size-induced suppression of the first-order phase transition is essential to the fast-charging capabilities of nanoscale MoO_2 (Chapter 2). Using operando X-ray diffraction on a series of size-controlled nanomaterials, we show that the large

first-order phase transformation in bulk MoO_2 shrinks dramatically, but remains first-order, in intermediately sized nanoporous MoO_2, and then becomes entirely single-phase (solid-solution) in smaller MoO_2 nanocrystals. With a series of electrochemical kinetic analyses, we identify specific signatures of slowed charge storage that arise due to the phase transformation in bulk MoO_2, and demonstrate their systematic attenuation as a function of size in the nanomaterials. For example, using galvanostatic intermittent titration technique (GITT), we show that the large overpotentials that occurs at the onset of the phase transformation in bulk MoO_2 decrease by an order of magnitude in the medium sized nanoporous materials, which have partly suppressed transitions, and then drop by another order of magnitude in the nanocrystals with fully suppressed transitions.

Using our size-controlled MoO_2, we also analyzed how phase transition behavior governs the emergence of pseudocapacitive properties. We conducted a series of analyses with electrochemical impedance spectroscopy (EIS) to distinguish the charge storage mechanism and connect it to our previous characterization of phase transition behavior during cycling. Notably, EIS was used to measure capacitance as a function of voltage, which was compared to the capacity, which includes both capacitive and diffusion-limited components of charge storage. the initial portion of lithiation, where all sizes of MoO_2 show solid-solution type behavior, the capacitance measured for nanoporous MoO_2 and MoO_2 nanocrystals were similar, but bulk MoO_2 showed about half the capacitance, despite having the same capacity at that voltage. During the phase transition region, the difference was even more dramatic, with the nanocrystals showing the highest peak capacitance at 800 F/g, even though they have the lowest capacity in this region. In contrast, bulk MoO_2 showed less than one fourth the capacitance of 150 F/g even though it has by far the highest capacity at this potential. The results of this analysis indicated that the combination of long Li^+ diffusion distances and the large first-order phase transition in bulk MoO_2 lead to its

diffusion-controlled charge storage mechanism. Importantly, the faster Li^+ diffusion and suppression of the phase transition in the nanoscale materials were key to realizing pseudocapacitive properties in MoO_2. Overall, these works emphasize the key role of structural dynamics on rate capability and charge storage mechanisms, and highlight how those phase transition dynamics can be effectively controlled using nanoscale size in Li-ion electrode materials.

Chapters 4 and 5 focus on $V_9Mo_6O_{40}$ (VMO), which is one of an emerging class of materials that transform into disordered rock salt (DRS) compounds upon electrochemical lithiation. These electrochemically-formed DRS materials have recently gained greater interest due to their impressive rate capability, but the specific factors that govern the formation process and the resulting charge storage performance remain poorly understood.[21-23] In chapter 4, we characterize the transformation mechanism and charge storage properties of electrochemically formed DRS VMO in micron-scale particles. The crystal structure of VMO has similar motifs to that of α-V_2O_5, a well-studied analog, but VMO has less mechanical flexibility due to additional corner-sharing octahedra in its structure. As a result, VMO undergoes a single-step transformation pathway, which we characterize through operando X-ray diffraction, and forms an unusual highly distorted lamellar microstructure, as we show with high-resolution transmission electron microscopy. The resulting material shows electrochemical characteristics and performance typical of many nanomaterials, even with relatively large particles. Then, in chapter 5, we synthesize nanoporous VMO to show how optimized Li^+ diffusion distances can improve the rate capability of VMO even further. Nanoporous VMO undergoes a similar, but more facile, transformation process, and the resulting microstructure does not show the same distortions as it did for the bulk. Additionally, we characterize the faster charge storage behavior with electrochemical kinetics analysis that highlight lower polarization in nanoporous VMO relative to the bulk material.

Chapter 6 describes the development of a platform for *in situ* contact measurements of electronic conductivity of the bronze phase electrode materials T-Nb_2O_5 and $Nb_{18}W_{16}O_{93}$ (NWO). Like many other high-rate anode materials, T-Nb_2O_5 and NWO are insulating as synthesized, but become conductive when lithiated.[12,16,17] However, the quantification of electronic conductivity during lithiation remains a major challenge, since most measurement geometries are incompatible with electrochemical cycling.[24,25] Here, we developed a method for quantitative *in situ* measurement electronic conductivity by depositing interdigitated microelectrodes onto thin films of active material. Using this method, we characterize the insulating to conductive transition in T-Nb_2O_5 and NWO. Both materials exhibit dramatic changes of at least four orders of magnitude change in conductivity with lithiation, but NWO's change occurs much more quickly in the early stages of lithiation. We support these contact measurements with magnetic characterization that shows significantly more delocalization of electrons in NWO at low Li content. These differences in the transition explain NWO's improved electrochemical performance compared to T-Nb_2O_5.

Chapter 7 focuses on the Wadsley-Roth (WR) shear phase $(W_{0.2}V_{0.8})_3O_7$ (WVO). WR shear materials have recently shown high rate capability, even in micron-scale particles, but most are based primarily on Nb as the redox-active transition metal.[26] For the first time, we demonstrated high rate, high capacity charge storage using a V-based WR structure, and investigated the mechanism for Li^+ storage using a combination of electrochemical techniques, X-ray measurements, and density functional theory calculations. Strong rate capability was observed for both the bulk material produced through a solid-state route and 100 nm nanorods synthesized with a solution-based process. This work extends the range of high-performing WR materials to those without Nb and opens up the possibility for compositional tuning within the family.

1.1 References

[1] Lopes, J. A. P.; Soares, F. J.; & Almeida, P. M. R. Integration of electric vehicles in the electric power system. *Proc. IEEE*, **2010**, *99*, 168-183

[2] Gür, T.M. Review of electrical energy storage technologies, materials and systems: challenges and prospects for large-scale grid storage. *Energy Environ. Sci.* **2018**, *11*(10), 2696–2767.

[3] Frith, J.T.; Lacey, M.J.; Ulissi, U. A non-academic perspective on the future of lithium-based batteries. *Nat. Commun.* **2023**, *14*(1), 420.

[4] Li, M.; Lu, J.; Chen, Z.; Amine, K. 30 years of lithium-ion batteries. *Adv. Mater.* **2018**, *30* (33), 1800561.

[5] Choi, C.; Ashby, D.S.; Butts, D.M.; DeBlock, R.H.; Wei, Q.; Lau, J.; Dunn, B. Achieving high energy density and high power density with pseudocapacitive materials. *Nat. Rev. Mater.* **2020**, *5*(1), 5–19.

[6] Ven, A. Van Der; Bhattacharya, J.; Belak, A. A. Understanding Li Diffusion in Li-Intercalation Compounds. *Acct. Chem. Res.* **2013**, *46*, 1216-1225.

[7] Chung, S.Y.; Bloking, J.T.; Chiang, Y.M. Electronically conductive phospho-olivines as lithium storage electrodes. *Nat. Mater.* **2002**, 1(2), 123–128.

[8] Kang, B.; Ceder, G. Battery materials for ultrafast charging and discharging. *Nature* **2009**, *458*, 190–193.

[9] Cook, J. B.; Lin, T. C.; Kim, H.-S.; Siordia, A.; Dunn, B. S.; Tolbert, S. H. Suppression of Electrochemically Driven Phase Transitions in Nanostructured MoS_2 Pseudocapacitors Probed Using Operando X-ray Diffraction. *ACS Nano*, **2019**, *13*, 1223–1231.

[10] Okubo, M.; Hosono, E.; Kim, J.; Enomoto, M.; Kojima, N.; Kudo, T.; Zhou, H.; Honma, I. Nanosize Effect on High-Rate Li-ion Intercalation in $LiCoO_2$ Electrode. *J Am. Chem. Soc.* **2007**, *129*, 7444-7452.

[11] Kang, B.; Ceder, G. Battery materials for ultrafast charging and discharging. *Nature* **2009**, *458*, 190-193.

[12] Augustyn, V.; Come, J.; Lowe, M. A.; Kim, J. W.; Taberna, P.; Tolbert, S. H.; Abruña, H. D.; Simon, P.; Dunn, B. High-Rate Electrochemical Energy Storage through Li^+ Intercalation Pseudocapacitance. *Nat. Mater.* **2013**, *12*, 518-522.

[13] Sun, H.; Mei, L.; Liang, J.; Zhao, Z.; Lee, C.; Fei, H.; Ding, M.; Lau, J.; Li, M.; Wang, C.; Xu, X. Three-dimensional holey-graphene/niobia composite architectures for ultrahigh-rate energy storage. *Science*, **2017**, *356* (6338), 599–604

[14] Wagemaker, M.; Mulder, F.M. Properties and promises of nanosized insertion materials for Li-ion batteries. *Acc. Chem. Res*. **2013**, *46*(5), 1206–1215.

[15] Jain, R.; Lakhnot, A.S.; Bhimani, K.; Sharma, S.; Mahajani, V.; Panchal, R.A.; Kamble, M.; Han, F.; Wang, C.; Koratkar, N. Nanostructuring versus microstructuring in battery electrodes. *Nat. Rev. Mater.* **2022**, *7*(9), 736–746.

[16] Griffith, K. J.; Wiaderek, K. M.; Cibin, G.; Marbella, L. E.; Grey, C. P. Niobium tungsten oxides for high-rate lithium-ion energy storage. *Nature*, **2018**, *559*, 556–563.

[17] Griffith, K.J.; Seymour, I.D.; Hope, M.A.; Butala, M.M.; Lamontagne, L.K.; Preefer, M.B.; Koçer, C.P.; Henkelman, G.; Morris, A.J.; Cliffe, M.J.; Dutton, S.E.; Grey, C.P. Ionic and Electronic Conduction in $TiNb_2O_7$. *J. Am. Chem. Soc.* **2019**, *141* (42), 16706–16725.

[18] Koçer, C. P.; Griffith, K. J.; Grey, C. P.; Morris, A. J. Lithium Diffusion in Niobium Tungsten Oxide Shear Structures. *Chem. Mater.* **2020**, *32* (9), 3980–3989.

[19] Dahn, J. R.; McKinnon, W. R. Structure and Electrochemistry of Li_xMoO_2. *Solid State Ion.* **1987**, *23* (1–2), 1–7.

[20] Kim, H.-S.; Cook, J. B.; Tolbert, S. H.; Dunn, B. The Development of Pseudocapacitive Properties in Nanosized-MoO_2. *J. Electrochem. Soc.* **2015**, *162*, A5083–A5090.

[21] Delmas, C.; Brèthes, S.; Ménétrier, M. ω-$Li_xV_2O_5$ - a New Electrode Material for Rechargeable Lithium Batteries. *J. Power Sources* **1991**, *34* (2), 113–118.

[22] Liu, H.; Zhu, Z.; Yan, Q.; Yu, S.; He, X.; Chen, Y.; Zhang, R.; Ma, L.; Liu, T.; Li, M.; Lin, R.; Chen, Y.; Li, Y.; Xing, X.; Choi, Y.; Gao, L.; Cho, H. S. yun; An, K.; Feng, J.; Kostecki, R.; Amine, K.; Wu, T.; Lu, J.; Xin, H. L.; Ong, S. P.; Liu, P. A Disordered Rock Salt Anode for Fast-Charging Lithium-Ion Batteries. *Nature* **2020**, *585* (7823), 63–67.

[23] Barnes, P.; Zuo, Y.; Dixon, K.; Hou, D.; Lee, S.; Ma, Z.; Connell, J. G.; Zhou, H.; Deng, C.; Smith, K.; Gabriel, E.; Liu, Y.; Maryon, O. O.; Davis, P. H.; Zhu, H.; Du, Y.; Qi, J.; Zhu, Z.; Chen, C.; Zhu, Z.; Zhou, Y.; Simmonds, P. J.; Briggs, A. E.; Schwartz, D.; Ong, S. P.; Xiong, H. Electrochemically Induced Amorphous-to-Rock-Salt Phase Transformation in Niobium Oxide Electrode for Li-Ion Batteries. *Nat. Mater.* **2022**, *21* (7), 795–803.

[24] Salinas, G.; Frontana-Uribe, B. A. Analysis of Conjugated Polymers Conductivity by in situ Electrochemical-Conductance Method. *ChemElectroChem* **2019**, *6* (16), 4105–4117.

[25] Zayat, B.; Das, P.; Thompson, B. C.; Narayan, S. R. In Situ Measurement of Ionic and Electronic Conductivities of Conductive Polymers as a Function of Electrochemical Doping in Battery Electrolytes. *J. Phys. Chem. C* **2021**, *125* (14), 7533–7541.

[26] Voskanyan, A. A.; Navrotsky, A. Shear Pleasure: The Structure, Formation, and Thermodynamics of Crystallographic Shear Phases. *Ann. Rev. Mater. Sci.* **2021**, *51*, 521–540.

CHAPTER 2

Size-Dependent Suppression of Phase Transitions Leads to Fast-Charging in Nanoscale Li_xMoO_2

2.1 Introduction

Electrochemical energy storage devices with both high energy density and high power density are technologically necessary for the electrification of transportation and many other applications.[1,2] Despite the continued development of next-generation energy storage technologies, insertion-based Li-ion batteries remain the standard for high capacity fast-charging devices.[3] These electrodes store energy through charge-transfer reactions in which Li^+ is reversibly inserted into a host material. Over decades of research, these electrodes have shown dramatic improvements in both energy and power density, but still possess limits on their achievable capacities at high rates, especially in thick electrodes used for commercial cells.[4-6] To improve power density, a fundamental understanding of the key parameters that allow for fast and reversible redox reactions in electrode materials is necessary.[7,8]

At high cycling rates, the solid-state diffusion of Li^+, the transport of electrons, and the need for phase transformations during (de)lithiation can all slow charge storage and limit the attainable capacity in insertion electrodes.[9-13] A common approach to decrease these kinetic limitations in electrode materials is to use nanostructured architectures of the active material instead of dense micron-scale particles.[14-24] By shortening the solid-state diffusion distances required for Li^+, nanostructuring can significantly increase the capacity at high cycling rates. More recent work has also emphasized that the smaller crystal domain sizes in nanostructured materials alter phase transformations induced by Li^+ insertion, as an important component of their faster rate capability. [53-36] In most bulk battery materials, lithiation requires one or more first-order phase

transitions, where the crystal structure transforms through nucleation and growth of a new phase.[37-40] While energetically favorable, these phase transitions are widely considered to slow lithiation kinetics, since they often require large activation energies and limit lithiation until they are complete. As such, the full or partial suppression of phase transitions in nanoscale battery materials has been broadly linked to the emergence of fast-charging[53-28] and the progression from a diffusion-limited to a pseudocapacitive charge storage mechanism.[4,7,29-36] Despite major interest in fast-charging and pseudocapacitive electrodes and the wide variety of materials where these effects has been observed, however, the current understanding of how suppression occurs in most materials remains largely anecdotal. Overall, a coherent picture of size effects in battery materials requires a better understanding of phase transformation behavior and its relationship to kinetics.

Here, we provide new insight into the size-dependent suppression of phase transitions in MoO_2, a model phase-transforming insertion electrode material. MoO_2 has a rutile-type tunnel structure that has seen interest as an insertion electrode since the 1970s.[41–43] Its crystal structure comprises chains of edge-sharing Mo-O octahedra arranged in alternating orientations. Between these chains are tunnels of interstitial sites for Li^+ diffusion and storage, while overlap of partially filled *d* orbitals between neighboring Mo atoms along the chains provides metallic electrical conductivity.[42] Despite these advantages, micron-scale MoO_2 shows rather slow (de)insertion kinetics, due to its need for a first-order phase transition during Li^+ insertion and its considerable 13% increase in unit cell volume at full lithiation.[43,44] More recently, nanostructured architectures of MoO_2 have shown much higher rate capability,[31,45-48] with limited *ex situ* evidence for changes in their phase transition mechanism during lithiation.

In this work, we use *operando* synchrotron X-ray diffraction (SXRD) to conclusively show that nanoscale MoO_2 undergoes a dramatically different structural response to Li^+ insertion

than bulk MoO_2, and analyze the stepwise progression of this behavior in a series of size-controlled nanoarchitectures. First, we characterize the large first-order phase transition in micron-scale bulk MoO_2, and use electrochemical kinetics techniques to highlight that severe electrode polarization directly arises from the onset of this phase transition. Then, we show that in nanoporous MoO_2 with intermediate crystal sizes, the same phase transformation remains first-order, but shows a decrease in both the miscibility gap between the two phases and the duration of their coexistence. Interestingly, this partial suppression of the phase transition decreases kinetic limitations considerably. In even smaller 15 – 20 nm MoO_2 nanocrystals, we observe a complete change in the phase transformation mechanism to a second-order-type solid-solution event, in which the material remains a single phase with no discontinuous changes in symmetry throughout lithiation. This change in behavior is accompanied by a near-complete disappearance of the polarization linked to the phase transition. Finally, we highlight the significantly improved cycle lifetime in all of the nanoscale MoO_2 materials compared to the bulk, which confirms that repeated discontinuous volume changes from phase transitions are a major source of electrode degradation. Overall, this work affirms the negative effects of large first-order phase transitions on cycling performance, but also emphasizes that complete first-order transition suppression is not required to observe improved kinetics in nanoscale materials.

2.2 Materials and Methods

2.2.1 Materials.

The following materials were obtained from commercial suppliers and used without further purification: ammonium molybdate (para) tetrahydrate $(NH_4)_6Mo_7O_{24}•4H_2O$ (99%, Alfa Aesar), ammonium persulfate (98%, Alfa Aesar), ammonium lauryl sulfate (~30% in H_2O, Sigma Aldrich),

molybdenum (V) chloride (99.6%, Alfa Aesar), methyl methacrylate (contains ≤ 30 ppm MEHQ as inhibitor, 99%, Sigma Aldrich).

2.2.2 Preparation of bulk and nanoporous MoO_2.

The bulk and nanoporous MoO_2 samples were synthesized through a modified sol-gel route using freeze-drying. In this process, an aqueous solution of dissolved Mo precursor is frozen in liquid N_2 and dried under vacuum, then subsequently calcined to crystallize the material. To produce the nanoporous MoO_2 materials, polymer colloids of various sizes were mixed with the Mo precursor in the initial solution in order to template the nanoscale architecture.

In a typical synthesis of bulk MoO_2, 200 mg of $(NH_4)_6Mo_7O_{24}•4H_2O$ was added to 3 mL of water, then heated at 60ºC until it was fully dissolved. The resulting solution was frozen by dropwise addition into liquid N_2 and lyophilized on a Schlenk line for 12 to 24 hours (<200 mtorr). The dried Mo precursor powder was then calcined in a quartz boat at for 1 hour at 625ºC in flowing $5\%H_2/95\%N_2$ (1 hour heating ramp time and natural cooling rate). For the nanoporous MoO_2 samples, a similar procedure was followed with slight modifications. In a typical synthesis, 200 mg of $(NH_4)_6Mo_7O_{24}•4H_2O$ was added to 2 mL of water, then heated at 60ºC until it was fully dissolved. Then, 2 – 4 mL of polymer colloid solution were added (depending on the density of colloids in solution) to obtain a 1:1 mass ratio of Mo precursor:colloid. The synthesis of the PMMA colloids with different sizes is described below. After the Mo precursor-polymer colloid solution was mixed thoroughly, it was frozen by dropwise addition to liquid N_2 and lyophilized on a Schlenk line for 12 to 24 hours (< 200 mtorr). The dried Mo precursor-polymer composite powder was calcined in a quartz boat in flowing Ar in two separate heating steps, with the powder cooled, removed from the furnace and exposed to air in between: first, at 550ºC for 1 hour, and then at 675ºC for 1 hour (1 hour heating ramp time for each step and natural cooling rate). This two-

heating-step process was employed to separate removal of the polymer templates from crystallization of the MoO_2 material. Since calcination occurs under anaerobic conditions, the polymer templates do not combust fully and, with a single step process, Mo carbides form at the temperatures needed to crystallize the nanoporous MoO_2. After the second calcination, nanoporous MoO_2 samples were stored in inert atmosphere to avoid ambient oxidation.

2.2.3 Synthesis of poly(methyl methacrylate)(PMMA) colloids.

The synthesis of PMMA colloids with different sizes was adapted from a previous procedure described by Wang et al.[58] Ammonium persulfate (APS) was used as the initiator and ammonium lauryl sulfate (ALS) as the surfactant. APS, ALS, and deionized water were put into a three-neck round-bottom flask (250 mL) equipped with a magnetic stirrer, a reflux condenser, and a thermometer. After the temperature was raised to 75 °C, the monomer methyl methacrylate (MMA) was added. After monomer addition, the reaction temperature was kept at 80–85 °C for an hour before a cooling operation was applied. The concentrations of reagents were varied to make different sizes of PMMA. The as-synthesized PMMA colloidal aqueous solutions were extracted with hexanes to remove excess monomer. Before use, the mass density of colloids in solution was measured by thermogravimetric analysis. Table S1 gives detailed synthesis conditions.

2.2.4 Synthesis of MoO_2 nanocrystals.

MoO_2 nanocrystals were synthesized in a hydrothermal autoclave according to previously reported method with minor adaptations. In a typical synthesis, 270 mg of $MoCl_5$, 15 mL water, and 5 mL ethanol were added to a 50 mL Teflon-lined Parr autoclave. The autoclave was sealed and heated for 6 hours at 180ºC, then allowed to cool overnight. The product was centrifuged washed with ethanol three times. After the final wash, the powder was dried at 80ºC under vacuum. The as-synthesized nanocrystals were stored under inert atmosphere to avoid ambient oxidation.

2.2.5 Structural characterization.

Scanning electron microscopy (SEM) images were obtained using a model JEOL JSM-6700F field emission electron microscope with 5 kV accelerating voltage and 6 mm working distance. Transmission electron microscopy (TEM) was performed using an FEI Titan S/TEM operating at 300 kV. Sample purity was assessed using laboratory X-ray diffraction collected with a PANalytical X'Pert Pro diffractometer operating with Cu Kα (λ = 1.5418 Å) using a 0.05° step size, an accelerating voltage of 45 kV, and a current of 40 mA. High resolution X-ray diffraction patterns of pristine materials were taken at Stanford Synchrotron Radiation Lightsource Beamline 11-3 with 12.7 keV energy.

2.2.6 Electrochemical testing.

All MoO_2 powders were assembled into composite slurry electrodes for electrochemical testing. Electrodes had an overall composition of 70% active material, 10% multiwalled carbon nanotubes, 10% vapor-grown carbon fibers, and 10% polyvinylidene fluoride (PVDF) binder. Prior to slurry preparation, the dry slurry components and current collector were heated at 100ºC under vacuum overnight. The active material was ground with the carbons in a mortar and pestle dry, then a PVDF binder solution (2.5 % wt in N-methyl pyrrolidone) was added and mixed to produce a homogeneous paste that was cast onto an aluminum current collector with a doctor blade. The electrodes were dried under vacuum at 100ºC overnight. Electrodes with 0.7 mm diameter were punched out for electrochemical testing with mass loadings of active material of 1 – 1.5 mg/cm^2. These moderate mass loadings were chosen to study the intrinsic performance of the active material, as they allow for reproducible electrode performance with minimal optimization of the slurry. High mass loadings, such as those used in most practical devices, lead to rate

limitations from electrode composition and distribution of active material that require extensive optimization to overcome.

All electrochemical measurements were conducted in stainless-steel 2032 coin cells (MTI) with a stainless-steel conical spring, two 0.5-mm stainless-steel spacers, a glass microfiber separator (Whatman), and a polished Li metal electrode (Sigma). The electrolyte was 1 M $LiPF_6$ in 1:1 ethylene carbonate (EC): dimethyl carbonate (DMC), with ~50 uL of electrolyte used per cell. All cycling experiments were performed between 1.1 V and 3 V *vs.* Li/Li^+ on a VMP3 potentiostat/galvanostat (Bio-Logic). While the potential window used here for MoO_2 makes it generally more suitable for use as an anode, for testing purposes MoO_2 electrodes were studied in a half cell configuration versus a Li metal anode. When calculating C-rates, the theoretical capacity used was 210 mAh/g, based on the 1 e^- Li^+ insertion reaction into MoO_2 (1C = 210 mA/g, 5C = 1.05 A/g, etc.). Galvanostatic intermittent titration technique analysis was performed with a series of current pulses, with each pulse consisting of applied current corresponding to a C/10 rate for 10 minutes, followed by 2 hours of relaxation under open circuit conditions.

2.2.7 Operando Synchrotron X-ray Diffraction - Bulk MoO_2 with AMPIX Cell

As discussed in the main text, two formats were used for *operando* SXRD experiments. The first, which involved AMPIX cells with pellet electrodes, was used for detailed structural characterization of bulk MoO_2 (**Figure 3**), since the high mass loading, lack of current collector, and high X-ray flux provides exceptional signal-to-noise ratio. These *operando* powder diffraction measurements were performed at beamline 11-ID-C at the APS at Argonne National Laboratory at 17.0 keV in transmission geometry with an area detector. For the experiment, freestanding pellet electrodes were made with 6:1:1:2 mass ratio of MoO_2: vapor-grown carbon fibers: multiwalled carbon nanotubes: PTFE binder. These electrodes were loaded into AMPIX cells in an argon

glovebox with lithium metal counter electrodes, glass fiber separators, and electrolyte (1M $LiPF_6$ in 1:1 EC:DMC).

2.2.8 Operando Synchrotron X-ray Diffraction - Modified Coin Cells with Be Spacers

The second format for *operando* SXRD is more similar to standard coin cell environment using standard slurry electrodes in modified coin cells with Be spacers, and was used to collect data on all the MoO_2 materials in a realistic cycling configuration (**Figure 4**). These experiments were conducted in a similar format, but at beamline 11-3 at the Stanford Synchrotron Radiation Lightsource at 12.7 keV. The design for the modified coin cells with Be spacers was adapted from Chien et al.[74] and is shown in **Figure S6**. While conventional modified coin cells use stainless steel spacers with holes to provide X-ray transparency, experiments done with these cells are susceptible to artifacts due to the lack of stack pressure and electrical conductivity in the region probed by the X-ray beam.[75] Our improved cell design uses Be spacers, which do not have holes, and thus remain both rigid and conductive to accurately recreate the cycling environment in a real coin cell. Beryllium metal discs 15 mm in diameter x 0.5 mm thick were purchased from American Elements (99%). Caution: Beryllium oxide particulates formed from machining or breaking beryllium are carcinogenic and the material should be handled with caution.

2.2.9 Operando Synchrotron X-ray Diffraction - Data Processing

All two-dimensional SXRD data was calibrated with a LaB_6 external standard and integrated into one-dimensional diffraction patterns using GSAS-II.[59] Background subtraction was performed on diffraction data to remove scattering from the electrolyte (**Figure S8**). Rietveld refinement of the unit cell parameters was also conducted in GSAS-II. Crystal structures were visualized with the VESTA software package.[60]

2.3 Results and Discussion

2.3.1 Synthesis and characterization of size-controlled MoO_2

A series of size-controlled MoO_2 nanomaterials were synthesized by adapting previously reported methods and characterized with electron microscopy and X-ray diffraction (XRD) (**Figure 1A – I, S2 – S4**).[31,47] Nanoporous MoO_2 powders were produced using a modified polymer-templated sol-gel-type method based on freeze drying. In this process, aqueous solutions of $(NH_4)_6Mo_7O_{24}$ mixed with poly(methyl methacrylate) (PMMA) colloids were vitrified in liquid N_2 and freeze dried through sublimation on a Schlenk line. The resulting organic-inorganic composite precursors were then calcined under inert atmosphere to burn off the polymer templates and crystallize MoO_2 powders with a nanoporous morphology. Freeze-drying is a well-established route to powders with high surface area and porosity, and, here, helps to maintain the mixing and distribution of colloids during drying.[61—64] With this method, the porosity and wall thickness of the powders can be varied by changing the size of the pre-synthesized PMMA colloids (**Figure S1**).[47] Scanning electron microscopy (SEM) images for two representative sizes (template size = 60 nm and 150 – 200 nm) show well-defined internal porosity distributed throughout the material (**Figure 1B**, **1C**). The synthetic method produces pores that are not ordered, but that still largely retain the size and shape of the templates used. Low magnification transmission electron microscopy (TEM) characterization on the nanoporous MoO_2 indicates that, while the porosity is nanoscale, the powders form interconnected micron-scale primary particles (**Figure S3A**, **S3D**). High-resolution TEM micrographs highlight individual crystalline domains in the material (**Figure 1F**, **1G**). In the higher magnification image (**Figure 1G**), multiple crystallites approximately 8 – 12 nm in diameter with various orientations are shown to form the wall between two individual pores. In the lower magnification image (**Figure 1F**), these domains can be seen to produce a polycrystalline network throughout the interconnected particle, as shown by the different contrast

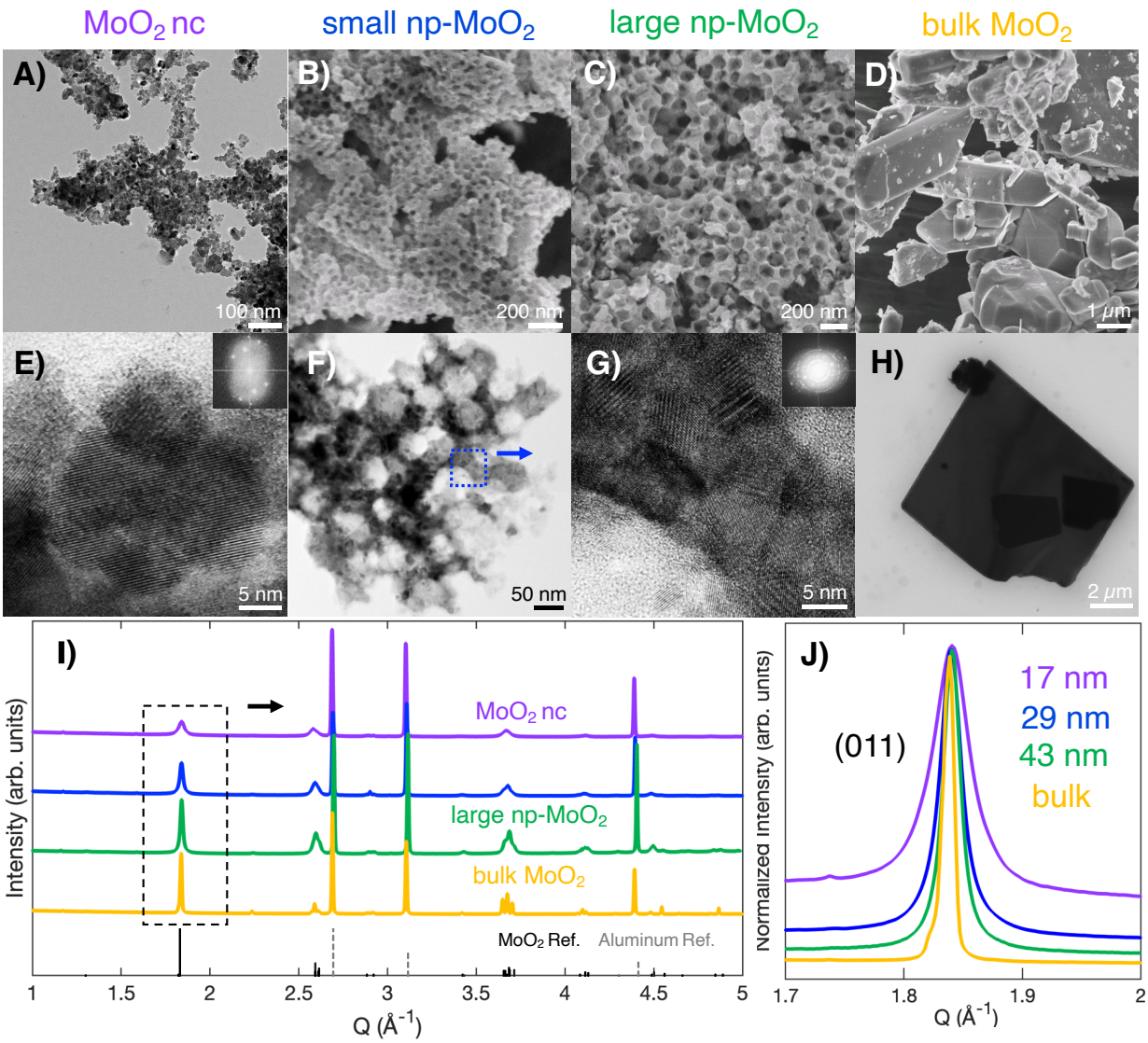

Figure 1. Structural characterization of the MoO_2 materials used in this study. 1A) Low magnification TEM / **(1B-1D)** SEM and **1E) – 1H)** high resolution TEM images of MoO_2 nanocrystals, small and large nanoporous MoO_2, and bulk MoO_2, respectively. The nanocrystals show single-domain nanoscale primary particles **(1E)** that aggregate into larger secondary particles **(1A)**, whereas the small and large nanoporous MoO_2 consist of micron-scale primary particles with nanoscale features **(1B,1C)**. The pore walls consist of many fused nanoscale crystallites **(1F,1G)**. The micron scale bulk crystals are single domain **(1D,1H). 1I)** Synchrotron-based X-ray diffraction of the MoO_2 materials in composite slurry electrodes, with the most prominent (011) reflection of MoO_2 highlighted in **1J)**, along with the calculated Scherrer size.

between neighboring domains. In all, these nanoporous powders consist of nanoscale crystallites that are fused together into micron-scale primary particles with a porous morphology. Additional

scanning and transmission electron microscopy characterization of both the small and large nanoporous MoO_2 can be found in the supporting information (**Figure S2**, **S3**).

Because very small but still well-ordered MoO_2 domains cannot be produced in nanoporous form, we also prepared hydrothermally-synthesized MoO_2 nanocrystals, which were first reported in a previous study.[31] SEM and low magnification TEM images of the MoO_2 nanocrystals show individual particles 15 – 30 nm in diameter (**Figure 1A**, **S2E** – **S2G**, **S4**). High-resolution TEM shows that the nanocrystals are single-domain, with lattice planes that extend across each individual particle (**Figure 1E**, **S4C**). In powder form, the nanocrystals appear to aggregate into much larger agglomerates, which likely form during the process of drying them out of solution. However, unlike the nanoporous MoO_2, in which crystallites are fused together at 675ºC, the individual nanoparticles should only be loosely associated. Importantly, despite their nanoscale size and good crystallinity, nanocrystals often form non-ideal architectures in composite electrodes due to the difficulty of distributing them into highly porous, electrically interconnected networks.[50,31] While these extrinsic limitations on their kinetics can be mitigated with appropriate electrode mixing and formulation techniques, the nanoporous materials offer similar, though slightly larger, sizes, but with the processing advantages of much larger primary particles.[52]

Finally, as a control to represent typical behavior of MoO_2 at large sizes, we synthesized bulk MoO_2 through the same sol-gel-based freeze drying method as the nanoporous MoO_2, except without any polymer template. The resulting bulk MoO_2 consists of anisotropic particles approximately 0.5 – 10 μm in diameter, which appear to be single-domain (**Figure 1D**, **1H**). To confirm the crystal structure and evaluate the crystallinity of the four different samples, synchrotron XRD was performed on pristine composite electrodes at beamline 11-3 at the Stanford Synchrotron Radiation Lightsource (SSRL). The resulting diffraction patterns confirm that all

samples are phase-pure crystalline MoO_2, with the only additional peaks arising from cell components like the Al current collector (**Figure 1J**). The most prominent (011) reflection of the patterns shows a clear progression in peak width (**Figure 1I**), with calculated Scherrer sizes of 17 nm, 29 nm, and 43 nm, for the MoO_2 nanocrystals, small nanoporous, and large nanoporous samples, respectively.

2.3.2 Electrochemistry of Size-Controlled MoO_2

To evaluate the effects of nanoscale size and morphology on electrochemical performance, the MoO_2 materials were assembled into composite electrodes with conductive carbon and binder and tested in a half-cell configuration in coin cells. MoO_2 is often studied for its high capacity conversion reaction, in which it is fully reduced to form Mo metal and Li_2O.[65-72] However, this reaction suffers from large volume changes and the formation of insulating Li_2O, which hinder its reversibility and rate capability. Here, we limit the lower voltage bound to 1.1 V vs. Li/Li^+ to access only the one electron insertion reaction, in which Li^+ is reversibly inserted into vacant interstitial sites within the tunnels of MoO_2 (Equation 1). This reaction has a moderate theoretical capacity of 210 mAh/g and shows significantly improved cyclability and scalability compared to conversion.

$$(1)\ MoO_2 + x\ e^- + x\ Li^+ \rightleftharpoons Li_xMoO_2 \quad (0 \leq x \leq 1)$$

The rate capabilities of the MoO_2 materials were evaluated with galvanostatic rate testing (**Figure 2A**). The nanoporous MoO_2 and the MoO_2 nanocrystals show nearly complete insertion reactions at slower rates, with capacities near theoretical at 1C. At higher rates, both nanoporous samples show excellent retention of this capacity, storing 128 and 130 mAh/g at 20C, for the small and large nanoporous MoO_2, respectively, corresponding to 70% of their 1C capacity maintained at 20C. The MoO_2 nanocrystals also exhibit excellent rate capabilities, with 130 mAh/g capacity at 20C (63% of their 1C capacity). Bulk MoO_2, on the other hand, shows comparatively poor

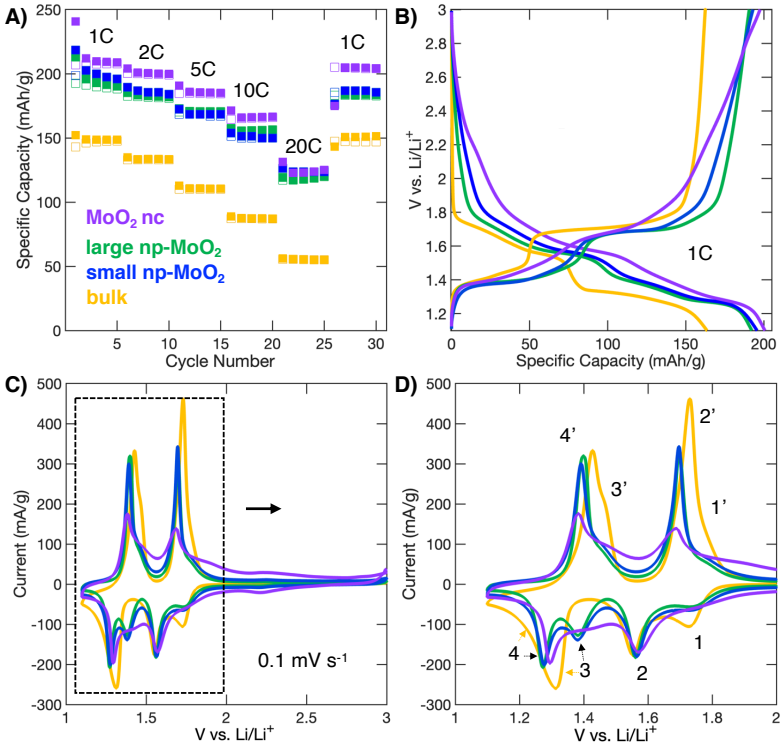

Figure 2. Electrochemical characterization of MoO_2 materials. 2A) Galvanostatic rate cycling performance statistics show near full theoretical capacity for the insertion reaction at 1C, and strong retention of capacity at higher current densities, for all of the nanostructured MoO_2. Bulk MoO_2, however, shows low capacity at 1C and poor rate capability. **2B)** Galvanostatic profiles and **2C,D)** cyclic voltammograms for each MoO_2 material at slow cycling rates highlight the intrinsic changes in redox. Peaks 1 and 3 diminish and broaden with decreasing crystal size.

cycling kinetics. Even at 1C, the bulk MoO_2 electrode only inserts about 0.7 Li^+ per unit cell, with a capacity of 145 mAh/g. At faster rates, this discrepancy widens, and by 20C, bulk MoO_2 only stores 38 mAh/g. This low capacity is only ~26% of that at 1C, indicating very slow lithiation kinetics. Overall, the clear differences in performance between the nanostructured and bulk MoO_2 highlight the importance of nanoscale size for high rate capability in this material. One well-understood reason for this is the shorter solid-state Li^+ diffusion distances in the nanostructured MoO_2, which facilitate fast Li^+ transport throughout the active material. However, the structural response to Li^+ insertion also plays an important role in the rate capability of the nanostructured samples, as we show later.

In addition to the differences in galvanostatic rate performance, the MoO_2 materials show distinct galvanostatic charge storage profiles, even at slow rates where the capacities are similar (**Figure 2B**). For bulk MoO_2, almost no charge is stored above 1.8 V, followed by a sloping region

between 1.8 and 1.6 V. A plateau region occurs at about 1.55 V, after which there is a brief sloping region until 1.35 V, where a second, more pronounced plateau occurs. Generally, plateau regions in a galvanostatic profile are attributed to first-order phase transitions, since the coexistence of two phases in a system implies a constant chemical potential, and equivalently a constant voltage, during the transition.[11,41,37] In the nanoporous samples, the general shape of the profile is retained, but it becomes more sloped in all regions. Up to about 30 mAh/g capacity is stored in the high voltage region above 1.8 V, and the second plateau, while still present, is shorter and more sloped than in the bulk sample. The MoO_2 nanocrystals demonstrate these changes to an even greater extent, with barely any plateau observed in the region around 1.35V and nearly 40 mAh/g capacity stored above 1.8 V.

These effects are also reflected in cyclic voltammetry (**Figure 2C, 2D**). The nanoporous samples show four identifiable peaks on lithiation, which are labeled according to their order of appearance. The two larger peaks (Peaks 2 and 4) occur at voltages that match the plateaus observed in the galvanostatic profile (1.55 V and 1.3 V). For bulk MoO_2, Peaks 1 and 2 match the nanoscale materials closely, but the third peak occurs at a lower potential than the analogous peak for the nanoporous samples due to kinetic limitations. For the same reason, there is no clear identifiable fourth peak for the bulk in the voltammogram. The considerable polarization of Peak 3 for the bulk material, even at the slow sweep rate of 0.1 mV/s, corroborates the lower capacity and poor rate capabilities observed in the galvanostatic testing. Notably, the size of these peaks changes for each sample. For bulk MoO_2, for example, Peak 3 has nearly twice the peak current than it does in the nanoporous samples, while for the MoO_2 nanocrystals, the same voltage region does not even have a well-defined peak, but rather shows a broad distribution of current. This pronounced decrease in the size of peaks occurs for the first peak as well, but not for the second

or fourth peaks. These types of changes in the cyclic voltammetry and galvanostatic profiles due to nanostructuring have been observed frequently in the literature, and the lessening of peaks and plateaus is often attributed to the high fraction of disordered surface sites in nanoscale materials.[2,4] In this case, however, two of the peaks systematically diminish with decreased material size, whereas the other two peaks show no significant changes, suggesting that this common explanation is not uniformly correct. While Peak 1 may indeed broaden due to site disorder, we will show unambiguously that the effect for Peak 3 is due to changes in the mechanism for structural phase transitions upon Li^+ insertion.

2.3.3 The structural evolution of bulk MoO_2 during cycling

To characterize the evolution of structural change in bulk MoO_2, we performed *operando* synchrotron-based X-ray diffraction (*operando* SXRD) at beamline 11-ID-C of the Advanced Photon Source (APS). In this experiment, the active material was assembled into pellet electrodes and cycled in AMPIX cells, which have rigid glassy carbon windows for uniform application of stack pressure during cycling.[73] In this format, the large active mass of sample, lack of current collector, and high X-ray energy and flux provide exceptional signal-to-noise to allow for detailed structural characterization. The cell was cycled at a C/5 rate while a series of X-ray diffraction patterns were taken. **Figure 3A** shows the *operando* SXRD on bulk MoO_2 with the galvanostatic cycling profile and diffraction patterns from Q = 1.5 – 4.5 $Å^{-1}$. The region around the intense (011) reflection is also expanded for clarity. Rietveld refinement of the diffraction data was performed to extract structural parameters as a function of state-of-charge (**Figure 3B**).

At the beginning of the experiment, the diffraction pattern shows pristine MoO_2, a rutile-type tunnel structure with a monoclinic unit cell (space group P_{nma}) (**Figure 3C**). During lithiation, the unit cell expands along the *b* and *c* axes perpendicular to the chains of octahedra, while the *a*

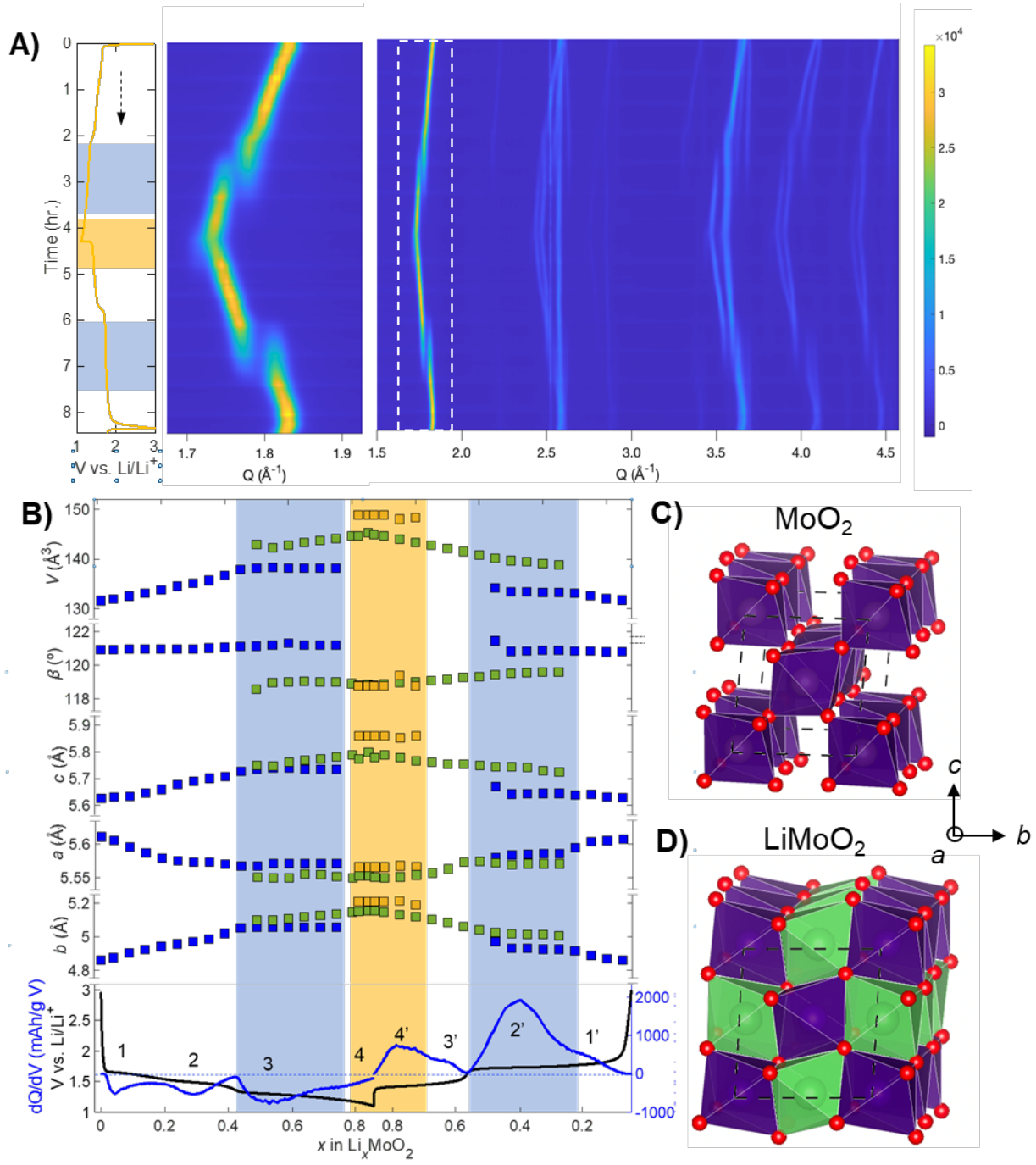

Figure 3. The structural evolution of bulk MoO_2 during cycling. 3A) *Operando* SXRD on bulk MoO_2 during galvanostatic cycling at C/5, collected on a freestanding pellet electrode in an AMPIX cell at beamline 11-ID-C at the APS. The galvanostatic profile is shown (left) along with the diffraction data (right), with a magnified view of the most prominent (011) reflection (middle). **3B)** The evolution of the Li_xMoO_2 crystal structure as determined by Rietveld refinement of the data in **3A),** along with the galvanostatic profile and differential capacity analysis (dQ/dV). Peaks in the dQ/dV are assigned according to the convention established in Figure **2C,D)**. The structure begins as pristine MoO_2 **(3C)** and undergoes expansion of the unit cell to $LiMoO_2$ **(3D)**, including two first-order phase transitions each (de)lithiation, which are highlighted in blue and yellow.

axis, parallel to the chains, contracts by a smaller amount. This structural evolution occurs continuously via a solid-solution type mechanism in the first part of Li^+ insertion. At about 1.4 V vs. Li/Li^+ ($x \approx 0.5$ in Li_xMoO_2), a first-order phase transition occurs, in which the structure undergoes a discontinuous change in symmetry. The diffraction peaks corresponding to the existing phase diminish while peaks of a new phase grow in. This process is most easily seen for the (011) reflection, but it occurs simultaneously across the entire manifold of peaks. This discontinuous symmetry change indicates a nucleation-and-growth type mechanism for the phase transition, which produces two-phase coexistence, as seen in the diffraction data by the simultaneous presence of peaks corresponding to both phases during the transformation.

The new phase formed retains the monoclinic unit cell symmetry and space group with larger *b* and *c* axes and smaller *a* axis and β angle parameters, indicating further expansion of the material perpendicular to the tunnels and contraction along them. The overall change in volume during the transformation alone is about 3.4%, which, while relatively large, is only about a quarter of the total volume increase of 13% experienced at full lithiation. After the phase transition completes, solid-solution evolution of the structure continues until 1.15 V ($x \approx 0.75$ in Li_xMoO_2), at which point another first-order phase transition occurs partially, but does not complete in the data presented here due to the cutoff voltage, which was chosen to prevent conversion reactions. The phase formed matches the fully lithiated $LiMoO_2$ previously characterized with neutron powder diffraction (**Figure 3D**).[44] This final, fully lithiated $LiMoO_2$ has even larger *b* and *c* axis parameters, and also a slightly increased *a* axis. Accordingly, the unit cell volume increases by 2.5% during the transition for an overall 13% expansion of the original MoO_2 unit cell's volume at full lithiation.

This structural evolution can be linked to the electrochemistry, as shown by the four regions with redox peaks in the galvanostatic profile and the differential capacity (dQ/dV) analysis. The first two regions correspond to continuous solid-solution evolution of the structure. Notably, the second region encompasses the first clear plateau identified in the galvanostatic profile, which confirms that even apparent plateaus in the galvanostatic profile do not necessarily represent first-order phase transitions. The third region, during the second GV plateau or CV Peak 3, involves the primary first-order phase transition, and the final redox peak corresponds to the other first-order phase transition that does not complete due to the voltage cutoff. The capacity from region four is noticeably lower for bulk MoO_2, even though a large CV peak occurs in this region in the nanostructured MoO_2 samples; the new phase diffraction intensity is also very low. Overall, this redox event appears to be too kinetically hindered in bulk MoO_2 to contribute significant capacity in this voltage window, which explains why bulk MoO_2 exhibits considerably lower than theoretical capacity, even at slow rates.

2.3.4 The effect of nanostructuring on phase transitions

Next, we evaluate the effect of nanoscale size on the structural change during cycling using *operando* SXRD on our full suite of MoO_2 materials. These experiments were performed at SSRL beamline 11-3 with standard slurry electrodes in modified coin cells with beryllium windows based on a design adapted from Chien et. al (**Figure S6**).[74] Traditional coin cells were modified with a Kapton-covered hole through the cell casing to decrease attenuation of the X-ray beam by the stainless steel. To maintain stack pressure,[75] beryllium spacers were used to combine mechanical rigidity with high X-ray penetration, providing an environment that is functionally identical to that in a normal coin cell for *operando* structural characterization. Additional discussion of the pros and cons of these modified coin cells compared to the AMPIX cells used to collect the data in

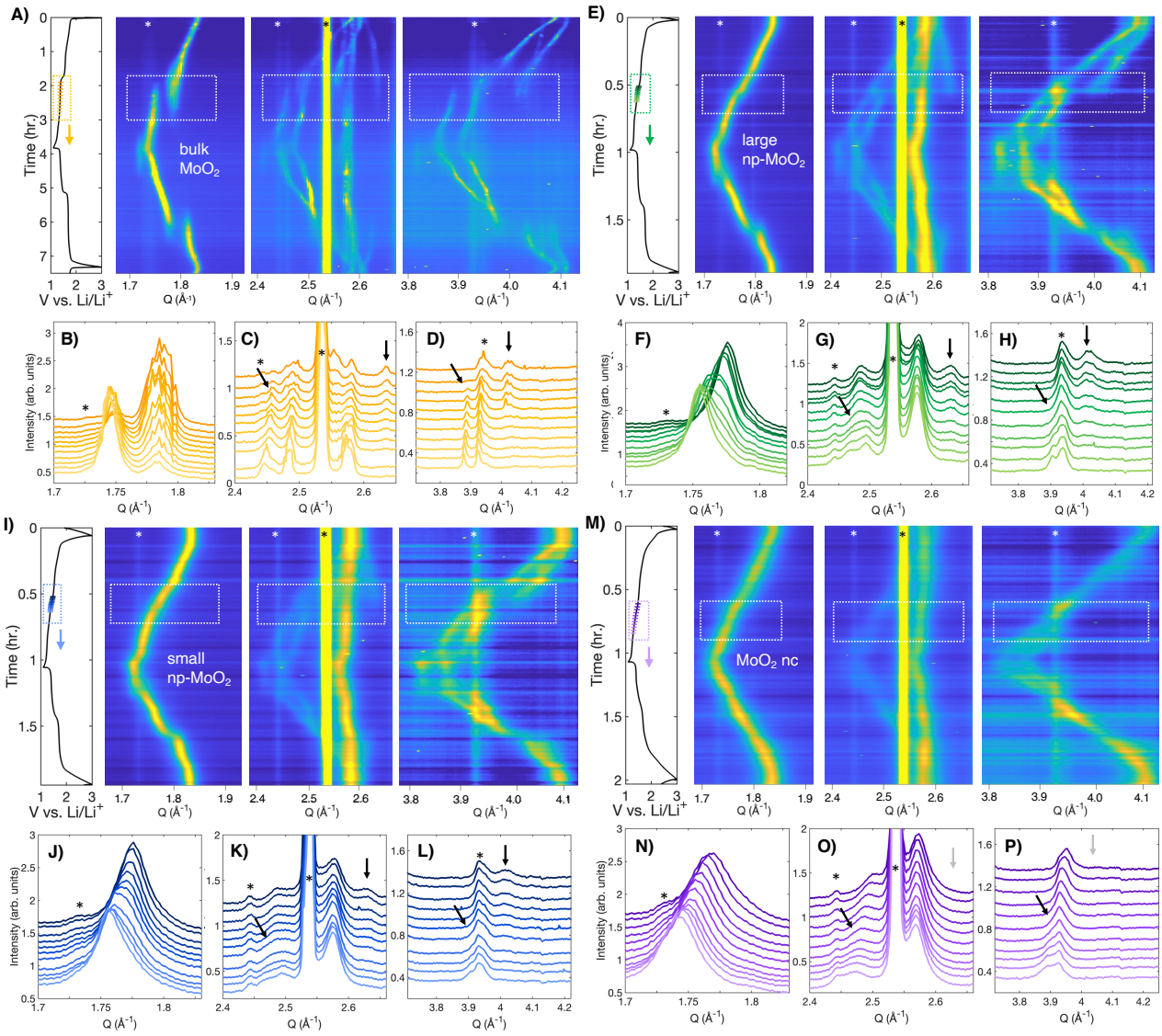

Figure 4. Size-dependent phase transition behavior in nanostructured Li_xMoO_2. 4A), 4B), 4E), and **4F)** show *operando* SXRD data during cycling of the different MoO_2 materials. The large first-order phase transition in bulk MoO_2 becomes dramatically smaller in the nanoporous MoO_2, and entirely second-order in the nanocrystals. The phase transition is shown by a discontinuous transformation of several peaks in the regions highlighted in waterfall plots (**4C**, **4D**, **4G**), but the structural evolution is entirely continuous in the nanocrystals **(4H)**.

Figure 3 can be found associated with Figure S6 in the SI. **Figure 4** shows *operando* SXRD data for bulk, large nanoporous, small nanoporous, and MoO_2 nanocrystal electrodes alongside their galvanostatic cycling traces during a single lithiation-delithiation cycle. For **Figure 4A**, **4B**, **4E**, and **4F**, contour plots of the diffraction data are shown for three selected regions of interest,

including the most intense (011) reflection as well as two other groups of peaks. At the beginning of the data collection, all diffraction patterns matched pristine MoO_2. As Li^+ is inserted, the samples exhibit expansion of the unit cell, demonstrated by the shift of the (011) peak to lower Q, and finish in the same Li_xMoO_2 phase (**Figure S8**). Despite the similarities in the starting and ending phases, however, the evolution between those points varies significantly, particularly during the region where bulk MoO_2 undergoes phase transformations. To provide a detailed look of the first phase transition region, selected diffraction patterns are highlighted for each sample in **Figure 4C**, **4D**, **4G**, and **4H**. The specific voltages where data is shown are indicated by colored symbols on the galvanostatic profiles. For bulk MoO_2, the data is consistent with the structural evolution observed in Figure 3 on pellet electrodes in AMPIX cells. The phase transition is seen clearly as a large discontinuous shift in the (011) reflection of the unit cell in the region Q = 1.7 – 1.8 $Å^{-1}$. The shift corresponds to a change in unit cell volume of about $\Delta V = 4.7$ A^3, as refined from the lattice parameters of the initial and final phases. In the higher Q regions, the discontinuous shift of the (011) reflection is accompanied by the disappearance of peaks at 2.56, 2.64, and 4.03 $Å^{-1}$ from the initial phase and their replacement by peaks at 2.46 $Å^{-1}$ and 3.87 $Å^{-1}$ that correspond to the transformed phase. The coexistence of two distinct phases seen in the diffraction data here is a signature of a first order phase transition that proceeds by nucleation and growth.

In the large and small nanoporous MoO_2 materials, the structural evolution in this region still proceeds through a first-order phase transition, as shown by a small, but clearly discontinuous shift of (011) peak, and other similar peak-shift discontinuities in the higher Q regions. Importantly, the miscibility gap and the duration of two-phase coexistence decreased considerably in all Q regions. The discontinuous shift of the (011) peak observed for the large and small nanoporous MoO_2 corresponds to a change in unit cell volume of $\Delta V = 2.8$ $Å^3$ and 2.4 $Å^3$, respectively, which

are only 60% and 51% of the size of the bulk values (**Figure 5A**). These changes in the miscibility gap can also be seen clearly in the (011) reflection during the process (**Figure 5B**). The duration of two-phase coexistence, measured in capacity, also decreased. Taking the phase transition as the region where two discernable phases are present in the diffraction, the large and small nanoporous samples exhibit two-phase regions over about 0.06 and 0.05 Li^+ per unit cell, respectively, whereas that for the bulk is over 0.25 Li^+ per unit cell (**Figure 7A**). These changes in the diffraction indicate that nanoscale crystal size significantly alters the mechanism for the phase transition in nanoporous MoO_2, likely due to the increased energetic costs transformation in a nanoscale crystal.[76-78] The phase transition does not begin until a lower voltage, producing a smaller ΔV and a shorter transition duration in a phenomenon that varies continually with size. Even between the two very similar nanoporous materials, the large nanoporous sample has a slightly bigger miscibility gap and more two-phase coexistence than the small nanoporous sample (2.8 $Å^3$ and 0.06 Li^+ per Mo, versus 2.4 $Å^3$ and 0.05 Li^+).

Notably, the very short duration of the transition seen here for the large and small nanoporous MoO_2 is consistent with a phase transition mechanism in which a phase boundary is not stable within an individual crystallite, which leads each domain to transform rapidly once the new phase has nucleated. This behavior arises naturally from a nucleation-limited process and is commonly referred to as the "domino-cascade" model to describe the behavior of nanoscale $LiFePO_4$.[79, 80] Unlike in $LiFePO_4$, however, for which the phase transformation nearly encompasses the full (de)lithiation process, the phase transition in nanoporous MoO_2 exists over a much narrower range of stoichiometries.[25]

In the even smaller MoO_2 nanocrystals, the phase transformation is no longer first-order and instead proceeds entirely through a second-order solid-solution mechanism. The (011)

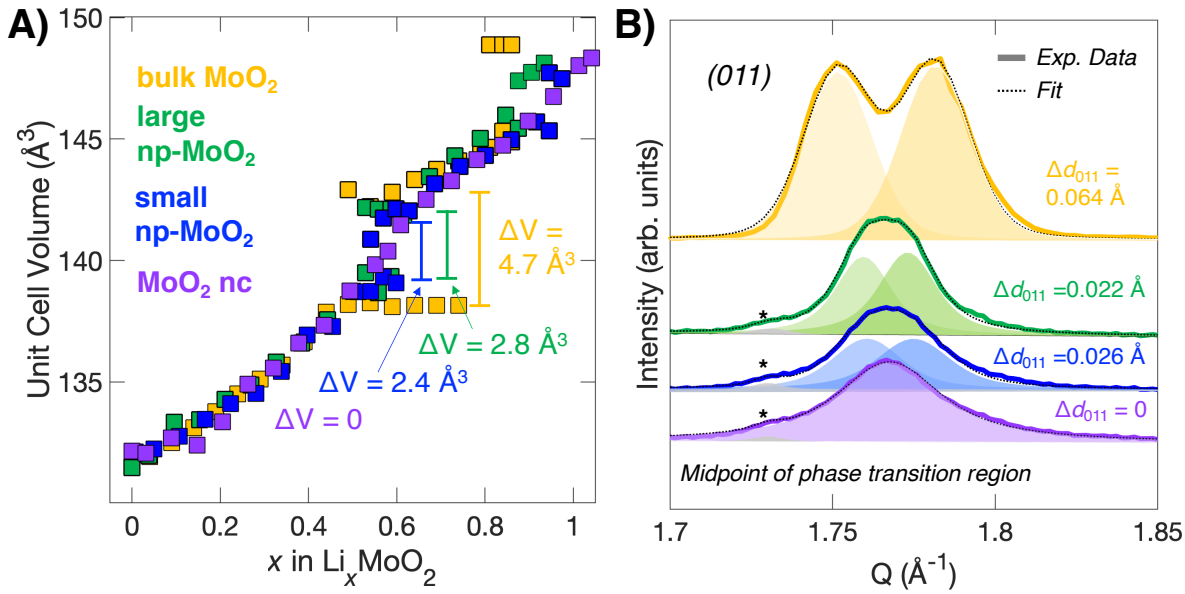

Figure 5. The size-dependent miscibility gap in nanostructured Li_xMoO_2. 5A) Progression of the unit cell volume for the different MoO_2 materials, as determined by Rietveld refinement. The size of the miscibility gap decreases from 4.7 $Å^3$ for bulk MoO_2 to 2.8 $Å^3$ and 2.4 $Å^3$ for large and small nanoporous MoO_2, respectively. The MoO_2 nanocrystals have no miscibility gap since they undergo entirely solid-solution behavior. **5B)** The decrease in miscibility gap is shown clearly by the difference in peak positions at the midpoint of the phase transition region.

reflection remains a single peak, with no discontinuous shift, throughout Li^+ insertion. Further evidence is shown in the higher order peaks: where the bulk and nanoporous MoO_2 show peaks disappearing at 2.65 $Å^{-1}$ and 4.02 $Å^{-1}$ and reappearing at 2.46 $Å^{-1}$ and 3.87 $Å^{-1}$, the MoO_2 nanocrystals evolve through a continuous change in symmetry, where a single peak shifts to lower Q, then splits into two separate reflections that continually evolve to the same final positions, without ever appearing at 2.65 $Å^{-1}$ and 4.02 $Å^{-1}$. The continuous change in symmetry seen here strongly indicates a second-order, solid-solution mechanism, through which Li^+ is inserted into the crystal structure without the need for nucleation of a new phase. Notably, the MoO_2 nanocrystals end up at the same $LiMoO_2$ crystal structure as the bulk and nanoporous MoO_2 materials, but reach that structure through an entirely different pathway. Thus, nanoscale size effects on the phase transition mechanism for the MoO_2 nanocrystals are even more pronounced than they were for the

nanoporous MoO_2 due to their smaller size. In the nanocrystals, the increased energetic penalty for a first-order transition makes this route entirely disfavored compared to single-phase Li^+ insertion.

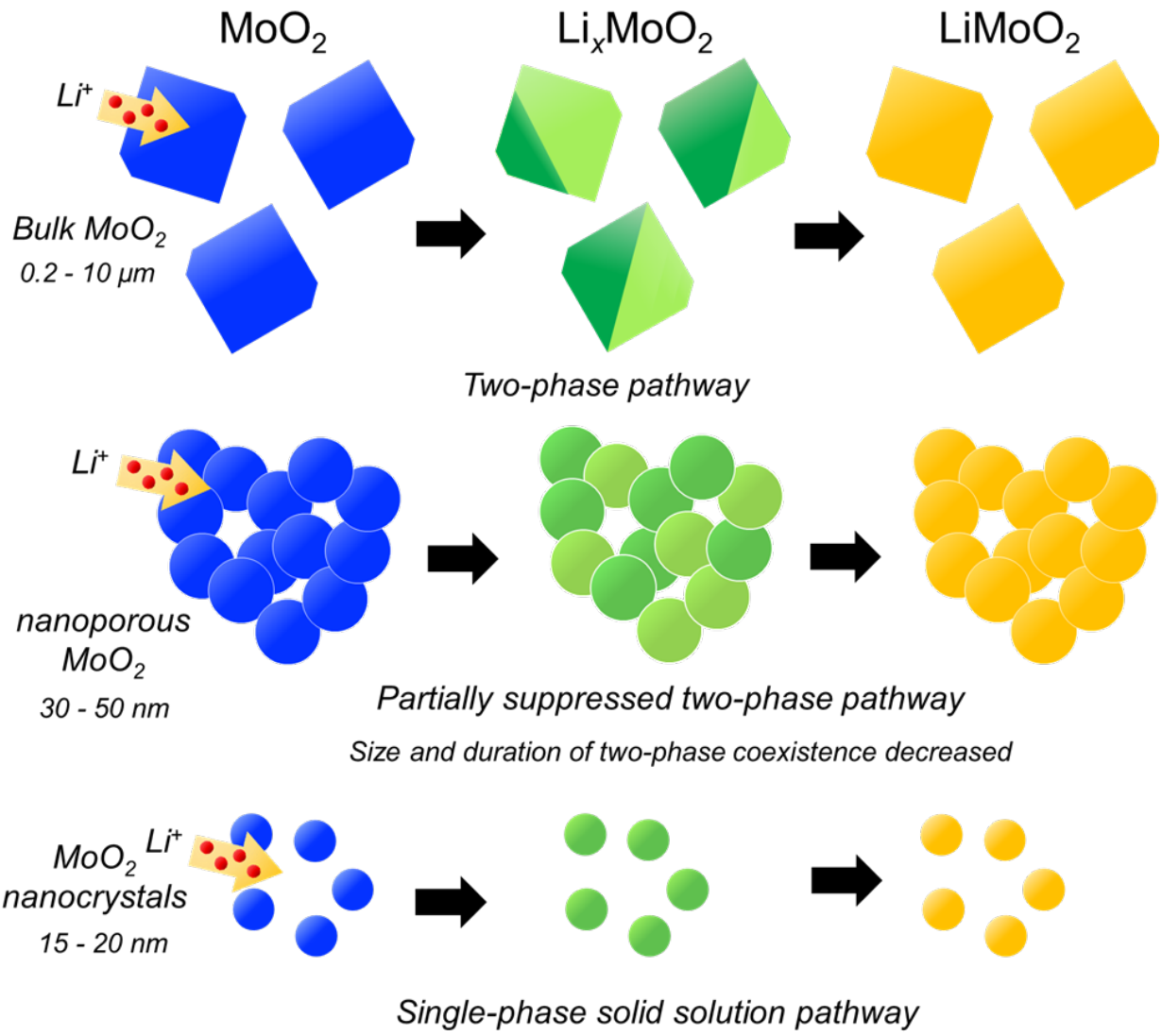

Figure 6. Schematic diagram of the changes in phase transition behavior shown in Li_xMoO_2. Bulk MoO_2 shows a large first-order phase transition that imposes kinetic limitations on charge storage. The same transition in nanoporous MoO_2 remains first-order but the miscibility gap and duration are decreased considerably. Finally, MoO_2 nanocrystals undergo complete single-phase solid solution lithiation behavior. The more continuous phase evolution in the nanostructured materials do not slow charge storage kinetics significantly.

The changes in the phase transition mechanism from nanostructuring are highlighted schematically in **Figure 6**. Once a critical amount of Li^+ is inserted, bulk Li_xMoO_2 undergoes a first-order phase transition in which a new crystal phase starts to nucleate. The two phases coexist

over a relatively large compositional region, and maintain a significant miscibility gap. For the nanoporous MoO_2, the phase transformation in the same region remains first-order, but with only about half the bulk miscibility gap and dramatically shorter duration of two-phase coexistence. In this case, the strain from having a first-order transition in materials with nanoscale crystallites has led to a smaller gap in lattice parameters and destabilized the coexistence of the two phases. This destabilization occurs to a greater extent in the small nanoporous MoO_2 than in the large nanoporous counterpart. Finally, the even smaller MoO_2 nanocrystals exhibit no first-order phase transition, and instead Li^+ insertion proceeds through a single-phase second order mechanism. The identification of these different phase transformation behaviors in materials with the same crystal structure but different size and morphology highlights the importance of these factors in governing phase transitions. To our knowledge, this full progression of phase transition behavior has not been reported for a single system in which only crystal size and morphology are varied. Importantly, the sequential progression from bulk first-order to partially suppressed first-order to fully second-order as size is decreased presents consistent evidence that the formation of a phase boundary within a nanoscale crystallite becomes increasingly destabilized as the size of the crystal decreases.

2.3.5 Electrochemical kinetics in nanostructured MoO_2

With the changes in phase transition behavior clearly identified, we now turn to a series of complementary electrochemical kinetics analyses to determine how these various behaviors affect Li^+ insertion kinetics. **Figure 7A**, **7B**, **7D** and **7E** show the cyclic voltammograms for bulk, large nanoporous, small nanoporous, and nanocrystal MoO_2, respectively, for sweep rates from 0.1 mV s^{-1} to 1 mV s^{-1}. The most obvious electrochemical signature of the changes in phase transition behavior can be found in the magnitude of Peak 3 in the anodic sweep: whereas the bulk MoO_2 shows a large peak corresponding to the primary first-order phase transition, the size of the peak

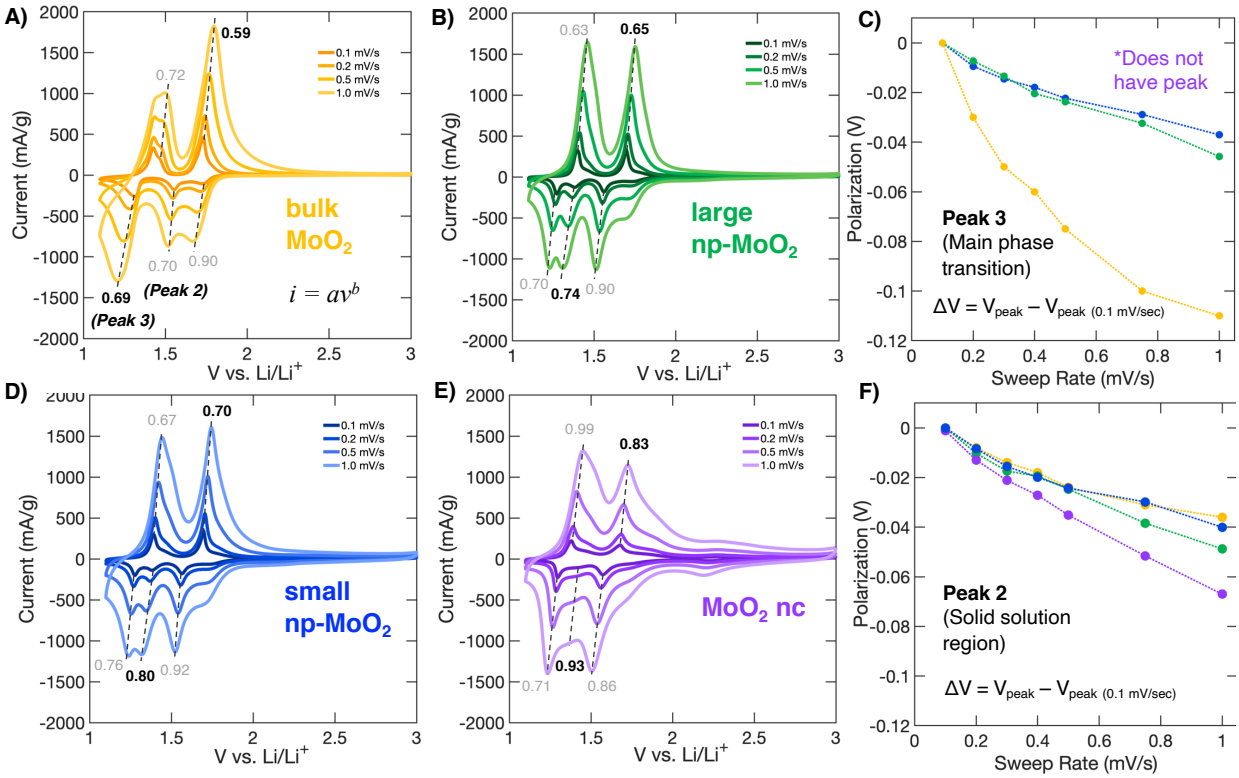

Figure 7. Electrochemical kinetics analysis of bulk and nanostructured MoO_2. 7A), 7B), 7D) and **7E)** show cyclic voltammograms for the MoO_2 materials at different sweep rates. Each peak is labeled with the exponential dependence of the peak current *b* according to Equation 1 in the main text. Peaks 3 and 2' are highlighted since they correspond to the phase transitions in MoO_2. As the phase transition is suppressed with nanoscale size, the current at these peaks becomes more capacitive. **7C,7E)** Relative polarization analysis for Peaks 3 and 2, respectively, as calculated by the difference between the peak position at a given rate and its position at the lowest rate (0.1 mV s^{-1}). The very large polarization for Peak 3 for bulk MoO_2 is due to its phase transition, and the partially suppressed phase transitions in the nanoporous materials lead to dramatically smaller polarization for the same peak **(7C)**. For Peak 2, which is a solid-solution region for all sizes of MoO_2, the polarization is much more similar, which confirms the detrimental effect of the phase transition, and not ionic diffusion, on the polarization of bulk MoO_2 **(7F)**.

is much smaller for the nanoporous samples, and it occurs only as a broad feature in the solid-solution MoO_2 nanocrystals. To assess the kinetics, we first calculated the relative polarization, or shift in position, of each peak compared to its position at the slowest rate (**Figure 7C**, **7F**). This value directly maps onto the kinetic barrier during each charge storage process, with no additional assumptions. To start, we analyzed the relative polarization of each peak for bulk MoO_2 (**Figure S11**). Peaks 1 and 2, which correspond to the two redox events within the solid-solution region of

lithiation, show similar, relatively low polarization values of 37 and 58 mV at a sweep rate of 1 mV s^{-1}, indicating that they have fast kinetics. However, Peak 3, which corresponds to the main first-order phase transition, shows a dramatically higher polarization of 110 mV at 1 mV s^{-1}). This high value strongly indicates a slowed kinetic response caused by the phase transition.

To evaluate the effect of the altered phase transition behavior, we determined the relative polarization of these peaks for the nanostructured MoO_2 materials. For Peak 3, the relative polarization for small and large nanoporous MoO_2 are 45 mV and 38 mV at 1 mV s^{-1}, respectively—less than half the 110 mV for the same peak for bulk MoO_2. We note that, due to the lack of a clear peak for the MoO_2 nanocrystals, the relative polarization in this region could not be accurately determined. This dramatic decrease in polarization for large and small nanoporous MoO_2 suggests that the considerably smaller phase transition in the nanoporous samples imposes little, if any, kinetic limitation on charge storage, unlike that for bulk MoO_2. Electrochemical polarization arises from any kinetic limitations, so the lower polarization for the nanoporous MoO_2 may reflect, in part, their shortened diffusion lengths compared to bulk MoO_2. To partially deconvolute the effects of nanoscale ion diffusion lengths on the polarization from the effects of changes to the phase transition mechanism, we also analyzed the relative polarization for Peak 2 in the anodic sweep, which corresponds to the solid-solution region for all of the MoO_2 materials. For Peak 2 the bulk, large nanoporous, and small nanoporous MoO_2 all show similar and low values for relative polarization of 38 mV, 48 mV, and 40 mV, respectively at 1 mV s^{-1}. Only the MoO_2 nanocrystals show a slightly higher polarization of 67 mV at the same 1 mV s^{-1}, which is likely due to the poorer electrical conductivity in the nanocrystal-based electrode. The fact that the bulk MoO_2 has similar polarization to the nanoporous MoO_2 for this peak indicates

that the change in phase transition mechanism, and not the decreased ion diffusion lengths, is primarily responsible for the low polarization seen for the nanoporous MoO_2 for Peak 3.

We also analyzed the cyclic voltammograms using power-law fits to each peak current (i_{peak}) as the sweep rate (v) is varied, according to the following equation:

$$i_{peak} = av^b$$

where a and b are constants. The value of b, determined by fitting the slope of $\log(i_{peak})$ versus $\log(v)$, should be 0.5 for a reaction limited by semi-infinite diffusion, and 1.0 for a capacitive process.[4,7,81] Intermediate values correspond to diffusion behavior that is between semi-infinite diffusion and purely capacitive reactions. This analysis has been used frequently in the literature to distinguish between diffusion-controlled or "battery-like" behavior, and pseudocapacitive redox reactions, which appear capacitive due to fast Li^+ diffusion.[50,55,56,29,30,31,32,82] We also note a longstanding hypothesis that redox reactions that require first-order phase transition are inherently diffusion-limited due to the need for propagation of a phase boundary. For example, Conway noted that the absence of "three-dimensional phase changes or reconstructions" was key to pseudocapacitive redox processes.[29,30] To evaluate this hypothesis based on our different models of phase transition behavior in MoO_2, we carried out the power law analysis on the different MoO_2 samples. The fitted values of b corresponding to each peak are shown along with the CV data in **Figures 7A**, **7B**, **7D**, and **7E**, with the values for Peak 3 highlighted in bold. For Peak 3, a direct trend is observed with size, as bulk MoO_2, large and small nanoporous MoO_2, and MoO_2 nanocrystals show b values of 0.69, 0.74, 0.80, and 0.93, respectively, which suggests that the suppression of the first-order phase transition does make charge storage more pseudocapacitive. A similar trend is also observed for Peak 3', which corresponds to the phase transition on delithiation.

A key challenge for understanding the specific role of phase transition behavior on kinetics is separating the associated effects of shortened Li^+ diffusion distances in nanoscale materials. To address this issue, we analyzed the electrode polarization as a function of state-of-charge using the galvanostatic intermittent titration technique (GITT). In this experiment, standard MoO_2 electrodes were cycled with a series of current pulses, followed by extended relaxation under open circuit conditions. While the magnitude and duration of the current pulse and the relaxation time can vary depending on the system, we applied a current analogous to a C/10 rate for 10 minutes each pulse, with two hours of relaxation time in between pulses. The difference between the closed circuit voltage at the end of the current pulse and the open circuit voltage at the end of relaxation is a measure of the overpotential, or additional electrode polarization required to drive the redox reaction.[83—85] Importantly, unlike the relative polarization derived from peaks shifting in a cyclic voltammogram discussed above, the polarization from GITT is measured while the electrode is under quasi-equilibrium conditions, so ionic and electronic transport should not contribute to the polarization unless they are considerably limited by another process. As such, this technique most rigorously isolates the effects of the changes in phase transition behavior on charge storage kinetics from those of the shortened diffusion lengths in the nanostructured MoO_2.

Figure 8A – 8D show the GITT lithiation profiles for bulk MoO_2, large and small nanoporous MoO_2, and MoO_2 nanocrystals, respectively. For each graph, the raw GITT voltage curve is plotted in black, while the overpotential, as measured by the difference between the open circuit and closed circuit voltage for each pulse, is shown in color. During lithiation, bulk MoO_2 shows low polarization during the upper plateau region of the profile, which corresponds to the single-phase lithium insertion region (Peaks 1 and 2 according to the labeling previously assigned). As the first plateau ends and the transition to the second plateau begins, a dramatic, but temporary,

increase in polarization occurs. This portion of the charge storage profile coincides with the beginning of the first-order phase transition, which strongly indicates that the nucleation of the new phase in this step is kinetically hindered. After the temporary increase, the baseline overpotential decreases and remains relatively low, although slightly higher than the initial value, until the end of lithiation, where another large increase occurs. This second rise in the overpotential can be attributed to the second first-order phase transition as well as the slowed kinetics of lithiation when the tunnels of MoO_2 are nearly full.

The GITT data on the nanostructured MoO_2 materials largely shows the same behavior, with low overpotential throughout most of the lithiation process followed by a large increase at the very end. However, one striking difference is that, where the bulk MoO_2 shows a large spike in polarization right before the first-order phase transition, the nanostructured MoO_2 shows a much smaller increase in overpotential. We quantified the local increase in overpotential in this region for each of the samples relative to the baseline overpotential. Whereas the bulk MoO_2 exhibits a $\Delta\eta_{max,local}$ = 124 mV related to the onset of the phase transition, the large and small nanoporous MoO_2 have $\Delta\eta_{max,local}$ = 10 mV and 11 mV, respectively. Despite still undergoing first-order phase transitions, the nanoporous MoO_2 materials show overpotentials an order of magnitude less than that for bulk MoO_2, which indicates that the modified phase transition, with its much smaller miscibility gap, imposes considerably decreased limitations on the charge storage kinetics. In the MoO_2 nanocrystals, the $\Delta\eta_{max,local}$ = 3 mV is smaller still than in the nanoporous materials, confirming that the lack of a first order phase transition and an entirely single-phase lithiation process leads to even lower overpotentials.

The GITT analysis in combination with the relative polarization measured from the cyclic voltammetry experiments, illustrates clearly and quantitatively that large first-order phase

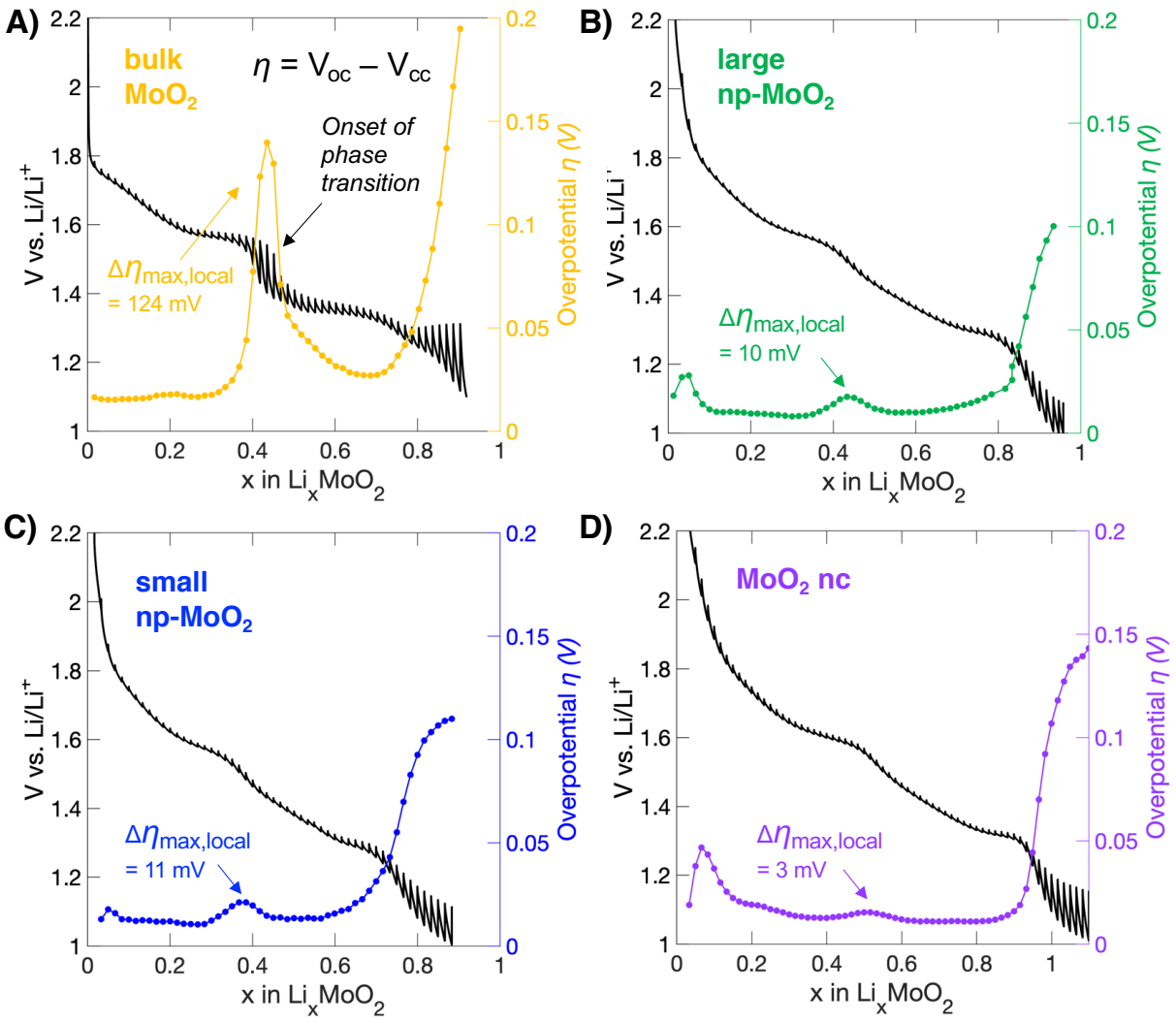

Figure 8. Galvanostatic intermittent titration testing (GITT) polarization analysis. 8A) – 8D) GITT data for each the MoO_2 materials with a series of C/10 current pulses followed by two hours of relaxation. The raw GITT data is shown alongside the overpotential (η), which was calculated by the difference between the open and closed circuit voltage for each pulse. The bulk MoO_2 shows a dramatic increase in overpotential immediately preceding the first-order phase transition. The size of the local increase in overpotential is much lower for the nanoporous MoO_2 and nearly zero for the nanocrystals, which indicate the size-induced suppression of the phase transition has removed the kinetic limitations from the process. All the samples show increases in overpotential as they near full capacity, likely due to slowed Li^+ diffusion in the filled tunnels.

transitions have a negative impact on charge storage kinetics. The next obvious question is: what aspect of the phase transition is primarily responsible for the slow kinetics? Relative polarizations and *b*-values are calculated at the redox peaks, which correspond to the plateau or two-phase coexistence region. Alternatively, the largest overpotentials in GITT occur at the onset of the

phase transition, which would be associated with nucleation of the new phase. In all of the nanostructured MoO_2 materials, these signatures of slow kinetics are diminished greatly, indicating that suppression of the phase transition due to finite size effects is a key component to their faster charge storage kinetics. Importantly, the nanoporous materials still show a much smaller increase in overpotential before their phase transition, even though it remains first-order.

A possible explanation can be gained by considering the driving force for the first-order transition. Peak 2 in the CV curves corresponds to solid-solution behavior, and this region should end when an ion-ordered state is reached, forcing a discontinuous phase transition to accommodate addition ion insertion. The most ion ordered state should occur just before the onset of the first-order phase transition, corresponding to the large oscillations at the midpoint in the GITT curve in Figure 8A. Similar to the large GITT oscillations observed when the channels are almost full, the ion-ordered state should also cause reduced Li^+ diffusivity. The smaller overpotentials in the nanoscale samples suggest reduced ion-ordering in those materials. In the nanoporous samples, there is still sufficient ion ordering to drive a weakly first-order phase transition, but not in the smaller nanocrystal MoO_2. Importantly, as soon as the ion-ordering is even partly relaxed, multiple aspects of the phase transitions kinetics become much faster.

2.3.6 Phase transitions and cycle life

Finally, we examine the effect of the phase transition behavior on the cell cycle life for our nanostructured MoO_2 materials (**Figure 9A**). Large changes in volume during cycling are well known to lead to capacity loss over time due to particle cracking and disconnection from the electrode.[86,87] Consistent with this idea, bulk MoO_2 shows relatively poor cycle life, with only 50% of its initial capacity retained after 1000 cycles at 5C. In contrast, the large and small nanoporous MoO_2 show excellent capacity retention, with 90% and 89% of their initial capacity remaining

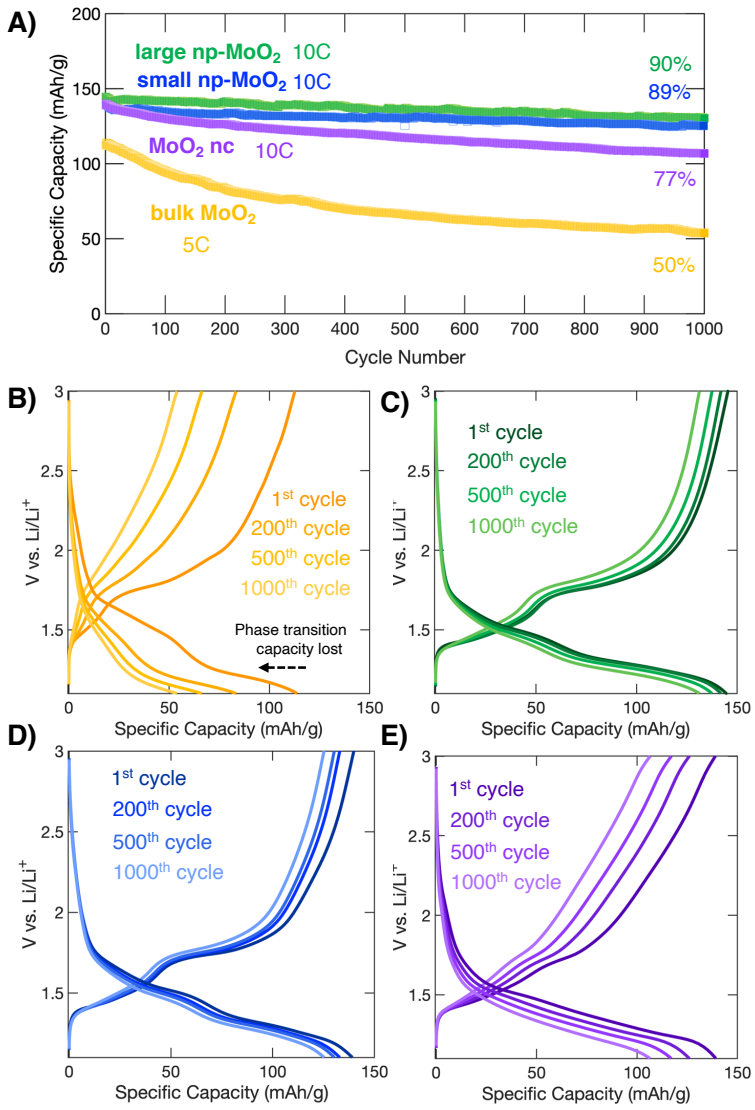

Figure 9. The effect of phase transitions on cycle life. A) Long term galvanostatic cycling performance for the different MoO_2 materials. While bulk MoO_2 shows poor retention of its capacity over 1000 cycles, the nanocrystals show strong and the nanoporous materials show exceptional capacity retention over 1000 cycles. **9B) – 9E)** Evolution of the galvanostatic charge storage profiles throughout the long term cycling experiment in **9A)**. While the nanostructured materials largely maintain the shape of their profiles, bulk MoO_2 shows rapid degradation of the capacity in the region of the phase transition, as shown by the disappearance of the plateau by the 200th cycle.

after 1000 cycles at 10C; the MoO_2 nanocrystals exhibit intermediate longevity at 77%. The reduced cycle life in the nanocrystal electrodes is likely due to the poorer electrical connectivity of the isolated nanocrystals, in combination with their increased reactive surface area.

The decreased volume change at the phase transitions in the nanoporous MoO_2 and the complete single-phase insertion process of the MoO_2 nanocrystals dramatically improve their cycle lifetimes. The negative effect of the first-order phase transition in bulk MoO_2 is seen in the changes in the galvanostatic profiles during extended cycling (**Figure 9B**). The plateau corresponding to the phase transition is present

during the first cycle, but decreases considerably during the first 200 cycles, and is no longer present by the 500th cycle. Notably, the rate of capacity loss is much higher during the first 500 cycles where the phase transition is still present, further indicating the role it plays in degradation. In contrast, the nanoporous MoO_2 and MoO_2 nanocrystals do not show significant changes in their charge storage profiles with prolonged cycling (**Figure 9C – 9E**) Importantly, these materials still undergo the same overall 13% change in volume as bulk MoO_2, but that expansion proceeds through mostly or entirely continuous processes, rather than through the large discontinuous changes of the first-order phase transition in bulk MoO_2. The excellent longevity of the nanostructured MoO_2 indicates that not all changes in volume are equally detrimental to capacity during extended cycling.

2.5 Conclusion

Using *operando* SXRD on a series of size-controlled materials, we have demonstrated the gradual evolution of phase behavior from strongly first-order phase transitions in bulk MoO_2 to fully second-order or solid-solution in MoO_2 nanocrystal-based electrodes. In intermediately-sized nanoporous MoO_2, the phase transformation remains first-order, but with only about half the miscibility gap and one-fifth the duration of two-phase coexistence. In all cases, the starting and ending structures are identical, but the intermediate structural evolution varies continuously with size. Importantly, even partly suppressed phase transition behavior dramatically improved cycling performance in the nanostructured materials: whereas bulk MoO_2 only stores 38 mAh/g, or 18% of its theoretical capacity, at 20C, the large and small nanoporous and MoO_2 nanocrystals all store about 130 mAh/g, or 62% of theoretical, at 20C. Using electrochemical kinetics analyses, we identified clear signatures of polarization at the onset of the phase transformation in bulk MoO_2, and found, accordingly, that this polarization decreased significantly from in the nanomaterials. In

specific, bulk MoO_2 showed a 124 mV increase in overpotential measured by GITT, whereas the nanoporous samples showed an order of magnitude lower increase in overpotential at 11 and 10 mV, and the nanocrystals had barely any increase at 3 mV, possibly due to decreased ion ordering. Finally, we highlighted the key role of phase transition behavior in cycle longevity, as bulk MoO_2 retained only 50% of its initial capacity after 1000 cycles, whereas the large and small nanoporous showed 90% and 89% retention after 1000 cycles. The fact that the nanostructured samples undergo their volume change through a mostly or entirely continuous process, instead of having a large discontinuous phase transition, favorably impacts all aspects of cycling kinetics and stability.

Suppression of first-order phase transitions has long been associated with improved Li^+ de(insertion) kinetics, and many common cathode materials use mixtures of elements to accomplish this goal in bulk materials.[88] A unique aspect of this work is the observation of dramatically improved kinetics in nanoscale materials that still show a discontinuous, first-order phase transition. We hypothesize that these effects may also be found in other battery materials. For example, the nanoporous MoO_2 shows fast kinetics, despite its first-order transition, similar to $LiFePO_4$[57-27] and $Li_4Ti_5O_{12}$,[28,89-91] which also have first-order transitions and high rate capability, but only when nanostructured. This may indicate that it is possible to have first order phase transitions that are mechanistically different from the bulk in nanoscale electrode materials because of reduced ion ordering or because of energetic changes to nucleation or growth of the phase transition in small domains. Overall, resolving these mechanistic changes is necessary for a complete understanding of how finite size effects contribute to high power density in Li-ion electrode materials.

2.6 References

[1]. Gür, T.M. Review of electrical energy storage technologies, materials and systems: challenges and prospects for large-scale grid storage. *Energy Environ. Sci.* **2018**, *11*(10), 2696–2767.

[2] . Simon, P.; Gogotsi, Y.; Dunn, B. Where do batteries end and supercapacitors begin? *Science* **2014**, *343*(6176), 1210–1211.

[3]. Frith, J.T.; Lacey, M.J.; Ulissi, U. A non-academic perspective on the future of lithium-based batteries. *Nat. Commun.* **2023**, *14*(1), 420.

[4]. Choi, C.; Ashby, D.S.; Butts, D.M.; DeBlock, R.H.; Wei, Q.; Lau, J.; Dunn, B. Achieving high energy density and high power density with pseudocapacitive materials. *Nat. Rev. Mater.* **2020**, *5*(1), 5–19.

[5]. Li, M.; Lu, J.; Chen, Z.; Amine, K. 30 years of lithium-ion batteries. *Adv. Mater.* **2018**, *30* (33), 1800561.

[6]. Wu, J.; Zhang, X.; Ju, Z.; Wang, L.; Hui, Z.; Mayilvahanan, K.; Takeuchi, K. J.; Marschilok, A. C.; West, A. C.; Takeuchi, E. S.; Yu, G. From Fundamental Understanding to Engineering Design of High-Performance Thick Electrodes for Scalable Energy-Storage Systems. *Adv. Mater.* **2021**, *33* (26), 2101275.

[7]. Fleischmann, S.; Mitchell, J.B.; Wang, R.; Zhan, C.; Jiang, D.E.; Presser, V.; Augustyn, V. Pseudocapacitance: From Fundamental Understanding to High Power Energy Storage Materials. *Chem. Rev.* **2020**, *120*(14), 6738–6782.

[8] . Van Den Bergh, W.; Stefik, M.; Van Den Bergh, W.; Stefik, M. Understanding Rapid Intercalation Materials One Parameter at a Time. *Adv. Funct. Mater.* **2022**, *32* (31), 2204126.

[9]. Griffith, K. J.; Wiaderek, K. M.; Cibin, G.; Marbella, L. E.; Grey, C. P. Niobium tungsten oxides for high-rate lithium-ion energy storage. *Nature*, **2018**, *559*, 556–563.

[10]. Chung, S.Y.; Bloking, J.T.; Chiang, Y.M. Electronically conductive phospho-olivines as lithium storage electrodes. *Nat. Mater.* **2002**, 1(2), 123–128.

[11]. Van Der Ven, A.; Bhattacharya, J.; Belak, A. A. Understanding Li Diffusion in Li-Intercalation Compounds. *Acc. Chem. Res.* **2013**, *46*, 1216–1225.

[12]. Griffith, K.J.; Seymour, I.D.; Hope, M.A.; Butala, M.M.; Lamontagne, L.K.; Preefer, M.B.; Koçer, C.P.; Henkelman, G.; Morris, A.J.; Cliffe, M.J.; Dutton, S.E.; Grey, C.P. Ionic and Electronic Conduction in $TiNb_2O_7$. *J. Am. Chem. Soc.* **2019**, *141* (42), 16706–16725.

[13]. Preefer, M.B.; Saber, M.; Wei, Q.; Bashian, N.H.; Bocarsly, J.D.; Zhang, W.; Lee, G.; Milam-Guerrero, J.; Howard, E.S.; Vincent, R.C.; Melot, B.C.; Van der Ven, A.; Seshadri, R.; Dunn, B. Multielectron Redox and Insulator-to-Metal Transition upon Lithium Insertion in the Fast-Charging, Wadsley-Roth Phase PNb_9O_{25}. *Chem. Mater.* **2020**, *32* (11), 4553–4563.

[14]. Sun, H.; Mei, L.; Liang, J.; Zhao, Z.; Lee, C.; Fei, H.; Ding, M.; Lau, J.; Li, M.; Wang, C.; Xu, X. Three-dimensional holey-graphene/niobia composite architectures for ultrahigh-rate energy storage. *Science*, **2017**, *356* (6338), 599–604

[15]. Wagemaker, M.; Mulder, F.M. Properties and promises of nanosized insertion materials for Li-ion batteries. *Acc. Chem. Res*. **2013**, *46*(5), 1206–1215.

[16]. Cook, J. B.; Kim, H. S.; Lin, T. C.; Lai, C. H.; Dunn, B.; Tolbert, S. H. Pseudocapacitive Charge Storage in Thick Composite MoS_2 Nanocrystal-Based Electrodes. *Adv. Energy Mater.* **2017**, *7*, 1601283.

[17]. Sun, H.; Mei, L.; Liang, J.; Zhao, Z.; Lee, C.; Fei, H.; Ding, M.; Lau, J.; Li, M.; Wang, C.; Xu, X. Three-dimensional holey-graphene/niobia composite architectures for ultrahigh-rate energy storage. *Science*, **2017**, *356* (6338), 599–604

[18]. Jain, R.; Lakhnot, A.S.; Bhimani, K.; Sharma, S.; Mahajani, V.; Panchal, R.A.; Kamble, M.; Han, F.; Wang, C.; Koratkar, N. Nanostructuring versus microstructuring in battery electrodes. *Nat. Rev. Mater.* **2022**, *7*(9), 736–746.

[19]. Okubo, M.; Hosono, E.; Kim, J.; Enomoto, M.; Kojima, N.; Kudo, T.; Zhou, H.; Honma, I. Nanosize Effect on High-Rate Li-Ion Intercalation in $LiCoO_2$ Electrode. *J. Am. Chem. Soc.* **2007**, *129* (23), 7444–7452.

[20]. Guo, B.; Yu, X.; Sun, X.G.; Chi, M.; Qiao, Z.A.; Liu, J.; Hu, Y.S.; Yang, X.Q.; Goodenough, J.B.; Dai, S. A long-life lithium-ion battery with a highly porous $TiNb_2O_7$ anode for large-scale electrical energy storage. *Energy Environ. Sci.* **2014**, 7(7), 2220–2226.

[21]. Augustyn, V.; Come, J.; Lowe, M. a; Kim, J. W.; Taberna, P.-L.; Tolbert, S. H.; Abruña, H. D.; Simon, P.; Dunn, B. High-Rate Electrochemical Energy Storage through Li^+ Intercalation Pseudocapacitance. *Nat. Mater.* **2013**, *12* (6), 518–522.

[22]. van den Bergh, W.; Lokupitiya, H.N.; Vest, N.A.; Reid, B.; Guldin, S.; Stefik, M. Nanostructure Dependence of T-Nb_2O_5 Intercalation Pseudocapacitance Probed Using Tunable Isomorphic Architectures. *Adv. Funct. Mater.* **2021**, *31* (1), 2007826.

[23]. Kang, B.; Ceder, G. Battery materials for ultrafast charging and discharging. *Nature* **2009**, *458*, 190–193.

[24]. Lin, T. C.; Yan, Y.; King, S. C.; Lai, C. H.; Tolbert, S. H. Fast-Charging Cathodes from Polymer-Templated Mesoporous $LiVPO_4F$. *ACS Appl. Mater. Interfaces* **2020**, *12*, 33775–33784.

[25]. Wagemaker, M.; Singh, D.P.; Borghols, W.J.; Lafont, U.; Haverkate, L.; Peterson, V.K.; Mulder, F.M. Dynamic Solubility Limits in Nanosized Olivine $LiFePO_4$. *J. Am. Chem. Soc.* **2011**, 133(26), 10222–10228.

[26]. Meethong, N.; Huang, H. Y. S.; Carter, W. C.; Chiang, Y. M. Size-dependent lithium miscibility gap in nanoscale $Li_{1-x}FePO_4$. *Electrochem. Solid State Lett.* **2007**, *10*, A134.

[27]. Gibot, P.; Casas-Cabanas, M.; Laffont, L.; Levasseur, S.; Carlach, P.; Hamelet, S.; Tarascon, J.M.; Masquelier, C. Room-temperature single-phase Li insertion/extraction in nanoscale Li_xFePO_4. *Nat. Mater.* **2008**, *7*, 741–747.

[28]. Borghols, W.J.H.; Wagemaker, M.; Lafont, U.; Kelder, E.M.; Mulder, F.M. Size Effects in the $Li_{4+x}Ti_5O_{12}$ Spinel. *J. Am. Chem. Soc.* **2009**, *131*(49), 17786–17792.

[29]. Conway, B. E. Transition from "Supercapacitor" to "Battery" Behavior in Electrochemical Energy Storage. *J. Electrochem. Soc.* **1991**, *138* (6), 1539–1549.

[30]. Conway, B. E.; Birss, V.; Wojtowicz, J. The role and utilization of pseudocapacitance for energy storage by supercapacitors. *J. Power Sources* **1997**, *66***,** 1–14.

[31]. Kim, H.-S.; Cook, J. B.; Tolbert, S. H.; Dunn, B. The Development of Pseudocapacitive Properties in Nanosized-MoO_2. *J. Electrochem. Soc.* **2015**, *162*, A5083–A5090.

[32]. Cook, J. B.; Lin, T. C.; Kim, H.-S.; Siordia, A.; Dunn, B. S.; Tolbert, S. H. Suppression of Electrochemically Driven Phase Transitions in Nanostructured MoS_2 Pseudocapacitors Probed Using Operando X-ray Diffraction. *ACS Nano*, **2019**, *13*, 1223–1231.

[33]. Muller, G. A.; Cook, J. B.; Kim, H.-S.; Tolbert, S. H.; Dunn, B. High Performance Pseudocapacitor Based on 2D Layered Metal Chalcogenide Nanocrystals. *Nano Lett.* **2015**, *15*, 1911–1917.

[34]. Lesel, B. K.; Cook, J. B.; Yan, Y.; Lin, T. C.; Tolbert, S. H. Using Nanoscale Domain Size to Control Charge Storage Kinetics in Pseudocapacitive Nanoporous $LiMn_2O_4$ Powders. *ACS Energy Lett.* **2017**, *2* (10), 2293–2298.

[35]. Mitchell, J.B.; Geise, N.R.; Paterson, A.R.; Osti, N.C.; Sun, Y.; Fleischmann, S.; Zhang, R.; Madsen, L.A.; Toney, M.F.; Jiang, D.E.; Kolesnikov, A.I.; Mamontov, E.l; Augustyn, V. Confined Interlayer Water Promotes Structural Stability for High-Rate Electrochemical Proton Intercalation in Tungsten Oxide Hydrates. *ACS Energy Lett.* **2019**, *4* (12), 2805–2812.

[36]. Cook, J. B.; Ko, J. S.; Lin, T. C.; Robertson, D. D.; Kim, H. S.; Yan, Y.; Yao, Y.; Dunn, B. S.; Tolbert, S. H. Ultrafast Sodium Intercalation Pseudocapacitance in MoS_2 Facilitated by Phase Transition Suppression. *ACS Appl. Energy Mater.* **2023**, *6* (1), 99–108.

[37]. Tang, M.; Carter, W. C.; Chiang, Y. M. Electrochemically Driven Phase Transitions in Insertion Electrodes For Lithium-Ion Batteries: Examples in Lithium Metal Phosphate Olivines. *Ann. Rev. Mater. Res.* **2010**, *40*, 501–529.

[38]. Dahn, J.R. Phase diagram of Li_xC_6. *Phys. Rev. B* **1991**, *44*(17), 9170.

[39]. Schweidler, S.; de Biasi, L.; Schiele, A.; Hartmann, P.; Brezesinski, T.; Janek, J. Volume Changes of Graphite Anodes Revisited: A Combined Operando X-ray Diffraction and *In Situ* Pressure Analysis Study. *J. Phys. Chem. C* **2018**, *122* (16), 8829–8835.

[40]. Reimers, J. N.; Dahn, J. R. Electrochemical and *In Situ* X-ray Diffraction Studies of Lithium intercalation in Li_xCoO_2. *J. Electrochem. Soc.* **1992**, *139*, 2–8.

[41]. Magnéli, A.; Andersson, G. On the MoO_2 Structure Type. *Acta Chem. Scand.* **1955**, *9* (8), 1378.

[42]. Rogers, D.B.; Shannon, R.D.; Sleight, A.W.; Gillson, J.L. Crystal Chemistry of Metal Dioxides with Rutile-Related Structures. *Inorg. Chem*. **1969**, *8* (4), 841–849.

[43]. Dahn, J. R.; McKinnon, W. R. Structure and Electrochemistry of Li_xMoO_2. *Solid State Ion.* **1987**, *23* (1–2), 1–7.

[44]. Cox, D. E.; Cava, R. J.; McWhan, D. B.; Murphy, D. W. A Neutron Powder Diffraction Study of the Lithium Insertion Compound $LiMoO_2$ from 4 – 440 K. *J. Phys. Chem. Solids* **1982**, *43* (8), 657–666.

[45]. Kumar Sen, U.; Shaligram, A.; Mitra, S. Intercalation Anode Material for Lithium Ion Battery Based on Molybdenum Dioxide. *ACS Appl. Mater. Interfaces* **2014**, *6* (16), 14311–14319.

[46]. Zhu, Y.; Ji, X.; Cheng, S.; Chern, Z.Y.; Jia, J.; Yang, L.; Luo, H.; Yu, J.; Peng, X.; Wang, J.; Zhou, W.; Liu, M. Fast Energy Storage in Two-Dimensional MoO_2 Enabled by Uniform Oriented Tunnels. *ACS Nano* **2019**, *13* (8), 9091–9099.

[47]. Yan, Y.; Chin, M.A.; Robertson, D.D.; Lesel, B.K.; Tolbert, S.H. Tuning the Porous Structure in PMMA-Templated Mesoporous MoO_2 for Pseudocapacitive Li-Ion Electrodes. *J. Electrochem. Soc.* **2022**, *169* (4), 040545.

[48]. Yan, Y.; Kim, H. S.; Cook, J. B.; Robbennolt, S.; Dunn, B.; Tolbert, S. H. Mesoporous MoO_2 Thin Films for High Rate Li^+ Storage: Effect of Crystallinity and Porous Structure. *Solid State Sci.* **2022**, *129*, 106890.

[49]. Wagemaker, M.; Mulder, F.M. Properties and promises of nanosized insertion materials for Li-ion batteries. *Acc. Chem. Res*. **2013**, *46*(5), 1206–1215.

[50]. Cook, J. B.; Kim, H. S.; Lin, T. C.; Lai, C. H.; Dunn, B.; Tolbert, S. H. Pseudocapacitive Charge Storage in Thick Composite MoS_2 Nanocrystal-Based Electrodes. *Adv. Energy Mater.* **2017**, *7*, 1601283.

[51]. Sun, H.; Mei, L.; Liang, J.; Zhao, Z.; Lee, C.; Fei, H.; Ding, M.; Lau, J.; Li, M.; Wang, C.; Xu, X. Three-dimensional holey-graphene/niobia composite architectures for ultrahigh-rate energy storage. *Science*, **2017**, *356* (6338), 599–604

[52]. Jain, R.; Lakhnot, A.S.; Bhimani, K.; Sharma, S.; Mahajani, V.; Panchal, R.A.; Kamble, M.; Han, F.; Wang, C.; Koratkar, N. Nanostructuring versus microstructuring in battery electrodes. *Nat. Rev. Mater.* **2022**, *7*(9), 736–746.

[53]. Okubo, M.; Hosono, E.; Kim, J.; Enomoto, M.; Kojima, N.; Kudo, T.; Zhou, H.; Honma, I. Nanosize Effect on High-Rate Li-Ion Intercalation in $LiCoO_2$ Electrode. *J. Am. Chem. Soc.* **2007**, *129* (23), 7444–7452.

[54]. Guo, B.; Yu, X.; Sun, X.G.; Chi, M.; Qiao, Z.A.; Liu, J.; Hu, Y.S.; Yang, X.Q.; Goodenough, J.B.; Dai, S. A long-life lithium-ion battery with a highly porous $TiNb_2O_7$ anode for large-scale electrical energy storage. *Energy Environ. Sci.* **2014**, 7(7), 2220–2226.

[55]. Augustyn, V.; Come, J.; Lowe, M. a; Kim, J. W.; Taberna, P.-L.; Tolbert, S. H.; Abruña, H. D.; Simon, P.; Dunn, B. High-Rate Electrochemical Energy Storage through Li^+ Intercalation Pseudocapacitance. *Nat. Mater.* **2013**, *12* (6), 518–522.

[56]. van den Bergh, W.; Lokupitiya, H.N.; Vest, N.A.; Reid, B.; Guldin, S.; Stefik, M. Nanostructure Dependence of T-Nb_2O_5 Intercalation Pseudocapacitance Probed Using Tunable Isomorphic Architectures. *Adv. Funct. Mater.* **2021**, *31* (1), 2007826.

[57]. Kang, B.; Ceder, G. Battery materials for ultrafast charging and discharging. *Nature* **2009**, *458*, 190–193.

[58]. Wang, T.; Sel, O.; Djerdj, I.; Smarsly, B. Preparation of a Large Mesoporous CeO_2 with Crystalline Walls Using PMMA Colloidal Crystal Templates. *Colloid Polym. Sci.* **2006**, *285* (1), 1–9.

[59]. Toby, B.H.; Von Dreele, R.B. GSAS-II: the genesis of a modern open-source all purpose crystallography software package. *J. Appl. Cryst.* **2013**, *46* (2), 544–549.

[60]. Momma, K.; Izumi, F. VESTA: a three-dimensional visualization system for electronic and structural analysis. *J. Appl. Cryst.* **2008**, *41* (3), 653–658.

[61]. Tamon, H.; Ishizaka, H.; Yamamoto, T.; Suzuki, T. Preparation of Mesoporous Carbon by Freeze Drying. *Carbon N. Y.* **1999**, *37* (12), 2049–2055.

[62]. Sudant, G.; Baudrin, E.; Dunn, B.; Tarascon, J.-M. Synthesis and Electrochemical Properties of Vanadium Oxide Aerogels Prepared by a Freeze-Drying Process. *J. Electrochem. Soc.* **2004**, *151* (5), A666.

[63]. Zhecheva, E.; Mladenov, M.; Zlatilova, P.; Koleva, V.; Stoyanova, R. Particle size distribution and electrochemical properties of $LiFePO_4$ prepared by a freeze-drying method. J. Phys. Chem. Solids **2010**, *71* (5), 848–853.

[64]. Shi, S.J.; Tu, J.P.; Tang, Y.Y.; Yu, Y.X.; Zhang, Y.Q.; Wang, X.L. Synthesis and electrochemical performance of $Li_{1.131}Mn_{0.504}Ni_{0.243}Co_{0.122}O_2$ cathode materials for lithium ion batteries via freeze drying. *J. Power Sources* **2013**, *221*, 300–307.

[65]. Shi, Y.; Guo, B.; Corr, S. a.; Shi, Q.; Hu, Y.-S.; Heier, K. R.; Chen, L.; Seshadri, R.; Stucky, G. D. Ordered Mesoporous Metallic MoO_2 Materials with Highly Reversible Lithium Storage Capacity. *Nano Lett.* **2009**, *9*, 4215–4220.

[66]. Guo, B.; Fang, X.; Li, B.; Shi, Y.; Ouyang, C.; Hu, Y. S.; Wang, Z.; Stucky, G. D.; Chen, L. Synthesis and Lithium Storage Mechanism of Ultrafine MoO_2 Nanorods. *Chem. Mater.* **2012**, *24* (3), 457–463.

[67]. Yang, L.; Liu, L.; Zhu, Y.; Wang, X.; Wu, Y. Preparation of Carbon Coated MoO_2 Nanobelts and Their High Performance as Anode Materials for Lithium Ion Batteries. *J. Mater. Chem.* **2012**, *22* (26), 13148.

[68]. Xia, C.; Zhou, Y.; Velusamy, D. B.; Farah, A. A.; Li, P.; Jiang, Q.; Odeh, I. N.; Wang, Z.; Zhang, X.; Alshareef, H. N. Anomalous Li Storage Capability in Atomically Thin Two-Dimensional Sheets of Nonlayered MoO_2. *Nano Lett.* **2018**, 18, 1506−1515.

[69]. Ni, J.; Zhao, Y.; Li, L.; Mai, L. Ultrathin MoO_2 Nanosheets for Superior Lithium Storage. *Nano Energy* **2015**, *11*, 129–135.

[70]. Yao, Y.; Chen, Z.; Yu, R.; Chen, Q.; Zhu, J.; Hong, X.; Zhou, L.; Wu, J.; Mai, L. Confining Ultrafine MoO_2 in a Carbon Matrix Enables Hybrid Li Ion and Li Metal Storage. *ACS Appl. Mater. Interfaces* **2020**, *12* (36), 40648-40654.

[71]. Chen, A.; Li, C.; Tang, R.; Yin, L.; Qi, Y. MoO_2-Ordered Mesoporous Carbon Hybrids as Anode Materials with Highly Improved Rate Capability and Reversible Capacity for Lithium-Ion Battery. *Phys. Chem. Chem. Phys.* **2013**, *15* (32), 13601–13610.

[72]. Sun, Y.; Hu, X.; Yu, J. C.; Li, Q.; Luo, W.; Yuan, L.; Zhang, W.; Huang, Y. Morphosynthesis of a Hierarchical MoO_2 Nanoarchitecture as a Binder-Free Anode for Lithium-Ion Batteries. *Energy Environ. Sci.* **2011**, *4* (8), 2870.

[73]. Borkiewicz, O.J.; Shyam, B.; Wiaderek, K.M.; Kurtz, C.; Chupas, P.J.; Chapman, K.W. The AMPIX electrochemical cell: a versatile apparatus for in situ X-ray scattering and spectroscopic measurements. *J. Appl. Cryst.* **2012**, *45* (6), 1261–1269.

[74]. Chien, Y.C.; Menon, A.S.; Brant, W.R.; Brandell, D.; Lacey, M.J. Simultaneous Monitoring of Crystalline Active Materials and Resistance Evolution in Lithium–Sulfur Batteries. *J. Am. Chem. Soc.* **2019**, *142* (3), 1449–1456.

[75]. Borkiewicz, O.J.; Wiaderek, K.M.; Chupas, P.J.; Chapman, K.W. Best Practices for Operando Battery Experiments: Influences of X-ray Experiment Design on Observed Electrochemical Reactivity. *J. Phys. Chem. Lett.* **2015**, *6* (11), 2081–2085.

[76]. Wagemaker, B. M.; Mulder, F. M.; Van Der Ven, A. The Role of Surface and Interface Energy on Phase Stability of Nanosized Insertion Compounds. *Adv. Mater.* **2009**, *21*, 2703–2709.

[77]. Tolbert, S.H.; Alivisatos, A.P. Size Dependence of a First Order Solid-Solid Phase Transition: The Wurzite to Rock Salt Transformation in CdSe Nanocrystals. *Science*. **1994**, *265*, 373–376

[78]. Gribb, A. A.; Banfield, J. F. Particle size effects on transformation kinetics and phase stability in nanocrystalline TiO_2. *Am. Mineral.* **1997**, *82*, 717–728.

[79]. Delmas, C.; Maccario, M.; Croguennec, L.; Le Cras, F.; Weill, F. Lithium deintercalation in $LiFePO_4$ nanoparticles via a domino-cascade model. *Nat. Mater.* **2008**, *7*, 665–671.

[80]. Brunetti, G.; Robert, D.; Bayle-Guillemaud, P.; Rouviere, J.L.; Rauch, E.F.; Martin, J.F.; Colin, J.F.; Bertin, F.; Cayron, C. Confirmation of the Domino-Cascade Model by $LiFePO_4/FePO_4$ Precession Electron Diffraction. *Chem. Mater.* **2011**, *23* (20), 4515–4524.

[81]. Wang, J.; Polleux, J.; Lim, J.; Dunn, B. Pseudocapacitive Contributions to Electrochemical Energy Storage in TiO_2 (Anatase) Aanoparticles. *J. Phys. Chem. C* **2007**, *111* (40), 14925–14931.

[82]. Ko, J. S.; Lai, C. H.; Long, J. W.; Rolison, D. R.; Dunn, B.; Nelson Weker, J. Differentiating Double-Layer, Pseudocapacitance, and Battery-like Mechanisms by Analyzing Impedance Measurements in Three Dimensions. *ACS Appl. Mater. Interfaces* **2020**, *12*, 14071–14078.

[83]. Weppner, W.; Huggins, R.A. Determination of the Kinetic Parameters of Mixed-Conducting Electrodes and Application to the System Li_3Sb. *J. Electrochem. Soc*. **1977**, *124*, 1569.

[84]. Zhu, Y.; Wang, C. Galvanostatic Intermittent Titration Technique For Phase-Transformation Electrodes. *J. Phys. Chem. C* **2010**, *114*, 2830-2841.

[85]. Verma, A.; Smith, K.; Santhanagopalan, S.; Abraham, D.; Yao, K. P.; Mukherjee, P. P. Galvanostatic Intermittent Titration and Performance Based Analysis of $LiNi_{0.5}Co_{0.2}Mn_{0.3}O_2$ Cathode. *J. Electrochem. Soc.* **2017**, *164*, A3380.

[86]. Pender, J.P.; Jha, G.; Youn, D.H.; Ziegler, J.M.; Andoni, I.; Choi, E.J.; Heller, A.; Dunn, B.S.; Weiss, P.S.; Penner, R.M.; Mullins, C.B. Electrode Degradation in Lithium-Ion Batteries. *ACS Nano*, **2020**, *14* (2), 1243–1295.

[87]. Merryweather, A.J.; Jacquet, Q.; Emge, S.P.; Schnedermann, C.; Rao, A.; Grey, C.P. Operando monitoring of single-particle kinetic state-of-charge heterogeneities and cracking in high-rate Li-ion anodes. *Nat. Mater.* **2022**, *21* (11), 1306–1313.

[88].Märker, K.; Reeves, P. J.; Xu, C.; Griffith, K. J.; Grey, C. P. Evolution of Structure and Lithium Dynamics in $LiNi_{0.8}Mn_{0.1}Co_{0.1}O_2$ (NMC811) Cathodes during Electrochemical Cycling. *Chem. Mater.* **2019**, *31* (7), 2545–2554.

[89]. Park, K.S.; Benayad, A.; Kang, D.J.; Doo, S.G. Nitridation-driven Conductive $Li_4Ti_5O_{12}$ for Lithium Ion Batteries. *J. Am. Chem. Soc.* **2008**, *130* (45), 14930–14931

[90]. Verde, M.G.; Baggetto, L.; Balke, N.; Veith, G.M.; Seo, J.K.; Wang, Z.; Meng, Y.S. Elucidating the Phase Transformation of $Li_4Ti_5O_{12}$ Lithiation at the Nanoscale. *ACS Nano* **2016**, *10* (4), 4312–4321.

[91]. Zhang, W.; Seo, D.H.; Chen, T.; Wu, L.; Topsakal, M.; Zhu, Y.; Lu, D.; Ceder, G.; Wang, F. Kinetic pathways of ionic transport in fast-charging lithium titanate. *Science* **2020** *367* (6481), 1030–1034.

CHAPTER 3

Analyzing How the Suppression of Phase Transitions Leads to Pseudocapacitive Properties in Li_xMoO_2 Using Electrochemical Impedance Spectroscopy

3.1 Introduction

Energy storage devices with both high energy density and high power density are needed for a variety of applications, including the widespread electrification of transportation and the implementation of grid-scale storage systems.[1,2] Pseudocapacitive energy storage devices, which rely on surface- or near-surface redox reactions for charge storage, are one promising avenue to meet performance needs for both energy and power density.[3-7] Li-ion pseudocapacitors, in particular, have seen extensive attention due to their intermediate properties between Li-ion batteries and electrochemical capacitors.[8-13] Li-ion batteries store charge through bulk redox reactions between a host material and an Li^+ electrolyte, and often show poor rate capability due to the need for long-range solid-state diffusion of ions in the host material and phase transitions between lithiated and delithiated phases.[14,15] On the other hand, electrochemical capacitors, which rely on electrostatic adsorption of ions to store charge, can cycle very quickly but provide low overall capacity since they do not use redox reactions.[16-18] Broadly, pseudocapacitors store charge through surface or near-surface redox reactions, which lead to their having higher energy density than electrochemical capacitors with significantly faster charge storage than bulk battery materials.[3-5] Originally, the term pseudocapacitance was first used by Conway in the 1990s to describe redox processes in thin films like $RuO_2 \bullet H_2O$.[5-7,19] Over the last fifteen years, however, the concept has seen renewed interest in nanostructured Li-ion battery materials. With short ion diffusion lengths in the solid state, some, though not all, nanoscale battery materials can become intercalation pseudocapacitors that maintain battery-like capacity with fast, pseudocapacitive

kinetics.[4,6] The blurring of the boundaries between battery and pseudocapacitor materials has led to confusion in the literature about the differences in their charge storage mechanisms.[2,20-22] The role of fast Li^+ ion diffusion has been identified as one prerequisite for pseudocapacitive mechanisms, but not all nanostructured battery materials become pseudocapacitors. An additional key component that has seen less attention is the role of structural phase transitions that occur during Li^+ (de)insertion.[23-28] Most battery materials undergo first-order phase transitions, which occur by nucleation of the new phase followed by its growth throughout an entire crystallite. The need for such a phase transformation slows charge storage since nucleation typically requires a high activation energy, and, during subsequent growth of the new phase, ion insertion is coupled to the diffusion of the phase front.[29,30] Naturally, these first-order phase transitions can be diffusion-limited, and their absence has been hypothesized as a key prerequisite for realizing pseudocapacitive charge storage.[6,24,26,27]

Recently, we analyzed the first-order phase transition in bulk Li_xMoO_2, a model tunnel-structure insertion anode material, and showed that the same Li^+ insertion process in nanoscale versions of MoO_2 led to significant changes in the phase transition mechanism.[31] In nanoporous MoO_2, the phase transition had a smaller miscibility gap and shorter duration, whereas in even smaller MoO_2 nanocrystals, the transformation changed to an entirely second-order solid solution-type mechanism. Importantly, these changes in the phase transition behavior were linked with dramatically improved rate capability of the nanoscale MoO_2 compared to bulk MoO_2 using electrochemical measurements of the polarization in the phase transition region. However, the charge storage mechanism could not be clearly identified as pseudocapacitive or battery-like due to limited information from the commonly used power law kinetic analysis.

Here, we apply a series of analyses based on electrochemical impedance spectroscopy (EIS) to MoO_2 to better understand the role of phase transition behavior in governing the charge storage mechanism. EIS-based techniques have been used for a variety of purposes, including the commonly used Bode analysis, which is a standard kinetic characterization for supercapacitors.[16,22,32,33] This method examines the EIS-derived real capacitance (C'), imaginary capacitance (C"), and the phase angle (ϕ) as a function of frequency, or time scale of the measurement, to distinguish the contribution of kinetically fast or slow processes. A series of recent studies adapted the Bode analysis to distinguish double-layer capacitive, pseudocapacitive, and battery-like charge storage mechanisms in different materials.[22,34-37] Based on measurements on electrodes of YP50, a standard carbon supercapacitor, T-Nb_2O_5, a well-known pseudocapacitor, and $LiFePO_4$, a fast battery, features of the EIS response were proposed as characteristic signatures of the respective charge storage mechanisms.[22] Specifically, YP50 showed virtually no change in its capacitance or phase angle at different voltages, consistent with its box-shaped cyclic voltammogram, whereas $LiFePO_4$ displayed a sharp spike in capacitance and dip in phase angle at its characteristic voltage for charge storage. T-Nb_2O_5 had intermediate behavior, with broad features across a range of voltage in both capacitance and phase angle. The frequency dependence of capacitance and phase angle also corroborated the mechanisms, with $LiFePO_4$ showing the most change, T-Nb_2O_5, showing intermediate, and YP50 showing the least change with frequency, which suggested increasingly fast kinetics. In this work, we carry out the Bode analysis on our series of size-controlled MoO_2 materials with distinct phase transition behavior, with the goal of determining how specific behaviors affect the charge storage mechanism. By contrasting the measured capacitance from EIS with the observed capacity in cyclic voltammetry, we differentiate regimes of diffusion-limited and capacitive charge storage in the various sized samples of MoO_2.

Notably, the least capacitive regions of charge storage occur during the first-order phase transitions in bulk MoO_2, indicating that the combination of long Li^+ diffusion distances and the kinetically slow first-order phase transition lead to diffusion-limited charge storage. In contrast, the same voltage region shows highly capacitive charge storage in the nanostructured MoO_2 materials with suppressed phase transition behavior, confirming the key role that suppression of phase transitions plays in the development of pseudocapacitive properties.

3.2 Materials and Methods

3.2.1 Materials.

The following materials were obtained from commercial suppliers and used without further purification: ammonium molybdate (para) tetrahydrate $(NH_4)_6Mo_7O_{24}•4H_2O$ (99%, Alfa Aesar), ammonium persulfate (98%, Alfa Aesar), ammonium lauryl sulfate (~30% in H_2O, Sigma Aldrich), molybdenum (V) chloride (99.6%, Alfa Aesar), methyl methacrylate (contains ≤ 30 ppm MEHQ as inhibitor, 99%, Sigma Aldrich).

3.2.2 Preparation of bulk and nanoporous MoO_2.

The bulk and nanoporous MoO_2 samples were synthesized through a modified sol-gel route using freeze-drying. In this process, an aqueous solution of dissolved Mo precursor is frozen in liquid N_2 and dried under vacuum, then subsequently calcined to crystallize the material. To produce the nanoporous MoO_2, 150 - 200 nm polymer colloids were mixed with the Mo precursor in the initial solution in order to template the nanoscale architecture.

In a typical synthesis of bulk MoO_2, 200 mg of $(NH_4)_6Mo_7O_{24}•4H_2O$ was added to 3 mL of water, then heated at 60ºC until it was fully dissolved. The resulting solution was frozen by dropwise addition into liquid N_2 and lyophilized on a Schlenk line for 12 to 24 hours (<200 mtorr). The dried Mo precursor powder was then calcined in a quartz boat at for 1 hour at 625ºC in flowing

5%H_2/95%N_2 (1 hour heating ramp time and natural cooling rate). For the nanoporous MoO_2, a similar procedure was followed with slight modifications. In a typical synthesis, 200 mg of $(NH_4)_6Mo_7O_{24}$•$4H_2O$ was added to 2 mL of water, then heated at 60ºC until it was fully dissolved. Then, 2 – 4 mL of polymer colloid solution were added (depending on the density of colloids in solution) to obtain a 1:1 mass ratio of Mo precursor:colloid. The synthesis of the PMMA colloids with different sizes is described below. After the Mo precursor-polymer colloid solution was mixed thoroughly, it was frozen by dropwise addition to liquid N_2 and lyophilized on a Schlenk line for 12 to 24 hours (< 200 mtorr). The dried Mo precursor-polymer composite powder was calcined in a quartz boat in flowing Ar in two separate heating steps, with the powder cooled, removed from the furnace and exposed to air in between: first, at 550ºC for 1 hour, and then at 675ºC for 1 hour (1 hour heating ramp time for each step and natural cooling rate). This two-heating-step process was employed to separate removal of the polymer templates from crystallization of the MoO_2 material. Since calcination occurs under anaerobic conditions, the polymer templates do not combust fully and, with a single step process, Mo carbides form at the temperatures needed to crystallize the nanoporous MoO_2. After the second calcination, nanoporous MoO_2 samples were stored in inert atmosphere to avoid ambient oxidation.

3.2.3 Synthesis of poly(methyl methacrylate)(PMMA) colloids.

The synthesis of PMMA colloids with different sizes was adapted from a previous procedure described by Wang et al.[38] Ammonium persulfate (APS) was used as the initiator and ammonium lauryl sulfate (ALS) as the surfactant. APS, ALS, and deionized water were put into a three-neck round-bottom flask (250 mL) equipped with a magnetic stirrer, a reflux condenser, and a thermometer. After the temperature was raised to 75 °C, the monomer methyl methacrylate (MMA) was added. After monomer addition, the reaction temperature was kept at 80–85 °C for an hour

before a cooling operation was applied. The concentrations of reagents were varied to make different sizes of PMMA. The as-synthesized PMMA colloidal aqueous solutions were extracted with hexanes to remove excess monomer. Before use, the mass density of colloids in solution was measured by thermogravimetric analysis.

3.2.4 Synthesis of MoO_2 nanocrystals.

MoO_2 nanocrystals were synthesized in a hydrothermal autoclave according to previously reported method with minor adaptations. In a typical synthesis, 270 mg of $MoCl_5$, 15 mL water, and 5 mL ethanol were added to a 50 mL Teflon-lined Parr autoclave. The autoclave was sealed and heated for 6 hours at 180ºC, then allowed to cool overnight. The product was centrifuged washed with ethanol three times. After the final wash, the powder was dried at 80ºC under vacuum. The as-synthesized nanocrystals were stored under inert atmosphere to avoid ambient oxidation.

3.2.5 Structural characterization.

Scanning electron microscopy (SEM) images were obtained using a model JEOL JSM-6700F field emission electron microscope with 5 kV accelerating voltage and 6 mm working distance. Sample purity was assessed using laboratory X-ray diffraction collected with a PANalytical X'Pert Pro diffractometer operating with Cu Kα (λ = 1.5418 Å) using a 0.05° step size, an accelerating voltage of 45 kV, and a current of 40 mA.

3.2.6 Electrochemical testing.

All MoO_2 powders were assembled into composite slurry electrodes for electrochemical testing. Electrodes had an overall composition of 70% active material, 10% multiwalled carbon nanotubes, 10% vapor-grown carbon fibers, and 10% polyvinylidene fluoride (PVDF) binder. Prior to slurry preparation, the dry slurry components and current collector were heated at 100ºC under vacuum overnight. The active material was ground with the carbons in a mortar and pestle

dry, then a PVDF binder solution (2.5 % wt in N-methyl pyrrolidone) was added and mixed to produce a homogeneous paste that was cast onto an aluminum current collector with a doctor blade. The electrodes were dried under vacuum at 100ºC overnight. Electrodes with 0.7 mm diameter were punched out for electrochemical testing with mass loadings of active material of 1 – 1.5 mg/cm^2.

All electrochemical measurements were conducted in stainless-steel 2032 coin cells (MTI) with a stainless-steel conical spring, two 0.5-mm stainless-steel spacers, a glass microfiber separator (Whatman), and a polished Li metal electrode (Sigma). The electrolyte was 1 M $LiPF_6$ in 1:1 ethylene carbonate (EC): dimethyl carbonate (DMC), with ~50 uL of electrolyte used per cell. All cycling experiments were performed between 1.1 V and 3 V *vs.* Li/Li^+ on a VMP3 potentiostat/galvanostat (Bio-Logic). When calculating C-rates, the theoretical capacity used was 210 mAh/g, based on the 1 e^- Li^+ insertion reaction into MoO_2 (1C = 210 mA/g, 5C = 1.05 A/g, etc.). Electrochemical impedance spectroscopy was conducted after samples had been rate tested galvanostatically. Measurements were conducted between 900 kHz and 5 mHz using a 10 mV amplitude input each 0.1 V between 1.1 and 2.7 V versus Li/Li^+.

3.2.7 Operando Synchrotron X-ray Diffraction

Operando SXRD was conducted at beamline 11-3 at the Stanford Synchrotron Radiation Lightsource at 12.7 keV, using modified coin cells with Be spacers as adapted from Chien et al.[39] While conventional modified coin cells use stainless steel spacers with holes to provide X-ray transparency, experiments done with these cells are susceptible to artifacts due to the lack of stack pressure and electrical conductivity in the region probed by the X-ray beam.[40] Our improved cell design uses Be spacers, which do not have holes, and thus remain both rigid and conductive to accurately recreate the cycling environment in a real coin cell. Beryllium metal discs 15 mm in

diameter x 0.5 mm thick were purchased from American Elements (99%). Caution: Beryllium oxide particulates formed from machining or breaking beryllium are carcinogenic and the material should be handled with caution.

3.3 Results and Discussion

For this study, we synthesized three characteristic versions of MoO_2 by adapting previously reported methods.[24,31,41] Briefly, bulk and nanoporous MoO_2 powders were produced with a modified aqueous sol-gel-type method based on freeze drying, followed by calcination under inert atmosphere. For the nanoporous MoO_2, polymer colloids were added to the initial precursor solution to template formation of the nanoporous architecture. MoO_2 nanocrystal powders were prepared hydrothermally. The three MoO_2 materials were characterized with scanning electron microscopy (SEM, **Figure 1A – 1C**). The MoO_2 nanocrystals comprise individual particles 15 – 30 nm in diameter loosely agglomerated into larger secondary particles, whereas the nanoporous MoO_2 consists of micron-scale particles with ~ 150 nm pores throughout the material. Finally, the bulk MoO_2 shows anisotropic particles approximately 0.5 – 10 μm in diameter.

The MoO_2 materials were assembled into composite electrodes with conductive carbon and binder and tested in half-cell configuration in coin cells. MoO_2 is often studied for the high capacity conversion reaction in which it is fully reduced to form Mo metal and Li_2O.[42-49] However, this reaction suffers from large volume change and the formation of insulating regions of Li_2O, which hinder its reversibility and rate capability. Here, we limit the lower voltage bound to 1.1 V vs. Li/Li^+ to access the one electron insertion reaction, in which Li^+ is reversibly (de)inserted into vacant interstitial sites within the tunnels of MoO_2 (**Equation 1**). This reaction has a moderate theoretical capacity of 210 mAh/g and shows significantly improved cyclability and scalability compared to conversion.[50]

$$(1)\ MoO_2 + x\ e^- + x\ Li^+ \rightleftharpoons Li_xMoO_2 \quad (0 \leq x \leq 1)$$

The rate capability of each material was assessed with galvanostatic rate testing from 1C to 20C (**Figure S1A**). Both the nanoporous MoO_2 and MoO_2 nanocrystals show excellent cycling performance, with near-completion of the insertion reaction at slow rates, and strong retention of capacity at faster ones. Bulk MoO_2, on the other hand, can only store about 150 mAh/g at 1C, and retains relatively little of that capacity out to 20C. The galvanostatic charge storage profiles of the three materials also show key differences, with the clear plateaus for bulk MoO_2 replaced by sloping profiles to different extents in the nanoscale MoO_2 (**Figure S1B**). Using operando X-ray

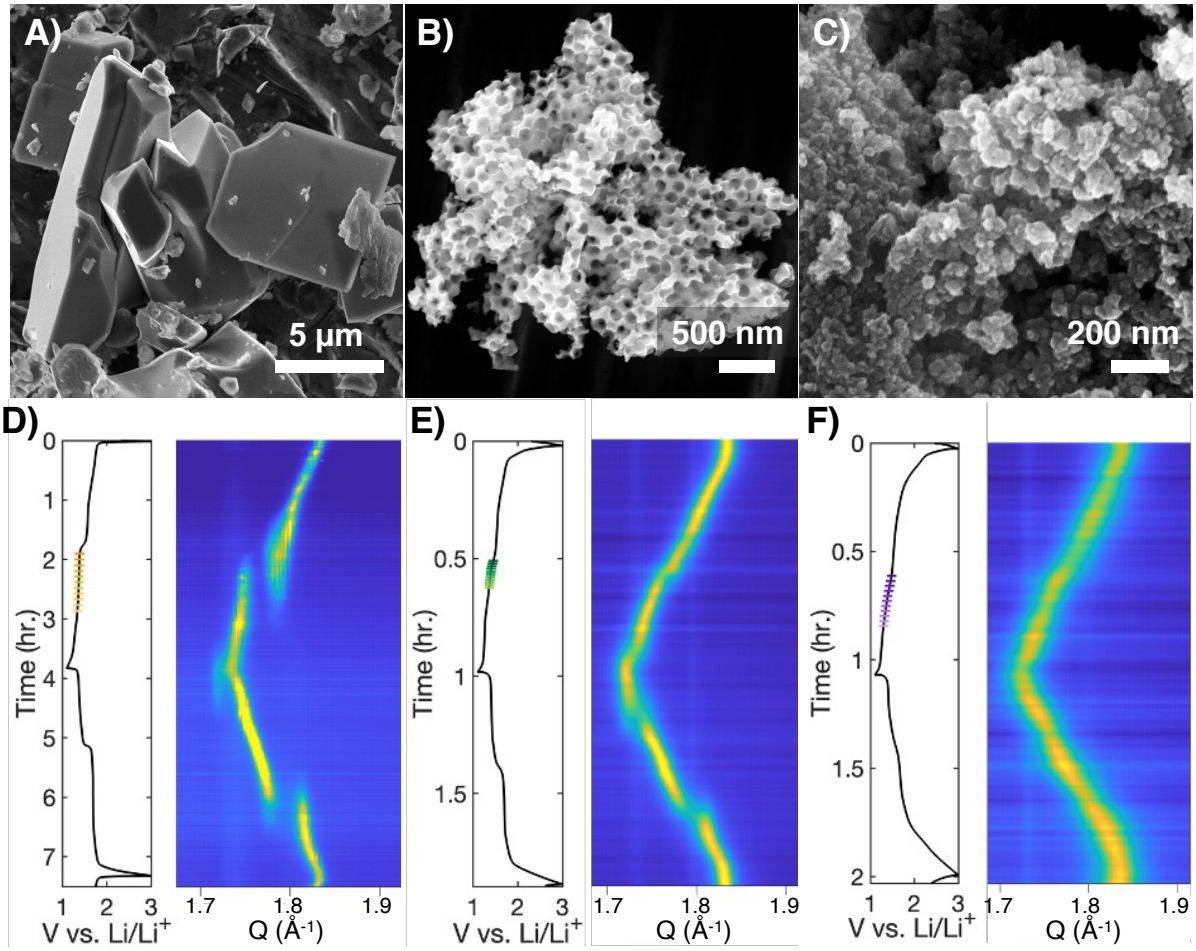

Figure 1. Scanning electron microscopy characterization of **A)** bulk MoO_2, **B)** nanoporous MoO_2, and **C)** MoO_2 nanocrystals. **D) – F)** The respective operando X-ray diffraction data during one lithiation-delithiation cycle. Bulk MoO_2 shows a large first-order phase transition that is partially suppressed in the nanoporous MoO_2 and then completely suppressed to a solid-solution behavior in the MoO_2 nanocrystals.

diffraction, we characterized the structural change of the MoO_2 materials during cycling, with the most intense (011) reflection highlighted (**Figure 1D – 1F**). Each material begins as pristine, unlithiated MoO_2, and finishes lithiation at the same $LiMoO_2$ phase. However, the pathway between these two endpoints varies for each type of MoO_2. Halfway through the lithiation, bulk MoO_2 shows a first-order phase transition with a large miscibility gap, followed by another first-order phase transition near the end of lithiation that does not complete due to the voltage cutoff. In the same regions for nanoporous MoO_2, there is still a first-order phase transition, but the miscibility gap is smaller, and the duration of two-phase coexistence is dramatically shorter. Finally, for the MoO_2 nanocrystals, the entire lithiation process occurs as a second-order-type continuous solid-solution process. As such, these MoO_2 materials provide a model system for comparison that has the same basic redox reaction for charge storage, but simultaneously has three distinct types of phase transformation behavior.

With the system characterized through these well-established methods, we now turn to analysis with EIS. A single EIS measurement involves application of a small, oscillating voltage to an electrode across a range of frequencies and recording its response. Here, 10 mV was chosen as the amplitude for the applied voltage, and the frequency (*f)* range was 5 mHz to 900 kHz. For each material, a set of EIS measurements was taken each 0.1 V throughout the voltage window (1.1 V to 2.7 V). The analysis method for the data was adapted based on the derivation described by Ko et al.[22] In summary, the real and imaginary components of the capacitance (C' and C", respectively) were derived from the real and imaginary components of the impedance (Z' and Z", respectively) based on the following relationships:

$$C' = \frac{-Z''(\omega)}{\omega|Z(\omega)|^2} \quad (2) \qquad C'' = \frac{-Z'(\omega)}{\omega|Z(\omega)|^2} \quad (3)$$

where ω is the angular frequency. These relationships are derived from the basic equations that govern the impedance of a simple equivalent circuit made up of a resistor and capacitor in series.[33] This extraction of the capacitance from the impedance is a standard method in the supercapacitor community to identify the capacitive response of a material, but has only more recently been applied to battery and pseudocapacitor materials.

The phase angle (ϕ) was another parameter of interest extracted from the EIS measurements, which was calculated by

$$\phi = \tan^{-1}\frac{Z'(\omega)}{Z''(\omega)} \quad (4)$$

By definition, ϕ represents the shift of the alternating current (AC) response of the cell relative to the alternating applied voltage during the EIS experiment. According to basic circuit equations, a pure resistor has a fully in-phase response (ϕ = 0º), whereas a double-layer capacitor current response lags out-of-phase with the voltage (ϕ = 90º).[33] A diffusion element can be modeled with an intermediate phase angle (ϕ = 45º). Based on these derivations, ϕ has been described as the weighted sum of these components according to their prevalence. For example, the hypothesis follows that a battery-like charge storage mechanism should exhibit ϕ somewhere between a diffusion-limited process and a resistive one, whereas a capacitor or pseudocapacitor would likely maintain much higher values for ϕ.[22] We caution, however, that the interpretation of this parameter, especially at intermediate values, is subject to oversimplification, as we discuss later.

To start, we analyzed the real capacitance and phase angle at the lowest frequency (f = 5 mHz) (**Figure 2A, 2B**). This timescale corresponds to a cyclic voltammetry experiment with a sweep rate of about 0.2 mV/s, or about a five hour charge or discharge, which is slow enough that most charge storage processes should occur. For all three MoO_2 materials, the capacitance remains low from 2.0 V - 2.5 V, where MoO_2 is not redox active, except for a small peak for the nanocrystals attributed to redox at undercoordinated surface sites. Below 1.9 V, the capacitance rises in two peaks with maxima at 1.6 V and 1.4 V, respectively. These two peaks correspond to different redox peaks in MoO_2, and based on the *operando* XRD data discussed above, coincide with two distinct types of structural change. Lithiation from 1.5 – 1.9 V involves a solid-solution-type process for all three materials, where no phase transformations are necessary and only continuous structural evolution occurs. In this region, the capacitance is similar for the nanoscale MoO_2, with a peak capacitance of 876 F/g for nanoporous MoO_2 and 819 F/g for MoO_2 nanocrystals. For bulk MoO_2, the value is less than half the same amount at 378 F/g, despite having the same capacity in this region in cyclic voltammetry. This decrease in capacitance is likely due

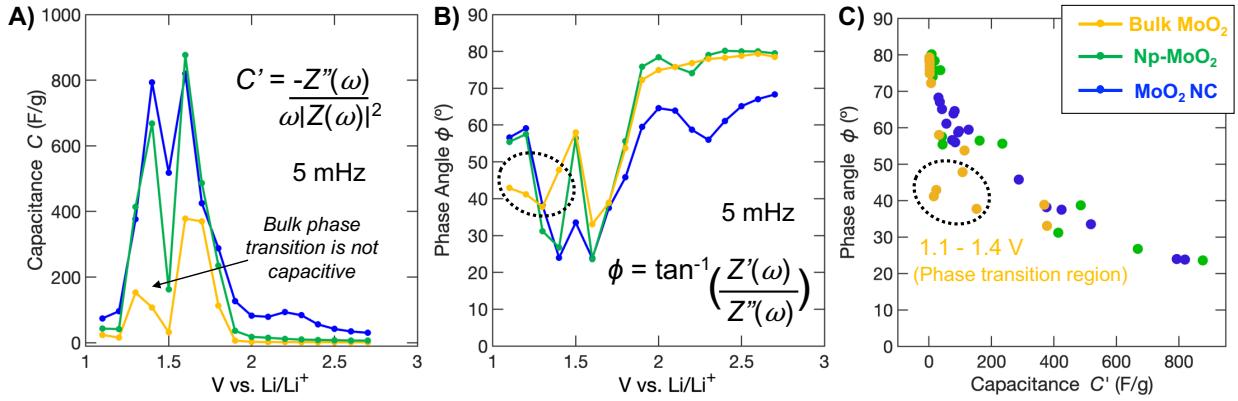

Figure 2. Results of voltage-dependent EIS analysis at low frequency (f = 5 mHz). **A)** Real capacitance C' and **B)** phase angle ϕ for the three types of MoO_2. Bulk MoO_2 shows lowered capacitance at the first redox peak at 1.6 V and dramatically decreased capacitance during its first-order phase transitions between 1.1 – 1.4 V. The nanostructured MoO_2 remains much more capacitive in this region due to the changed phase transition behavior. **C)** The inverse relationship between capacitance and phase angle is clear for most points, except those circled, which correspond to the phase transition region for bulk MoO_2.

to the longer Li^+ diffusion distances for bulk MoO_2, confirming the importance of fast ion diffusion in promoting pseudocapacitive properties in the nanoscale MoO_2.

During the second peak from 1.2 – 1.4 V, more than just the diffusion distances vary, as the type of structural change depends on the material. In this region, bulk MoO_2 undergoes a first-order phase transition, while nanoporous MoO_2 has a partially suppressed version of the phase transition, and the MoO_2 nanocrystals have a fully suppressed solid-solution-type process. These differences in structural change lead to even more dramatic effects on the capacitance. At 1.4 V, the MoO_2 nanocrystals have the highest peak capacitance at 793 F/g, despite having the lowest capacity at this potential in cyclic voltammetry. The nanoporous MoO_2 exhibits good, but still lowered, capacitance at 668 F/g, while bulk MoO_2 shows much lower peak capacitance of 153 F/g. This disparity indicates that the type of structural change is a key factor that determines whether charge storage is included in the measured capacitance. The large first-order phase transition for bulk MoO_2 in this region, in combination with its long diffusion lengths, make its charge storage diffusion-limited. This result is consistent with previous work, where we demonstrated that the onset of the phase transition induces a large overpotential in galvanostatic intermittent titration technique (GITT) experiments. When the phase transition is partly suppressed and mediated by nanoscale diffusion lengths in the nanoporous MoO_2, much more of the charge storage is capacitive, even though the transition remains first-order. Finally, when the structural change becomes fully second-order solid-solution-type in the nanocrystals, the effect on the capacitance is the least.

We also examined the phase angle ϕ across the voltage window at this frequency. The observed trends in the capacitance strongly indicate that bulk MoO_2 is the least pseudocapacitive sample and the MoO_2 nanocrystals are the most pseudocapacitive. Accordingly, we expected the

former to exhibit relatively low phase angles that show resistive behavior, and vice versa for the latter. However, we found the opposite to be true: bulk MoO_2 maintains the highest phase angles during charge storage, with angles of 34º and 38º at the local minima for 1.6 V and 1.3 V, respectively, compared to values of 23º and 24º for the MoO_2 nanocrystals at their local minima. We also found the phase angle data inconsistent within the bulk MoO_2 sample, as the solid solution region peak had a lower phase angle than the phase transition region did, in contrast to the higher portion of capacitive charge storage indicated by the capacitance for the former. Rather than supporting the capacitance data and the variety of other analysis techniques that corroborate the slow, diffusion-limited nature of the phase transition in bulk MoO_2, the phase angle directly contradicts it. In fact, we noticed a strong inverse correlation between the magnitude of the capacitance and the phase angle throughout all charge storage regions in the samples. This relationship was consistent for the peak values for all of the samples, as listed above, and throughout the entire voltage window. For example, at the small peak in the capacitance for the nanocrystals between 2.0 – 2.5 V, that does not exist for the other samples, there is an inverse minimum in the phase angle for the nanocrystals, but not for the other two samples. These results demonstrate that the phase angle is a poor predictor for evaluating the charge storage mechanism. The main reason is that diffusion-limited or battery-like charge storage is not registered in the impedance measurement, as evidenced by its absence from the capacitance, even at the very low frequency tested here. As such, the phase angle counterintuitively ends up the highest for the least capacitive samples.

To demonstrate this observation, we plotted the phase angle versus the capacitance to examine their relationship (**Figure 2C**). The inverse correlation between these two values is clear for all three samples, as nearly every point falls along a pseudolinear trajectory. The highest capacitances,

which correspond to the redox peaks for the two types nanostructured MoO_2, also possess the lowest phase angles out of the points. The opposite is also mostly true, where large clusters of points with phase angle > 50º correspond to the redox inactive region from 2 – 2.5 V. Four points from bulk MoO_2, however, appear as exceptions to this rule and fall below the other points with relatively low phase angles despite their low capacitance. Notably, these points are all from the low end of the voltage window (1.1 – 1.4 V), where bulk MoO_2 is undergoing first-order phase transitions. These exceptions suggest that the battery-like charge storage mechanism still influences the phase angle, but to a much lesser extent than a high capacitance would. Overall, the phase angle remains a misleading metric in these battery-to-pseudocapacitor systems.

The observed capacitance, on the other hand, appears to be a strong indicator for the charge storage mechanism. To explore this concept further, we plotted the low frequency capacitance measured by EIS alongside the capacity measured by cyclic voltammetry (**Figure 3A – 3C**). To enable comparison, we multiplied the current measured during the anodic sweep in the CV experiment by the sweep rate to get units of capacitance, rather than current. This technique is frequently used to determine the capacitance of supercapacitor materials, but cannot be used to calculate capacitance when Faradaic reactions are present.[16,17] Instead, we note that we apply the method here simply to allow comparison between capacity from CV and capacitance by EIS. The resulting graphs provide a semi-quantitative measurement of how much of the observed capacity is capacitive in nature. This quantification has been performed a number of times using sweep rate dependence in CV,[2,10-12,51] but has not been done with the method here to our knowledge. This analysis yields similar results as the capacitance alone, discussed above, but more clearly emphasizes the disparity between the different MoO_2 samples as the phase transition behavior changes. For the overall analysis, bulk MoO_2 shows only 17% capacitive charge storage, compared

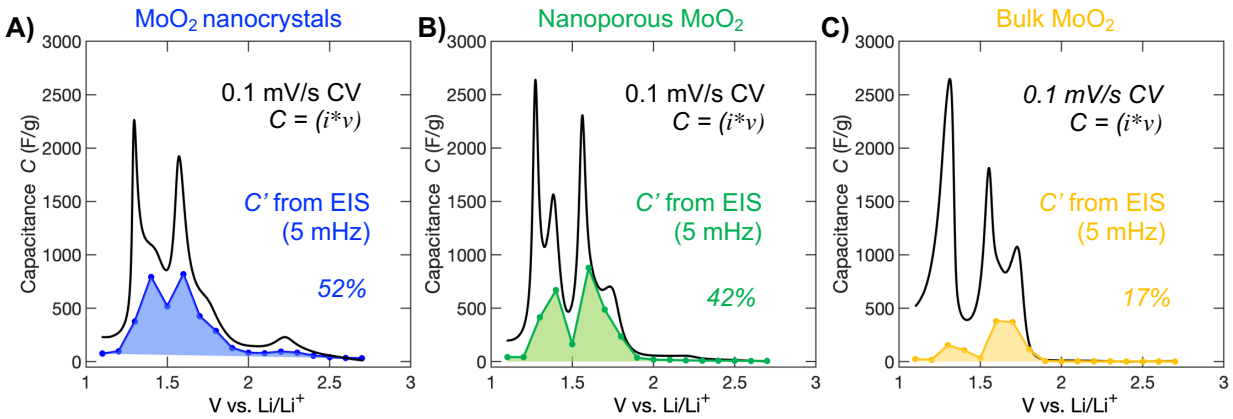

Figure 3. A) – C) Relative contribution of capacitance to capacity for the three MoO_2 materials. For each graph, the capacitance *C'* measured by EIS at low frequency (f = 5 mHz) is compared to the capacity from CV with a sweep rate of 0.1 mV/s to determine how capacitive the overall charge storage is. The current from CV was divided by the sweep rate to give equivalent units for accurate comparison. The percentage shown reflects the relative contribution of the capacitance to the overall capacity.

to 44% for the nanoporous MoO_2 and 52% for the nanocrystals. These fractional values are considerably lower than suggested by other analyses, and should be considered semi-quantitative but not exact. Beyond the overall amount of capacitance, this technique gives information about which parts of charge storage are the most or least capacitive. For example, clear from the analysis once again is that the first-order phase transition that slows charge storage in bulk MoO_2 makes it the most battery-like. For the third peak in the CV around 1.3 – 1.4 V, bulk MoO_2 shows the highest capacity, but lowest capacitance by a significant amount. The MoO_2 nanocrystals, on the other hand, have the smallest third peak in CV at 1.4 V, but the highest capacitance of the samples in this region, confirming that their solid-solution-type structural change is key to achieving pseudocapacitive charge storage.

Beyond the low frequency behavior, we can also conduct traditional Bode analysis, which looks at the frequency dependence of the capacitance and/or phase angle for a specific voltage. We highlighted these parameters for a range of frequencies (f = 5 mHz – 50 Hz) for the phase transition region at 1.4 V (**Figure 4A, 4C**) and for the solid-solution region at 1.6 V (**Figure 4B,**

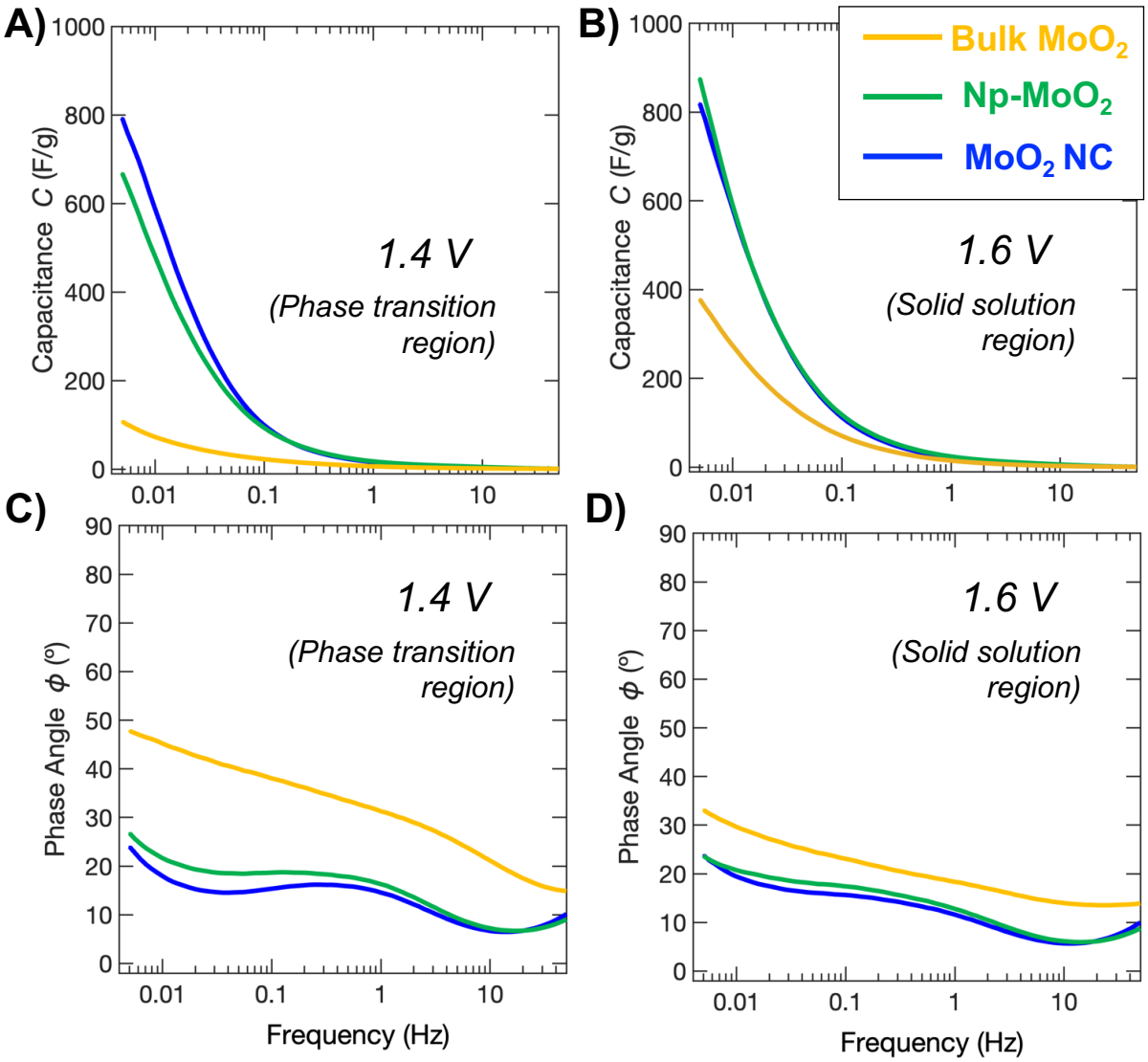

Figure 4. Traditional Bode analysis showing the capacitance *C'* and the phase angle ϕ as a function of frequency for **A), C)** 1.4 V and **B),D)** 1.6 V, which correspond to the phase transition region, and solid solution region of the lithiation, respectively.

4D). Previous work noted that supercapacitor materials showed less dependence on frequency in this frequency range compared to pseudocapacitor or battery materials, since supercapacitors should maintain their full capacity well above the lowest frequency here, which corresponds to a scan rate of 0.2 mV/s.[22] In contrast, the pseudocapacitor and battery materials showed a steep increase in capacitance towards lower frequency, with the battery showing a steeper slope. Here, our results indicate a different conclusion, with bulk MoO_2 showing the least slope, while

nanoporous and nanocrystals show much more dramatic increases in capacitance at low frequency for both the 1.4 V and 1.6 V plots. For bulk MoO_2, the increase in capacitance as frequency decreases is greater for the solid-solution region at 1.6 V, while the 1.4 V region shows low capacitance even to the lowest frequency. Once again, the long solid-state diffusion distances and first-order phase transition for bulk MoO_2 greatly limit its capacitance, especially during the phase transition, despite the low frequencies tested here. Ironically, the frequency dependence of bulk MoO_2's capacitance looks most similar to that of YP50, although for a completely different reason. Whereas YP50 showed a relatively flat curve due to its high rate capability, bulk MoO_2 shows a similar shape since its charge storage is so slow that it is excluded from capacitance. Clearly, this result highlights a potential pitfall in conducting Bode analysis for battery and pseudocapacitor materials. Although the shape of the capacitance-frequency curve is not a clear indicator of the charge storage mechanism, the relative magnitude of the capacitance remains insightful, as discussed in the previous sections. Unlike supercapacitors, pseudocapacitor materials like the MoO_2 nanocrystals still show decreases in their capacitance as frequency is increased, even at low frequencies.

As the other metric examined in the Bode analysis, the phase angle ϕ shows non-monotonic changes with frequency for all three materials and for both main redox peaks. As frequency is decreased from 50 Hz, ϕ decreases, then increases, multiple times. This non-monotonic shift is also shown for T-Nb_2O_5 and $LiFePO_4$ in previous work, and may reflect a varying weight of the resistive and capacitive components in the circuit. Notably, the pattern holds for all samples tested here. Again, as we noted before, however, the phase angle is a misleading metric for these systems and should not be considered on its own.

Finally, the charge storage dynamics are shown in greatest detail in three-dimensional Bode plots, where C' or ϕ is plotted versus both voltage and *f*. For C', each MoO_2 sample shows two local maxima that correspond to the redox peaks, with both MoO_2 nanocrystals and nanoporous MoO_2 exhibiting much larger peaks than bulk MoO_2, which is much less capacitive (**Figure 5A – 5C).** For all samples, the peaks have the highest capacitance at low frequencies, and diminish rapidly as frequency is increased and the experiment time scale becomes too short for the Faradaic processes in the material. Conversely, the phase angle shows local minima in the same regions, with the deepest minima for the MoO_2 nanocrystals and the shallowest for the bulk MoO_2 at low frequency (**Figure 5D – 5F**). At higher frequencies, all samples show significantly lower phase angle, confirming the transition to purely resistive behavior. Overall, these three-dimensional plots

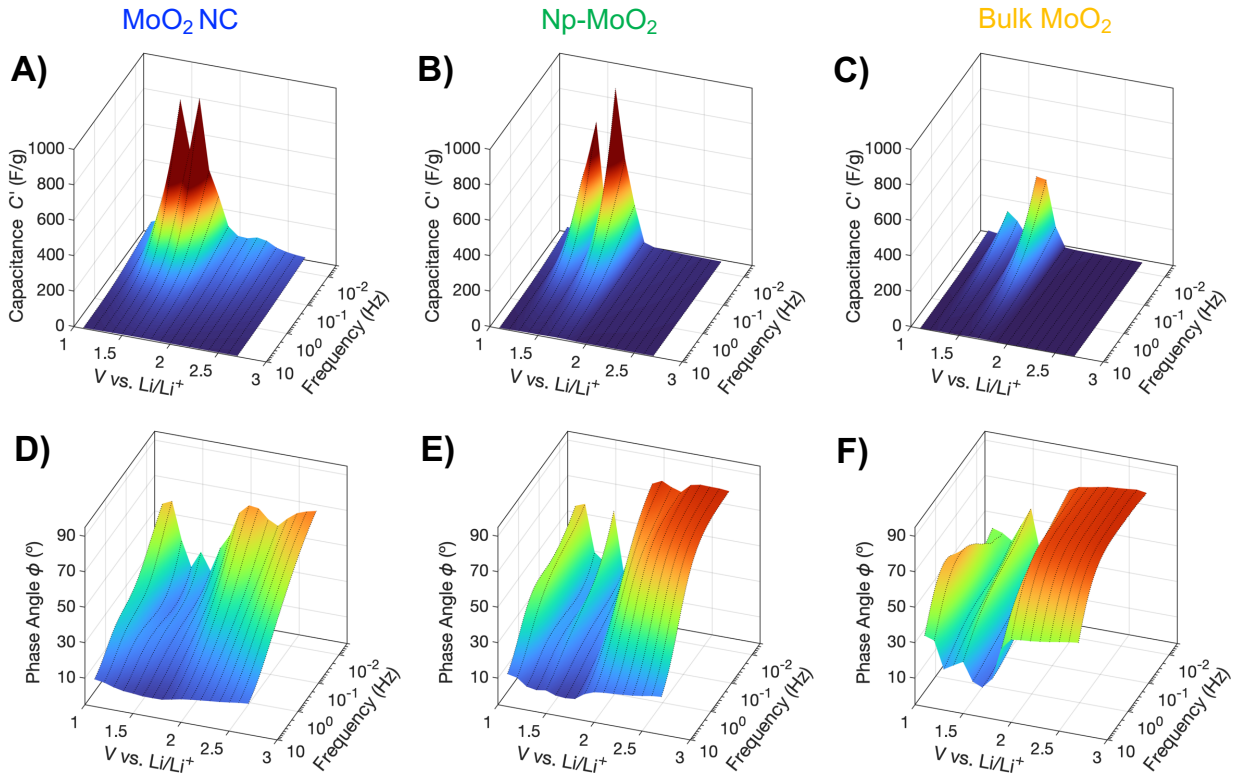

Figure 5. Three dimensional Bode plots showing **A) – C)** capacitance *C'* and **D) – F)** phase angle ϕ as a function of voltage and frequency.

confirm the pseudocapacitive properties of the nanostructured MoO_2 and the fully diffusion-limited charge storage mechanism in bulk MoO_2.

3.4 Conclusion

In conclusion, we evaluated the charge storage mechanisms of three representative MoO_2 materials that show similar redox, but distinct types of phase transition behavior, using an EIS-based analysis. This method for analyzing charge storage mechanism with EIS has been applied frequently to supercapacitor materials but only recently used for Li-ion battery materials and pseudocapacitors. We find that the measured capacitance in MoO_2 relative to the total capacity depends strongly on the specifics of charge storage, with redox associated with the first-order phase transition in bulk MoO_2 demonstrating very low capacitance. When that same phase transition is partially or fully suppressed in the nanostructured MoO_2, the measured capacitance is much closer to the capacity. Notably, the phase angle ϕ extracted from the same analysis showed highly misleading results, with the bulk MoO_2 counterintuitively maintaining the highest phase angle during its charge storage. Overall, this work emphasizes the impact of structural change of charge storage mechanism and highlights important potential pitfalls of EIS-based analysis on battery-to-pseudocapacitor materials.

3.5 References

[1] Gür, T.M. Review of electrical energy storage technologies, materials and systems: challenges and prospects for large-scale grid storage. *Energy Environ. Sci.* **2018**, *11*(10), 2696–2767.

[2] Simon, P.; Gogotsi, Y.; Dunn, B. Where do batteries end and supercapacitors begin? *Science* **2014**, *343*(6176), 1210–1211.

[3] Fleischmann, S.; Mitchell, J.B.; Wang, R.; Zhan, C.; Jiang, D.E.; Presser, V.; Augustyn, V. Pseudocapacitance: From Fundamental Understanding to High Power Energy Storage Materials. *Chem. Rev.* **2020**, *120*(14), 6738–6782.

[4] Choi, C.; Ashby, D.S.; Butts, D.M.; DeBlock, R.H.; Wei, Q.; Lau, J.; Dunn, B. Achieving high energy density and high power density with pseudocapacitive materials. *Nat. Rev. Mater.* **2020**, *5*(1), 5–19.

[5] Conway, B. E.; Pell, W. G. Double-layer and Pseudocapacitance Types of Electrochemical Capacitors and their Applications to the Development of Hybrid Devices. *J. Solid State Electrochem.* **2003**, *7*, 637-644.

[6] Conway, B. E. Transition from "Supercapacitor" to "Battery" Behavior in Electrochemical Energy Storage. *J. Electrochem. Soc.* **1991**, *138* (6), 1539–1549.

[7] Conway, B. E.; Birss, V.; Wojtowicz, J. The role and utilization of pseudocapacitance for energy storage by supercapacitors. *J. Power Sources* **1997**, *66***,** 1–14.

[8] Augustyn, V.; Simon, P.;Dunn, B. Pseudocapacitive Oxide Materials for High-Rate Electrochemical Energy Storage. *Energy Environ. Sci.* **2014**, *7*, 1597-1614.

[9] Augustyn, V.; Come, J.; Lowe, M. A.; Kim, J. W.; Taberna, P.; Tolbert, S. H.; Abruña, H. D.; Simon, P.; Dunn, B. High-Rate Electrochemical Energy Storage through Li^+ Intercalation Pseudocapacitance. *Nat. Mater.* **2013**, *12*, 518-522.

[10] Cook, J. B.; Kim, H. S.; Lin, T. C.; Lai, C. H.; Dunn, B.; Tolbert, S. H. Pseudocapacitive Charge Storage in Thick Composite MoS_2 Nanocrystal-Based Electrodes. *Adv. Energy Mater.* **2017**, *7*, 1601283.

[11] Brezesinski, T.; Wang, J.; Tolbert, S. H.; Dunn, B. Ordered Mesoporous α-MoO_3 with Iso-Oriented Nanocrystalline Walls for Thin-Film Pseudocapacitors. *Nat. Mater.* **2010**, *9*, 146-151.

[12] Kim, H. S.; Cook, J. B.; Lin, H.; Ko, J. S.; Tolbert, S. H.; Ozolins, V.; Dunn, B. Oxygen vacancies enhance pseudocapacitive charge storage properties of MoO_{3-x}. *Nature Mater.* **2017**, *16*, 454-460.

[13] Cook, J. B.; Kim, H.; Yan, Y.; Ko, J. S.; Robbennolt, S.; Dunn, B.; Tolbert, S. H. Mesoporous MoS_2 as a Transition Metal Dichalcogenide Exhibiting Pseudocapacitive Li and Na-Ion Charge Storage. *Adv. Energy Mater.* **2016**, *6*, 1501937.

[14] Li, M.; Lu, J.; Chen, Z.; Amine, K. 30 years of lithium-ion batteries. *Adv. Mater.* **2018**, *30* (33), 1800561.

[15] Van Der Ven, A.; Bhattacharya, J.; Belak, A. A. Understanding Li Diffusion in Li-Intercalation Compounds. *Acc. Chem. Res.* **2013**, *46*, 1216–1225.

[16] Taberna, P. L.; Simon, P.; Fauvarque, J. F. Electrochemical Characteristics and Impedance Spectroscopy Studies of Carbon-Carbon Supercapacitors. *J. Electrochem. Soc.* **2003**, *150* (3), A292.

[17] Simon, P.; Gogotsi, Y. Materials for Electrochemical Capacitors. *Nat. Mater*. **2008**, *7* (11), 845–854.

[18] Sassin, M. B.; Chervin, C. N.; Rolison, D. R.; Long, J. W. Redox Deposition of Nanoscale Metal Oxides on Carbon for Next-Generation Electrochemical Capacitors. *Acc. Chem. Res.* **2013**, *46* (5), 1062–1074.

[19] Zheng, J. P.; Cygan, P. J.; Jow, T. R. Hydrous Ruthenium Oxide as an Electrode Material for Electrochemical Capacitors. *J. Electrochem. Soc.* **1995**, *142* (8), 2699–2703.

[20] Costentin, C.; Savéant, J. M. Energy storage: pseudocapacitance in prospect. *Chem. Sci.*, **2019**, *10*, 5656-5666.

[21] Brousse, T.; Bélanger, D.; Long, J. W. To be or not to be pseudocapacitive. *J. Electrochem. Soc*, **2015**, *162*, 5185-5189.

[22] Ko, J. S.; Lai, C. H.; Long, J. W.; Rolison, D. R.; Dunn, B.; Nelson Weker, J. Differentiating Double-Layer, Pseudocapacitance, and Battery-like Mechanisms by Analyzing Impedance Measurements in Three Dimensions. *ACS Appl. Mater. Interfaces* **2020**, *12*, 14071–14078.

[23] Cook, J. B.; Lin, T. C.; Kim, H.-S.; Siordia, A.; Dunn, B. S.; Tolbert, S. H. Suppression of Electrochemically Driven Phase Transitions in Nanostructured MoS_2 Pseudocapacitors Probed Using Operando X-ray Diffraction. *ACS Nano*, **2019**, *13*, 1223–1231.

[24] Kim, H.-S.; Cook, J. B.; Tolbert, S. H.; Dunn, B. The Development of Pseudocapacitive Properties in Nanosized-MoO_2. *J. Electrochem. Soc.* **2015**, *162*, A5083–A5090.

[25] Muller, G. A.; Cook, J. B.; Kim, H.-S.; Tolbert, S. H.; Dunn, B. High Performance Pseudocapacitor Based on 2D Layered Metal Chalcogenide Nanocrystals. *Nano Lett.* **2015**, *15*, 1911–1917.

[26] Lesel, B. K.; Cook, J. B.; Yan, Y.; Lin, T. C.; Tolbert, S. H. Using Nanoscale Domain Size to Control Charge Storage Kinetics in Pseudocapacitive Nanoporous $LiMn_2O_4$ Powders. *ACS Energy Lett.* **2017**, *2* (10), 2293–2298

[27] Mitchell, J.B.; Geise, N.R.; Paterson, A.R.; Osti, N.C.; Sun, Y.; Fleischmann, S.; Zhang, R.; Madsen, L.A.; Toney, M.F.; Jiang, D.E.; Kolesnikov, A.I.; Mamontov, E.l; Augustyn, V. Confined Interlayer Water Promotes Structural Stability for High-Rate Electrochemical Proton Intercalation in Tungsten Oxide Hydrates. *ACS Energy Lett.* **2019**, *4* (12), 2805–2812.

[28] Cook, J. B.; Ko, J. S.; Lin, T. C.; Robertson, D. D.; Kim, H. S.; Yan, Y.; Yao, Y.; Dunn, B. S.; Tolbert, S. H. Ultrafast Sodium Intercalation Pseudocapacitance in MoS_2 Facilitated by Phase Transition Suppression. *ACS Appl. Energy Mater.* **2023**, *6* (1), 99–108.

[29] Tang, M.; Carter, W. C.; Chiang, Y. M. Electrochemically Driven Phase Transitions in Insertion Electrodes For Lithium-Ion Batteries: Examples in Lithium Metal Phosphate Olivines. *Ann. Rev. Mater. Res.* **2010**, *40*, 501–529.

[30] Meethong, N.; Huang, H. Y. S.; Carter, W. C.; Chiang, Y. M. Size-dependent lithium miscibility gap in nanoscale $Li_{1-x}FePO_4$. *Electrochem. Solid State Lett.* **2007**, *10*, A134.

[31] Robertson, D.D.; Cumberbatch, H.; Pe, D.J.; Yao, Y.; Tolbert, S.H.; Size-Dependent Suppression of Phase Transitions Leads to Fast-Charging in Nanoscale Li_xMoO_2. *Submitted.*

[32] Bai, L.; Conway, B. E. AC Impedance of Faradaic Reactions Involving Electrosorbed Intermediates: Examination of Conditions Leading to Pseudoinductive Behavior Represented in Three-Dimensional Impedance Spectroscopy Diagrams. *J. Electrochem. Soc.* **1991**, *138*, 2897.

[33] Vivier, V.; Orazem, M. E. Impedance Analysis of Electrochemical Systems. *Chem. Rev.* **2022**, *122* (12), 11131–11168.

[34] Ko, J. S.; Sassin, M. B.; Rolison, D. R.; Long, J. W. Deconvolving Double-Layer, Pseudocapacitance, and Battery-like Charge-Storage Mechanisms in Nanoscale $LiMn_2O_4$ at 3D Carbon Architectures. *Electrochim. Acta* **2018**, *275*, 225–235.

[35] Ko, J. S.; Sassin, M. B.; Parker, J. F.; Rolison, D. R.; Long, J. W. Combining Battery-like and Pseudocapacitive Charge Storage in 3D MnO_x@carbon Electrode Architectures for Zinc-Ion Cells. *Sustain. Energy Fuels* **2018**, *2* (3), 626–636.

[36] Ko, J. S.; Donakowski, M. D.; Sassin, M. B.; Parker, J. F.; Rolison, D. R.; Long, J. W. Deciphering Charge-Storage Mechanisms in 3D MnOx@carbon Electrode Nanoarchitectures for Rechargeable Zinc-Ion Cells. *MRS Commun.* **2019**, *9* (1), 99–106.

[37] Mitchell, J. B.; Wang, R.; Ko, J. S.; Long, J. W.; Augustyn, V. Critical Role of Structural Water for Enhanced Li+ Insertion Kinetics in Crystalline Tungsten Oxides. *J. Electrochem. Soc.* **2022**, *169* (3), 030534.

[38]. Wang, T.; Sel, O.; Djerdj, I.; Smarsly, B. Preparation of a Large Mesoporous CeO_2 with Crystalline Walls Using PMMA Colloidal Crystal Templates. *Colloid Polym. Sci.* **2006**, *285* (1), 1–9.

[39] Chien, Y.C.; Menon, A.S.; Brant, W.R.; Brandell, D.; Lacey, M.J. Simultaneous Monitoring of Crystalline Active Materials and Resistance Evolution in Lithium–Sulfur Batteries. *J. Am. Chem. Soc.* **2019**, *142* (3), 1449–1456.

[40] Borkiewicz, O.J.; Wiaderek, K.M.; Chupas, P.J.; Chapman, K.W. Best Practices for Operando Battery Experiments: Influences of X-ray Experiment Design on Observed Electrochemical Reactivity. *J. Phys. Chem. Lett.* **2015**, *6* (11), 2081–2085.

[41] Yan, Y.; Chin, M.A.; Robertson, D.D.; Lesel, B.K.; Tolbert, S.H. Tuning the Porous Structure in PMMA-Templated Mesoporous MoO_2 for Pseudocapacitive Li-Ion Electrodes. *J. Electrochem. Soc.* **2022**, *169* (4), 040545.

[42] Shi, Y.; Guo, B.; Corr, S. a.; Shi, Q.; Hu, Y.-S.; Heier, K. R.; Chen, L.; Seshadri, R.; Stucky, G. D. Ordered Mesoporous Metallic MoO_2 Materials with Highly Reversible Lithium Storage Capacity. *Nano Lett.* **2009**, *9*, 4215–4220.

[43] Guo, B.; Fang, X.; Li, B.; Shi, Y.; Ouyang, C.; Hu, Y. S.; Wang, Z.; Stucky, G. D.; Chen, L. Synthesis and Lithium Storage Mechanism of Ultrafine MoO_2 Nanorods. *Chem. Mater.* **2012**, *24* (3), 457–463.

[44] Yang, L.; Liu, L.; Zhu, Y.; Wang, X.; Wu, Y. Preparation of Carbon Coated MoO_2 Nanobelts and Their High Performance as Anode Materials for Lithium Ion Batteries. *J. Mater. Chem.* **2012**, *22* (26), 13148.

[45] Xia, C.; Zhou, Y.; Velusamy, D. B.; Farah, A. A.; Li, P.; Jiang, Q.; Odeh, I. N.; Wang, Z.; Zhang, X.; Alshareef, H. N. Anomalous Li Storage Capability in Atomically Thin Two-Dimensional Sheets of Nonlayered MoO_2. *Nano Lett.* **2018**, 18, 1506−1515.

[46] Ni, J.; Zhao, Y.; Li, L.; Mai, L. Ultrathin MoO_2 Nanosheets for Superior Lithium Storage. *Nano Energy* **2015**, *11*, 129–135.

[47] Yao, Y.; Chen, Z.; Yu, R.; Chen, Q.; Zhu, J.; Hong, X.; Zhou, L.; Wu, J.; Mai, L. Confining Ultrafine MoO_2 in a Carbon Matrix Enables Hybrid Li Ion and Li Metal Storage. *ACS Appl. Mater. Interfaces* **2020**, *12* (36), 40648-40654.

[48] Chen, A.; Li, C.; Tang, R.; Yin, L.; Qi, Y. MoO_2-Ordered Mesoporous Carbon Hybrids as Anode Materials with Highly Improved Rate Capability and Reversible Capacity for Lithium-Ion Battery. *Phys. Chem. Chem. Phys.* **2013**, *15* (32), 13601–13610.

[49] Sun, Y.; Hu, X.; Yu, J. C.; Li, Q.; Luo, W.; Yuan, L.; Zhang, W.; Huang, Y. Morphosynthesis of a Hierarchical MoO_2 Nanoarchitecture as a Binder-Free Anode for Lithium-Ion Batteries. *Energy Environ. Sci.* **2011**, *4* (8), 2870.

[50] Kumar Sen, U.; Shaligram, A.; Mitra, S. Intercalation Anode Material for Lithium Ion Battery Based on Molybdenum Dioxide. *ACS Appl. Mater. Interfaces* **2014**, *6* (16), 14311–14319.

[51] Wang, J.; Polleux, J.; Lim, J.; Dunn, B. Pseudocapacitive Contributions to Electrochemical Energy Storage in TiO_2 (Anatase) Aanoparticles. *J. Phys. Chem. C* **2007**, *111* (40), 14925–14931.

CHAPTER 4

Electrochemically-Formed Disordered Rock Salt ω-$V_9Mo_6O_{40}$ as a Fast-Charging Li-Ion Electrode Material

4.1 Introduction

Electrochemical energy storage devices with both high energy density and high power density are essential to a number of important technologies, including electric vehicles and grid-scale storage.[1,2] While next-generation energy storage chemistries show great promise, traditional insertion-based Li-ion batteries currently show the optimal balance of capacity, rate capability, and stability with extended cycling.[3] Despite these advantages, however, Li-ion batteries still have significant rate limitations, especially with the high mass loadings used in commercial cells.[4,5] During charging, stored charge in the device is balanced by solid-state redox reactions between a host material and a Li^+ electrolyte, and achieving full capacity requires transport of Li^+ and electrons throughout all of the host material in the electrode. Typically, slowed kinetics arise from this process, since the diffusion of Li^+ in the solid state is several orders of magnitude slower than than in the liquid electrolyte, even in the best performing host materials.[6] As such, a fundamental understanding of how crystal structure and particle morphology influence both ionic and electronic transport is necessary in the search for even better electrode materials.

One class of compounds of particular interest as electrodes in Li-ion batteries is the rock salt-derived family of materials. The base rock salt structure, which comprises a densely packed edge-sharing network of cations and anions extending in three-dimensions, serves as a basis for a variety of relevant materials, including several conversion-type anodes,[7-10] the layered Ni-based and disordered rock salt cathodes,[11-14] and spinel $LiMn_2O_4$[15] and $Li_4Ti_5O_{12}$.[16] Accordingly, extensive experimental and theoretical work has focused on understanding the details of charge

storage in this family. While the dense bonding environment in the rock salt crystal structure typically leads to high activation energies for Li^+ hopping and thus poor ionic diffusion, an appropriate balance of weakly repulsive cation species (typically Li^+) can lower the activation energies dramatically.[13,17,18] For example, in the layered Ni-based cathodes, cations order into alternating slabs of smaller (Li^+) and larger (Ni^{3+}, Co^{3+}, Mn^{3+}, etc.) cations, and this well-defined ordering is essential for good ionic transport throughout the structure.[17] Alternatively, in disordered rock salt structures, a large amount of weakly repulsive Li^+ cations can still provide sufficient ionic diffusion, provided that they form a percolating network of hopping pathways in the crystal structure.[13,18]

Rock salt structures can also be formed electrochemically during initial ion insertion, and often remain electrochemically active in subsequent cycles. Most famously, this process occurs for V_2O_5, which undergoes a series of reversible phase transitions at moderate Li^+ contents ($0 < x < 1.5$), and then transforms irreversibly to a disordered-rock-salt-type ω-$Li_xV_2O_5$ phase at deep lithiation ($2 < x < 3$).[19,20] ω-V_2O_5 has been extensively studied as a potential cathode material cycled between 2.0 – 4.0 V vs. Li/Li^+ ($0 < x < 2$) due to its excellent rate capability when nanostructured, especially in composite structures with conductive carbons.[21-24] Recently, Liu et. al highlighted that ω-V_2O_5 could be lithiated significantly further, and the resulting disordered rock salt $Li_{3+x}V_2O_5$ showed exceptional performance in a voltage region ideal for a fast-charging anode material (0.01 – 2.0 V vs. Li/Li^+).[25] Importantly, these results firmly establish the potential for application of electrochemically-formed disordered rock salt compounds in commercial cells.

The electrochemical formation of disordered rock salt structures is not unique to V_2O_5. Previous work has shown this process occurs upon Li^+ insertion in Li_2MoO_4,[26] $Li_2W_2O_7$,[27] and TiO_2.[28,29] Notably, TiO_2 undergoes a similar transformation on Na^+ insertion.[30] Most recently,

Barnes et al. demonstrated that amorphous films of Nb oxide crystallize into a rock salt phase when cycled with Li^+, unlike in previous cases where crystalline precursor materials were used.[29] Broadly, these examples all tend to form at deep lithiation, and produce disordered structures, likely since they are synthesized at room temperature. Beyond these trends, however, relatively little is known about this wide-ranging class of materials, since they have only recently gained greater attention. In particular, there is a clear need for design principles about the role of precursor structure and composition in governing the transformation process, the structure of the resulting material, and its electrochemical performance.

In this work, we characterize the electrochemical formation of a disordered rock salt phase from the crystalline compound $V_9Mo_6O_{40}$ (VMO). VMO was first reported in 1982, and has seen relatively little attention aside from basic characterization of its charge storage performance.[31]-[33] While a range of vanadium molybdenum oxides with lower Mo content form solid-solutions in the α-V_2O_5 crystal structure, which consists of layers of edge-sharing pyramids held together by van der Waals forces, VMO and the related phase V_2MoO_8[34] make the lowest Mo content structures that are not isostructural with α-V_2O_5. The crystal structure of VMO possess the same edge-sharing pyramids that are seen in α-V_2O_5, but instead of extending infinitely in two-dimensions, they alternate with planes of corner-sharing octahedra.[32] Importantly, this change imparts rigidity into the crystal structure, and makes VMO a three-dimensionally-connected tunnel structure instead of a layered van der Waals compound. Here, we study the Li^+ insertion properties of micron-scale particles of VMO. Using *operando* X-ray diffraction, we demonstrate that VMO transforms directly into a disordered rock salt structure upon lithiation, in contrast to the multiphase pathway seen for α-V_2O_5. Subsequent cycling in the resulting disordered rock salt VMO shows good rate capability and cycling longevity, with clear increases in the phase intensity upon insertion,

followed by decrease in intensity and formation of a broad, disordered phase during deinsertion of Li^+. High-resolution transmission electron microscopy shows that the disordered rock salt VMO has an unusual microstructure consisting of a collection of highly distorted, loosely coherent atomic planes. This data suggests that the increased rigidity in the pristine VMO crystal structure relative to α-V_2O_5 dramatically changes the formation pathway and microstructure of the resulting disordered rock salt material, and more broadly highlights the role of precursor structure and composition in this family of compounds.

4.2 Materials and Methods

4.2.1 Preparation of VMO

Micron-scale bulk $V_9Mo_6O_{40}$ was prepared through a modified aqueous sol-gel route based on freeze-drying. In a typical synthesis, 200 mg NH_4VO_3 (Sigma-Aldrich) and 200 mg $(NH_4)_6Mo_7O_{24}$•$4H_2O$ (Alfa Aesar) was dissolved with stirring in 5 mL deionized water in a 20 mL scintillation vial at 85ºC. Once the precursors were fully dissolved, the precursor solution was vitrified by dropwise addition to liquid N_2, then lyophilized in a custom-built vacuum chamber on a Schlenk line for 12 to 24 hours (< 200 mtorr). The resulting dried precursor powder was calcined in a muffle furnace in air at 550ºC (30 min ramp, 1 hr. hold). A variety of calcination temperatures were found to result in phase pure $V_9Mo_6O_{40}$, and this procedure was chosen since it provides a balance between moderate particle size and good crystallinity. After calcination and prior to electrode fabrication, VMO powders were ground in a mortar and pestle.

4.2.2 Structural Characterization

Scanning electron microscopy (SEM) images and energy dispersive spectroscopy (EDS) spectra were obtained using a model JEOL JSM-6700F field emission electron microscope. Imaging was conducted with 5 kV accelerating voltage and 6 mm working distance. EDS spectra were taken

with 15 kV accelerating voltage and 15 mm working distance. Transmission electron microscopy (TEM) was performed using an FEI Technai G^2 T20 high-resolution EM operating at 200 kV. Sample purity was assessed using laboratory X-ray diffraction collected with a PANalytical X'Pert Pro diffractometer operating with Cu Kα (λ = 1.5418 Å) using a 0.05° step size, an accelerating voltage of 45 kV, and a current of 40 mA. X-ray photoelectron spectroscopy (XPS) analysis was performed using a Kratos Axis Ultra DLD with a monochromatic Al K-α radiation source. A charge neutralizer filament was used to control charging of the sample, a 20 eV pass energy was used with a 0.1 eV step size, and scans were calibrated using the C 1s peak shifted to 284.8 eV. The integrated areas of the XPS peaks and atomic ratios were found using CasaXPS software. The atomic sensitivity factors used were from the Kratos library within the Casa software. All samples were loaded into the instrument without exposure to air. For *ex situ* characterization of materials after cycling, including SEM, TEM, and XPS, electrodes were cycled in coin cells, which were subsequently opened inside of a glovebox. The electrodes were then washed multiple times in dimethyl carbonate (DMC) and dried under vacuum before sample preparation for the given technique.

4.2.3 Electrochemical testing

VMO powders were assembled into composite slurry electrodes for electrochemical testing. Electrodes had an overall composition of 80% active material, 5% multiwalled carbon nanotubes, 5% vapor-grown carbon fibers, and 10% polyvinylidene fluoride (PVDF) binder. Prior to slurry preparation, the dry slurry components and current collector were heated at 100ºC under vacuum overnight. The active material was ground with the carbons in a mortar and pestle dry, then a PVDF binder solution (2.5 % wt in N-methyl pyrrolidone) was added and mixed to produce a homogeneous paste that was cast onto an aluminum current collector with a doctor blade. The

electrodes were dried under vacuum at 100ºC overnight. Electrodes with 0.7 mm diameter were punched out for electrochemical testing with mass loadings of active material of 1 – 1.5 mg/cm^2. These moderate mass loadings were chosen to study the intrinsic performance of the active material, as they allow for reproducible electrode performance with minimal optimization of the slurry. High mass loadings, such as those used in most practical devices, lead to rate limitations from electrode composition and distribution of active material that require extensive optimization to overcome.

All electrochemical measurements were conducted in stainless-steel 2032 coin cells (MTI) with a stainless-steel conical spring, a 0.5-mm stainless-steel spacer for the anode, a 0.5-mm aluminum spacer for the cathode, and a glass microfiber separator (Whatman). The electrolyte was 1 M LiPF6 in 1:1 ethylene carbonate (EC): dimethyl carbonate (DMC), with ~50 uL of electrolyte used per cell. All cycling experiments were performed between 1.5 V and 3.5 V or 4.0 V *vs.* Li/Li$^+$ on a VMP3 potentiostat/galvanostat (Bio-Logic). For testing purposes, VMO electrodes were studied in a half cell configuration versus a Li metal anode. When calculating C-rates, the theoretical capacity used was 240 mAh/g, based on the 1 e$^-$ Li$^+$ insertion reaction into $V_9Mo_6O_{40}$ (1C = 240 mA/g, 5C = 1.20 A/g, etc.).

4.2.4 Operando Synchrotron X-ray Diffraction

All *operando* synchrotron X-ray diffraction measurements were performed at beamline 11-ID-C at the Advanced Photon Source at Argonne National Laboratory at 17.0 keV in transmission geometry with an area detector. For this experiment, freestanding pellet electrodes of VMO were made with 6:1:1:2 mass ratio of VMO:vapor-grown carbon fibers :multiwalled carbon nanotubes: PTFE binder. These electrodes were loaded into AMPIX cells in an argon glovebox with Li metal counter electrodes, glass fiber separators, and electrolyte (1M $LiPF_6$ in 1:1 EC:DMC). All two-

dimensional SXRD data was calibrated with a LaB_6 external standard and integrated into one-dimensional diffraction patterns using GSAS-II.[35] Background subtraction was performed on diffraction data to remove scattering from the electrolyte. Crystal structures were visualized with the VESTA software package.[36]

4.3 Results and Discussion

4.3.1 Synthesis and structure of $V_9Mo_6O_{40}$

The crystal structure of $V_9Mo_6O_{40}$ consists of alternating planes of edge-sharing pyramids and corner sharing octahedra along the *a* axis, and these planes extend infinitely in the *b* axis direction (**Figure 1A**, middle).[32] The corner sharing octahedra also connect parallel to the *c* axis, while the pyramids repeat without connecting along that direction. $V_9Mo_6O_{40}$ is near the middle composition of the fully oxidized V-Mo oxides, of which the binary oxides α-V_2O_5 and α-MoO_3 are end members (**Figure 1A**). Both α-V_2O_5 and α-MoO_3 are layered van der Waals compounds, although the different size, charge, and preferred coordination number of V^{5+} and Mo^{6+} lead them to have different arrangements within this structure type. Whereas α-V_2O_5 layers are made of edge-sharing square pyramid dimers that corner share with alternating orientation along the layer direction,[37] α-MoO_3 consists of

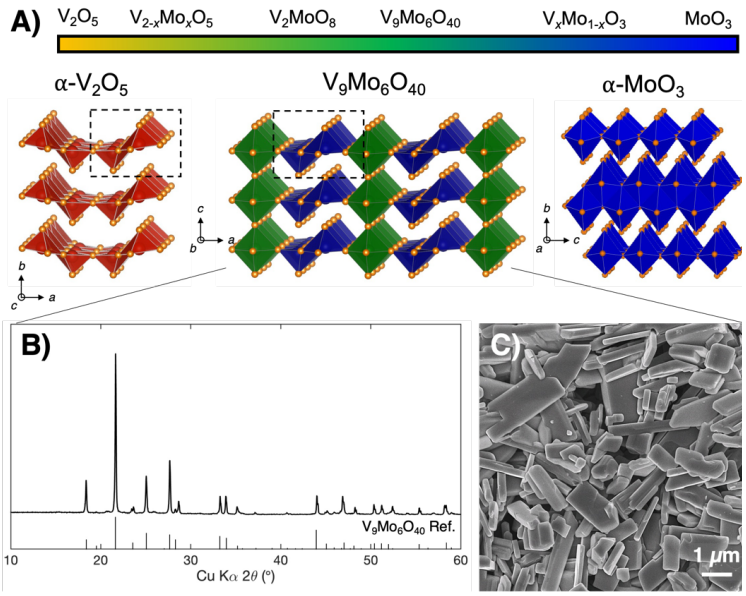

Figure 1. A) Structure space of the fully oxidized V-Mo oxides, with the crystal structures of $V_9Mo_6O_{40}$ (**middle**) and the two end members α-V_2O_5 (**left**) and α-MoO_3 (**right**) highlighted. The dashed boxes indicate edge-sharing pyramid dimers, a structural feature shared by α-V_2O_5 and $V_9Mo_6O_{40}$. **B)** Powder X-ray diffraction pattern and **C)** scanning electron micrograph of the bulk $V_9Mo_6O_{40}$ in this study.

a bilayer network of edge-sharing octahedra, with bilayers separated by the van der Waals gap.[38,39] α-V_2O_5 shows an extended solid solution region where $V_{2-x}Mo_xO_5$ is stable ($0 \leq x \leq 0.6$) with only minor changes in structure.[40] For example, in $V_{2-x}Mo_xO_5$, Mo^{5+} can exist to better fit within the structure with a more similar stable coordination environment to V^{5+}. However, by $x = 1$, the greater stability of Mo^{6+} favors the inclusion of corner-sharing octahedra, in which each transition metal cation is coordinated by six oxygen atoms, with decreased electrostatic repulsion between sites compared to the edge-sharing pyramid dimers in α-V_2O_5. This transition leads to the middle region of the phase diagram, which includes $V_9Mo_6O_{40}$ (VMO), the focus of this study, and the isostructural V_2MoO_8. Importantly, the three-dimensional connectivity of the planes of corner-sharing octahedra makes VMO a tunnel structure without a van der Waals gap, although the structure is still anisotropic due to the presence of edge-sharing pyramid dimer units.

We synthesized micron-scale powders of VMO through a modified sol-gel-type method based on freeze-drying. In this process, aqueous solutions of NH_4VO_3 and $(NH_4)_6Mo_7O_{24}$ precursors were vitrified in liquid N_2 and dried through sublimation on a Schlenk line. The resulting dried V-Mo precursor powder was then calcined in air at 550ºC to crystallize VMO. We note that freeze-drying is a well-established route to powders with high surface area and porosity, and, here, helps to improve purity by preventing the precipitation of NH_4VO_3, which often occurs with traditional sol-gel synthesis.[41-44] Powder X-ray diffraction on as-synthesized powders shows formation of the VMO phase with greater than 99% purity, confirming the benefits of our approach (**Figure 1B**). Scanning electron microscopy (SEM) characterization of the VMO shows anisotropic particles with a distribution of sizes and shapes (**Figure 1C**). Most commonly observed is a bar-shape morphology, where particles are about 2 – 10 microns long, 1 – 2 microns wide, and only about 100 – 500 nm deep, which clearly indicates a preferred axis of growth for VMO

crystals. These bar-like particles often possess L-shaped bends, which presumably form where two sections of crystal extend in different directions within the same particle. Additional SEM characterization of the pristine VMO is available in Figure S1 of the Supporting Information.

4.3.2 Electrochemistry of $V_9Mo_6O_{40}$

To evaluate the electrochemical behavior of VMO when cycled with Li^+, these VMO powders were assembled into composite electrodes with conductive carbon and binder and tested in half-cell configuration in coin cells. For galvanostatic cycling experiments, we calculated a theoretical capacity of 240 mAh/g for VMO, which assumes the insertion of 1 Li^+ per transition metal (T.M.) in the VMO structure. All C-rates used were based on this capacity (1C = 0.24 A/g, 5C = 1.2 A/g, etc.).

Initial charge storage in VMO occurs through a sloping profile with a few small features until about 0.5 Li^+/T.M. inserted, where a large plateau occurs (**Figure 2A**). This plateau encompasses a considerable range of stoichiometry (about 0.9 Li^+/T.M.), and corresponds to the transformation to a disordered rock salt phase, as we show later. After the plateau completes, little additional charge storage is observed until the voltage cutoff at 1.5 V. On delithiation, and during subsequent cycles, charge storage occurs through a highly sloped profile without recurrence of the plateau seen during the first lithiation. During the first delithiation, more than 1 Li^+/T.M. is deinserted (255 mAh/g), but this capacity is not fully sustained in subsequent cycles, during which a moderate capacity of about 0.75 – 0.85 Li^+/T.M., or 180 – 200 mAh/g, is reversibly achieved. Galvanostatic rate testing was performed to evaluate the rate capability of the VMO electrodes within two different voltage windows, 1.5 – 4.0 V vs. Li/Li^+ and 1.5 – 3.5 V vs. Li/Li^+ (**Figure 2B**). VMO shows good retention of its capacity at high rates, despite the relatively large size of the particles tested. For the 1.5 – 4.0 V window, nearly 150 mAh/g (0.63 Li^+/T.M.), or about 75%

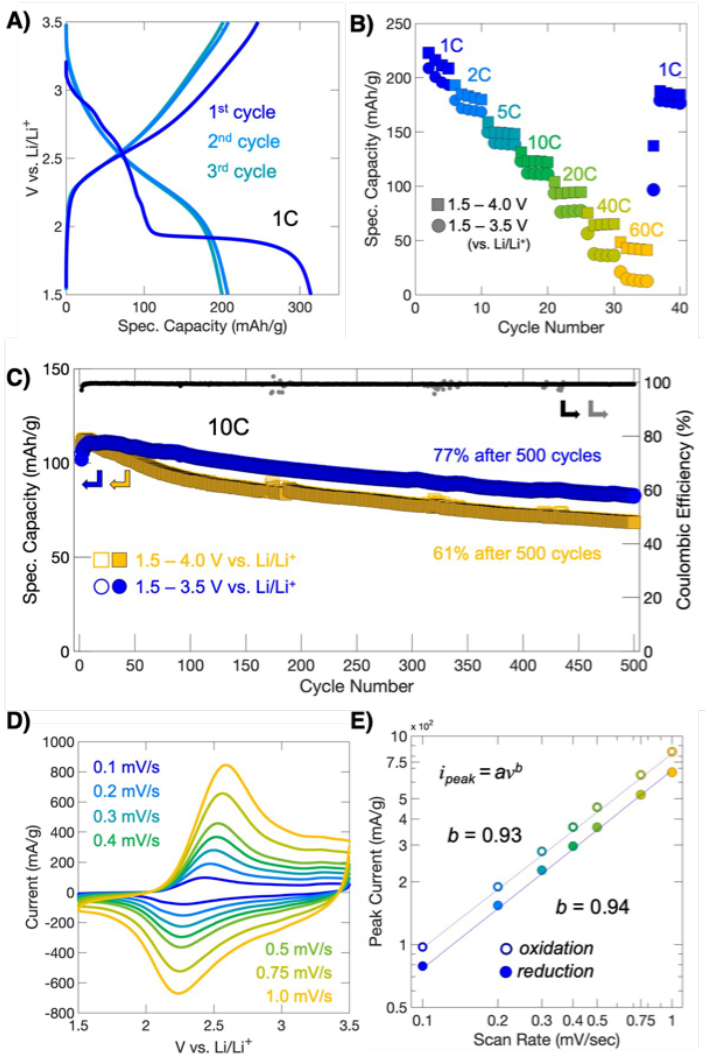

Figure 2. Electrochemical performance of VMO. A) Galvanostatic charge storage profiles of VMO electrodes for the first three cycles. During the first lithiation, the material undergoes an irreversible transformation to a disordered rock salt phase, as shown by the large plateau. **B)** Galvanostatic cycling performance of VMO electrodes at different rates. **C)** Long term galvanostatic cycling at 10C. **D)** Cyclic voltammetry of VMO electrodes at different rates. **E)** Variation of the peak current of the main redox peak as a function of scan rate on a logarithm scale. The near-linear dependence suggests a pseudocapacitive charge storage mechanism.

of the slow rate capacity, is stored at 5C, while at 20C, 95 mAh/g (0.40 Li^+/T.M.), or about 48% of slow rate capacity is accessed. At 60C, which corresponds to less than a 1-minute full charge or discharge, a respectable capacity of 48 mAh/g (0.2 Li^+/T.M.) or about 25% of the slow rate capacity is obtained. At these higher rates, the sloping GV profile is maintained (**Figure S2**). When the narrower window is used (1.5 V – 3.5 V vs. Li/Li^+), similar performance is observed at slow and moderate rates, with a greater difference at the highest rates tested. For example, at 5C and 20C, 140 mAh/g and 77 mAh/g are stored, but at 60C, the narrower voltage window leads to greater losses from polarization, and only about 14 mAh/g is retained. Overall, this charge storage performance demonstrates fast kinetics

in relatively large particles of VMO, and even better performance can likely be achieved with optimization of particle shape and size, as has been done extensively with V_2O_5.[23]

To assess the reversibility and stability of charge storage processes in VMO electrodes, long term galvanostatic cycling was performed over 500 cycles at 10C (**Figure 2C**). In the narrower voltage window up to 3.5 V vs. Li/Li^+, VMO shows good retention of its capacity, with 77% of its initial capacity maintained after 500 cycles. In many bulk battery materials, Li^+ insertion is accompanied by first-order phase transitions, which decrease cycle life considerably due to repeated discontinuous changes in volume. VMO, on the other hand, shows a sloping galvanostatic charge storage profile, which suggests the absence of a first-order phase transition, and is likely the reason for comparatively better capacity retention. When the voltage window is expanded up to 4.0 V vs. Li/Li^+, the improved cycling kinetics are accompanied by a tradeoff in stability, since in this window VMO shows a considerably lower capacity retention of 61% after 500 cycles. Notably, the galvanostatic profile remains sloping and shows no change in shape over the extended cycling, regardless of voltage window (**Figure S3**).

Cyclic voltammetry for sweep rates from 0.1 mV/s to 1.0 mV/s was also performed on VMO electrodes after they had undergone precycling (**Figure 2D**). The cyclic voltammogram for VMO shows a single broad redox peak centered around 2.2 V for the anodic sweep and 2.4 V for the cathodic sweep. Additionally, an even broader shoulder feature is seen for the higher voltage region (> 2.5 V). The broad signatures of redox seen here for VMO are unlike those for most bulk battery materials, which typically show sharp peaks in cyclic voltammetry. This behavior can be attributed to the disordered structure of the electrochemically-formed rock salt VMO, which we characterize later. To further characterize the charge storage behavior of VMO, we analyzed the

cyclic voltammograms using the power-law dependence of each peak current (i_{peak}) as the sweep rate (v) is varied according to the following equation:

$$i_{\text{peak}} = av^b$$

where a and b are constants. The value of b, determined by fitting the slope of $\log(i_{peak})$ versus $\log(v)$, indicates whether the reaction is diffusion-limited ($b = 0.5$) or capacitive (b = 1.0) (**Figure 2E**).[2,4,45] Intermediate values correspond to diffusion behavior that is between semi-infinite diffusion and purely capacitive surface reactions. This analysis has been used frequently in the literature to distinguish diffusion-controlled or "battery-like" and pseudocapacitive redox reactions, which appear capacitive due to fast Li^+ diffusion and the absence of large first-order phase transitions.[4,46-48] The value of b at the main redox peak of VMO is 0.94 and 0.93 for the anodic and cathodic sweep, respectively, which suggests a highly capacitive charge storage process, despite the relatively large particle sizes studied here. This result is likely due to the absence of a first-order phase transition during Li^+ insertion in VMO, along with its fast charge storage kinetics.

4.3.3 The electrochemical formation of disordered rock salt ω-VMO

To characterize the transformation of VMO during its 1st lithiation, we performed *operando* synchrotron X-ray diffraction (SXRD) at beamline 11-ID-C at the Advanced Photon Source. In this experiment, the active material is assembled with conductive carbon and binder into freestanding pellets, which are cycled in AMPIX cells at a C/5 rate.[49] The operando SXRD data from Q = 1 – 5 $Å^{-1}$ is shown in **Figure 3A** along with the galvanostatic cycling profile during the experiment. The pristine VMO starts out with small shifts of the peaks during the initial sloping region, which suggest some expansion of the lattice with minor lithiation. As the plateau begins, shifting stops and instead a steady decrease in the intensity of the starting VMO phase is observed

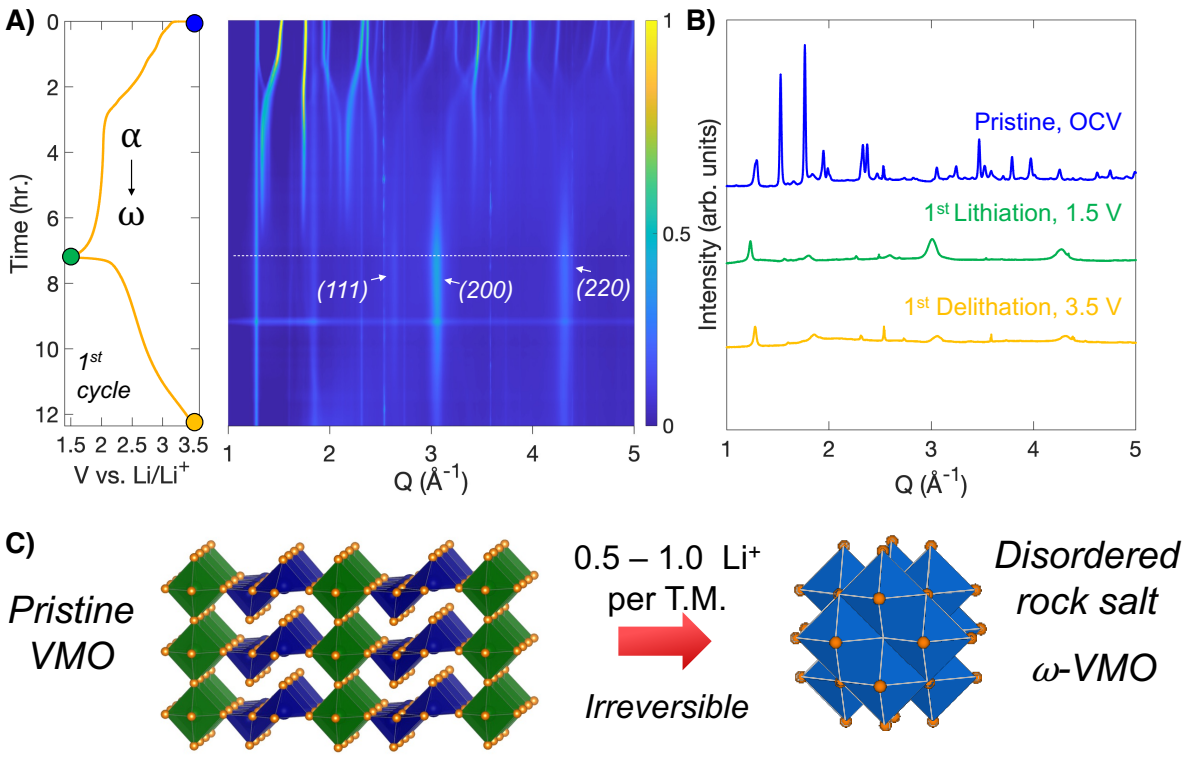

Figure 3. Transformation of VMO to a disordered rock salt phase during its first cycle. A) *Operando* X-ray diffraction data on VMO plotted alongside the galvanostatic profile during the first cycle. The pristine VMO transforms during the first lithiation into a disordered rock salt phase. **B)** Selected patterns from the data in A) showing the pristine VMO and the disordered rock salt phase after the 1st lithiation and delithiation. **C)** Schematic of the transformation.

as its transforms into a different structure. Two broad peaks emerge at 3.1 $Å^{-1}$ and 4.3 $Å^{-1}$ by the middle of the plateau and continue to increase in intensity until the end of the cycle, by which the initial VMO phase has completely disappeared. These peaks are characteristic of a rock salt phase, which we denote here as ω-VMO, after the convention used for V_2O_5. During delithiation, the rock salt phase remains and its peaks do not shift, although they do decrease in intensity. Selected diffraction patterns are highlighted in **Figure 3B**, along with a schematic of the transformation in **Figure 3C**. The highly crystalline pristine VMO shows minor shifts in structure during its initial lithiation, but by 0.5 Li^+/T.M. inserted it begins to undergo a transformation to a rock salt phase with broad peaks that indicate disorder. During delithiation, this rock salt phase remains, which

shows that the change in structure is irreversible, though there is some decrease in intensity of the rock salt phase, which we will examine more closely later.

As we discussed previously, α-V_2O_5, which shares the edge sharing pyramid structural motif with VMO, also transforms into a disordered rock salt phase at deep lithiation. However, prior to becoming the rock salt phase, α-V_2O_5 goes through three additional discrete structural phase transformations involving puckering of the layers to better coordinate the inserted Li^+.[20,25] VMO, on the other hand, shows minimal change in structure before it directly transitions to the rock salt phase. We hypothesize that this change in pathway originates from the additional rigidity imparted by the planes of corner sharing octahedra in the VMO crystal structure. Whereas the edge sharing pyramid dimers can distort relatively freely in V_2O_5, their connection to the octahedra in VMO pins their movement and prevents significant distortion until the full-scale transformation of the crystal structure to the rock salt phase.

We further characterized the disordered rock salt VMO using electron microscopy to analyze how the dramatic change in atomic-scale crystal structure affects the morphology and microstructure of the material. Particles with the bar-like morphology seen for pristine VMO (**Figure 4A**,**4B**) were readily observed throughout a cycled VMO electrode that had transformed to the rock salt phase (**Figure 4E, Figure S4**). Although there was some evidence of cracks forming, this data indicates that the particle morphology is largely preserved through the structural transition during cycling. Additionally, energy-dispersive spectroscopy (EDS) on the cycled electrode confirmed the presence of V and Mo (**Figure S5**). To characterize the microstructure of disordered rock salt VMO, we performed high resolution transmission electron microscopy (HRTEM) on particles from a VMO electrode cycled through the first delithiation. Unlike the rigid, crystalline planes seen for pristine VMO (**Figure 4C**), the cycled VMO showed a collection

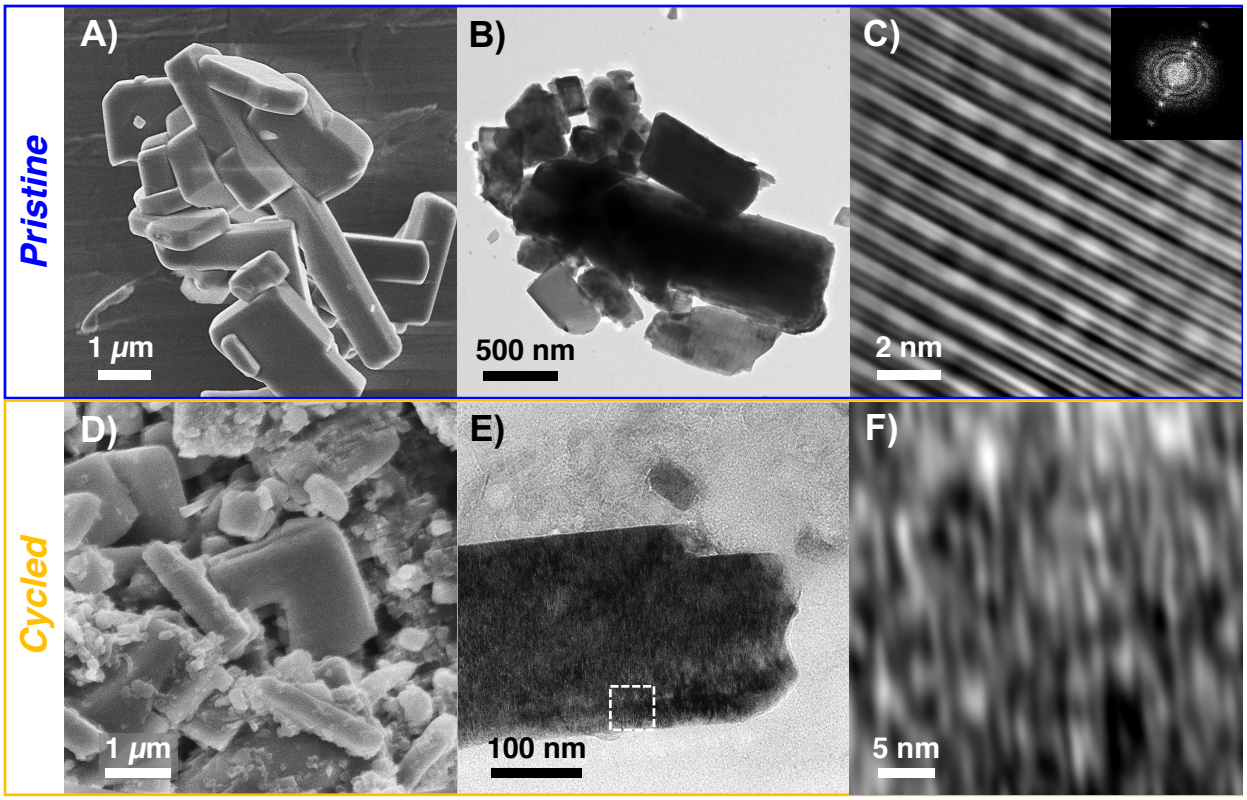

Figure 4. Characterization of the disordered rock salt VMO. Electron microscopy of the A) – C) pristine VMO and D) – E) delithiated disordered rock salt VMO. The morphology is retained after transformation, but the cycled VMO shows an unusual microstructure consisting of highly distorted planes of atoms.

of kinked, highly distorted planes of atoms that loosely cohered together (**Figure 4G**). This highly distorted "lattice" extends throughout the entirety of individual particles (**Figure 4F**), and we confirmed its rock salt atomic-scale crystal structure with selected area electron diffraction (**Figure S6**).

To our knowledge, the unusual distorted microstructure of rock salt VMO is unique among the family of electrochemically formed rock salt materials, and may result from its more direct formation pathway. We hypothesize, for example, that the structural rigidity in the pristine VMO crystal structure that likely leads to its direct transformation to the rock salt structure, imposes strain in the microstructure of the material during the process. As a result, the material partially fragments along specific crystal axes to alleviate the strain, leading to the lamellar morphology of

the distorted microstructure lattice. While the disorder in the rock salt VMO prevented us from obtaining sufficient resolution to see individual crystallites in the material, it is clear based on the size of individual lamellae (< 1 nm), that the crystal domains are very small, at least along one axis. The resulting material has nanoscale crystal domains within a dense micron-scale particle. The small crystallite size is responsible for the sloping galvanostatic profile and highly capacitive electrochemical kinetics of the ω-VMO that was shown earlier.

4.3.4 The charge storage mechanism in disordered rock salt VMO

To investigate the mechanism for charge storage in the disordered rock salt VMO, we performed operando SXRD during the second lithiation-delithiation cycle, after the material had already transformed into the disordered rock salt phase. The operando SXRD data is shown in

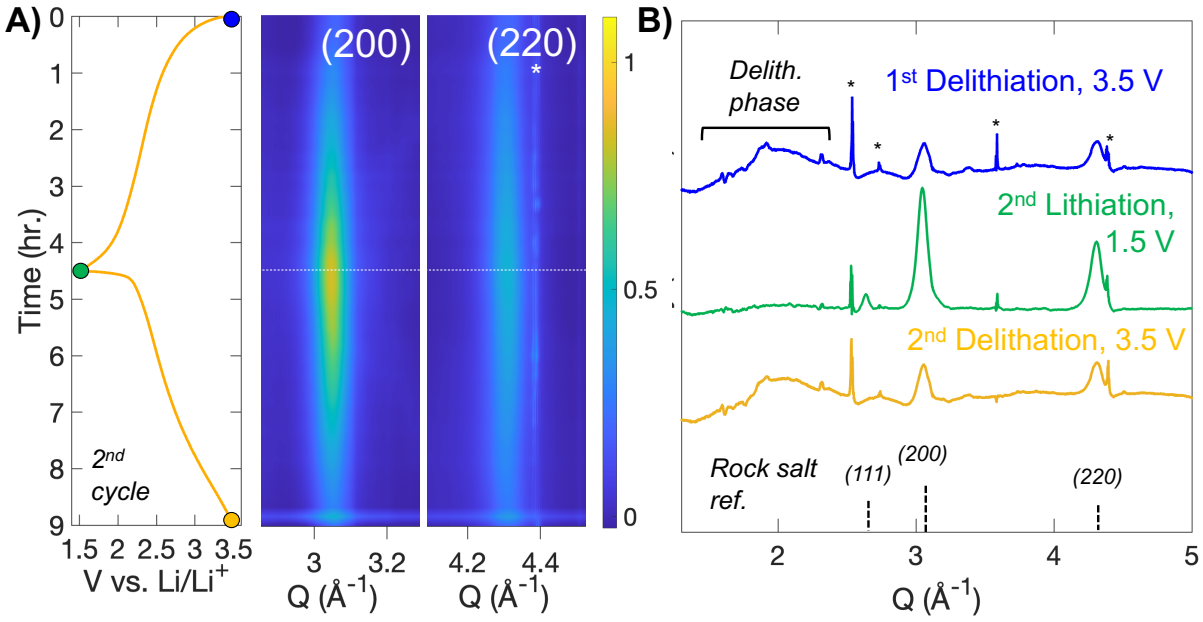

Figure 5. Structural change during cycling of disordered rock salt VMO. A) *Operando* X-ray diffraction data on VMO plotted alongside the galvanostatic profile during the second cycle. For clarity, data is shown for the two most intense lattice planes of the phase. **B)** Selected patterns from the data in A). When delithiated, the rock salt phase decreases in intensity, and a broad feature appears between Q = 1.8 – 2.5 Å^{-1}.

Figure 5A for the (200) and (220) regions, the two most intense reflections of the phase, along with the galvanostatic cycling profile. As the lithiation proceeds, no shifting of either peak is observed, but a clear increase in the intensity of the phase is observed. During delithiation, the intensity decreases back to a similar level as at the beginning of the cycle. Selected diffraction patterns at the beginning, middle, and end of the lithiation-delithiation cycled are highlighted in **Figure 5B**. The increase in intensity of the rock salt VMO as it is lithiated is clearly shown. The individual line plots in the delithiation also provide evidence for the decreasing intensity seen during delithiation: in either delithiated pattern, a very broad scattering feature from Q = 1.5 – 2.5 $Å^{-1}$ appears, and then disappears during lithiation. This data suggests that removal of Li^+ from the rock salt VMO produces an even more disordered phase. While the low intensity precludes identification of the phase by diffraction alone, similar behavior has been shown for rock salt V_2O_5. A pair distribution function analysis by Christensen et al. identified the delithiated phase as a highly disordered analogue of β-$Li_xV_2O_5$, which consists of 2x2 chains of edge-sharing distorted octahedra that are connected by corner sharing with edge-sharing pyramid dimers.[50] This phase exists over a narrow compositional range ($0.22 < x < 0.37$), and is favored electrostatically at low Li^+ content since the rock salt structure is too densely packed for the highly charged transition metal cations in the delithiated state (V^{5+} in the case of V_2O_5). Importantly, the β-$Li_xV_2O_5$ showed a short crystalline coherence length of 10 – 15 Å, which is consistent with the very broad nature of the peak in diffraction seen here and the feature size in our HRTEM data. While we cannot verify the identity of the phase for VMO, a number of parallels in behavior are shown for V_2O_5, including the reversible change in intensity of the rock salt phase during cycling, which suggest that the atomic-scale processes for Li^+ insertion and deinsertion are similar for these two disordered rock salt phases.

To characterize the changes in oxidation state of V and Mo during cycling, we carried out *ex situ* X-ray photoelectron spectroscopy (XPS, **Figure 6, Figure S7**). For these experiments, VMO electrodes were cycled to the desired point, removed from the cell, washed, and dried, then transferred to the instrument for data collection. The removal and cleaning process was done in an Ar glovebox and the transfer to the instrument was conducted without exposure to air to prevent oxidation or other degradation of the cycled electrode. For the pristine VMO, only V^{5+} and Mo^{6+} are present, as expected. At the end of the 1st lithiation, when the disordered rock salt VMO has formed and is fully lithiated, both V and Mo exist in partially reduced states, with large amounts of V^{4+} and Mo^{5+} and some doubly reduced V^{3+} and Mo^{4+}.[51,52] At the 1st delithiation, when the rock salt phase is delithiated, the doubly reduced species disappear, but significant amounts of V^{4+} and Mo^{5+} remain alongside fully oxidized V^{5+} and Mo^{6+}. The presence of reduced species after delithiation suggests that some Li^+ remains in the lattice as a structural component of the rock salt phase, as has been seen in other electrochemically formed rock salt materials.[25,29] When the rock salt phase is lithiated, the doubly reduced V^{3+} and Mo^{4+} return to a similar, though slightly lesser, extent, confirming the reversibility of cycling both elements in the rock salt structure. The results

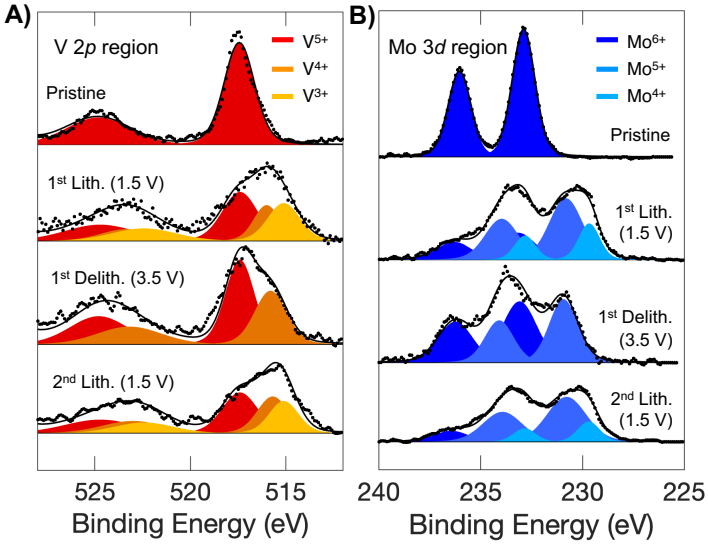

Figure 6. Redox activity of VMO. *Ex situ* X-ray photoelectron spectroscopy on VMO electrodes cycled to different points highlighting the **A)** V *2p* region and **B)** Mo *3d* region. Both elements begin in their fully oxidized state, and become reduced during lithiation. The delithiated disordered rock salt shows some remnant reduced species, suggesting that some Li^+ remains in the material after the first lithiation.

of the XPS data are quantified in **Table 1**. While the XPS technique is fully quantitative, only the near-surface region of the sample is probed, so the oxidation states in general are more oxidized than would be expected by the electrochemistry.

Table 1. Quantitative summary of the X-ray photoelectron spectroscopy data.

	V *2p* region					Mo 3*d* region				
	% V^{5+}	% V^{4+}	% V^{3+}	average V^{+x}	expected V^{+x} (electrochem.)	% Mo^{6+}	% Mo^{5+}	% Mo^{4+}	average Mo^{+x}	expected Mo^{+x} (electrochem.)
Pristine	100	0	0	5.0	5.0	100	0	0	6.0	6.0
1^{st} Lithiation (1.5 V)	45	24	31	4.1	3.7	25	55	21	5.0	4.7
1^{st} Delithiation (3.5 V)	59	46	0	4.6	4.7	54	46	0	5.5	5.7
2^{nd} Lithiation (1.5 V)	41	32	27	4.1	3.8	20	63	16	5.0	4.8

4.4 Conclusion

Using a combination of *operando* X-ray diffraction, microscopy, and XPS, we have characterized the electrochemical formation and reversible cycling of a disordered rock salt phase from a $V_9Mo_6O_{40}$ precursor. Unlike the well-known example of ω-V_2O_5, VMO transforms directly into its rock salt structure during the first cycle without any intermediate phases. Additionally, we showed an unusual microstructure in rock salt VMO that consists of highly distorted nanoscale lamellae arranged in a loosely coherent lattice. We hypothesize that these features are due to the increased structural rigidity in the VMO lattice relative to α-V_2O_5. Overall, this work provides insight into the role of precursor structure in electrochemically formed disordered rock salt phases.

4.5 References

[1] Gür, T.M. Review of electrical energy storage technologies, materials and systems: challenges and prospects for large-scale grid storage. *Energy Environ. Sci.* **2018**, *11*(10), 2696–2767.

[2] Simon, P.; Gogotsi, Y.; Dunn, B. Where do batteries end and supercapacitors begin? *Science* **2014**, *343*(6176), 1210–1211.

[3]. Frith, J.T.; Lacey, M.J.; Ulissi, U. A non-academic perspective on the future of lithium-based batteries. *Nat. Commun.* **2023**, *14*(1), 420.

[4] Choi, C.; Ashby, D.S.; Butts, D.M.; DeBlock, R.H.; Wei, Q.; Lau, J.; Dunn, B. Achieving high energy density and high power density with pseudocapacitive materials. *Nat. Rev. Mater.* **2020**, *5*(1), 5–19.

[5]. Li, M.; Lu, J.; Chen, Z.; Amine, K. 30 years of lithium-ion batteries. *Adv. Mater.* **2018**, *30* (33), 1800561.

[6] Griffith, K. J.; Wiaderek, K. M.; Cibin, G.; Marbella, L. E.; Grey, C. P. Niobium tungsten oxides for high-rate lithium-ion energy storage. *Nature*, **2018**, *559*, 556–563.

[7] Poizot, P.; Laruelle, S.; Grugeon, S.; Dupont, L.; Tarascon, J.-M. Nano-Sized Transition-Metal Oxides as Negative-Electrode Materials for Lithium-Ion Batteries. *Nature* **2000**, *407* (6803), 496–499.

[8] Liu, H.; Wang, G.; Liu, J.; Qiao, S.; Ahn, H. Highly Ordered Mesoporous NiO Anode Material for Lithium Ion Batteries with an Excellent Electrochemical Performance. *J. Mater. Chem.* **2011**, *21* (9), 3046.

[9] Sun, Y.; Hu, X.; Luo, W.; Huang, Y. Ultrathin CoO/Graphene Hybrid Nanosheets: A Highly Stable Anode Material for Lithium-Ion Batteries. *J. Phys. Chem. C* **2012**, *116* (39), 20794–20799.

[10] Sarkar, A.; Velasco, L.; Wang, D.; Wang, Q.; Talasila, G.; de Biasi, L.; Kübel, C.; Brezesinski, T.; Bhattacharya, S. S.; Hahn, H.; Breitung, B. High Entropy Oxides for Reversible Energy Storage. *Nat. Commun.* **2018**, *9* (1).

[11] Yabuuchi, N.; Takeuchi, M.; Nakayama, M.; Shiiba, H.; Ogawa, M.; Nakayama, K.; Ohta, T.; Endo, D.; Ozaki, T.; Inamasu, T.; Sato, K.; Komaba, S. High-Capacity Electrode Materials for Rechargeable Lithium Batteries: Li_3NbO_4-Based System with Cation-Disordered Rocksalt Structure. *Proc. Natl. Acad. Sci.* **2015**, *112* (25), 7650–7655.

[12] Lee, J.; Kitchaev, D. A.; Kwon, D. H.; Lee, C. W.; Papp, J. K.; Liu, Y. S.; Lun, Z.; Clément, R. J.; Shi, T.; McCloskey, B. D.; Guo, J.; Balasubramanian, M.; Ceder, G. Reversible Mn^{2+}/Mn^{4+} Double Redox in Lithium-Excess Cathode Materials. *Nature* **2018**, *556* (7700), 185–190.

[13] Clément, R. J.; Lun, Z.; Ceder, G. Cation-Disordered Rocksalt Transition Metal Oxides and Oxyfluorides for High Energy Lithium-Ion Cathodes. *Energy Environ. Sci.* **2020**, *13* (2), 345–373.

[14] Fan, Y.; Zhang, W.; Zhao, Y.; Guo, Z.; Cai, Q. Fundamental Understanding and Practical Challenges of Lithium-Rich Oxide Cathode Materials: Layered and Disordered-Rocksalt Structure. *Energy Storage Mater.* **2021**, *40*, 51–71.

[15] Tarascon, J.M., Wang, E., Shokoohi, F.K., McKinnon, W.R. and Colson, S. The spinel phase of $LiMn_2O_4$ as a cathode in secondary lithium cells. *J. Electrochem. Soc.* **1991**, *138* (10), 2859.

[16] Zhao, B., Ran, R., Liu, M. and Shao, Z., 2015. A comprehensive review of $Li_4Ti_5O_{12}$-based electrodes for lithium-ion batteries: The latest advancements and future perspectives. *Materials Science and Engineering: R: Reports*, *98*, 1-71.

[17] Kang, K.; Meng, Y. S.; Bréger, J.; Grey, C. P.; Ceder, G. Electrodes with High Power and High Capacity for Rechargeable Lithium Batteries. *Science* **2006**, *311* (5763), 977–980.

[18] Lee, J.; Urban, A.; Li, X.; Su, D.; Hautier, G.; Ceder, G. Unlocking the Potential of Cation-Disordered Oxides for Rechargeable Lithium Batteries. *Science* **2014**, *343* (6170), 519–522.

[19] Delmas, C.; Brèthes, S.; Ménétrier, M. ω-$Li_xV_2O_5$ - a New Electrode Material for Rechargeable Lithium Batteries. *J. Power Sources* **1991**, *34* (2), 113–118.

[20] Delmas, C.; Cognac-Auradou, H.; Cocciantelli, J. M.; Ménétrier, M.; Doumerc, J. P. The $Li_xV_2O_5$ System: An Overview of the Structure Modifications Induced by the Lithium Intercalation. *Solid State Ionics* **1994**, *69* (3–4), 257–264.

[21] Chen, Z.; Augustyn, V.; Wen, J.; Zhang, Y.; Shen, M.; Dunn, B.; Lu, Y.; Chen, Z.; Wen, J.; Zhang, Y.; Lu, Y.; Augustyn, V.; Dunn, B.; Shen, M. High-Performance Supercapacitors Based on Intertwined CNT/V_2O_5 Nanowire Nanocomposites. *Adv. Mater.* **2011**, *23* (6), 791–795.

[22] Sathiya, M.; Prakash, A. S.; Ramesha, K.; Tarascon, J. M.; Shukla, A. K. V_2O_5-Anchored Carbon Nanotubes for Enhanced Electrochemical Energy Storage. *J. Am. Chem. Soc.* **2011**, *133* (40), 16291–16299.

[23] Yue, Y.; Liang, H.; Yue, Y.; Liang, H. Micro- and Nano-Structured Vanadium Pentoxide (V_2O_5) for Electrodes of Lithium-Ion Batteries. *Adv. Energy Mater.* **2017**, *7* (17), 1602545.

[24] Zhong, W.; Huang, J.; Liang, S.; Liu, J.; Li, Y.; Cai, G.; Jiang, Y.; Liu, J. New Prelithiated V_2O_5 Superstructure for Lithium-Ion Batteries with Long Cycle Life and High Power. *ACS Energy Lett.* **2020**, *5* (1), 31–38.

[25] Liu, H.; Zhu, Z.; Yan, Q.; Yu, S.; He, X.; Chen, Y.; Zhang, R.; Ma, L.; Liu, T.; Li, M.; Lin, R.; Chen, Y.; Li, Y.; Xing, X.; Choi, Y.; Gao, L.; Cho, H. S. yun; An, K.; Feng, J.; Kostecki, R.; Amine, K.; Wu, T.; Lu, J.; Xin, H. L.; Ong, S. P.; Liu, P. A Disordered Rock Salt Anode for Fast-Charging Lithium-Ion Batteries. *Nature* **2020**, *585* (7823), 63–67.

[26] Mikhailova, D.; Voss, A.; Oswald, S.; Tsirlin, A. A.; Schmidt, M.; Senyshyn, A.; Eckert, J.; Ehrenberg, H. Lithium Insertion into Li_2MoO_4: Reversible Formation of $(Li_3Mo)O_4$ with a Disordered Rock-Salt Structure. *Chem. Mater.* **2015**, *27* (12), 4485–4492.

[27] Pralong, V.; Venkatesh, G.; Malo, S.; Caignaert, V.; Baies, R.; Raveau, B. Electrochemical Synthesis of a Lithium-Rich Rock-Salt-Type Oxide $Li_5W_2O_7$ with Reversible Deintercalation Properties. *Inorg. Chem.* **2014**, *53* (1), 522–527.

[28] Xiong, H.; Yildirim, H.; Shevchenko, E. V.; Prakapenka, V. B.; Koo, B.; Slater, M. D.; Balasubramanian, M.; Sankaranarayanan, S. K. R. S.; Greeley, J. P.; Tepavcevic, S.; Dimitrijevic, N. M.; Podsiadlo, P.; Johnson, C. S.; Rajh, T. Self-Improving Anode for Lithium-Ion Batteries Based on Amorphous to Cubic Phase Transition in TiO_2 Nanotubes. *J. Phys. Chem. C* **2012**, *116* (4), 3181–3187.

[29] Barnes, P.; Zuo, Y.; Dixon, K.; Hou, D.; Lee, S.; Ma, Z.; Connell, J. G.; Zhou, H.; Deng, C.; Smith, K.; Gabriel, E.; Liu, Y.; Maryon, O. O.; Davis, P. H.; Zhu, H.; Du, Y.; Qi, J.; Zhu, Z.; Chen, C.; Zhu, Z.; Zhou, Y.; Simmonds, P. J.; Briggs, A. E.; Schwartz, D.; Ong, S. P.; Xiong, H.

Electrochemically Induced Amorphous-to-Rock-Salt Phase Transformation in Niobium Oxide Electrode for Li-Ion Batteries. *Nat. Mater.* **2022**, *21* (7), 795–803.

[30] Li, W.; Fukunishi, M.; Morgan, B. J.; Borkiewicz, O. J.; Chapman, K. W.; Pralong, V.; Maignan, A.; Lebedev, O. I.; Ma, J.; Groult, H.; Komaba, S.; Dambournet, D. A Reversible Phase Transition for Sodium Insertion in Anatase TiO_2. *Chem. Mater.* **2017**, *29* (4), 1836–1844.

[31] Jarman, R. H.; Dickens, P. G.; Jacobson, A. J. Preparation and Characterization of the Mixed Oxide $V_9Mo_6O_{40}$. *Mater. Res. Bull.* **1982**, *17* (3), 325–328.

[32] Slade, R. C. T.; Ramanan, A.; West, B. C.; Prince, E. The Structure of $V_9Mo_6O_{40}$ Determined by Powder Neutron Diffraction. *J. Solid State Chem.* **1989**, *82* (1), 65–69.

[33] Hu, M.; Liang, J.; Chen, X.; Wei, J.; Zhou, Z. Preparation and electrochemical performance of $Mo_6V_9O_{40}$ nanorods as cathode materials for Li batteries. *RSC Adv.* **2015**, *5* (20), 15395-15398.

[34] Eick, H.A. and Kihlborg, L. 1The crystal structure of V_2MoO_8. *Acta Chem. Scand*. **1966**, *20*(6).

[35]. Toby, B.H.; Von Dreele, R.B. GSAS-II: the genesis of a modern open-source all purpose crystallography software package. *J. Appl. Cryst.* **2013**, *46* (2), 544–549.

[36] Momma, K.; Izumi, F. VESTA: a three-dimensional visualization system for electronic and structural analysis. *J. Appl. Cryst.* **2008**, *41* (3), 653–658.

[37] Enjalbert, R.; Galy, J. A Refinement of the Structure of V_2O_5. **1986**, *42* (11), 1467–1469.

[38] Wooster, N. The crystal structure of molybdenum trioxide, MoO_3. *Z. Kristallogr. Cryst. Mater*, **1931**, *80* (1-6), 504-512.

[39] Kim, H.S.; Cook, J.B.; Lin, H.; Ko, J.S.; Tolbert, S.H.; Ozolins, V.; Dunn, B. Oxygen vacancies enhance pseudocapacitive charge storage properties of MoO_{3-x}. *Nat. Mater.* **2017**, *16*(4), 454-460.

[40] Adams, A. H.; Haaß, F.; Buhrmester, T.; Kunert, J.; Ott, J.; Vogel, H.; Fuess, H. Structure and Reaction Studies on Vanadium Molybdenum Mixed Oxides. *J. Mol. Catal. A Chem.* **2004**, *216* (1), 67–74.

[41] Sudant, G.; Baudrin, E.; Dunn, B.; Tarascon, J.-M. Synthesis and Electrochemical Properties of Vanadium Oxide Aerogels Prepared by a Freeze-Drying Process. *J. Electrochem. Soc.* **2004**, *151* (5), A666.

[42] Zhecheva, E.; Mladenov, M.; Zlatilova, P.; Koleva, V.; Stoyanova, R. Particle size distribution and electrochemical properties of $LiFePO_4$ prepared by a freeze-drying method. J. Phys. Chem. Solids **2010**, *71* (5), 848–853.

[43] Shi, S.J.; Tu, J.P.; Tang, Y.Y.; Yu, Y.X.; Zhang, Y.Q.; Wang, X.L. Synthesis and electrochemical performance of $Li_{1.131}Mn_{0.504}Ni_{0.243}Co_{0.122}O_2$ cathode materials for lithium ion batteries via freeze drying. *J. Power Sources* **2013**, *221*, 300–307.

[44] Yan, Y.; Chin, M.A.; Robertson, D.D.; Lesel, B.K.; Tolbert, S.H. Tuning the Porous Structure in PMMA-Templated Mesoporous MoO_2 for Pseudocapacitive Li-Ion Electrodes. *J. Electrochem. Soc.* **2022**, *169* (4), 040545.

[45] Wang, J.; Polleux, J.; Lim, J.; Dunn, B. Pseudocapacitive Contributions to Electrochemical Energy Storage in TiO_2 (Anatase) Nanoparticles. *J. Phys. Chem. C* **2007**, *111* (40), 14925–14931.

[46] Cook, J. B.; Kim, H. S.; Lin, T. C.; Lai, C. H.; Dunn, B.; Tolbert, S. H. Pseudocapacitive Charge Storage in Thick Composite MoS_2 Nanocrystal-Based Electrodes. *Adv. Energy Mater.* **2017**, *7*, 1601283.

[47] Cook, J. B.; Lin, T. C.; Kim, H.-S.; Siordia, A.; Dunn, B. S.; Tolbert, S. H. Suppression of Electrochemically Driven Phase Transitions in Nanostructured MoS_2 Pseudocapacitors Probed Using Operando X-ray Diffraction. *ACS Nano*, **2019**, *13*, 1223–1231.

[48] Cook, J. B.; Ko, J. S.; Lin, T. C.; Robertson, D. D.; Kim, H. S.; Yan, Y.; Yao, Y.; Dunn, B. S.; Tolbert, S. H. Ultrafast Sodium Intercalation Pseudocapacitance in MoS_2 Facilitated by Phase Transition Suppression. *ACS Appl. Energy Mater.* **2023**, *6* (1), 99–108.

[49] Borkiewicz, O.J.; Shyam, B.; Wiaderek, K.M.; Kurtz, C.; Chupas, P.J.; Chapman, K.W. The AMPIX electrochemical cell: a versatile apparatus for in situ X-ray scattering and spectroscopic measurements. *J. Appl. Cryst.* **2012**, *45* (6), 1261–1269.

[50] Christensen, C. K.; Sørensen, D. R.; Hvam, J.; Ravnsbæk, D. B. Structural Evolution of Disordered $Li_xV_2O_5$ Bronzes in V^2O_5 Cathodes for Li-Ion Batteries. *Chem. Mater.* **2019**, *31* (2), 512–520.

[51] Silversmit, G.; Depla, D.; Poelman, H.; Marin, G. B.; De Gryse, R. Determination of the V2p XPS Binding Energies for Different Vanadium Oxidation States (V^{5+} to V^{0+}). *J. Electron Spectros. Relat. Phenomena* **2004**, *135* (2–3), 167–175.

[52] Scanlon, D. O.; Watson, G. W.; Payne, D. J.; Atkinson, G. R.; Egdell, R. G.; Law, D. S. L. Theoretical and Experimental Study of the Electronic Structures of MoO_3 and MoO_2. *J. Phys. Chem. C* **2010**, *114* (10), 4636–4645.

CHAPTER 5

Fast-Charging Disordered Rock Salt Li-Ion Electrodes from Nanoporous $V_9Mo_6O_{40}$

5.1 Introduction

Electrochemical energy storage is an essential component of many important technologies, including personal electronics, electric vehicles, and grid scale storage, and further improvements to energy and power density are necessary to decrease our society's reliance on fossil fuels.[1-4] Insertion-based Li-ion batteries, which rely on reversible redox reactions between host materials and a Li-ion electrolyte, remain the most widely used electrochemical energy storage technology.[3] Despite their widespread use, traditional Li-ion batteries using micron-scale host particles show relatively low power density, especially with the high mass loadings used in commercial cells.[5] In these devices, achieving full capacity requires transport of Li^+ and electrons throughout the entire electrode, which can lead to sluggish kinetics since the diffusion of Li^+ through solid particles is an intrinsically slow process.[6] To circumvent these rate limitations, nanoscale active materials, which have short solid-state diffusion lengths for Li^+, have been utilized to realize much greater power densities while maintaining similar battery-like energy density.[7-14] Additionally, the shortened Li^+ diffusion time and the size-dependent suppression of phase transitions in nanoscale battery materials has often been linked to the progression from a diffusion-limited to a pseudocapacitive charge storage mechanism.[15-19,20] These effects have been employed broadly to achieve fast-charging Li-ion electrodes across a range of host materials.

One emerging class of Li-ion electrode materials are the electrochemically-formed disordered rock salts (DRS), which typically begin as open-framework crystal structures that rearrange into a densely packed rock salt phase upon lithiation. The most well-known of these materials is α-V_2O_5, which transforms irreversibly into a DRS ω-$Li_xV_2O_5$ phase at deep lithiation

($2 < x < 3$), and has been studied for decades as a potential cathode material.[21-27] Recent work, however, has renewed interest in this class of materials. Most notably, Liu et. al demonstrated that ω-V_2O_5 could be lithiated significantly further, and the resulting DRS $Li_{3+x}V_2O_5$ showed exceptional performance in a voltage region ideal for a fast-charging anode material (0.01 – 2.0 V vs. Li/Li^+).[28] Additionally, other reports have considerably broadened the scope of materials that form DRS compounds electrochemically, including Li_2MoO_4,[29] $Li_2W_2O_7$,[30] TiO_2,[31-33] anodized Nb oxide,[32] and others. Given the wide range of phases that form DRS structures, there is an ongoing need to better understand how different precursors materials affect the composition, structure, and electrochemical properties in the resulting DRS phase.

We recently reported and characterized the electrochemical formation of a DRS phase from micron-scale particles of the crystalline compound $V_9Mo_6O_{40}$ (VMO).[34-36] VMO and the related phase V_2MoO_8[37] represent the lowest Mo content vanadium molybdenum oxides that are not isostructural with α-V_2O_5, a van der Waals compounds that consists of layers of edge-sharing pyramids. VMO's crystal structure also possesses similar edge-sharing pyramidal units, but instead of extending infinitely, they alternate with planes of corner-sharing octahedra. The latter impart rigidity into VMO's crystal structure, and cause it to undergo a single-step transformation pathway to the DRS phase, in contrast to the multiphase pathway seen for α-V_2O_5. The resulting DRS ω-VMO showed good rate capability, with sloping voltage profiles and a highly capacitive charge storage mechanism, despite the micron-scale particles of the starting VMO.

In this work, we report the synthesis and electrochemical performance of fast-charging nanoporous VMO with optimized diffusion distances for Li^+. Using a solution-based synthetic method in combination with polymer-templating, we developed a route to introduce nanoscale porosity while maintaining good crystallinity in the parent material. The resulting nanoporous

VMO is comprised of nanoscale crystallites fused into a porous, electrically interconnected backbone to ensure good Li^+ and electron transport throughout the electrode. Compared to bulk VMO, which already shows good rate capability, the nanoporous VMO shows even better kinetics, which we characterize through electrochemical polarization analyses.

5.2 Materials and Methods

5.2.1 Materials preparation.

Nanoporous $V_9Mo_6O_{40}$ was prepared through a modified aqueous sol-gel route based on freeze-drying in combination with polymer templating. In this process, an aqueous solution of dissolved Mo precursor is frozen in liquid N_2 and dried under vacuum, then subsequently calcined to crystallize the material. To produce the nanoporous MoO_2 materials, 150 - 200 nm poly(methyl methacrylate) (PMMA) colloids of various sizes were mixed with the V and Mo precursors in the initial solution in order to template the nanoscale architecture.

In a typical synthesis, 100 mg NH_4VO_3 (Sigma-Aldrich) and 100 mg $(NH_4)_6Mo_7O_{24}•4H_2O$ (Alfa Aesar) were dissolved with stirring in 2 mL deionized water in a 20 mL scintillation vial at 85ºC with stirring. Once the precursors were fully dissolved, the solution was allowed to cool, and 2 - 4 mL of 150 - 200 nm solution were added (depending on the density of colloids in solution) to obtain a 1:0.5 mass ratio of T.M. precursor:colloid. The synthesis of PMMA colloids is described below. After the V/Mo precursor-polymer colloid solution was mixed thoroughly, it was frozen by dropwise addition to liquid N_2 and lyophilized on a Schlenk line for 12 to 24 hours (< 200 mtorr). The dried V/Mo precursor-polymer composite powder was calcined in two separate steps: first, at 550ºC in flowing Ar for 1 hour, then subsequently at 400ºC in static air for 12 hours. This two-heating-step process was found to show the best retention of the nanoscale architecture. The first step crystallizes the nanoporous inorganic backbone in Ar, where combustion of the polymer templates is less facile, and the second converts the material to the correct VMO phase.

Micron-scale bulk $V_9Mo_6O_{40}$ was prepared through a similar process without polymer templating. In a typical synthesis, 200 mg NH_4VO_3 (Sigma-Aldrich) and 200 mg $(NH_4)_6Mo_7O_{24}•4H_2O$ (Alfa Aesar) was dissolved with stirring in 5 mL deionized water in a 20 mL scintillation vial at 85ºC with stirring. Once the precursors were fully dissolved, the precursor solution was vitrified by dropwise addition to liquid N_2, then lyophilized for 12 to 24 hours (< 200 mtorr). The resulting dried precursor powder was calcined in a muffle furnace in air at 550ºC (30 min ramp, 1 hr. hold).

5.2.2 Synthesis of poly(methyl methacrylate) (PMMA) colloids

The synthesis of 150 - 200 nm PMMA colloids was adapted from a previous procedure described by Wang et al.[38] Ammonium persulfate (APS) was used as the initiator and ammonium lauryl sulfate (ALS) as the surfactant. 0.08 g APS, 0.01 mL ALS, and 165 mL deionized water were put into a three-neck round-bottom flask (250 mL) equipped with a magnetic stirrer, a reflux condenser, and a thermometer. After the temperature was raised to 75 °C, 10 mL of monomer methyl methacrylate (MMA) was added. After monomer addition, the reaction temperature was kept at 80–85 °C for an hour before cooling. The as-synthesized PMMA colloidal aqueous solutions were extracted with hexanes to remove excess monomer. Before use, the mass density of colloids in solution was measured by thermogravimetric analysis.

5.2.3 Structural characterization

Scanning electron microscopy (SEM) images were obtained using a ZEISS Supra 40VP field emission electron microscope with 5 kV accelerating voltage and 6 mm working distance. Scanning/transmission electron microscopy (S/TEM) imaging and STEM-EDS was performed using a FEI Titan scanning transmission electron microscope operated at an accelerating voltage of 300 kV. This instrument is equipped with Oxford X-MaxTEM 100 N TLE Windowless silicon drift detector (SDD) 100 mm 2 EDS and a Gatan Ultrascan 2 K × 2 K charge-coupled device

(CCD) camera. STEM-EDS was performed and analyzed using Aztec software. Laboratory X-ray diffraction was collected with a PANalytical X'Pert Pro diffractometer operating with Cu Kα (λ = 1.5418 Å) using a 0.05° step size, an accelerating voltage of 45 kV, and a current of 40 mA. For *ex situ* TEM characterization of materials after cycling, electrodes were cycled in coin cells, which were subsequently opened inside of a glovebox. The electrodes were then washed multiple times in dimethyl carbonate (DMC) and dried under vacuum before sample preparation for the given technique.

5.2.4 Electrochemical testing

All VMO powders were assembled into composite slurry electrodes for electrochemical testing. Electrodes had an overall composition of 80% active material, 2% multiwalled carbon nanotubes (CNT), 8% Super P carbon black, and 10% polyvinylidene fluoride (PVDF) binder. The CNT and PVDF components were added as a commercially available pre-dispersed ink mixture (0.75% CNT, 2.0 % PVDF in N-methyl pyrrolidone, NMP). Prior to slurry preparation, the dry slurry components and current collector were heated at 100ºC under vacuum overnight. The active material was ground with carbon black in a mortar and pestle dry, then the CNT-PVDF ink and several drops of NMP were added and mixed to produce a homogeneous paste that was cast onto a carbon-coated aluminum current collector with a doctor blade. The tapes were dried under vacuum at 100ºC overnight. Electrodes with 0.7 mm diameter were punched out for electrochemical testing with mass loadings of active material of 1 – 1.5 mg/cm^2. These moderate mass loadings were chosen to study the intrinsic performance of the active material, as they allow for reproducible electrode performance with minimal optimization of the slurry. High mass loadings, such as those used in most practical devices, lead to rate limitations from electrode composition and distribution of active material that require extensive optimization to overcome.

All electrochemical measurements were conducted in stainless-steel 2032 coin cells (MTI) with a stainless-steel conical spring, a 0.5-mm stainless-steel spacer for the anode, a 0.5-mm aluminum spacer for the cathode, and a glass microfiber separator (Whatman). The electrolyte was 1 M LiPF6 in 1:1 ethylene carbonate (EC): dimethyl carbonate (DMC), with ~50 uL of electrolyte used per cell. All cycling experiments were performed between 1.5 V and 3.5 V *vs.* Li/Li^+ on a VMP3 potentiostat/galvanostat (Bio-Logic). For testing purposes, VMO electrodes were studied in a half cell configuration versus a Li metal anode. When calculating C-rates, the theoretical capacity used was 240 mAh/g, based on the 1 e^- Li^+ insertion reaction into $V_9Mo_6O_{40}$ (1C = 240 mA/g, 5C = 1.20 A/g, etc.).

5.2.5 Operando synchrotron X-ray diffraction

All *operando* synchrotron X-ray diffraction measurements were performed at beamline 11-ID-C at the Advanced Photon Source at Argonne National Laboratory at 105.7 keV in transmission geometry with an area detector. For this experiment, freestanding pellet electrodes of VMO were made with 6:1:1:2 mass ratio of VMO:vapor-grown carbon fibers :multiwalled carbon nanotubes: PTFE binder. These electrodes were loaded into AMPIX cells in an argon glovebox with lithium metal counter electrodes, glass fiber separators, and electrolyte (1M LiPF6 in 1:1 EC:DMC). All two-dimensional SXRD data was calibrated with a LaB_6 external standard and integrated into one-dimensional diffraction patterns using GSAS-II.[39] Background subtraction was performed on diffraction data to remove scattering from the electrolyte. Crystal structures were visualized with the VESTA software package.[40]

5.3 Results and Discussion

We synthesized nanoporous powders of VMO through a modified sol-gel type method based on freeze drying in combination with polymer templating.[41,42] In this process, aqueous solutions of NH_4VO_3 and $(NH_4)_6Mo_7O_{24}$ precursors mixed with 150 - 200 nm poly(methyl) methacrylate (PMMA) colloids were vitrified in liquid N_2 and dried through sublimation on Schlenk line. The resulting dried V-Mo precursor powder was then calcined in argon at 550ºC to crystallize the nanoporous backbone, followed by a lower temperature conversion to VMO by heating in air at 400ºC. This two-step calcination process provides optimal retention of the nanoscale architecture compared to direct crystallization of VMO in air, which results in to considerable rearrangement. Scanning electron microscopy (SEM) characterization of the nanoporous VMO shows micron-scale powder particles with nanoscale pore wall thicknesses (**Figure 1a**). The pore walls are comprised of nanoscale VMO crystallites fused together into a continuous backbone. Powder X-ray diffraction on as-synthesized powders confirms formation of the VMO phase with varied peak intensities compared to micron-scale bulk VMO (**Figure 1b**). In particular, the (001) reflection at 21 degrees shows considerably higher intensity for the bulk VMO powder than the nanoporous VMO, likely due to preferred orientation effects from the bar-like

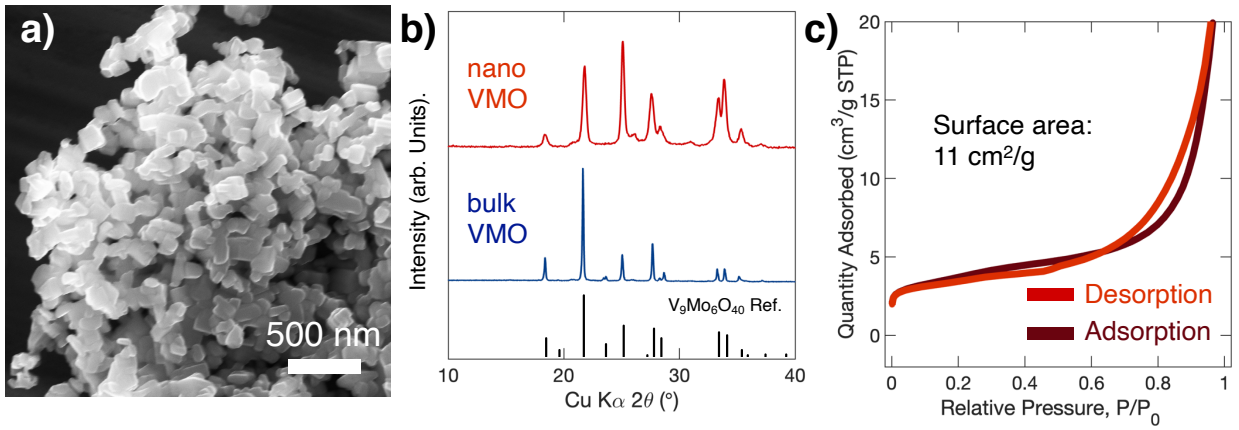

Figure 1. a) SEM micrograph of nanoporous VMO, showing the nanoscale porosity within micron-scale powder particles. **b)** Powder XRD pattern confirming phase purity and demonstrating decreased preferential orientation of nanoporous VMO compared to bulk VMO. **c)** N_2 porosimetry isotherm of nanoporous VMO, showing the moderate surface area.

bulk particle morphology. The porous structure of nanoporous VMO was characterized by N_2 porosity (**Figure 1c**). The isotherm was type IV according to the IUPAC classification, indicating that the porous network consists of macropores that were not completely filled with moderate surface area of 11cm^2/g for the optimized nanoporous VMO.[43]

We further characterized the structure of nanoporous VMO using scanning/transmission electron microscopy (S/TEM). **Figures 2a - 2c** show high resolution TEM micrographs of nanoporous VMO. At low magnifications, the micron-scale powder can be seen with nanoscale porosity. Bar-shaped crystallites, similar to those seen for bulk VMO but smaller, form the interconnected backbone of the pore network. At higher magnification, the lattice structure of a pore wall is resolved. The lattice encompasses an entire bar-like grain of the pore wall, confirming

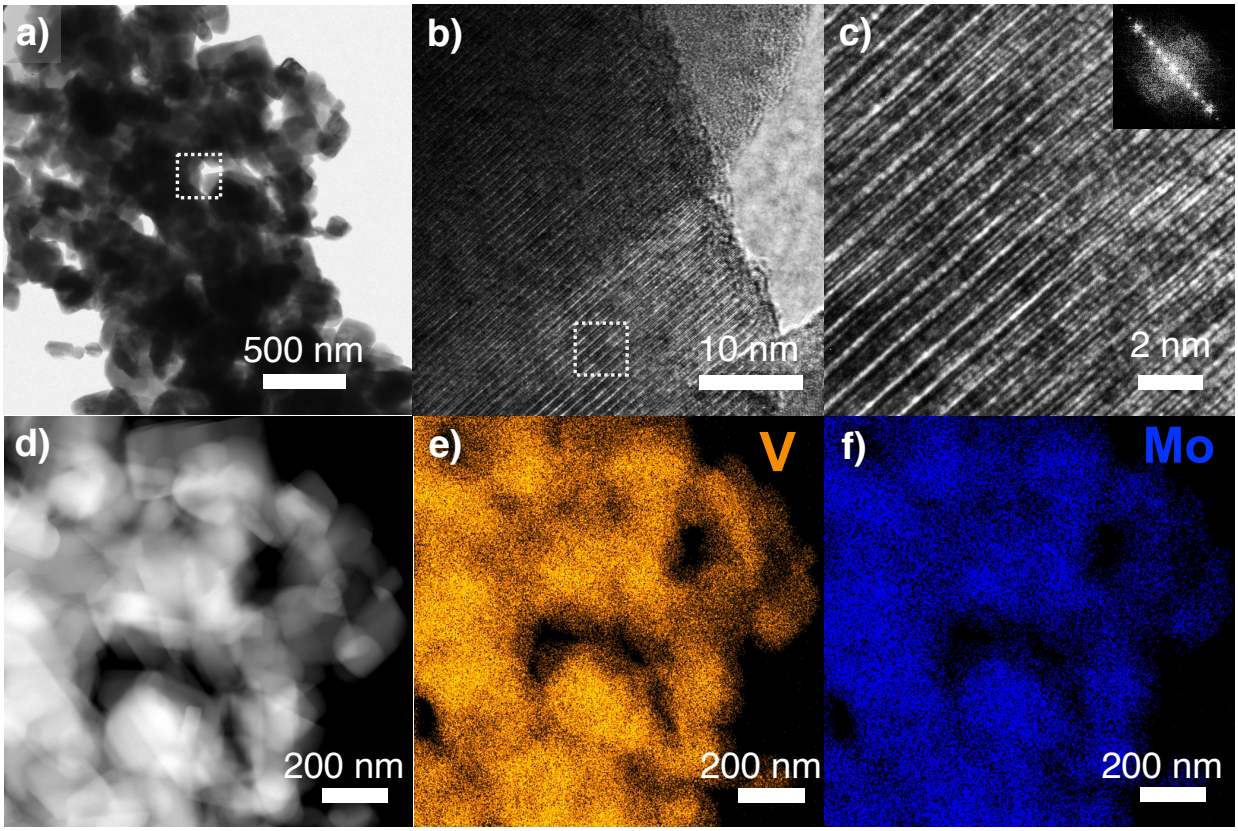

Figure 2. a) – c) High resolution TEM imaging of nanoporous VMO. At low magnification, the nanoscale porosity is shown for a micron-scale powder particle. At high magnification, the VMO lattice is shown within individual grains. Inset shows the Fast Fourier Transform of c). d) – f) STEM-EDS mapping of nanoporous VMO, showing that both V and Mo are distributed throughout the nanoscale structure.

that each individual grain comprises a single crystallite within the full polycrystalline porous network. The grains can likewise be seen with high-angle annular dark field STEM in combination with STEM-energy dispersive spectroscopy (EDS) (**Figure 2d - 2e**). Both V and Mo are distributed uniformly throughout the material, confirming the elemental composition of the nanoporous VMO material.

To evaluate the electrochemical performance of nanoporous VMO, powders were assembled into composite electrodes with conductive carbon and binder and tested in half-cell configuration in coin cells. For galvanostatic cycling experiments, we calculated a theoretical capacity of 240 mAh/g for VMO, which assumes the insertion of 1 Li^+ per transition metal (T.M.) in the VMO structure. All C-rates used were based on this capacity (1C = 0.24 A/g, 5C = 1.2 A/g, etc.).

The first lithiation of VMO proceeds through a sloping profile initially, then encompasses the transformation to a disordered rock salt structure, as shown by a large plateau observed around 2.0 V (**Figure 3a**). Additional lithiation beyond 1 Li^+/T.M occurs during the first cycle as a result of the transformation, as nearly 320 mAh/g (1.3 Li^+/T.M). is stored. On delithiation and subsequent cycles, this plateau does not occur, and instead charge storage occurs through a sloping profile. During the first delithiation, 272 mAh/g (1.1 Li^+/T.M.) is accessed, but this high capacity steadily decreases over the first few cycles until about 0.8 - 0.9 Li^+/T.M., or 190 - 210 mAh/g is stably cycled at 1C. Notably, the galvanostatic profile varies between the nanoporous VMO and micron-scale bulk VMO. Both materials show a pronounced plateau corresponding to the transformation to a disordered rock salt structure, but while the plateau begins above 2 V for nanoporous VMO, for bulk VMO it starts closer to 1.9 V, indicating significant overpotential, likely due to kinetic limitations from transforming large particles. Interestingly, despite these apparent kinetic

limitations, the transformation actually begins with a lower amount of Li^+ inserted for bulk VMO, with about 110 mAh/g of capacity in the sloping region before the plateau, compared to about 140 mAh/g for the nanoporous material.

We further evaluated the impact of nanoscale architecture by comparing bulk and nanoporous VMO during galvanostatic rate testing (**Figure 3b**). While bulk VMO shows good rate capability up to moderate rates, the optimized Li^+ diffusion in the nanoporous VMO leads to excellent capacity retention up to 60C. For example, at 10C, over 140 mAh/g, or about 0.6 Li^+/T.M. is stored for the nanoporous material compared to 110 mAh/g (0.45 Li^+/T.M.) for the bulk. At higher rates, this difference becomes more evident, with bulk VMO showing little capacity retention at 60C, the

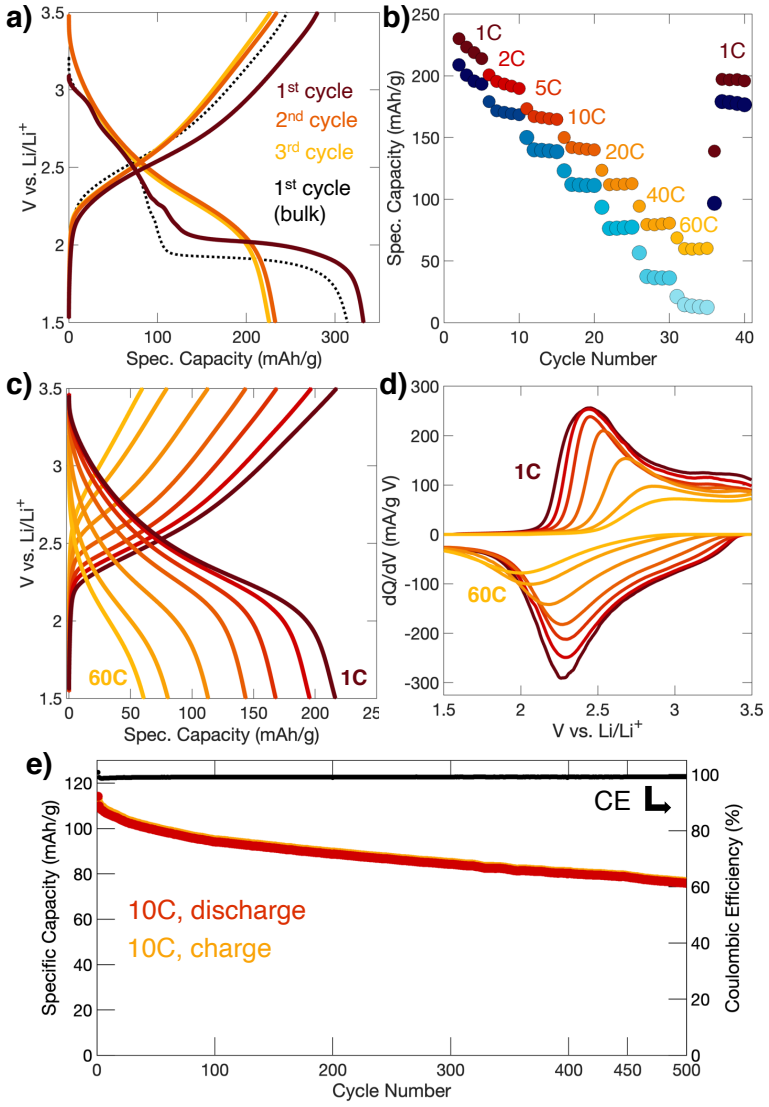

Figure 3. Galvanostatic (GV) cycling performance of nanoporous VMO. a) GV profile of the first three cycles, showing the initial transformation of nanoporous VMO compared to bulk VMO, followed by the subsequent sloping GV profile of cycling within the disordered rock salt phase. **b)** GV rate performance comparing bulk and nanoporous VMO. Rate dependent **c)** GV profiles and **d)** differential capacity (dQ/dV) analysis of nanoporous VMO for the rates in **b)**. **e)** Long term GV cycling for 500 cyles at 10C.

highest rate tested. Nanoporous VMO, on the other hand, can store over 60 mAh/g at 60C. We further characterized the rate capability of the nanoporous VMO with the galvanostatic profile and differential capacity analysis (dQ/dV) for each rate (**Figure 3c,3d**). At 1C, charge storage proceeds through a sloping galvanostatic profile and broad peak in the dQ/dV centered near 2.3 and 2.4 V for the lithiation and delithiation, respectively. At moderate rates, the sloping profile and peak shape are retained, but with additional polarization shifting the peak position slightly. At higher rates, the polarization leads to greater capacity loss, as the peak is broadened considerably and significant amounts of charge storage extend out of the voltage window. This basic pattern is reflected for bulk VMO, which also shows sloping profiles and similar peaks in dQ/dV, but which has much greater polarization, especially at the highest rates. Finally, we tested the stability of nanoporous VMO with long term GV testing at 10C, which showed a moderate capacity retention of 68% (**Figure 3e**).

To evaluate the electrochemical kinetics of nanoporous VMO further, we performed cyclic voltammetry (CV) analyses from 0.1 mV/s to 1.0 mV/s (**Figure 4a,4b**). After their transformation to the disordered rock salt phase during the first lithiation, both materials show the characteristically broad redox signatures typically seen for this class and for other disordered materials.[32] We analyzed the CV results using power-law dependence of each peak current (i_{peak}) as the sweep rate (v) is varied according to the following equation:

$$i_{\text{peak}} = av^b$$

where a and b are constants. The value of b, determined by fitting the slope of $\log(i_{peak})$ versus log(v), indicates whether the reaction is diffusion-limited (b = 0.5) or capacity (b = 1.0).[4445] Intermediate values correspond to diffusion behavior that is between semi-infinite diffusion and purely capacitive surface reactions. This analysis has been applied frequently to distinguish

diffusion-controlled or "battery-like" and pseudocapacitive redox reactions, which appear capacitive due to fast Li^+ diffusion and the absence of large first-order phase transitions.[5,19] Despite its large particle size, bulk VMO shows a highly capacitive charge storage mechanism, with *b* values of 0.94 and 0.93 for the anodic and cathodic sweep, respectively (**Figure 4c,4d**). These high values are likely due to the absence of a first-order phase transition during Li^+ insertion in VMO, as well as the disorder and small crystal size characteristic of electrochemically-formed disordered rock salts. Even still, the nanoporous VMO shows even higher *b* values of 1.0 and 0.96 for the anodic and cathodic sweep, confirming that shorter diffusion lengths can make charge storage even more capacitive.[46]

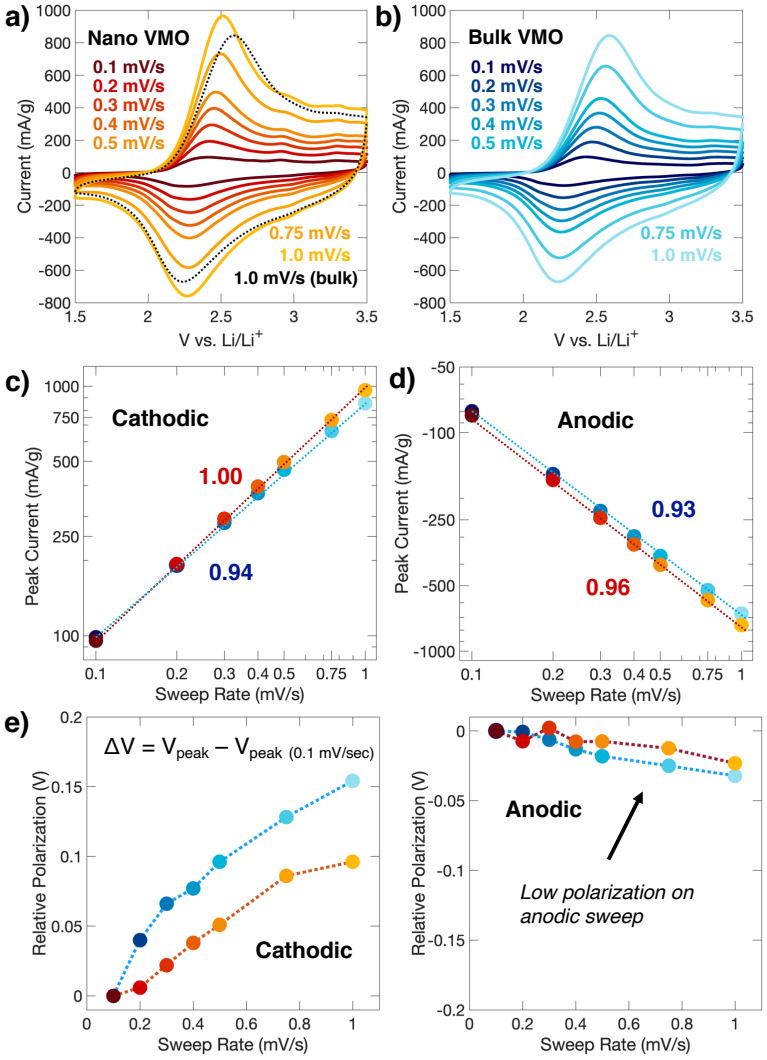

Figure 4. Cyclic voltammetry (CV) and kinetic analyses of VMO. CV curves for **a)** nanoporous and **b)** bulk VMO for a range of sweep rates along with the corresponding **c),d)** power law dependence analysis and **e),f)** relative polarization analysis.

We also extracted the relative polarization of charge storage in VMO as a function of sweep rate by measuring the shift in redox peak position from its value at the lowest sweep rate, 0.1 mV/s (**Figure 4e,4f**). The resulting values for relative polarization provide a straightforward quantification of charge storage

kinetics. For the cathodic sweep, bulk VMO shows steadily increasing polarization with faster sweep rates, with a maximum relative polarization of 154 mV at 1 mV/s. In contrast, nanoporous VMO shows lower relative polarization at all sweep rates, with only a 96 mV shift in peak position at 1 mV/s. This nearly 40% lower relative polarization compared to bulk VMO highlights the role of optimized Li^+ diffusion from the nanoscale architecture for this material. Notably, both bulk and nanoporous VMO show dramatically lower relative polarization for the anodic sweep (3 and 2 mV, respectively, at 1 mV/s). This difference indicates a delithiation-limited charge storage mechanism, likely due to the fact that delithiation from a disordered rock salt leaves highly charged transition metals (V^{5+}, Mo^{6+}) in a densely packed crystal structure.[27]

To characterize the impact of nanoscale architecture on electrochemical formation of the disordered rock salt structure, we performed operando synchrotron X-ray diffraction (SXRD) at beamline 11-ID-C at the Advanced Photon Source. In this experiment, the active material is assembled with conductive carbon and binder into freestanding pellets, which are cycled in AMPIX cells at a C/5 rate.[47] The operando SXRD data from Q = 1 – 5 $Å^{-1}$ is shown for the first cycle for nanoporous VMO in **Figure 5a** along with the galvanostatic cycling profile during the experiment. During the initial sloping region, peaks undergo small shifts, indicating topotactic changes in the lattice from lithiation. Once the plateau begins, the shifting is replaced by a continual decrease in the intensity of the starting VMO phase, while peaks corresponding to the rock salt phase emerge at 3.1 $Å^{-1}$ and 4.3 A^{-1}. This transformation is irreversible, and further cycling in the rock salt phase involves small structural change that we characterized in previous work on bulk VMO. We summarized the transformation and compared the kinetics between bulk and nanoporous VMO by determining the amount of each phase as a function of Li^+ content (**Figure 5b**). Both materials show a similar trajectory, where the starting VMO decreases in

intensity as the rock salt phase emerges. However, as we noted in the galvanostatic profile data, the transformation appears to be more facile in nanoporous VMO, as it starts earlier, but also persists longer. On the other hand, bulk VMO shows a sharper decrease in intensity of its starting phase. These observations support and explain the more pronounced plateau in the GV profile for bulk VMO compared to the broadened plateau seen for the nanoporous VMO.

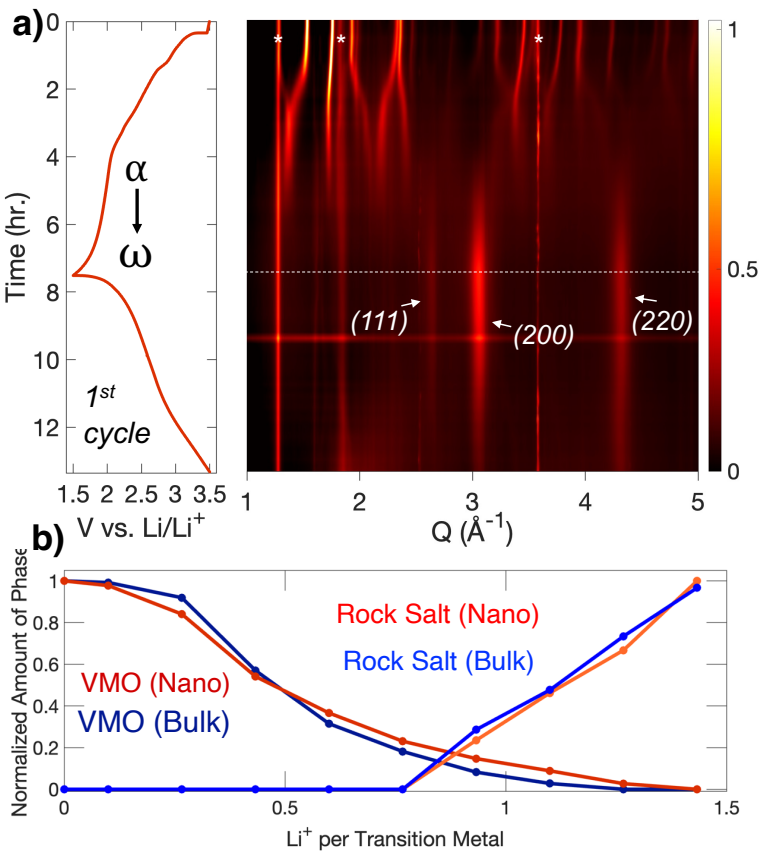

Figure 5. a) *Operando* synchrotron X-ray diffraction of nanoporous VMO during the first cycle, highlighting the transformation to a rock salt structure. Peaks from cell components are denoted with an asterisk. **b)** The relative amount of pristine versus rock salt phase as a function of lithiation for bulk and nanoporous VMO.

We further characterized the disordered rock salt VMO using HRTEM to visualize how the dramatic change in atomic-scale crystal structure affects the microstructure of the material. We previously noted that the pristine lattice planes of bulk VMO give way to a highly distorted lamellar microstructure after the transformation to a disordered rock salt phase (**Figure 6a,6b**). The stress involved in reforming a highly rigid crystal structure into the new phase, we hypothesized, likely caused localized microstructural fragmentation along specific crystal axes to alleviate the strain. Notably, this process does not appear to occur for nanoporous VMO, and

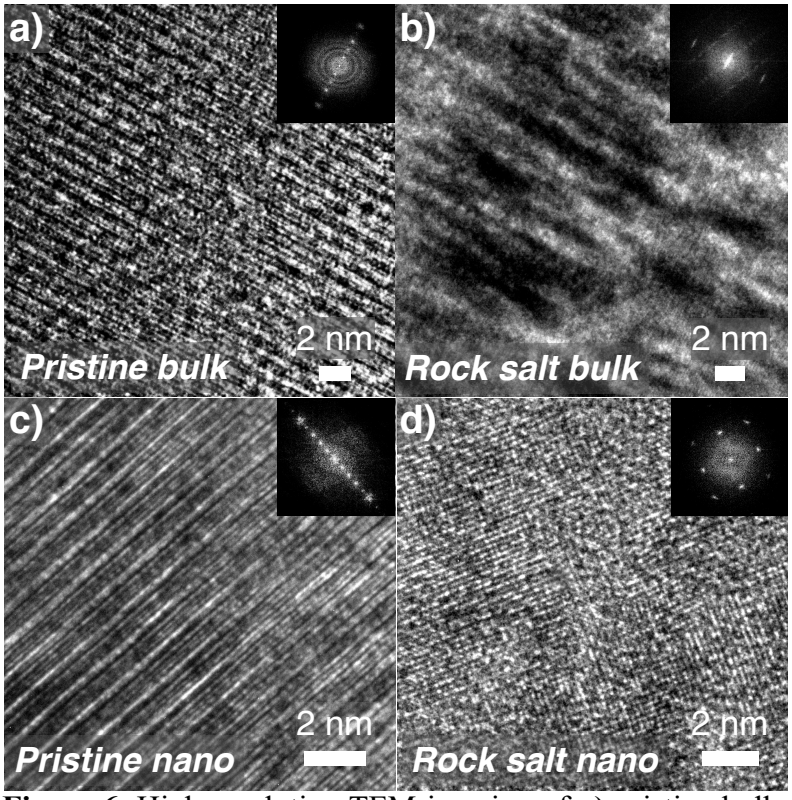

Figure 6. High resolution TEM imaging of **a)** pristine bulk, **b)** cycled bulk, **c)** pristine nano, and **d)** cycled nano VMO. The disorted lamellar microstructure that occurs in bulk VMO does not appear in nano VMO. Insets show Fast Fourier Transforms of the respective micrographs.

instead, an apparently pristine rock salt lattice is formed (**Figure 6d**). This difference in microstructure emphasizes that nanoscale size is an important component that can alter the material formed in this class of disordered rock salts.

5.4 Conclusion

In conclusion, we synthesized fast-charging nanoporous VMO through polymer templating. The optimized Li^+ diffusion from the nanoscale architecture increased charge storage kinetics significantly compared to micron-scale bulk VMO, especially at the highest rates tested. These changes in performance were characterized with electrochemical kinetics analyses that highlighted the much lower relative polarization in nanoporous VMO. Finally, we demonstrated that nanoscale size alters the pathway for transformation in the galvanostatic charge storage profile and with operando SXRD, which both showed a more facile process for the nanoporous material compared to the bulk. The resulting disordered rock salt from nanoporous VMO did not show the fragmented, distorted lamellar microstructure seen for the bulk material. Overall, this work emphasizes the key role of optimized nanoscale architecture for fast-charging

and shows that precursor size and morphology can be important factors for the electrochemical formation of disordered rock salts.

5.5 References

[1] Lopes, J. A. P.; Soares, F. J.; & Almeida, P. M. R. Integration of electric vehicles in the electric power system. *Proc. IEEE*, **2010**, *99*, 168-183

[2] Gür, T.M. Review of electrical energy storage technologies, materials and systems: challenges and prospects for large-scale grid storage. *Energy Environ. Sci.* **2018**, *11*(10), 2696–2767.

[3] Frith, J.T.; Lacey, M.J.; Ulissi, U. A non-academic perspective on the future of lithium-based batteries. *Nat. Commun.* **2023**, *14*(1), 420.

[4] Li, M.; Lu, J.; Chen, Z.; Amine, K. 30 years of lithium-ion batteries. *Adv. Mater.* **2018**, *30* (33), 1800561.

[5] Choi, C.; Ashby, D.S.; Butts, D.M.; DeBlock, R.H.; Wei, Q.; Lau, J.; Dunn, B. Achieving high energy density and high power density with pseudocapacitive materials. *Nat. Rev. Mater.* **2020**, *5*(1), 5–19.

[6] Ven, A. Van Der; Bhattacharya, J.; Belak, A. A. Understanding Li Diffusion in Li-Intercalation Compounds. *Acct. Chem. Res.* **2013**, *46*, 1216-1225.

[7] Okubo, M.; Hosono, E.; Kim, J.; Enomoto, M.; Kojima, N.; Kudo, T.; Zhou, H.; Honma, I. Nanosize Effect on High-Rate Li-ion Intercalation in $LiCoO_2$ Electrode. *J Am. Chem. Soc.* **2007**, *129*, 7444-7452.

[8] Kang, B.; Ceder, G. Battery materials for ultrafast charging and discharging. *Nature* **2009**, *458*, 190-193.

[9] Augustyn, V.; Come, J.; Lowe, M. A.; Kim, J. W.; Taberna, P.; Tolbert, S. H.; Abruña, H. D.; Simon, P.; Dunn, B. High-Rate Electrochemical Energy Storage through Li^+ Intercalation Pseudocapacitance. *Nat. Mater.* **2013**, *12*, 518-522.

[10] Sun, H.; Mei, L.; Liang, J.; Zhao, Z.; Lee, C.; Fei, H.; Ding, M.; Lau, J.; Li, M.; Wang, C.; Xu, X. Three-dimensional holey-graphene/niobia composite architectures for ultrahigh-rate energy storage. *Science*, **2017**, *356* (6338), 599–604

[11] Wagemaker, M.; Mulder, F.M. Properties and promises of nanosized insertion materials for Li-ion batteries. *Acc. Chem. Res*. **2013**, *46*(5), 1206–1215.

[12] Lin, T. C.; Yan, Y.; King, S. C.; Lai, C. H.; Tolbert, S. H. Fast-Charging Cathodes from Polymer-Templated Mesoporous $LiVPO_4F$. *ACS Appl. Mater. Interfaces* **2020**, *12*, 33775-33784.

[13] Jain, R.; Lakhnot, A.S.; Bhimani, K.; Sharma, S.; Mahajani, V.; Panchal, R.A.; Kamble, M.; Han, F.; Wang, C.; Koratkar, N. Nanostructuring versus microstructuring in battery electrodes. *Nat. Rev. Mater.* **2022**, *7*(9), 736–746.

[14] Cook, J. B.; Kim, H. S.; Lin, T. C.; Lai, C. H.; Dunn, B.; Tolbert, S. H. Pseudocapacitive Charge Storage in Thick Composite MoS_2 Nanocrystal-Based Electrodes. *Adv. Energy Mater.* **2017**, *7*, 1601283.

[15] Conway, B. E.; Birss, V.; Wojtowicz, J. The role and utilization of pseudocapacitance for energy storage by supercapacitors. *J. Power Sources* **1997**, *66***,** 1–14.

[16] Conway, B. E. Transition from "Supercapacitor" to "Battery" Behavior in Electrochemical Energy Storage. *J. Electrochem. Soc.* **1991**, *138* (6), 1539–1549.

[17] Kim, H.-S.; Cook, J. B.; Tolbert, S. H.; Dunn, B. The Development of Pseudocapacitive Properties in Nanosized-MoO_2. *J. Electrochem. Soc.* **2015**, *162*, A5083–A5090.

[18] Cook, J. B.; Lin, T. C.; Kim, H.-S.; Siordia, A.; Dunn, B. S.; Tolbert, S. H. Suppression of Electrochemically Driven Phase Transitions in Nanostructured MoS_2 Pseudocapacitors Probed Using Operando X-ray Diffraction. *ACS Nano*, **2019**, *13*, 1223–1231.

[19] Fleischmann, S.; Mitchell, J.B.; Wang, R.; Zhan, C.; Jiang, D.E.; Presser, V.; Augustyn, V. Pseudocapacitance: From Fundamental Understanding to High Power Energy Storage Materials. *Chem. Rev.* **2020**, *120*(14), 6738–6782.

[20] Cook, J. B.; Ko, J. S.; Lin, T. C.; Robertson, D. D.; Kim, H. S.; Yan, Y.; Yao, Y.; Dunn, B. S.; Tolbert, S. H. Ultrafast Sodium Intercalation Pseudocapacitance in MoS_2 Facilitated by Phase Transition Suppression. *ACS Appl. Energy Mater.* **2023**, *6* (1), 99–108.

[21] Delmas, C.; Brèthes, S.; Ménétrier, M. ω-$Li_xV_2O_5$ - a New Electrode Material for Rechargeable Lithium Batteries. *J. Power Sources* **1991**, *34* (2), 113–118.

[22] Delmas, C.; Cognac-Auradou, H.; Cocciantelli, J. M.; Ménétrier, M.; Doumerc, J. P. The $Li_xV_2O_5$ System: An Overview of the Structure Modifications Induced by the Lithium Intercalation. *Solid State Ionics* **1994**, *69* (3–4), 257–264

[23] Chen, Z.; Augustyn, V.; Wen, J.; Zhang, Y.; Shen, M.; Dunn, B.; Lu, Y.; Chen, Z.; Wen, J.; Zhang, Y.; Lu, Y.; Augustyn, V.; Dunn, B.; Shen, M. High-Performance Supercapacitors Based on Intertwined CNT/V_2O_5 Nanowire Nanocomposites. *Adv. Mater.* **2011**, *23* (6), 791–795.

[24] Sathiya, M.; Prakash, A. S.; Ramesha, K.; Tarascon, J. M.; Shukla, A. K. V_2O_5-Anchored Carbon Nanotubes for Enhanced Electrochemical Energy Storage. *J. Am. Chem. Soc.* **2011**, *133* (40), 16291–16299.

[25] Yue, Y.; Liang, H.; Yue, Y.; Liang, H. Micro- and Nano-Structured Vanadium Pentoxide (V_2O_5) for Electrodes of Lithium-Ion Batteries. *Adv. Energy Mater.* **2017**, *7* (17), 1602545.

[26] Zhong, W.; Huang, J.; Liang, S.; Liu, J.; Li, Y.; Cai, G.; Jiang, Y.; Liu, J. New Prelithiated V_2O_5 Superstructure for Lithium-Ion Batteries with Long Cycle Life and High Power. *ACS Energy Lett.* **2020**, *5* (1), 31–38.

[27] Christensen, C. K.; Sørensen, D. R.; Hvam, J.; Ravnsbæk, D. B. Structural Evolution of Disordered $Li_xV_2O_5$ Bronzes in V_2O_5 Cathodes for Li-Ion Batteries. *Chem. Mater.* **2019**, *31* (2), 512–520.

[28] Liu, H.; Zhu, Z.; Yan, Q.; Yu, S.; He, X.; Chen, Y.; Zhang, R.; Ma, L.; Liu, T.; Li, M.; Lin, R.; Chen, Y.; Li, Y.; Xing, X.; Choi, Y.; Gao, L.; Cho, H. S. yun; An, K.; Feng, J.; Kostecki, R.; Amine, K.; Wu, T.; Lu, J.; Xin, H. L.; Ong, S. P.; Liu, P. A Disordered Rock Salt Anode for Fast-Charging Lithium-Ion Batteries. *Nature* **2020**, *585* (7823), 63–67.

[29] Mikhailova, D.; Voss, A.; Oswald, S.; Tsirlin, A. A.; Schmidt, M.; Senyshyn, A.; Eckert, J.; Ehrenberg, H. Lithium Insertion into Li_2MoO_4: Reversible Formation of $(Li_3Mo)O_4$ with a Disordered Rock-Salt Structure. *Chem. Mater.* **2015**, *27* (12), 4485–4492.

[30] Pralong, V.; Venkatesh, G.; Malo, S.; Caignaert, V.; Baies, R.; Raveau, B. Electrochemical Synthesis of a Lithium-Rich Rock-Salt-Type Oxide $Li_5W_2O_7$ with Reversible Deintercalation Properties. *Inorg. Chem.* **2014**, *53* (1), 522–527.

[31] Xiong, H.; Yildirim, H.; Shevchenko, E. V.; Prakapenka, V. B.; Koo, B.; Slater, M. D.; Balasubramanian, M.; Sankaranarayanan, S. K. R. S.; Greeley, J. P.; Tepavcevic, S.; Dimitrijevic, N. M.; Podsiadlo, P.; Johnson, C. S.; Rajh, T. Self-Improving Anode for Lithium-Ion Batteries Based on Amorphous to Cubic Phase Transition in TiO_2 Nanotubes. *J. Phys. Chem. C* **2012**, *116* (4), 3181–3187.

[32] Barnes, P.; Zuo, Y.; Dixon, K.; Hou, D.; Lee, S.; Ma, Z.; Connell, J. G.; Zhou, H.; Deng, C.; Smith, K.; Gabriel, E.; Liu, Y.; Maryon, O. O.; Davis, P. H.; Zhu, H.; Du, Y.; Qi, J.; Zhu, Z.; Chen, C.; Zhu, Z.; Zhou, Y.; Simmonds, P. J.; Briggs, A. E.; Schwartz, D.; Ong, S. P.; Xiong, H. Electrochemically Induced Amorphous-to-Rock-Salt Phase Transformation in Niobium Oxide Electrode for Li-Ion Batteries. *Nat. Mater.* **2022**, *21* (7), 795–803.

[33] Li, W.; Fukunishi, M.; Morgan, B. J.; Borkiewicz, O. J.; Chapman, K. W.; Pralong, V.; Maignan, A.; Lebedev, O. I.; Ma, J.; Groult, H.; Komaba, S.; Dambournet, D. A Reversible Phase Transition for Sodium Insertion in Anatase TiO_2. *Chem. Mater.* **2017**, *29* (4), 1836–1844.

[34] Jarman, R. H.; Dickens, P. G.; Jacobson, A. J. Preparation and Characterization of the Mixed Oxide $V_9Mo_6O_{40}$. *Mater. Res. Bull.* **1982**, *17* (3), 325–328.

[35] Slade, R. C. T.; Ramanan, A.; West, B. C.; Prince, E. The Structure of $V_9Mo_6O_{40}$ Determined by Powder Neutron Diffraction. *J. Solid State Chem.* **1989**, *82* (1), 65–69.

[36] Hu, M.; Liang, J.; Chen, X.; Wei, J.; Zhou, Z. Preparation and electrochemical performance of $Mo_6V_9O_{40}$ nanorods as cathode materials for Li batteries. *RSC Adv.* **2015**, *5* (20), 15395-15398.

[37] Eick, H.A. and Kihlborg, L. 1The crystal structure of V_2MoO_8. *Acta Chem. Scand*. **1966**, *20*(6).

[38] Wang, T.; Sel, O.; Djerdj, I.; Smarsly, B. Preparation of a Large Mesoporous CeO_2 with Crystalline Walls Using PMMA Colloidal Crystal Templates. *Colloid Polym. Sci.* **2006**, *285* (1), 1–9.

[39] Toby, B.H.; Von Dreele, R.B. GSAS-II: the genesis of a modern open-source all purpose crystallography software package. *J. Appl. Cryst.* **2013**, *46* (2), 544–549.

[40] Momma, K.; Izumi, F. VESTA: a three-dimensional visualization system for electronic and structural analysis. *J. Appl. Cryst.* **2008**, *41* (3), 653–658.

[41] Sudant, G.; Baudrin, E.; Dunn, B.; Tarascon, J.-M. Synthesis and Electrochemical Properties of Vanadium Oxide Aerogels Prepared by a Freeze-Drying Process. *J. Electrochem. Soc.* **2004**, *151* (5), A666.

[42] Yan, Y.; Chin, M.A.; Robertson, D.D.; Lesel, B.K.; Tolbert, S.H. Tuning the Porous Structure in PMMA-Templated Mesoporous MoO_2 for Pseudocapacitive Li-Ion Electrodes. *J. Electrochem. Soc.* **2022**, *169* (4), 040545.

[43] Thommes, M.; Kaneko, K.; Neimark, A. V.; Olivier, J. P.; Rodriguez-Reinoso, F.; Rouquerol, J.; Sing, K. S. W. Physisorption of Gases, with Special Reference to the Evaluation of Surface Area and Pore Size Distribution (IUPAC Technical Report). *Pure Appl. Chem.* **2015**, *87* (9–10), 1051–1069.

[44] Simon, P.; Gogotsi, Y.; Dunn, B. Where do batteries end and supercapacitors begin? *Science* **2014**, *343*(6176), 1210–1211.

[45] Wang, J.; Polleux, J.; Lim, J.; Dunn, B. Pseudocapacitive Contributions to Electrochemical Energy Storage in TiO_2 (Anatase) Nanoparticles. *J. Phys. Chem. C* **2007**, *111* (40), 14925–14931.

[46] Rauda, I. E.; Augustyn, V.; Dunn, B; Tolbert, S.H. Enhancing Pseudocapacitive Charge Storage In Polymer Templated Mesoporous Materials. *Acct. Chem. Res.* **2013***, 46*, 1113-1124.

[47] Borkiewicz, O.J.; Shyam, B.; Wiaderek, K.M.; Kurtz, C.; Chupas, P.J.; Chapman, K.W. The AMPIX electrochemical cell: a versatile apparatus for in situ X-ray scattering and spectroscopic measurements. *J. Appl. Cryst.* **2012**, *45* (6), 1261–1269.

CHAPTER 6

Measuring electronic conduction in Nb-based high-rate anode materials *in situ*

Electrochemical energy storage is an essential technology for the electrification of our society, as it plays a key role in enabling electric vehicles, renewable energy sources, and grid-scale storage systems.[1-4] In particular, Li-ion devices with both high-power density and high energy density promise to facilitate this process with faster recharge times compared to traditional Li-ion batteries.[5,6] Li-ion electrodes store charge through reversible charge transfer reactions with a Li-ion electrolyte. During this process, diffusion of Li^+, transport of electrons, or structural changes of the host material can impede the rate of charge storage.[7-10] Over the past few decades, a number of engineering solutions to transport have been implemented, including nanostructuring the active material and carbon additives for improved ion and electron mobility.[7,9,11-16] Recently, micron-scale electrode materials with intrinsically fast ion diffusion have demonstrated potential for increased volumetric density at the anode in fast-charging cells.[17] Notably, the family of Wadsley-Roth shear phases,[18-23] including $TiNb_2O_7$,[24,25] $Nb_{16}W_5O_{55}$,[17] and PNb_9O_{25},[26,27] as well as the bronze-type phases T-Nb_2O_5[28,29] and $Nb_{18}W_{16}O_{93}$,[17] have all shown high rate capability up to large particle sizes, primarily due to the facile ion diffusion within their open-framework crystal structures.[17,29,30]

Within this class of high performance compounds, a major goal is to establish fundamental design rules to link structure and composition to properties and performance. In particular, electronic conduction is a key material property for these electrodes, especially since their ionic diffusion tends to be so fast. However, accurately quantifying the intrinsic electronic conductivity of electrode materials at various points of lithiation remains an ongoing challenge within the energy storage community.[24,26,31-35] Standard contact probe measurement methods are

incompatible with most cycling protocols: for example, when using typical electrodes, which are composites of active material, conductive carbon, and binder, measurements give a mixed conductivity value that primarily reflects the structure of the electrode rather than the intrinsic behavior of the active material.[32,33] Alternatively, pure electrodes can be prepared with no carbon or binder and cycled slowly to the desired composition before testing.[24,26] Due to the need for a current collector during cycling, however, the electrodes must be removed and the measurements performed *ex situ*, which introduces error and therefore lowers the attainable accuracy and resolution. Moreover, the pure pellets are pressed from powders, but cannot be sintered to improve interparticle contact after lithiation, and thus the conductivity measured contains large contributions from grain boundaries.[18] Overall, these challenges have prevented meaningful measurements of the intrinsic electronic conductivity of many lithiated electrode materials to date, despite the essential role of electronic transport in high rate Li-ion cells.

In this work, we develop a platform for *in situ* contact measurements on thin film electrodes without any additives and use it to characterize the insulating to conductive transition in the bronze phase materials T-Nb_2O_5 (**Figure 1a**) and $Nb_{18}W_{16}O_{93}$, which we refer to as NWO (**Figure 1b**). Both T-Nb_2O_5 and NWO have bronze-like crystal structures made of distorted Nb-O (or W-O) pentagonal and octahedral units, with different relative amounts and connectivity of the units within the structure for the two materials.[17,29,36] The open framework of the structures provides clear channels for facile Li^+ transport, and both T-Nb_2O_5 and NWO have been reported to show superionic diffusion of Li^+ within their structure based on pulsed-field gradient NMR measurements.[17,29,37] Accordingly, these materials show high rate capability as intercalation hosts for Li^+. T-Nb_2O_5 has been studied as an electrode material for decades, and has recently gained

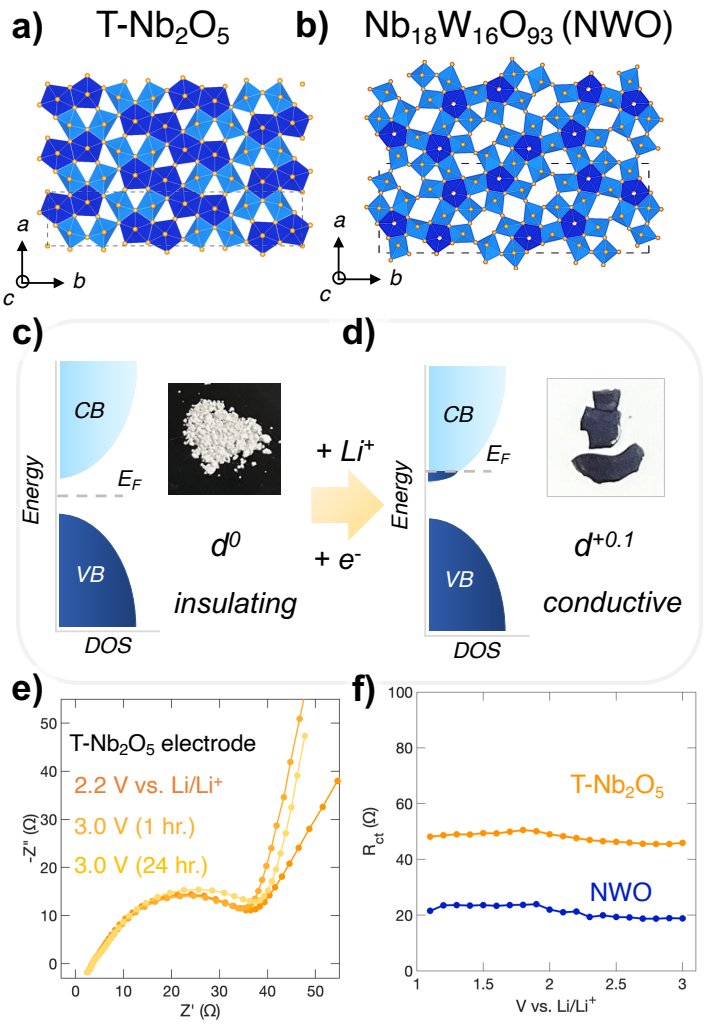

Figure 1. Crystal structures of **a)** T-Nb_2O_5 and **b)** $Nb_{18}W_{16}O_{93}$ (NWO). Both structures are composed of distorted pentagonal and octahedral Nb-O/W-O units. Schematic band diagrams for **c)** pristine and **d)** lithiated T-Nb_2O_5/NWO. The materials begin as wide-bandgap semiconductors or insulators, but become conductive with lithiation. Insets show photographs of T-Nb_2O_5 powder before and after lithiation. **e)** Nyquist plot from electrochemical impedance spectroscopy (EIS) on T-Nb_2O_5 composite electrode and f) representative charge transfer resistance of T-Nb_2O_5 and NWO composite electrodes from EIS as a function of voltage. No significant change in resistance is observed upon delithiation at 3.0 V due to the conductive carbon additives in the electrode.

even greater interest for its exceptional rate capability, especially when nanostructured and paired with conductive carbon in composites.[28,29,38-44] NWO, on the other hand, was originally reported in the 1960s but its performance in Li-ion cells was not demonstrated until recently.[17] Notably, NWO shows exceptional rate capability with micron-scale particles, with no apparent need for nanostructuring or carbon modification, unlike T-Nb_2O_5. Given the similar ionic diffusion rates and structural responses of these materials, the differences in performance in micron-scale particles potentially arises from their capabilities for electronic conduction.[17,29,41]

Like many high-rate anode materials, both T-Nb_2O_5 and NWO

as synthesized can be described as wide band-gap semiconductors or insulators, since the bonding between transition metals (TM) and oxygen leads to a formally d^0 TM oxidation state with no free carriers, as we show schematically in **Figure 1c**.[45] These electronic properties are evidenced by the white color of the pristine materials (shown for T-Nb_2O_5, **Figure 1c, inset**) and supported by first-principles calculations on T-Nb_2O_5 and a variety of similar compounds.[20,24,26,27,46,47] Upon cycling, however, lithiation is expected to n-dope the materials, leading to significantly improved conductivity from a dramatic increase in carrier density and possibly a change to a metallic band structure (**Figure 1d**).[18,20,24,26,27,46] This insulating to conductive transition is essential to these materials' fast charge storage kinetics, since resistive materials cannot conduct the large current densities necessary for high rates of cycling. While this transition is widely known to occur, the systematic errors associated with current measurement methods have complicated efforts to reliably compare different compounds.

As an initial test to characterize this change in conductivity, we first turned to standard electrochemical impedance spectroscopy (EIS) measurements on composite slurry electrodes of micron-scale T-Nb_2O_5 and NWO at different states-of-charge. For each EIS spectrum, the Nyquist plot shows a characteristic semicircle, with the series and charge transfer resistances as the high and low frequency intercepts, respectively, along with a low frequency tail to represent ionic diffusion (**Figure 1e**).[48,49] Here, the charge transfer resistance represents a composite electronic resistance of the electrode mixture. Both electrodes show relatively low charge transfer resistances of about ~50 and 25 **Ω**, respectively, indicating relatively facile electron transport. However, the charge transfer resistance shows almost no change at different states-of-charge, and even when the electrodes are delithiated, there is no evidence of a transition to insulating behavior (**Figure 1f**). Here, the presence of conductive carbon obscures the influence of the active material, since the

carbon additives provide conductive pathways even when the active material is highly insulating. As a result, the measured charge transfer resistance primarily reflects the resistance of the composite network, and no meaningful insight can be gained about the intrinsic conductivity of the active material.

In this work, we circumvent these errors using a new platform for *in situ* contact measurements on thin film electrodes without any additives. This method is commonly used for polymer thin films, but has not been employed successfully for inorganic battery materials.[50-53] The overall approach is depicted schematically in **Figure 2**. In brief, pure thin films of T-Nb_2O_5 or NWO are synthesized through a sol-gel process and crystallized using calcination. Then, interdigitated microelectrodes (IDEs) are printed onto these films by sputtering gold through a shadow mask template. The resulting thin film electrodes can cycle stably without the need for carbon or binder additives to allow for precise control over state-of-charge. At the same time, the interdigitated electrode provides an in-plane measurement geometry across the film that can be accessed in a working electrochemical cell.[50,52] Using this platform, we demonstrate quantitative measurement of the insulating to conductive transition upon lithiation in T-Nb_2O_5 and NWO.

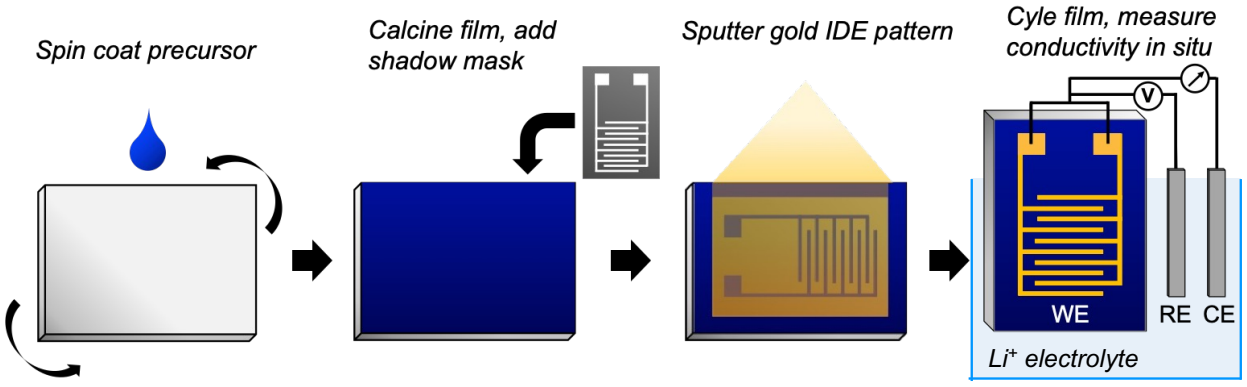

Figure 2. Schematic of the procedure used in this work for the *in situ* electrical conductivity measurement. Thin films of pure active material are produced by spin coating precursors onto an insulating substrate. Once the films are crystallized with calcination, interdigitated electrode (IDE) current collectors are deposited by sputtering gold through a shadow mask. Then, the *in situ* conductivity measurement is performed on the thin film in a flooded cell.

While both compounds undergo dramatic changes in their electronic conductivity upon lithiation, NWO's change occurs much more quickly, explaining its improved rate capability in micron-scale particles without the need for additional carbon coating. We support these *in situ* contact measurements with magnetic characterization of the materials electronic structure, which confirm significantly more delocalization of electrons at low Li^+ content in NWO than in T-Nb_2O_5.

Thin films of T-Nb_2O_5 and NWO were synthesized with a sol-gel process by spin coating stoichiometric solutions of $NbCl_5$ or both $NbCl_5$ and WCl_6 in ethanol. Once deposited, the films were calcined at high temperature to crystallize the desired structures. This method produces dense polycrystalline films, shown by scanning electron microscopy (SEM) from a top view, with uniform thickness across a large area of substrate (**Figure 3a, 3b**). Both films consist of fused crystallites connected in the plane of the film, with moderate grain sizes for NWO, and larger grains for T-Nb_2O_5 due to its more facile crystallization. Powder X-ray diffraction of the films confirms formation of T-Nb_2O_5 and NWO, but shows highly oriented versions of their crystal structures, with the (*h00)* lattice reflections preferentially expressed in intensity (**Figure 3c**). The films are polycrystalline, meaning their conductivity will have some contribution from grain boundaries. Unlike pellet electrodes made from powders, however, the films can be readily lithiated even after they are calcined at high temperature (800 - 1000 ºC), which fuses grains together and mitigates the grain boundaries' effects on conductivity.[18,24] Overall, these thin films provide crystalline active material with a controlled, planar geometry, which will be necessary to accurately calculate their intrinsic conductivity from measured values of resistance.

In standard electrochemical cycling experiments, films are typically placed onto a metal or metallized substrate to serve as a current collector.[38,40] However, during conductivity measurements, these conductive substrates provide a facile path for electron conduction that shorts

the measurement and cannot be used.[50,52] Instead, we deposited our films onto insulating silicon substrates to avoid influence of the substrate on the measured resistance. Then, to provide a current collector for electrochemical cycling and conductivity experiments, an interdigitated microelectrode (IDE) pattern was placed onto each film. The upper left portion of a representative microelectrode pattern on a T-Nb_2O_5 thin film is shown with optical microscopy in **Figure 3d**. As depicted schematically in Figure 2, the IDE consists of two separate current collectors with interlocking digits. Based on the desired measurement range and capabilities of the fabrication approach, we used IDEs with 200 µm µm digits with 200 µm gaps in between. As shown by the optical micrograph in Figure 3d, the method accurately reproduces these dimensions in the current collector, confirming the successful deposition of the IDE pattern. After

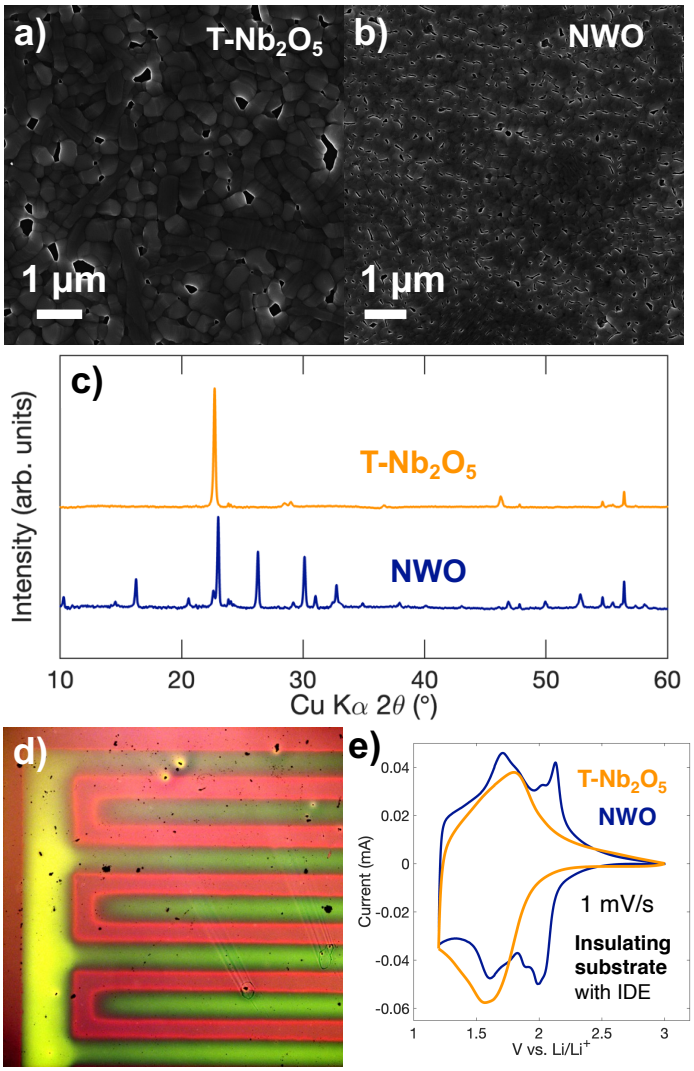

Figure 3. Top view scanning electron micrographs of calcined **a)** T-Nb_2O_5 and **b)** NWO thin films. The films have a dense, polycrystalline morphology. **c)** Powder X-ray diffraction on the calcined films confirms the formation of oriented versions of the T-Nb_2O_5 and NWO crystal structures. **d)** Optical micrograph of one section of the as-deposited interdigitated electrode (IDE) current collector on a T-Nb_2O_5 thin film. **e)** Cyclic voltammograms of T-Nb_2O_5 and NWO thin films on insulating substrates that are cycled using deposited IDEs.

the IDE current collector was placed, films were tested with cyclic voltammetry (CV) in a conventional Li-ion electrolyte in a flooded cell. **Figure 3e** shows representative cyclic voltammograms of T-Nb_2O_5 and NWO films cycled at 1 mV/s. The T-Nb_2O_5 film shows a characteristic broad redox peak,[37-39] while NWO shows a two more pronounced peaks in each sweep direction superimposed onto a broad, capacitive current feature.[17] The CV characteristics confirm the ability to cycle these films even on an insulating substrate by using the deposited IDE current collector.

With the thin film IDE platform successfully developed, we then performed *in situ* electronic conductivity measurements. This technique was adapted based on a method for polymer thin films with a similar measurement geometry, but has not yet been implemented with films of transition metal oxides or other inorganic active materials.[50-53] The experiment involves the IDE thin film within a standard flooded electrochemical cell with two separate circuits, shown schematically in **Figure 4a**, connected to the film electrode. The first circuit is a three-electrode configuration with the thin film as the working electrode and Li metal counter and reference electrodes, and is used to potentiostatically control state-of-charge of the film. The second is a two-electrode configuration with the two separate terminals of the IDE microelectrode as the working and counter/reference electrodes, respectively, to conduct resistance measurements across the film using EIS. This dual set of circuits enables both control over state-of-charge and resistance measurements in a single measurement geometry, without the need to remove the electrode from the electrochemical cell. Once the resistance, R_e, is measured, the conductivity, σ_e, can be calculated based on the measurement geometry dictated by the IDE microelectrode according to Equation 1:

$$(1) \quad \sigma_e = \frac{1}{R_e} \times \frac{d}{l \times (N - 1) \times h}$$

where *d* is the distance between the digits of the IDE, *l* and *N* are the length and the number of digits in the IDE, respectively, and *h* is the thickness of the active material film.[52]

Using this experimental platform, the electronic conductivity of the T-Nb_2O_5 and NWO thin films was measured as a function of Li content in a standard Li-ion battery electrolyte (1M LiTFSI in 1:1 EC/DMC). For a typical *in situ* conductivity measurement, thin films were precycled at least three times with CV between 1.2 – 3.0 V vs. Li/Li^+, then held at 3.0 V for at least 12 hours to delithiate the material as much as possible. Then, the film was gradually lithiated by decreasing the voltage in steps of 0.1 V at a time, with an EIS measurement for each step. The voltage and current profiles of the thin film working electrode for three representative steps are shown in **Figure 4b**. The film is set to a desired voltage versus Li/Li^+, and current flows through the circuit to reach that voltage, with a large initial spike that decreases rapidly as the system equilibrates. After five minutes of potentiostatic hold, EIS is performed to measure the resistance across the film. The EIS is reflected in the measured voltage profile as a 10 mV oscillation that begins at high frequency, and gradually decreases in frequency. A typical spectrum from the resistance measurement showed a semicircular arc along with a Warburg tail element, as shown in **Figure 4c**, and resistance values were extracted using the Debye equivalent circuit model for mixed conduction through the film.[54,55] In brief, the high frequency intercept represents the contact resistance, while the lower frequency intercept of the semicircle represents the mixed electronic and ionic resistance. After the EIS technique is complete, the voltage is stepped by 0.1 V and the next equilibration step begins.

Conductivity measurements with the five-minute voltage step followed by the EIS technique were carried out in steps of 0.1 V throughout the entire voltage window from 3.0 V vs. Li/Li^+ to 1.2 V. The resulting EIS spectra for NWO are shown in **Figure 4e** with logarithmically

scaled axes, with the specific voltage for each data point indicated by colored symbols on the CV curve in **Figure 4d**. At the beginning of the experiment, when the film is delithiated (3.0 V), the resistance is high, such that only half a semicircle appears in the accessible frequencies measured, with the lowest frequency data point reaching a resistance of approximately 600,000 Ω (6 MΩ). Extrapolation of this curve to a full semicircle gives a resistance of about 10 MΩ, which

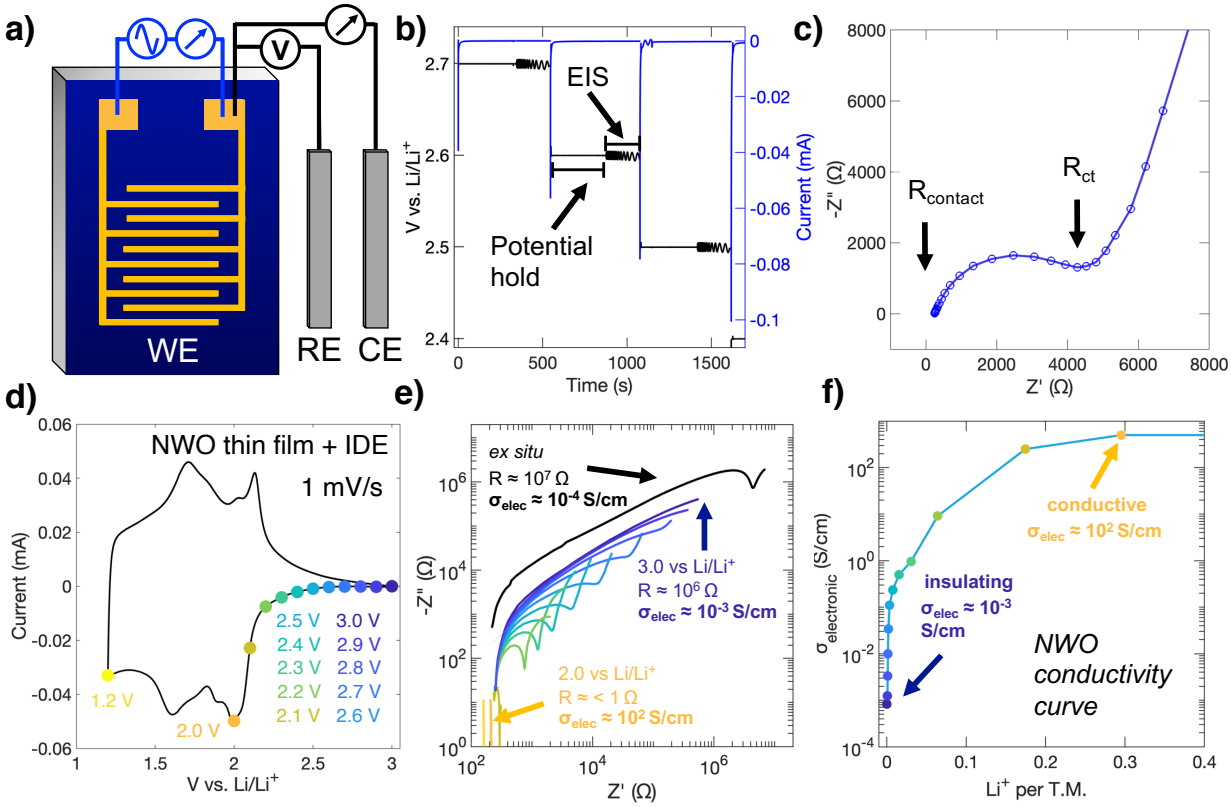

Figure 4. Measuring the electrical conductivity of NWO *in situ*. a) Schematic depiction of thin film with interdigitated electrode (IDE) current collector during the in situ conductivity measurement. The three-electrode circuit in black adjusts potential with Li counter and reference electrodes, while the two-electrode circuit in blue is used to perform resistance measurements between the two halves of the IDE. **b)** Potential (left axis, black) and current (right axis, blue) data from the three electrode circuit during three representative steps of the conductivity measurement. **c)** Representative Nyquist plot from an EIS spectrum during the measurement at 2.5 V. The electronic resistance is extracted from the low frequency intercept of the semicircle. **d) – f)** Data from conductivity measurement on an NWO thin film. An EIS spectrum is taken at each potential point noted in **d)**, with the CV of the film shown for clarity. **e)** EIS spectra shown on a logarithmic scale. The color of each spectrum matches the point in **d)** to show its corresponding potential. **f)** Full conductivity curve from the data in **e)** as a function of Li stoichiometry, showing the dramatic increase in electronic conductivity as NWO is lithiated.

.

corresponds to an electronic conductivity of 5 x 10^{-4} S/cm. The validity of the extrapolation is supported by the *ex situ* spectrum before cycling, which shows a full semicircle with an even higher resistance of nearly 100 MΩ. Based on these high resistance values and low conductivities, the film is highly insulating in the delithiated state. However, as the voltage of the film is decreased and the NWO film is lithiated, the semicircles in the EIS spectra decrease in size considerably, indicating a drop in the material's electronic resistance. By 2.6 V, for example, the resistance has decreased by two orders of magnitude to ~15 kΩ (3 x 10^{-2} S/cm), even though only a small amount of Li^+ has been inserted (~ 0.004 Li^+ per T.M). The trend continues as the film of NWO is lithiated: by 2.2 V (0.06 Li^+ per T.M.), the resistance has gone down by another two orders of magnitude to 300 Ω (2 S/cm). Finally, once the NWO has been stepped to 2.0 V (0.3 Li^+ per T.M.) the observed semicircle becomes so small as to have no measurable diameter, indicating a resistance below 1 Ω (> 500 S/cm). After this point, the NWO has reached the lower limit of the measurement's resistance resolution attainable with this geometry, and any changes within this regime cannot be accurately quantified. Notably, the film maintains this low resistance throughout the rest of the voltage window.

The results of the conductivity measurements on NWO are summarized in the conductivity-stoichiometry curve in **Figure 4f**. In its delithiated state, NWO shows insulating behavior characteristic of a wide-bandgap semiconductor. However, with the insertion of only 0.01 Li^+ per T.M., NWO undergoes a dramatic increase in its electrical conductivity of about three orders of magnitude due to the associated reduction of the material. As more Li^+ is introduced, the conductivity continues to increase at a slower rate, until it reaches the upper limit of the measurement (500 S/cm), where it remains throughout the rest of the voltage window. Overall, we measure an increase in conductivity of five orders of magnitude on the same film without removing

it from the electrochemical cell. With this result, we have quantified the insulating to conductive transition that NWO undergoes during lithiation. To the best of our knowledge, this result represents the first quantitative *in situ* measurement of the transition in a standard electrochemical cell, both for NWO and for any battery material more broadly.

We also performed *in situ* conductivity measurements on T-Nb_2O_5, with the conductivity-stoichiometry curve shown alongside NWO's in **Figure 5a**. Like NWO, T-Nb_2O_5 also begins with insulating behavior in its delithiated state and undergoes a dramatic increase in its electronic conductivity when Li^+ is inserted. Unlike NWO, however, T-Nb_2O_5 shows a slower increase in conductivity at very low Li^+ content. Where NWO attains a conductivity of 0.1 S/cm by only 0.003 Li^+ per T.M. inserted, T-Nb_2O_5 requires about three times as much Li^+ inserted to reach the same conductivity, indicating a delayed onset of conductive behavior. Importantly, this distinction appears to explain the difference in performance of micron-scale T-Nb_2O_5 and NWO: whereas T-Nb_2O_5 needs to be combined in carbon composites for optimal performance due to its delayed increase in conductivity, NWO maintains high rate capability without extra carbon because the onset of its conductive behavior occurs at low Li content. Notably, T-Nb_2O_5 becomes just as conductive as NWO at intermediate Li content, and both reach the maximum conductivity resolved by the measurement geometry at a similar point. While the absolute conductivity in the conductive state is similar, the slower transition to conductive behavior appears to negatively impact the performance T-Nb_2O_5 as an active material.

The slower transition to a conductive state for T-Nb_2O_5 can likely be attributed to the presence of localized trap states in its electronic structure, which were recently identified with density functional theory calculations.[46] Based on the calculated electronic structure, these localized electronic states are filled before the material can exhibit metallic behavior, so some of

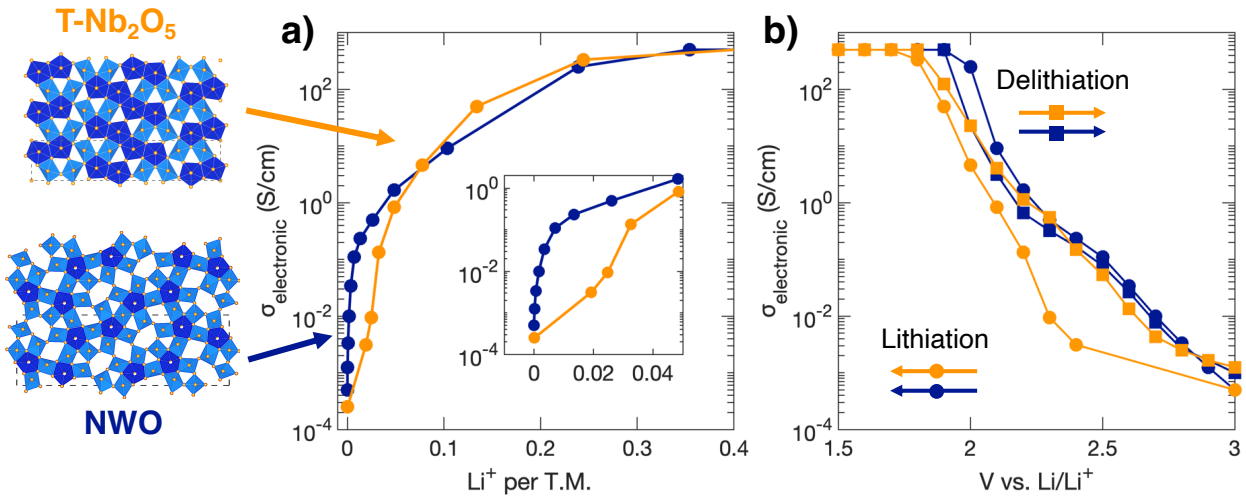

Figure 5. a) Conductivity curves as a function of Li content for T-Nb_2O_5 (orange) and NWO (blue). Both materials undergo dramatic increases in electronic conductivity with lithiation, but NWO does so more quickly at low Li content. **b)** Lithiation and delithiation conductivity curves as a function of voltage. T-Nb_2O_5 shows a hysteresis due to a delayed increase in conductivity that is not present for NWO.

the earliest carriers introduced through lithiation do not significantly increase the conductivity. Further experimental evidence for trap states can be seen by comparing the conductivity measurements performed during lithiation and delithiation as a function of voltage (**Figure 5b**). NWO exhibits close similarities in the measured conductivity between the forward and reverse sweeps, which suggests that all of the carriers introduced and removed through cycling contribute. For T-Nb_2O_5, however, there is a clear hysteresis where the conductivity does not increase during the lithiation until a later voltage, despite the close similarities with NWO on delithiation. This hysteresis suggests that the earliest electronic states filled contribute little to increasing conductivity, but during delithiation, they do not delay the decrease in conductivity since they are the last to be emptied. Importantly, the presence of trap states has been predicted in the electronic structure of many other high-rate electrode materials,[20,24,26,47] so NWO's very fast onset of conductivity appears to distinguish it and potentially explain its exceptional performance.

We supported this *in situ* conductivity characterization with *ex situ* measurements of the materials' magnetic properties using superconducting quantum interference device (SQuID)

magnetometry. Magnetic susceptibility characterization has been employed previously as a qualitative non-contact probe of conduction electrons on lithiated samples.[24,26] In these lithiated nonmagnetic oxides, unpaired electrons exhibit either temperature-dependent Curie-Weiss paramagnetism, which describes localized spins according to equation 2, or temperature-independent Pauli paramagnetism, which occurs for delocalized spins and can be modeled with equation 3:

$$(2) \quad \chi_{CW} = \frac{C}{T - \theta_{CW}} \qquad (3) \quad \chi_P = \mu_B^2 g(E_F)$$

where χ is the susceptibility, T is temperature, C and θ_{CW} are fitted parameters, μB is the magnetic moment of a Bohr magneton, and g represents the density of states at E_F, the Fermi energy.[56] The relative amount of Curie-Weiss and Pauli paramagnetism indicates how many carriers are localized versus free to conduct, respectively.

Figure 6a and 6b show the magnetic susceptibility of T-Nb_2O_5 and NWO as a function of temperature for three different amounts of lithiation, with the inverse susceptibility curves after subtraction of diamagnetic background components shown in **Figure 6c** and **6d**. Based on equation 2, a perfect Curie-Weiss paramagnet exhibits hyperbolic susceptibility and linear inverse susceptibility curves, and deviations from these characteristics in magnetic properties in these materials can be attributed to Pauli-type behavior from delocalized spins.[56] At 0.06 Li^+ per T.M., T-Nb_2O_5 shows nearly ideal Curie-Weiss behavior, indicating that carriers introduced up to this point are localized in trap states. By 0.11 Li^+ per T.M. inserted, and through to 0.22 Li^+ per T.M., its susceptibility exhibits dominant contributions from Pauli paramagnetism, as evidenced by the sublinear inverse susceptibility curves. This transition to electronic delocalization we observe is supported by DFT calculations that show metallic behavior in T-Nb_2O_5 after initial trap states are filled.[46] NWO shows similar behavior, with more Curie-Weiss behavior at low Li^+ content and

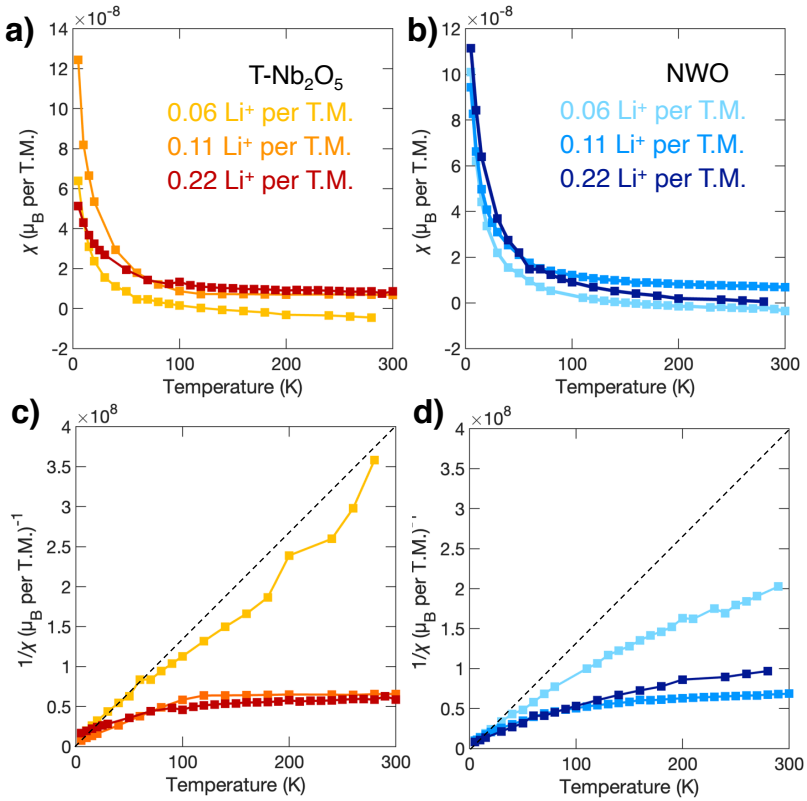

Figure 6. Magnetic susceptibility curves for **a)** T-Nb_2O_5 and **b)** NWO at various states of lithiation. After subtraction of diamagnetic background, the inverse susceptibility of each curve is shown in **c)** and **d)**, with dashed lines included for clarity. Linear inverse susceptibility, like that seen for T-Nb_2O_5 at 0.06 Li^+ per T.M., indicates Curie-Weiss paramagnetism, which corresponds to localized electrons. Sublinear curves indicate deviation from Curie-Weiss behavior due to Pauli paramagnetism, which occurs from delocalized electrons. All curves at +0.11 Li^+ per T.M. show dominantly Pauli behavior. However, NWO also shows mostly Pauli behavior even at 0.06 Li^+ per T.M., unlike T-Nb_2O_5, indicating greater delocalization at low Li content.

more delocalized behavior at 0.11 Li^+ and beyond. Importantly, however, at 0.06 Li^+ per T.M., NWO exhibits sublinear inverse susceptibility, indicating significant amounts of electronic delocalization, unlike T-Nb_2O_5 at the same point. These magnetic measurements corroborate the presence of trap states at early stages of lithiation in T-Nb_2O_5 that localize carriers and decrease its electronic conductivity. At the same lithium content, NWO shows significant delocalization, which explains the earlier onset of conductive behavior identified with the contact measurements.

In conclusion, we have reported the successful quantification of the insulating to conductive transition in T-Nb_2O_5 and NWO using a newly developed platform for *in situ* measurement of electronic conductivity. Both materials exhibit dramatic changes in their

electronic conductivity due to the introduction of carriers with lithiation: we measured increases in conductivity of five orders of magnitude *in situ*, although the change is potentially even greater, since the upper limit of the measurement geometry was reached. We supported these measurements with *ex situ* magnetic characterization that showed significantly more delocalized carriers at early lithiation in NWO compared to T-Nb_2O_5. Taken together, these results suggest that the more rapid transition to a conductive state in NWO is key to its exceptional performance without the need for carbon composites. Overall, this work highlights the role of electronic conduction in high rate anodes and the importance of *in situ* characterization to understand structure-property relationships for these materials.

Experimental

Materials preparation.

T-Nb_2O_5 and NWO thin films were produced using spin coating. In a typical synthesis for T-Nb_2O_5, 200 mg of $NbCl_5$ was combined with 1.0 mL of dry ethanol and stirred for ~ 30 minutes. Films were deposited onto insulating undoped Si substrates (~ 1.0 cm x 0.6 cm) with a thick layer of thermal oxide to avoid to the influence of substrate conduction during conductivity measurements. During spin coating, approximately 50 uL of precursor solution was added onto a substrate, which was then spun at 4000 rpm for 1 minute to produce an ~100 nm film. The as-coated film was dried at 50ºC on a hot plate and then calcined at 600ºC (1 hour ramp, no hold).

The synthesis process was similar for NWO films, except the precursor solution was 100 mg $NbCl_5$ and 130 mg WCl_6 in 1.0 mL of dry ethanol and the calcination occurred at 850ºC.

Bulk T-Nb_2O_5 and NWO powders were synthesized by modifying previously-reported solid state preparation methods. In a typical synthesis for T-Nb_2O_5, 500 mg of NbO_2 powder was heated to

575 C in air for 24 hours. For NWO, a stoichiometric mix of NbO_2 and WO_2 adding up to 500 mg was mixed with a mortar and pestle for about five minutes, and then heated at 1050ºC in air for ten hours. The resulting powders were ground with a mortar and pestle before electrochemical testing.

Structural characterization

Scanning electron microscopy (SEM) images were obtained using a ZEISS Supra 40VP field emission electron microscope with 5 kV accelerating voltage and 6 mm working distance. X-ray diffraction was collected with a PANalytical X'Pert Pro diffractometer operating with Cu Kα (λ = 1.5418 Å) using a 0.05° step size, an accelerating voltage of 45 kV, and a current of 40 mA.

Fabrication of interdigitated microelectrodes

Interdigitated microelectrodes were produced on top of fully synthesized films through a flexible, low-cost sputtering approach. A custom stainless-steel shadow mask (Stencils Unlimited) was secured onto four films at a time (one IDE electrode per film) with clips to ensure intimate contact between the films and the mask. The assembly was placed into a sputtering chamber and gold was sputtered for 15 minutes (10 mA output). Each IDE pattern is composed of two interdigitated gold electrodes with two connection tracks. The microelectrodes have 8 pairs of digits with a digit length of 0.4 cm, a width of 200 μm, and a gap of 200 μm between the digits. Depending on the film roughness and the shadow mask assembly, variations in digit thickness can occur. These geometric factors were taken into account when calculating the conductivity for a given electrode.

Electrochemical testing and conductivity measurements on IDE thin films.

All electrochemical tests were performed at room temperature in an argon glovebox with O_2 and H_2O levels below 1 ppm. A three-electrode cell was used for testing the IDE thin film

microelectrodes, with the microelectrode for the working electrode and pieces of polished Li foil as the counter and reference electrodes. The electrolyte was 1 M bis(trifluoromethane)sulfonimide lithium salt (LiTFSI) in a mixture of 1:1 by volume ethylene carbonate (EC) and dimethyl carbonate (DMC). The volume of electrolyte was fixed to ensure similar amounts of the film were submerged between different samples. A second circuit was used to connect the two halves of the microelectrode on the film of active material, with a two-electrode setup involving one half as the working electrode and the other half as the counter and reference electrodes. The two halves were held at the same potential except during electrochemical impedance spectroscopy (EIS) measurements.

In a typical *in situ* conductivity measurement, thin films were precycled at least three times with cyclic voltammetry between 1.2 – 3.0 V vs. Li/Li^+, then held at 3.0 V for at least 12 hours to delithiate the material as much as possible. Then, the film was gradually lithiated by decreasing the voltage in steps of 0.1 V at a time, with an EIS measurement for each step. After decreasing the voltage, the film was allowed to equilibrate for five minutes, during which the measured current dropped considerably. The exact current after this hold depended strongly on the specific voltage, but ranged from < 500 nA in the mostly inactive region near 3 V to < 5 uA where the film was undergoing redox 1.2 – 1.8 V. After voltage equilibration, EIS was used to measure the resistance of the active material film between the two halves of the IDE. The EIS technique was conducted between 900 kHz and 20 mHz using a sinusoidal excitation of ±10 mV while the two halves of the IDE were held at the same potential. During the EIS measurement between the two halves of the IDE, a small current was applied to the film using the three-electrode circuit vs. Li/Li^+ to prevent unwanted drifting of the state-of-charge. This adjustment improves the precision of the experiment significantly, and was necessary to measure resistance at low levels of lithiation, where the film

was found to drift significantly when left under open-circuit conditions. Importantly, the presence of this adjustment current was found to have no influence on the resistance measurement except for small shifts in the series resistance intercept of the Nyquist plot. Conductivity measurements with the five-minute voltage step followed by the EIS technique were carried out in steps of 0.1 V throughout the entire voltage window from 3.0 V vs. Li/Li^+ to 1.2 V in a single session.

The active material resistance was extracted from the EIS measurements by taking the difference between the low frequency and high frequency intercepts of the semicircle in the Nyquist plot. The resistance was converted to conductivity based on the measurement geometry using Equation 1: $\sigma_{elec} = \frac{1}{R_{elec}} \times \frac{d}{l \times (N-1) \times h}$ where R_{elec} is the measured resistance of the active material, d and l are the distance between digits and length of digits for the microelectrode, respectively, and h is the film height.

Electrochemical measurements

For EIS testing of bulk T-Nb_2O_5 and NWO powders, the material was assembled into composite slurry electrodes with an overall composition of 80% active material, 8% carbon black, 2% multiwalled carbon nanotubes (CNT), and 10% polyvinylidene fluoride (PVDF) binder. The CNT and PVDF components were added as a commercially available pre-dispersed ink mixture (0.75% CNT, 2.0 % PVDF in N-methyl pyrrolidone, NMP). Prior to slurry preparation, the dry slurry components and current collector were heated at 100ºC under vacuum overnight. The active material was ground with carbon black in a mortar and pestle dry, then the CNT-PVDF ink and several drops of NMP were added and mixed to produce a homogeneous paste that was cast onto a copper current collector with a doctor blade. The electrodes were dried under vacuum at 100ºC overnight. Electrodes with 0.7 mm diameter were punched out for electrochemical testing with mass loadings of active material of 1 – 1.5 mg/cm^2. These moderate mass loadings were chosen to

study the intrinsic performance of the active material, as they allow for reproducible electrode performance with minimal optimization of the slurry. High mass loadings, such as those used in most practical devices, lead to rate limitations from electrode composition and distribution of active material that require extensive optimization to overcome. Electrochemical measurements were conducted in stainless-steel 2032 coin cells (MTI) with a stainless-steel conical spring, a 0.5-mm stainless-steel spacer for the anode, a 0.5-mm aluminum spacer for the cathode, and a glass microfiber separator (Whatman). The electrolyte was 1 M $LiPF_6$ in 1:1 ethylene carbonate (EC): dimethyl carbonate (DMC), with ~50 uL of electrolyte used per cell. All cycling experiments were performed between 1.0 V and 3.0 V *vs.* Li/Li^+ on a VMP3 potentiostat/galvanostat (Bio-Logic). For testing purposes, electrodes were studied in a half cell configuration versus a Li metal anode. When calculating C-rates, the theoretical capacity used was 200 mAh/g for T-Nb_2O_5 or 150 mAh/g for NWO, based on the 1 e^- Li^+ insertion reactions.

For the *ex situ* magnetic measurements, pure pellet electrodes with only T-Nb_2O_5 or NWO were prepared. Approximately 100 mg of material were ground in a mortar and pestle and pressed into circular free-standing pellets at 6000 psi. The pellet electrodes were cycled in stainless-steel Swagelok cells under the same conditions as above, but cycled with much lower current densities (~0.2 mA/g) to ensure uniform lithiation of the entire pellet electrode. After the desired state-of-charge was reached, the cells were opened inside of an argon glovebox to extract the electrodes, which were washed multiple times in DMC and dried under vacuum without exposure to air.

Magnetic Susceptibility

The magnetic susceptibility of lithiated T-Nb_2O_5 and NWO was measured with a Quantum Design Magnetic Property Measurement System 3 (MPMS) superconducting quantum interference device (SQUID) magnetometer. Samples of ~30 mg of pure powder were packed into

a polypropylene capsule in an argon glovebox (<1 ppm O_2, H_2O). Magnetization vs. field (M-H) hysteresis loops were measured from 300 to 2 K. Magnetic susceptibility was extracted from each loop using the slope.

6.1 References

[1] Lopes, J. A. P.; Soares, F. J.; & Almeida, P. M. R. Integration of electric vehicles in the electric power system. *Proc. IEEE*, **2010**, *99*, 168-183

[2] Gür, T.M. Review of electrical energy storage technologies, materials and systems: challenges and prospects for large-scale grid storage. *Energy Environ. Sci.* **2018**, *11*(10), 2696–2767.

[3] Frith, J.T.; Lacey, M.J.; Ulissi, U. A non-academic perspective on the future of lithium-based batteries. *Nat. Commun.* **2023**, *14*(1), 420.

[4] Li, M.; Lu, J.; Chen, Z.; Amine, K. 30 years of lithium-ion batteries. *Adv. Mater.* **2018**, *30* (33), 1800561.

[5] Choi, C.; Ashby, D.S.; Butts, D.M.; DeBlock, R.H.; Wei, Q.; Lau, J.; Dunn, B. Achieving high energy density and high power density with pseudocapacitive materials. *Nat. Rev. Mater.* **2020**, *5*(1), 5–19.

[6] Fleischmann, S.; Mitchell, J.B.; Wang, R.; Zhan, C.; Jiang, D.E.; Presser, V.; Augustyn, V. Pseudocapacitance: From Fundamental Understanding to High Power Energy Storage Materials. *Chem. Rev.* **2020**, *120*(14), 6738–6782.

[7] Chung, S.Y.; Bloking, J.T.; Chiang, Y.M. Electronically conductive phospho-olivines as lithium storage electrodes. *Nat. Mater.* **2002**, 1(2), 123–128.

[8] Van Der Ven, A.; Bhattacharya, J.; Belak, A. A. Understanding Li Diffusion in Li-Intercalation Compounds. *Acc. Chem. Res.* **2013**, *46*, 1216–1225.

[9] Kang, B.; Ceder, G. Battery materials for ultrafast charging and discharging. *Nature* **2009**, *458*, 190–193.

[10] Cook, J. B.; Lin, T. C.; Kim, H.-S.; Siordia, A.; Dunn, B. S.; Tolbert, S. H. Suppression of Electrochemically Driven Phase Transitions in Nanostructured MoS_2 Pseudocapacitors Probed Using Operando X-ray Diffraction. *ACS Nano*, **2019**, *13*, 1223–1231.

[11] Jain, R.; Lakhnot, A.S.; Bhimani, K.; Sharma, S.; Mahajani, V.; Panchal, R.A.; Kamble, M.; Han, F.; Wang, C.; Koratkar, N. Nanostructuring versus microstructuring in battery electrodes. *Nat. Rev. Mater.* **2022**, *7*(9), 736–746.

[12] Sun, H.; Mei, L.; Liang, J.; Zhao, Z.; Lee, C.; Fei, H.; Ding, M.; Lau, J.; Li, M.; Wang, C.; Xu, X. Three-dimensional holey-graphene/niobia composite architectures for ultrahigh-rate energy storage. *Science*, **2017**, *356* (6338), 599–604

[13] Cook, J. B.; Kim, H. S.; Lin, T. C.; Lai, C. H.; Dunn, B.; Tolbert, S. H. Pseudocapacitive Charge Storage in Thick Composite MoS_2 Nanocrystal-Based Electrodes. *Adv. Energy Mater.* **2017**, *7*, 1601283.

[14] Wagemaker, M.; Mulder, F.M. Properties and promises of nanosized insertion materials for Li-ion batteries. *Acc. Chem. Res*. **2013**, *46*(5), 1206–1215.

[15] Guo, B.; Yu, X.; Sun, X.G.; Chi, M.; Qiao, Z.A.; Liu, J.; Hu, Y.S.; Yang, X.Q.; Goodenough, J.B.; Dai, S. A long-life lithium-ion battery with a highly porous $TiNb_2O_7$ anode for large-scale electrical energy storage. *Energy Environ. Sci.* **2014**, 7(7), 2220–2226.

[16] Wu, J.; Zhang, X.; Ju, Z.; Wang, L.; Hui, Z.; Mayilvahanan, K.; Takeuchi, K. J.; Marschilok, A. C.; West, A. C.; Takeuchi, E. S.; Yu, G. From Fundamental Understanding to Engineering Design of High-Performance Thick Electrodes for Scalable Energy-Storage Systems. *Adv. Mater.* **2021**, *33* (26), 2101275.

[17] Griffith, K. J.; Wiaderek, K. M.; Cibin, G.; Marbella, L. E.; Grey, C. P. Niobium tungsten oxides for high-rate lithium-ion energy storage. *Nature*, **2018**, *559*, 556–563.

[18] Cava, R. J.; Murphy, D. W.; Zahurak, S. M. Lithium Insertion in Wadsley-Roth Phases Based on Niobium Oxide. *J. Electrochem. Soc.* **1983**, *130* (12), 2345–2351.

[19] Wyckoff, K.E.; Robertson, D.D.; Preefer, M.B.; Teicher, S.M.; Bienz, J.; Kautzsch, L.; Mates, T.E.; Cooley, J.A.; Tolbert, S.H.; Seshadri, R.. High-Capacity Li^+ Storage through Multielectron Redox in the Fast-Charging Wadsley–Roth Phase $(W_{0.2}V0_{.8})_3O_7$. *Chem. Mater.* **2020**, *32* (21), 9415-9424.

[20] Koçer, C. P.; Griffith, K. J.; Grey, C. P.; Morris, A. J. Cation Disorder and Lithium Insertion Mechanism of Wadsley–Roth Crystallographic Shear Phases from First Principles. *J. Am. Chem. Soc.* **2019**, *141*, 15121-15134.

[21] Zhu, X.; Xu, J.; Luo, Y.; Fu, Q.; Liang, G.; Luo, L.; Chen, Y.; Lin, C.; Zhao, X.S. $MoNb_{12}O_{33}$ as a New Anode Material for High-Capacity, Safe, Rapid and Durable Li^+ Storage: Structural Characteristics, Electrochemical Properties and Working Mechanisms. *J. Mater. Chem. A* **2019**, *7*, 6522-6532.

[22] Voskanyan, A. A.; Navrotsky, A. Shear Pleasure: The Structure, Formation, and Thermodynamics of Crystallographic Shear Phases. *Ann. Rev. Mater. Sci.* **2021**, *51*, 521–540.

[23] Lawrence, E. A.; Davenport, M. A.; Devi, R.; Cai, Z.; Avdeev, M.; Belnap, J. R.; Liu, J.; Alnaser, H.; Ho, A.; Sparks, T. D.; Sai Gautam, G.; Allred, J. M.; Ji, H. Reversible Electrochemical Lithium Cycling in a Vanadium(IV)- and Niobium(V)-Based Wadsley-Roth Phase. *Chem. Mater.* **2023**, *35* (9), 3470–3483.

[24] Griffith, K.J.; Seymour, I.D.; Hope, M.A.; Butala, M.M.; Lamontagne, L.K.; Preefer, M.B.; Koçer, C.P.; Henkelman, G.; Morris, A.J.; Cliffe, M.J.; Dutton, S.E.; Grey, C.P. Ionic and Electronic Conduction in $TiNb_2O_7$. *J. Am. Chem. Soc.* **2019**, *141* (42), 16706–16725.

[25] Voskanyan, A. A.; Abramchuk, M.; Navrotsky, A. Entropy Stabilization of TiO_2-Nb_2O_5 Wadsley-Roth Shear Phases and Their Prospects for Lithium-Ion Battery Anode Materials. *Chem. Mater.* **2020**, *32* (12), 5301–5308.

[26] Preefer, M.B.; Saber, M.; Wei, Q.; Bashian, N.H.; Bocarsly, J.D.; Zhang, W.; Lee, G.; Milam-Guerrero, J.; Howard, E.S.; Vincent, R.C.; Melot, B.C.; Van der Ven, A.; Seshadri, R.; Dunn, B. Multielectron Redox and Insulator-to-Metal Transition upon Lithium Insertion in the Fast-Charging, Wadsley-Roth Phase PNb_9O_{25}. *Chem. Mater.* **2020**, *32* (11), 4553–4563.

[27] Saber, M.; Preefer, M. B.; Kolli, S. K.; Zhang, W.; Laurita, G.; Dunn, B.; Seshadri, R.; Van Der Ven, A. Role of Electronic Structure in Li Ordering and Chemical Strain in the Fast Charging Wadsley-Roth Phase PNb_9O_{25}. *Chem. Mater.* **2021**, *33* (19), 7755–7766.

[28] Augustyn, V.; Come, J.; Lowe, M. a; Kim, J. W.; Taberna, P.-L.; Tolbert, S. H.; Abruña, H. D.; Simon, P.; Dunn, B. High-Rate Electrochemical Energy Storage through Li^+ Intercalation Pseudocapacitance. *Nat. Mater.* **2013**, *12* (6), 518–522.

[29] Griffith, K. J.; Forse, A. C.; Griffin, J. M.; Grey, C. P.. High-Rate Intercalation Without Nanostructuring in metastable Nb_2O_5 bronze phases. *J. Am. Chem. Soc.* **2016**, *138*(28), 8888-8899.

[30] Koçer, C. P.; Griffith, K. J.; Grey, C. P.; Morris, A. J. Lithium Diffusion in Niobium Tungsten Oxide Shear Structures. *Chem. Mater.* **2020**, *32* (9), 3980–3989.

[31] Haetge, J.; Hartmann, P.; Brezesinski, K.; Janek, J.; Brezesinski, T. Ordered Large-Pore Mesoporous $Li_4Ti_5O_{12}$ Spinel Thin Film Electrodes with Nanocrystalline Framework for High Rate Rechargeable Lithium Batteries: Relationships among Charge Storage, Electrical Conductivity, and Nanoscale Structure. *Chem. Mater.* **2011**, *23* (19), 4384–4393.

[32] Saadoune, I.; Profile, S.; Ménétrier, M.; Levasseur, S.; Delmas, C. The Insulator-Metal Transition upon Lithium Deintercalation from $LiCoO_2$: Electronic Properties and 7Li NMR Study. *J. Mater. Chem.* **1999**. *9* (5) 1135-1140.

[33] Shibuya, M.; Nishina, T.; Matsue, T.; Uchida, I. In Situ Conductivity Measurements of $LiCoO_2$ Film during Lithium Insertion/Extraction by Using Interdigitated Microarray Electrodes. *J. Electrochem. Soc.* **1996**, *143* (10), 3157–3160.

[34] Nishizawa, M.; Ise, T.; Koshika, H.; Itoh, T.; Uchida, I. Electrochemical In-Situ Conductivity Measurements for Thin Film of $Li_{(1-x)}Mn_2O_4$ Spinel. *Chem. Mater.* **2000**, *12* (5), 1367–1371.

[35] Sauvage, F.; Tarascon, J. M.; Baudrin, E. In Situ Measurements of Li Ion Battery Electrode Material Conductivity: Application to Li_xCoO_2 and Conversion Reactions. *J. Phys. Chem. C* **2007**, *111* (26), 9624–9630.

[36] Krumeich, F. The Complex Crystal Chemistry of Niobium Tungsten Oxides. *Chem. Mater.* **2022**, *34* (3), 911–934.

[37] Chen, D.; Wang, J. H.; Chou, T. F.; Zhao, B.; El-Sayed, M. A.; Liu, M. Unraveling the Nature of Anomalously Fast Energy Storage in T-Nb_2O_5. *J. Am. Chem. Soc.* **2017**, *139* (20), 7071–7081.

[38] Brezesinski, K.; Wang, J.; Haetge, J.; Reitz, C.; Steinmueller, S. O.; Tolbert, S. H.; Smarsly, B. M.; Dunn, B.; Brezesinski, T. Pseudocapacitive Contributions to Charge Storage in Highly Ordered Mesoporous Group v Transition Metal Oxides with Iso-Oriented Layered Nanocrystalline Domains. *J. Am. Chem. Soc.* **2010**, *132* (20), 6982–6990.

[39] Wang, X.; Li, G.; Chen, Z.; Lu, Y.; Ma, X.; Augustyn, V.; Dunn, B.; Wang, G.; Wang, X.; Li, G.; Chen, Z.; Augustyn, V.; Ma, X.; Wang, G.; Dunn, B.; Lu, Y. High-Performance Supercapacitors Based on Nanocomposites of Nb_2O_5 Nanocrystals and Carbon Nanotubes. *Adv. Energy Mater.* **2011**, *1* (6), 1089–1093.

[40] Kim, J. W.; Augustyn, V.; Dunn, B. The Effect of Crystallinity on the Rapid Pseudocapacitive Response of Nb_2O_5. *Adv. Energy Mater.* **2012**, *2* (1), 141–148.

[41] Come, J.; Augustyn, V.; Kim, J. W.; Rozier, P.; Taberna, P.-L.; Gogotsi, P.; Long, J. W.; Dunn, B.; Simon, P. Electrochemical Kinetics of Nanostructured Nb_2O_5 Electrodes . *J. Electrochem. Soc.* **2014**, *161* (5), A718–A725.

[42] Kong, L.; Zhang, C.; Wang, J.; Qiao, W.; Ling, L.; Long, D. Free-Standing T-Nb_2O_5/Graphene Composite Papers with Ultrahigh Gravimetric/Volumetric Capacitance for Li-Ion Intercalation Pseudocapacitor. *ACS Nano* **2015**, *9* (11), 11200–11208.

[43] Lai, C. H.; Ashby, D.; Moz, M.; Gogotsi, Y.; Pilon, L.; Dunn, B. Designing Pseudocapacitance for Nb2O5/Carbide-Derived Carbon Electrodes and Hybrid Devices. *Langmuir* **2017**, *33* (37), 9407–9415.

[44] van den Bergh, W.; Lokupitiya, H. N.; Vest, N. A.; Reid, B.; Guldin, S.; Stefik, M. Nanostructure Dependence of T-Nb_2O_5 Intercalation Pseudocapacitance Probed Using Tunable Isomorphic Architectures. *Adv. Funct. Mater.* **2021**, *31* (1), 2007826.

[45] Cava, R. J.; Batlogg, B.; Krajewski, J. J.; Poulsen, H. F.; Gamrnel, P.; Peck, W. F.; Rupp, L. W. Electrical and Magnetic Properties of $Nb_2O_{5-\delta}$ Crystallographic Shear Structures. *Phys. Rev. B* **1991**, *44*.

[46] Han, H.; Jacquet, Q.; Jiang, Z.; Sayed, F. N.; Jeon, J. C.; Sharma, A.; Schankler, A. M.; Kakekhani, A.; Meyerheim, H. L.; Park, J.; Nam, S. Y.; Griffith, K. J.; Simonelli, L.; Rappe, A. M.; Grey, C. P.; Parkin, S. S. P. Li Iontronics in Single-Crystalline T-Nb_2O_5 Thin Films with Vertical Ionic Transport Channels. *Nat. Mater. 2023* **2023**, 1–8.

[47] Koçer, C. P.; Griffith, K. J.; Grey, C. P.; Morris, A. J. First-Principles Study of Localized and Delocalized Electronic States in Crystallographic Shear Phases of Niobium Oxide. *Phys. Rev. B* **2019**, *99* (7), 075151.

[48] Mei, B. A.; Lau, J.; Lin, T.; Tolbert, S. H.; Dunn, B. S.; Pilon, L. Physical Interpretations of Electrochemical Impedance Spectroscopy of Redox Active Electrodes for Electrical Energy Storage. *J. Phys. Chem. C* **2018**, *122* (43), 24499–24511.

[49] Vivier, V.; Orazem, M. E. Impedance Analysis of Electrochemical Systems. *Chem. Rev.* **2022**, *122* (12), 11131–11168.

[50] Salinas, G.; Frontana-Uribe, B. A. Analysis of Conjugated Polymers Conductivity by in situ Electrochemical-Conductance Method. *ChemElectroChem* **2019**, *6* (16), 4105–4117.

[51] Das, P.; Zayat, B.; Wei, Q.; Salamat, C. Z.; Magdău, I. B.; Elizalde-Segovia, R.; Rawlings, D.; Lee, D.; Pace, G.; Irshad, A.; Ye, L.; Schmitt, A.; Segalman, R. A.; Miller, T. F.; Tolbert, S. H.; Dunn, B. S.; Narayan, S. R.; Thompson, B. C. Dihexyl-Substituted Poly(3,4-Propylenedioxythiophene) as a Dual Ionic and Electronic Conductive Cathode Binder for Lithium-Ion Batteries. *Chem. Mater.* **2020**, *32* (21), 9176–9189.

[52] Zayat, B.; Das, P.; Thompson, B. C.; Narayan, S. R. In Situ Measurement of Ionic and Electronic Conductivities of Conductive Polymers as a Function of Electrochemical Doping in Battery Electrolytes. *J. Phys. Chem. C* **2021**, *125* (14), 7533–7541.

[53] Das, P.; Elizalde-Segovia, R.; Zayat, B.; Salamat, C. Z.; Pace, G.; Zhai, K.; Vincent, R. C.; Dunn, B. S.; Segalman, R. A.; Tolbert, S. H.; Narayan, S. R.; Thompson, B. C. Enhancing the Ionic Conductivity of Poly(3,4-Propylenedioxythiophenes) with Oligoether Side Chains for Use as Conductive Cathode Binders in Lithium-Ion Batteries. *Chem. Mater.* **2022**, *34* (6), 2672–2686.

[54] Huggins, R. A. Simple Method to Determine Electronic Conductivity and Ionic Components of the Conductors in Mixed a Review. In *Ionics*; 2002; Vol. 8, pp 300–313.

[55] Jamnik, J.; Maier, J. Treatment of the Impedance of Mixed Conductors Equivalent Circuit Model and Explicit Approximate Solutions. *J. Electrochem. Soc.* **1999**, *146* (11), 4183–4

[56] Mugiraneza, S.; Hallas, A.M. Tutorial: a beginner's guide to interpreting magnetic susceptibility data with the Curie-Weiss law. *Commun. Phys.* **2022**, *5* (1), 95.

CHAPTER 7

High-Capacity Li^+ Storage through Multielectron Redox in the Fast-Charging Wadsley-Roth Phase $(W_{0.2}V_{0.8})_3O_7$

This chapter was reprinted from Wyckoff, K.E.; Robertson, D.D.; Preefer, M.B.; Teicher, S.M.; Bienz, J.; Kautzsch, L.; Mates, T.E.; Cooley, J.A.; Tolbert, S.H.; Seshadri, R. High-Capacity Li^+ Storage through Multielectron Redox in the Fast-Charging Wadsley–Roth Phase $(W_{0.2}V0_{.8})_3O_7$. *Chem. Mater.* **2020**, *32* (21), 9415-9424. Copyright 2020 American Chemical Society. A reprint of the supporting information is given in Appendix D.

High-Capacity Li^+ Storage through Multielectron Redox in the Fast-Charging Wadsley–Roth Phase $(W_{0.2}V_{0.8})_3O_7$

Kira E. Wyckoff,[#] Daniel D. Robertson,[#] Molleigh B. Preefer, Samuel M. L. Teicher, Jadon Bienz, Linus Kautzsch, Thomas E. Mates, Joya A. Cooley, Sarah H. Tolbert,* and Ram Seshadri*

Cite This: *Chem. Mater.* 2020, 32, 9415–9424

ABSTRACT: The Wadsley–Roth phase $(W_{0.2}V_{0.8})_3O_7$, crystallizing in a structure obtained through crystallographic shear of $3 \times 3 \times \infty$ ReO_3 blocks, is a somewhat rare exemplar for this class of compounds in that it contains a relatively small amount of 4d and/or 5d transition elements. Here, we demonstrate that it functions as a high-rate, high-capacity material for lithium-ion batteries. Electrochemical insertion and deinsertion in micron-sized particles made by conventional solid-state preparation and in sub-100 nm particles made by combining sol–gel precursors with freeze-drying methods indicate good rate capabilities. The materials display high capacity—close to 300 mA h g^{-1} at low rates—corresponding to the insertion of up to 1.3 Li per transition metal at voltages above 1 V. Li insertion is associated with multielectron redox for both V and W observed from ex situ X-ray photoelectron spectroscopy. The replacement of 4d and 5d elements with vanadium results in a higher voltage than seen in other, usually niobium-containing shear-structured electrode materials, and points to new opportunities for tuning voltage, electrical conductivity, and capacity in compounds in this structural class.

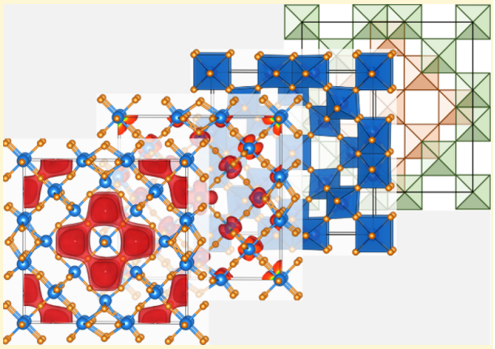

INTRODUCTION

The ability to tune the chemistry of electrode materials across multiple length scales provides opportunities for developing electrodes for a variety of Li-ion battery applications, ranging from portable electronics, to electric vehicles, and grid-scale storage.[1,2] Research on Li-ion battery technology has particularly focused on improving both the energy density and rate capabilities of electrode materials.[3] Materials capable of being charged in the course of minutes as opposed to hours could have important ramifications across a broad range of applications. For many currently used and studied materials, fast charging is hindered because of intrinsic materials properties often associated with the crystal structure, namely, the ease of ion and electron transport, structural and electronic phase transitions, and so forth. A common work-around to address limited ion mobility has been to optimize the particle morphology through meso- and nanostructuring,[4,5] with the goal of decreasing Li-ion diffusion distances within the particle, sometimes with concomitant suppression of phase transitions.[6−9] Carbon additives and carbon-coating has also been frequently employed to overcome inherently poor electron transport.[10,11] These impressive feats of engineering, exemplified by materials such as $LiFePO_4$,[10,11] have allowed for broad adoption of Li-ion batteries in many applications, but the search for new materials continues.

Anode materials with voltages close to 0 V versus Li/Li^+, while providing the greatest energy density, are contraindicated for high-rate applications. Graphite for example, effectively transports Li^+ ions and electrons but is associated with detrimental electrolyte reactions,[12] dendrite formation that leads to thermal runaway,[13−15] and volume expansion that leads to particle fracture.[16] Highly engineered (i.e., nanoscaled and carbon-coated) $Li_4Ti_5O_{12}$ with a higher average voltage of 1.5 V has good capacity retention at high rates.[17] The higher voltage minimizes dendrite growth but the costs associated with elaborate electrode preparation decreases widespread adoption.[18]

The focus of this work are on materials that possess crystallographic shear. These are structures that derive from anion vacancies that are accommodated through shear of the basic polyhedral structural motifs. First described by Magnéli,[19] the process of shear results in greater sharing of anions between polyhedra. A class of materials that possess such crystallographic shear are the so-called Wadsley–Roth

Received: August 29, 2020
Revised: October 13, 2020
Published: October 29, 2020

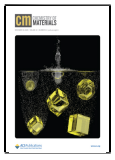

family of compounds, which have shear structures described as blocks of corner-connected MO_3 octahedra. These generally comprise of oxides of early transition metals such as Ti, V, Nb, Mo, and W.[20−23] While the earliest reports on these structures were based on electron diffraction and model-building, neutron diffraction has revealed the most intricate structural details.[24,25]

Early studies on Li insertion in this class of materials showed that a broad array of compositions could be used as electrodes.[26−30] The utility of $TiNb_2O_7$ was rediscovered by Goodenough and co-workers.[31,32] Recent studies have demonstrated that large micron-sized particles of the shear structured phases $Nb_{12}WO_{33}$,[33] H−Nb_2O_5,[34,35] $TiNb_{24}O_{62}$,[36] $Nb_{16}W_5O_{55}$,[37] $TiNb_2O_7$,[38] $MoNb_{12}O_{33}$,[39] and PNb_9O_{25},[40] are all capable of impressive lithium storage capacity at high cycling rates.

From a design perspective, compounds displaying features of crystallographic shear are exciting because they contain specific structural motifs that allow for excellent Li-ion diffusion and the potential for electron delocalization. The compounds typically possess some combination of edge- and corner-connected octahedra. How these combine in the structure, along with the specific chemical composition, critically impacts the electrochemical performance. The edge-sharing octahedra allow for electron delocalization pathways while also providing structural integrity.[41] This integrity protects against octahedral tilting and rotation seen in pure ReO_3 structures (all corner- and no edge-sharing) that are detrimental to reversible cycling.[26,29,42] However, the corner connectivity deriving from the ReO_3 blocks also plays an essential role in creating channels that facilitate ion insertion and transport. Evidence from nuclear magnetic resonance (NMR), magnetism, and conductivity measurements confirms that these structural features contribute to low activation barriers for lithium diffusion.[35,36,38,40,43] These materials are additionally compelling because of their high capacities. This is due in large part to the fact that these materials comprise of early transition metals capable of multielectron redox, where it is possible to insert more than 1 Li per transition metal.

While many Wadsley−Roth phases contain Nb, V-containing phases appear to have been much less studied, despite the fact that vanadium is more earth-abundant and more geographically and industrially widespread, compared to niobium.[44] Here, we characterize the electrochemical insertion properties of the Wadsley−Roth phase $(W_{0.2}V_{0.8})_3O_7$, whose crystal structure is shown in Figure 1. First reported by Galy in 1972, the crystallography of this $3 \times 3 \times \infty$ block structure was determined from single-crystal studies.[45] From the viewpoint of composition, this is an interesting compound because the closest vanadium phase to V_3O_7 is formed under high-pressure with a distinctly different structure,[46] and a W_3O_7 phase does not appear to have been reported. There is a high likelihood that $(W_{0.2}V_{0.8})_3O_7$ is stabilized by configurational entropy, as suggested by Navrotsky and co-workers for related phases.[47]

Early studies examined related compounds as electrodes,[27,28,30] but not for high-rate performance. Here, using both small particles prepared through a solution freeze-drying (FD) method, and conventionally prepared larger particles, we develop an understanding of the intrinsic capabilities of the materials for Li storage. Reversible and stable cycling at rates up to 20 C are demonstrated. The relatively minor perturbation of the structure arising from Li insertion is confirmed with operando X-ray diffraction. Ex situ X-ray photoelectron spectroscopy (XPS) studies show the reduction

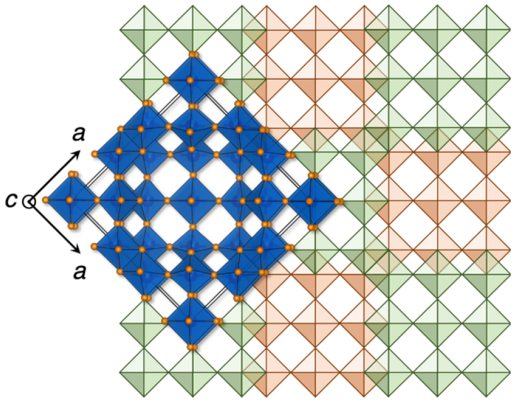

Figure 1. Crystal structure of $(W_{0.2}V_{0.8})_3O_7$ (space group is I_4/mmm, no. 139) comprising of $3 \times 3 \times \infty$ blocks of corner-connected (W, V)O_3 octahedra, offset and connected through edge-sharing (shear planes). The real structure is overlaid onto a schematic that depicts the arrangement of the 3×3 blocks. The two different colors employed for the blocks of octahedra are used here to indicate that they are offset along the *c* direction.

of the transition metals, respectively, to V^{3+} and W^{4+}, explaining the relatively high capacity. Despite the competitive capacity retention in bulk particles of $(W_{0.2}V_{0.8})_3O_7$, there are kinetic advantages displayed by the smaller particles made by the solution FD route, particularly at intermediate rates.

The materials studied here differentiate themselves from other Wadsley−Roth phases in that they are not fully oxidized even in the pristine, delithiated state, which contributes to some electronic conductivity prior to lithium insertion. Additionally, the compound stores charge at voltages higher than found in related structures and provides the basis for exploration of voltage tuning within the family of crystallographic shear structures.

EXPERIMENTAL SECTION

The title material was conventionally prepared (labeled conv.) through solid-state methods. Stoichiometric quantities of WO_3 (Sigma-Aldrich, 99.9%), V_2O_5 (Materion, 99.9%), and V_2O_3 (Strem Chemicals, 95%) were ground together and pressed into pellets weighing between 250 and 300 mg. The pellets were then placed in a vitreous silica tube and sealed with a methane−oxygen torch, evacuated three times, and subsequently filled with 40 mm Hg partial pressure of Ar. The tube was annealed in a furnace at 700 °C for 24 h followed by a water quench to room temperature. Small particles were prepared by FD (henceforth labeled FD) a stoichiometric solution of precursors and subsequently calcining under flowing Ar. In a typical preparation, 200 mg of NH_4VO_3 and 105 mg of $(NH_4)_{10}(H_2W_{12}O_{42})$ were added to 5 cm^3 of distilled water and heated until the solids were fully dissolved. The resulting yellow solution was added dropwise to liquid N_2. After the removal of the remaining liquid N_2, the frozen solution was subjected to vacuum (<100 mTorr) on a Schlenk line for 10−20 h to remove water. Once dry, the powder was calcined in flowing Ar in a tube furnace at 700 °C for 1 h (30 °C per min ramp rate). The furnace was then cooled to room temperature. The obtained particles were stored under inert atmosphere to prevent unwanted surface oxidation.

Both materials were cast on copper foil in an 80:10:10 (wt %) ratio of active material:conductive carbons:polyvinylidene fluoride. Cycling of the conv. material employed carbon black (TIMCAL Super P) while for the FD material, a 50:50 mixture of carbon nanotubes and carbon nanofibers were used. The active material was ball-milled for 30 min in a 2 cm^3 canister with the appropriate amount of carbon-based additives. This mixture was combined with poly(vinylidene

difluoride) dissolved in NMP to form a slurry that was mixed in a FlackTek speed mixer at 2000 rpm for 30 min. A 120 μm doctor blade was used to cast the material onto copper foil, and this film was dried at 110 °C under vacuum for 2 h. The electrodes were punched as 10 mm diameter disks with a loading of 1−2 mg cm^{-2}.

All electrochemical cells were fabricated in an Ar-filled glove box. Unless noted otherwise, Swagelok cells were employed with 1 M $LiPF_6$ in EC/DMC 50/50 v/v (Sigma-Aldrich) with a polished Li foil counter electrode and a glass fiber separator (Whatman GF/D). Cells were discharged to 1 V and charged to 3.2 V. All electrochemical experiments were performed using BioLogic potentiostats.

The compound $(W_{0.2}V_{0.8})_3O_7$ can be considered to comprise 0.6 WO_3 + 1.6 VO_2 + 0.8 $VO_{2.5}$. W can be reduced to the 4$^+$ state and V to the 3$^+$ state (as we shall also demonstrate presently), so on this basis, 4.4 electrons (along with the corresponding Li^+ ions) can in principle be incorporated. However, following the usual convention for this class of materials, C-rates were calculated based off the reduction of one electron per redox−active transition metal. In this case, three Li were assumed to insert into the crystal structure for calculating C rates, for example, C/5 = 3 Q/5 = 233 mA h g^{-1}/5 h = 46.6 mA g^{-1}, where Q is the charge.

Electrochemical impedance spectroscopy was carried out on a BioLogic VSP potentiostat/galvanostat. Impedance measurements were performed on two-electrode coin cells between 900 kHz and 100 mHz using a 10 mV input. Impedance spectra were collected at every 0.2 V versus Li/Li$^+$ between +1.0 and +3.2 V versus Li/Li$^+$ on electrodes that had been previously cycled with galvanostatic rate testing between +1.0 V and +3.5 V versus Li/Li$^+$. A one hour potentiostatic hold was applied before impedance measurements, during which the current dropped below 50 μA/g.

Powder diffraction data to establish sample purity were collected on a Panalytical Empyrean diffractometer with a Cu Kα source (λ = 1.5406 Å). The materials were ground and loaded on a silicon zero diffraction plate. Rietveld refinements to the previously published structure[45] were carried out with TOPAS.[48] VESTA was used for visualization of the crystal structure.[49]

Particle sizes and morphologies were studied using an FEI Apreo C scanning electron microscope. The powder samples were pressed onto double-sided copper tape and sputter-coated with gold for 60 s. Images were collected with a voltage of 15 kV and a current of 0.8 nA.

For operando X-ray diffraction, the electrode mixture was pressed into a 15 mm diameter pellet and placed into a custom electrochemical cell with a Be window. A glass fiber separator (Whatman, GF/D) was soaked in 1 M $LiPF_6$ (Sigma-Aldrich), and the counter electrode was a polished Li metal disc pressed into a stainless steel current collector. The cell was cycled galvanostatically at a rate of C/10 (assuming 3 Li per formula unit) for one complete cycle. X-ray diffraction patterns were collected repeatedly using the Panalytical Empyrean diffractometer referenced above, from 2θ = 13 to 50° over 17 min intervals. The amorphous background (because of the glass fiber separator) and the signal for each scan was separately smoothed and fit using Tikhonov regularization.[50]

Samples for XPS were prepared by discharging/charging the cast electrodes described earlier to the desired voltages in a Swagelok cell. These cells were then disassembled inside of an Ar-filled glove box, the electrodes were removed and washed for 2 h in dimethyl carbonate to remove $LiPF_6$ from the electrolyte, with subsequent centrifuging and drying in the glove box atmosphere overnight. A section of the electrode was cut and the copper foil side of the disk was gently pressed onto the XPS sample holder using double-sided tape. A custom-built, capped XPS holder was used, equipped with a Viton seal and a screw-down lid that could be removed after the sample achieved vacuum in the XPS antechamber. All samples were measured using a Thermo Fisher Escalab Xi$^+$ XPS equipped with a monochromatic Al anode (E = 1486.7 eV). Samples were etched using a cluster gun for 40 s to clean the surface and improve count intensity. Survey scans were measured at 100 eV pass energy, and high-resolution scans were measured in the V 4p, W 4f, and Li 1s regions at 20 eV pass energy. Ex situ spectra were referenced to the F 1s peak from LiF at 685.5 eV and the pristine spectrum was referenced to adventitious carbon at 285 eV.[51−53] CasaXPS was used to fit the data using Shirley backgrounds and GL(30) peak shapes. High resolution scans of V and W were fit using appropriate spin−orbit splitting and peak area ratios.[54]

Density functional theory (DFT)—based electronic structure calculations were performed using the Vienna Ab initio Simulation Project v5.4.4[55−57] employing projector augmented wave potentials[58,59] with energy convergence better than 10^{-6} eV. PAW potentials were selected based on the version 5.2 recommendations. Simulations were found to be well-converged for an energy cutoff of 500 eV and an automatically generated k-mesh with the length−density parameter l = 50 (l = 50 corresponds to 14 × 5 × 5 and 4 × 4 × 13 Γ-centered meshes for the primitive cell and the conventional cell displayed in the text, respectively). PBE[60] and SCAN[61] functionals were employed for calculations on the V_3O_7 model structure. The SCAN functional often provides improvements over PBE accuracy for systems with localized electrons, and previous studies have found improvements with SCAN estimates of magnetic moments specifically for transition metal oxide battery materials.[62] However, in these simulations, for ferromagnetic initialization with and without spin−orbit coupling, we find no stable magnetization in either structure regardless of functional choice. PBE and SCAN densities of states (DOS) and charge densities are visually indistinguishable and only the results obtained with the SCAN functional are reported in the text. The projected density of states was postprocessed using lobster.[63−66] Mapping of the bond valence in the space of the crystal structure was carried out using the script PyAbstantia.[67] All visualization involving crystal structures were carried out using VESTA.[49]

RESULTS AND DISCUSSION

Preparation of the conv. material through the solid state methods described previously results in a jet-black pellet, a dramatic color change from the unreacted starting materials. The black color was maintained upon grinding. The FD resulted in loose powder similarly displaying a black coloration. When handling these materials side by side, the FD was fluffy and light, as opposed to the denser conv. material.

The structures were characterized with powder X-ray diffraction as shown in Figure 2. Refinement statistics for both materials are included in the Supporting Information. After the first report of the $(W_{0.2}V_{0.8})_3O_7$ structure by Galy in 1964, solved from a single crystal, difficulties in the preparation of pure powders of the material have been reported.[27] After extensive optimization, the target crystal structure in the $I4/mmm$ space group could be obtained, containing 9% of 4 × 4 Wadsley block defects. These defects are well-established in the literature and commonly occur where some of the blocks have a different size than the main structure.[68,69] The 4 × 4 block unit cell is presented in the Supporting Information. Because the fundamental structure and chemistry is unchanged with the small inclusion of the block defects, the analyses will not be significantly impacted. Particles obtained from the FD route yielded a single phase corresponding to the 3 × 3 structure as seen in Figure 2b. This phase pure sample was possible for a number of reasons, most notably, mixing stoichiometric solutions of aqueous precursors allows for mixing on the atomic scale, as opposed to mixing on micron-sized length scales associated with reactions between bulk oxide powders. It is additionally important to note that lyophilizing the solution provided a much finer control of the stoichiometry, due in part to the poor solubility of the V precursor. Flash-freezing prevents the precipitation of V that would otherwise occur because of poor solubility in water. Besides agreeing well with the single crystal structure of Galy,[45] XPS survey scans and energy-dispersive X-ray spectroscopy

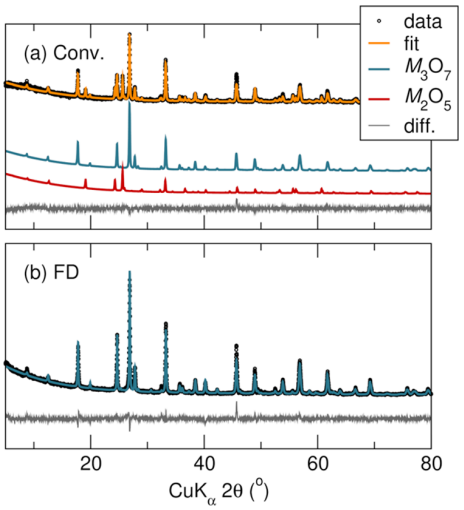

Figure 2. X-ray powder diffraction data for (a) conventionally prepared material (labeled conv.) and (b) material prepared through the solution FD route (labeled FD), with the corresponding Rietveld fits to the appropriate crystal structure(s). The material made through the conventional route was refined to be 91% of the target 3 × 3 block structure with the general formula M_3O_7 and 9% being the 4 × 4 block structure compound with the M_2O_5 formula in the same space group. The FD sample in (b) is the single phase of the target 3 × 3 block structure. Refinement statistics can be found in the Supporting Information.

measurements (figures presented in the Supporting Information) showed very close agreement of the measured V/W ratio to the expected ratio of 4:1.

Because solution-based methods provide diffusion pathways on the atomic scale, the FD preparation method allows for much shorter heating times compared to the conv. preparation. Short calcination times equate to smaller particles seen in Figure 3 where scanning electron microscopy reveals the conv. particles to have a short rod-like morphology on the order of 1−2 μm in the shortest direction. The inset of Figure 3a shows the resulting jet-black powder upon grinding the pellet. Figure 3b shows how the FD preparation resulted in much smaller, rod-like particles about 100 nm in the shortest direction. A higher magnification of the FD particles is shown in the Supporting Information. The rod-like morphology is consistent with earlier transmission electron microscopy work on these compounds.[68]

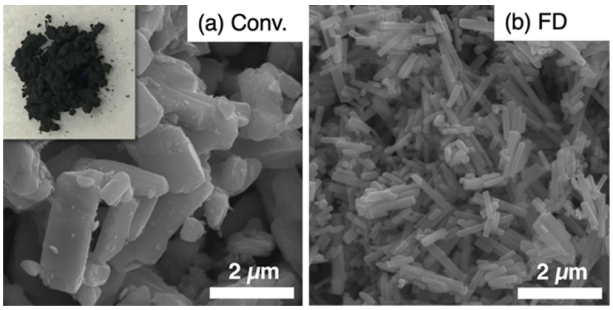

Figure 3. Scanning electron micrographs: (a) conventionally prepared material (conv.) displaying multiple-micron sized particles and (b) material prepared through the FD route, displaying narrow lath-shaped particles up to a few microns in length but under 100 nm in width. A higher magnification image of the FD material can be found in the Supporting Information. The inset in (a) is a photograph of the as-prepared conv. material showing the color associated with a partially filled d band.

Electrochemical lithiation revealed very comparable cycling between the conv. and FD particles, and therefore the majority of the electrochemistry presented here focuses on the FD material. Additional electrochemistry of the conv. material is included in the Supporting Information. At a C/5 rate on first discharge, more than 1 Li/TM is inserted. The impressive capacity retention by both large and small particles points to the crystal structure of $(W_{0.2}V_{0.8})_3O_7$ being conducive to the mobility of lithium.

Cyclic voltammetry was performed at different rates to determine an optimum voltage window for the electrochemistry, in addition to understanding the evolution of the redox peaks at varying sweep rates (Figure 4a). To avoid anomalous capacity contributions from lithium storage in carbon and electrolyte decomposition, a lower cutoff voltage of 1 V was selected.[70] Cyclic voltammetry reveals two major peaks on both reduction and oxidation. There is minimal redox

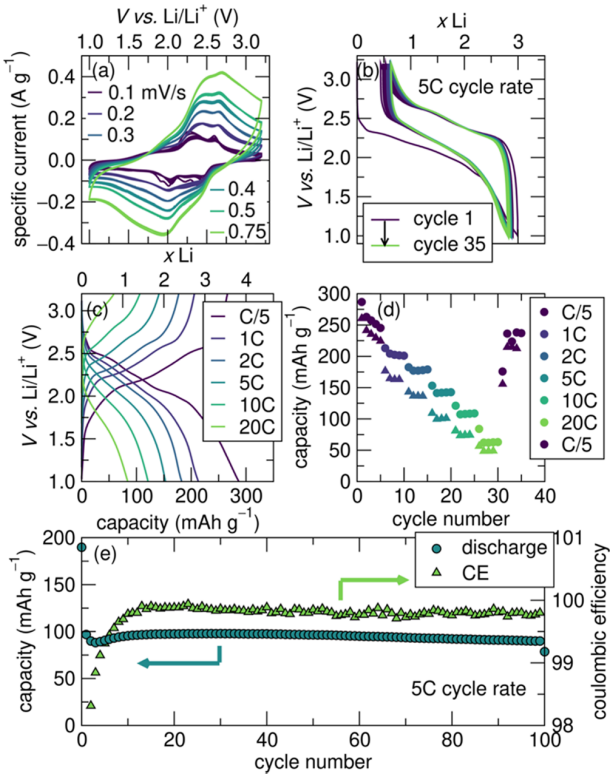

Figure 4. Electrochemistry of the FD $(W_{0.2}V_{0.8})_3O_7$ sample. (a) Variable rate cyclic voltammetry performed at sweep rates from 0.10 to 0.75 mV s^{-1}. (b) Galvanostatic cycling at a 5 C rate shows slight irreversible capacity loss after the first cycle and moderate polarization. (c) Galvanostatic cycling at rates from C/5 to 20 C and its recovery. (d) Summary of rate performance during discharge as a function of cycle number from data depicted in (c). Circles represent the FD material, and triangles representing the conv. material are displayed to compare rate performance between the different sizes of particles. (e) Extended cycling at a 5 C rate. The FD material shows high capacity retention and Coulombic efficiency over 100 cycles.

activity until 2.4 V, where the first peak occurs, followed by an additional redox peak at 2 V. We note that the cyclic voltammetry reveals a significant amount of charge stored at potentials above 2 V, which differentiates this material from other, usually niobium-containing shear structures in the same family that typically store the majority of charge below 2 V.

Galvanostatic cycling at a 5 C rate shown in Figure 4b shows that after the first cycle, features of the discharge/charge curves are highly reproducible, with some capacity loss after the first cycle. The structure of the discharge curve displays three main regions, related to the trends we see in the cyclic voltammetry. At first, there is a steep voltage drop to 2.4 V where a small amount (0.25 Li) of lithium is incorporated into the structure. This leads to a small plateau that extends as a moderately sloping region until 2 V where 2.25 Li is inserted. Both of these redox events are consistent with the voltages observed from the cyclic voltammetry. The slope angles downward at this point until the 1 V cutoff where an additional 0.5 Li is incorporated. We observe moderate polarization between the discharge and charge curves.

The material exhibits impressive rate capabilities, shown in Figure 4c. At the slowest C/5 rate, we observe the three regions of the discharge/charge curves described earlier. As the cycling rate is increased to 20 C, the discharge curve becomes smooth and sloping, and the bulk of the capacity is instead stored below 2 V, as opposed to the slower rates where more charge is stored above 2 V. Figure 4d compares the variable rate galvanostatic cycling of the small particles to the micron-sized particles. Upon returning to slow rates after more rapid cycling, both materials recover most of the capacity observed at the beginning of cycling. The large conv. particles show a comparable charge storage capacity at low and high rates, while the FD material shows the largest kinetic advantage at intermediate rates. As seen in Figure 4e, $(W_{0.2}V_{0.8})_3O_7$ retains stable capacity at a 5 C rate over 100 cycles.

Highly electrically conducting electrodes, or ones that turn into electrical conductors upon lithiation have the advantage of permitting fast cycling. Evidence for the effective electrical conductivity of $(W_{0.2}V_{0.8})_3O_7$ is seen from electrochemical impedance on the full cell. Potentiostatic electrochemical impedance spectroscopy was used to measure the charge transfer resistance of FD $(W_{0.2}V_{0.8})_3O_7$ slurry electrodes at different stages of lithiation (Figure 5). The initial insertion of 0.6 Li^+ per unit cell results in an increase in the charge transfer resistance from about 30 to 130 Ω. Additional lithiation results only in minor changes, and the electrode maintains a moderate charge transfer resistance of 100 to 130 Ω up to insertion of 3 Li^+ per unit cell. These data suggest that the electrical resistivity of $(W_{0.2}V_{0.8})_3O_7$ remains reasonably low across the full range of electrochemical cycling.

In order to understand the nature of Li insertion and deinsertion, a kinetic study was carried out using the established relationship between the peak currents, I_p, in cyclic voltammetry to the voltage scan rate, v, through the power law: $I_p = av^b$, where a and b are constants. The exponent b extracted for each redox peak is then indicative of the underlying diffusion mechanism, with b = 0.5 corresponding to semi-infinite diffusion, and b = 1.0 corresponding to a nondiffusion controlled process.[34,71] $(W_{0.2}V_{0.8})_3O_7$ has two obvious redox peaks on both reduction and oxidation in the range of voltages scanned, as seen in Figure 6a. By extracting the peak currents and fitting to the power law equation above, as demonstrated for the oxidation peaks in Figure 6b and the reduction peaks in

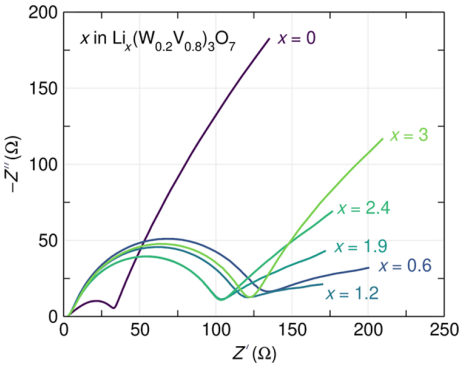

Figure 5. Electrochemical impedance spectra of $(W_{0.2}V_{0.8})_3O_7$ slurry electrodes as a function of Li content. The charge transfer resistance increases upon initial insertion of Li^+ but otherwise remains relatively constant at stoichiometries between x = 0.6 and x = 3 in $Li_x(W_{0.2}V_{0.8})_3O_7$. The spectra were collected on an electrode that had been previously cycled through galvanostatic rate testing so that initial SEI formation does not affect the data.

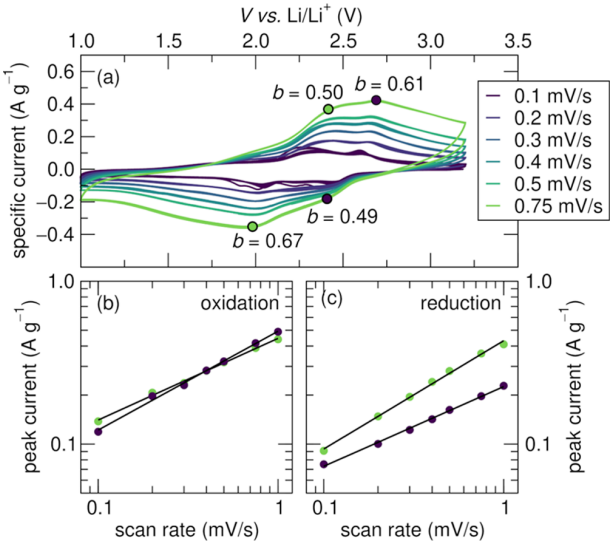

Figure 6. (a) Cyclic voltammetry of the FD material at varying sweep rates, used to obtain the exponent b for the different peaks in the voltammograms (indicated on the figure). (b) Power law fits for each oxidation peak based on the relationship between the scan rate and the current. (c) Corresponding fits for each reduction peak.

Figure 6c, the various values of the exponent b are obtained, which are presented against the respective redox peaks in Figure 6a. The values of b for all redox processes are close to 0.5, which indicates processes limited by bulk semi-infinite diffusion. This strongly points to the electrode materials storing charge though conventional electrochemical Li insertion rather than for example, capacitive storage taking place at the interface.

Operando X-ray powder diffraction of $(W_{0.2}V_{0.8})_3O_7$ performed at a C/10 rate provides insightful information about the evolution of the structure during lithium insertion and extraction. Select diffraction peaks during cycling are displayed in panels in Figure 7. Data collected over the full 2θ range is presented in the Supporting Information, along with a summary of the Rietveld refinements during lithiation. $(W_{0.2}V_{0.8})_3O_7$ appears to display mostly solid solution

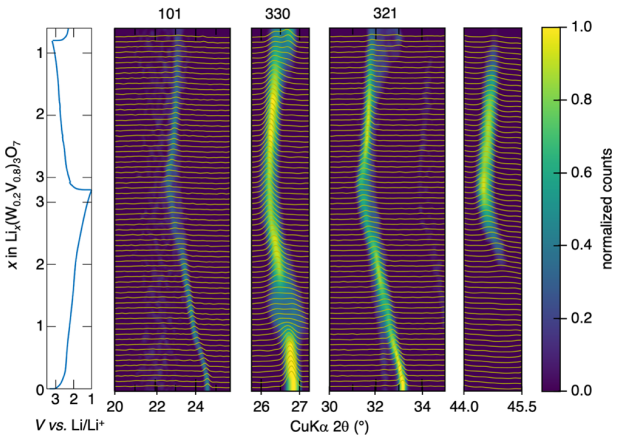

Figure 7. Select regions in the operando X-ray diffraction patterns of the FD $(W_{0.2}V_{0.8})_3O_7$ material during the first galvanostatic cycle at a rate of C/10. The corresponding electrochemistry is shown on the left most panel.

behavior. At the start of Li insertion and up to 1 Li/formula unit, a slight expansion of the unit cell is observed in the presented reflections. After this point, the (330) peak splits in the composition range between 1 Li per formula to 2 Li per formula. The peak splitting is attributed to the existence of a narrow two-phase region that then disappears above 2 Li per formula and then reappears on the following discharge cycle. Shortly after the disappearance of the peak splitting at (330), a new diffraction peak emerges at $2\theta \approx 45°$. Along with the (110), (330), and (321) peaks that are tracked, this new peak similarly indicates unit cell expansion with increasing lithiation, followed by contraction as Li is removed. This feature indicates a phase change that disappears at the end of charge. At full discharge, the *a* and *b* planes expand by only 2.5% while the *c* plane expands by 6.4%. We see an overall volume expansion of 13%, in good agreement with previous chemical insertion on related compound $W_{0.2}V_{2.8}O_7$.[28] The refinements of the lithiated material are summarized in the Supporting Information as is the evolution of the cell parameters and cell volume with lithiation. The observed expansion on the basis of the number of electrons per transition element is relatively large compared with what has been observed in related Nb-rich oxides. This may in part help understanding why the high-rate cycling of $(W_{0.2}V_{0.8})_3O_7$ results in reduced storage capacity compared with compounds in the structurally related the Nb−W−O series.[37]

The structural evolution of this material seen through operando powder diffraction explicitly shows how $(W_{0.2}V_{0.8})_3O_7$ behaves as a battery material, in agreement with the analysis of the exponent *b* in the variable-rate cyclic voltammetry. In the parent ReO_3 structure, Li conduction through the three-dimensional octahedral network is hampered because of the rotation and tilting of the solely corner-connected octahedra. When there are edge-sharing features associated with crystallographic shear, rotation and tilting are prevented and Li transport is not impeded.[42,72] However, the channels in the structure created by octahedral corner-sharing create highways for Li diffusion.

Both constituent transition metals are capable of multi-electron redox, with a maximum theoretical capacity of 342 mA h g^{-1} if 4.4 e^- are inserted (where we assume W^{6+} reduces to W^{4+}, V^{4+} reduces to V^{3+}, and V^{5+} reduces to V^{3+}), based off initial oxidation states of the transition metals according to the equation $(1 - y)V_2O_5 + (1 + y)VO_2 + yWO_3 \rightarrow W_yV_{3-y}O_7$. Although this level of lithiation is not observed experimentally in the voltage ranges employed, the electrochemistry shows that 1.3 Li^+/TM are inserted at a C/5 rate, indicating that at least one of the transition metals is participating in a multielectron redox process. Ex situ XPS allows this to be understood, however is not quantitatively relatable to the bulk oxidation states because of surface sensitivity to oxidation. Figure 8b and 9b display spectra at different states of charge for

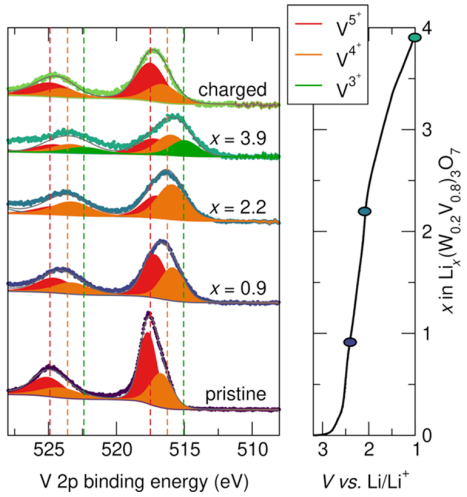

Figure 8. X-ray photoelectron spectra displaying the region of V 2p spin−orbit doublets $2p_{3/2}$ and $2p_{1/2}$ for the conv. material. The total fit and contributions from the different oxidation states are indicated. On the right is the first galvanostatic discharge for Li insertion with the points indicating where the ex situ XPS spectra were acquired.

V and W, respectively, in the conv. material. The pristine material appears to be a combination of $V^{5+}$and V^{4+} but only

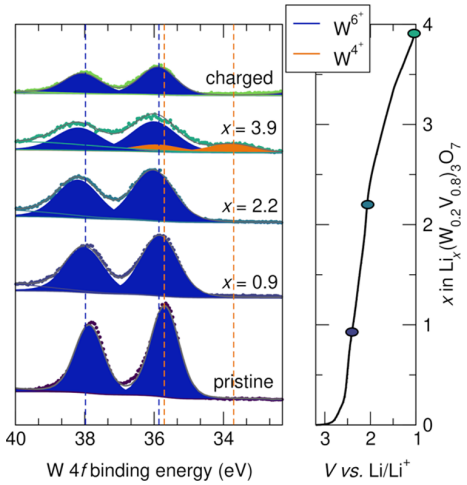

Figure 9. (left) X-ray photoelectron spectra of the W 4f binding energy region displaying the lower-energy W $4f_{7/2}$ and higher binding energy W $4f_{5/2}$ spin−orbit doublets. The gray line on each spectrum shows the total fit that combines the fits from each of the individual oxidation states. (right) First, galvanostatic discharge for Li insertion into conv. $(W_{0.2}V_{0.8})_3O_7$ material. States of charge corresponding to XPS spectra are overlaid on discharge curve.

W^{6+}. As 0.9 Li inserts into the structure, further reduction of the V^{5+} species to V^{4+} is observed. After 2.2 Li inserts, the proportion of V^{5+} to V^{4+} inverts and the majority of V states are V^{4+}. At full discharge with insertion of 3.9 Li, 27% of the V is reduced to V^{3+}. Upon charge, the V oxidizes back to V^{5+} and V^{4+}, but with a slightly higher ratio of V^{4+} than observed in the pristine material. This could be attributed to part of the irreversible capacity loss seen after the first cycle.

In contrast to V, W reduction is quite different. W remains in its W^{6+} oxidation state almost until full discharge where 23% of the W is reduced to W^{4+}. There appears to be no evidence in the XPS signatures for any intermediate W^{5+} state[73] which could suggest a tendency to valence-skip in this structure type. W returns to being fully oxidized after charging. These results confirm multielectron redox in both of the transition metals. As confirmed with XPS, the pristine $(W_{0.2}V_{0.8})_3O_7$ begins in a non-d^0 state due to a fraction of partially reduced V Figure 8b. This is what results in the compound, even prior to lithiation, displaying some evidence of electrical conduction and being black in color.

As discussed above, although the samples were transferred from the glovebox using an air-free sample holder, some surface oxidation can occur which skews measurements toward higher oxidation states. This means that we cannot expect the XPS to quantitatively reflect the bulk oxidation state, but it should still be an excellent indication of the redox states present in the material as a function of the Li content.

Density-functional theory-based electronic structure calculations are employed to provide qualitative understanding these 3 × 3 block structured materials as Li hosts. A complete analysis of the electronic structure of the parent $(W_{0.2}V_{0.8})_3O_7$ compound must account for the combination of electron correlation and disorder (the latter enhancing the former) which is beyond the scope of this work. However, calculations on the isostructural model compound V_3O_7 provide some useful insights. From the DOS displayed for V_3O_7 Figure 10a, we see a combination of oxygen, but primarily transition metal states at the Fermi energy, arising from the formally, 1d electron for every three V, which is also consistent with what is observed in the XPS of the starting $(W_{0.2}V_{0.8})_3O_7$ compound. The as-calculated structure does not stabilize magnetization, even with the DFT simulations performed using the SCAN functional, which usually enhances magnetic localization. The partial charge density in Figure 10b corresponds to a visualization of states in the energy range around E_F. The data suggests that the electron prefers the central metal site on an octahedron that is purely corner-sharing. This has also been noted in other shear phases, for example in $Li_xPNb_9O_{25}$ where the initial doped electrons localize (albeit magnetically in that case) on the central corner-connected octahedron.[40] As stated above, W/V substitution is likely to further hinder electron transport due to disorder and potentially yield some local moment behavior in the magnetism.

Bond valence mapping provides a simple means of estimating ion transport pathways and mechanisms for mobile ions placed arbitrarily within a 3D crystal structure. For each location in the 3D space of the structure, the absolute value of the difference Δv between the valence calculated for the probe ion (here Li^+) at that site and its actual electrostatic valence (1 for Li^+) is mapped.[74,75] It is possible to relate this valence difference Δv to energies of defect formation and defect migration, allowing for rough predictions of the activation energy required for ion transport.[74,75] Isosurfaces for a value of

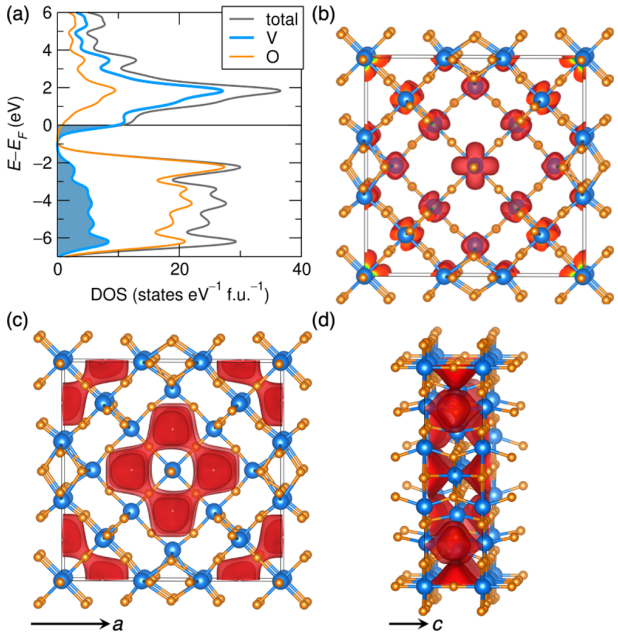

Figure 10. (a) Density of states for model compound V_3O_7 showing contributions from filled vanadium states at the Fermi level. (b) Charge density isosurface level of 0.005 e $Å^{-3}$ depicted within the unit cell of V_3O_7 showing the 1 d electron in the formula prefers the middle of the 3 × 3 block. (c) and (d) View of the bond valence difference map for Li in the space of the structure of V_3O_7 displayed for an isosurface value Δv = 0.1 valence units.

Δv = 0.1 in valence units for the model compound V_3O_7 are displayed in panels (c,d) of Figure 10. This isosurface illustrates probable 3D lithium migration paths in the structure. Empirically, it has been noted that the activation energy in eV is equivalent to approximately 2 × Δv in units,[76] so the displayed isosurface, forming channels down the *c* axis of the structure, indeed suggests a low energy pathway for Li^+ migration. This is consistent with other, prior work showing in related shear structures that ion conduction occurs most rapidly in the center of the blocks in related shear structures.[77] ReO_3 has itself been shown to display an activation energy of migration for Li^+ of 0.1 eV,[78] which is in line with the values presented here. More detailed DFT studies to complement experimental investigations by impedance spectroscopy and NMR are necessary to establish the complete picture.[79]

CONCLUSIONS

Electrochemical insertion studies of $(W_{0.2}V_{0.8})_3O_7$ show that this vanadium-rich shear-structured Wadsley–Roth phase is a promising high-rate electrode material. While both the larger conventionally synthesized particles and smaller particles obtained by solution FD and calcination have capacity retention at up to 20 C, there appears to be a clear advantage at all rates in having smaller particles. Distinct from other, mostly niobium-containing shear structured compounds, the pristine material is a black powder that begins with some finite d state population and therefore could be an intrinsically better electrical conductor than comparable d^0 oxides. Multielectron redox of both W and V lead to high specific capacities, while slight and reversible structural changes allow for capacity retention over one hundred cycles. This compound stores more charge at higher voltages than most other reported

Wadsley–Roth compounds and points to promising directions for tuning the voltage in this high-performance class of electrode materials.

■ ASSOCIATED CONTENT

Supporting Information

The Supporting Information is available free of charge at https://pubs.acs.org/doi/10.1021/acs.chemmater.0c03496.

Crystal structures, electrochemistry, diffraction, and XPS (PDF)

■ AUTHOR INFORMATION

Corresponding Authors

Sarah H. Tolbert − *Department of Chemistry and Biochemistry and Department of Materials Science and Engineering, University of California, Los Angeles, Los Angeles, California 90095, United States;* orcid.org/0000-0001-9969-1582; Email: tolbert@chem.ucla.edu

Ram Seshadri − *Materials Department and Materials Research Laboratory and Department of Chemistry and Biochemistry, University of California, Santa Barbara, Santa Barbara, California 93106, United States;* orcid.org/0000-0001-5858-4027; Email: seshadri@mrl.ucsb.edu

Authors

Kira E. Wyckoff − *Materials Department and Materials Research Laboratory, University of California, Santa Barbara, Santa Barbara, California 93106, United States*

Daniel D. Robertson − *Department of Chemistry and Biochemistry, University of California, Los Angeles, Los Angeles, California 90095, United States*

Molleigh B. Preefer − *Department of Chemistry and Biochemistry, University of California, Santa Barbara, Santa Barbara, California 93106, United States;* orcid.org/0000-0002-3699-8613

Samuel M. L. Teicher − *Materials Department and Materials Research Laboratory, University of California, Santa Barbara, Santa Barbara, California 93106, United States;* orcid.org/0000-0002-5922-4258

Jadon Bienz − *Department of Chemistry and Biochemistry, University of California, Santa Barbara, Santa Barbara, California 93106, United States*

Linus Kautzsch − *Materials Department and Materials Research Laboratory, University of California, Santa Barbara, Santa Barbara, California 93106, United States*

Thomas E. Mates − *Materials Department and Materials Research Laboratory, University of California, Santa Barbara, Santa Barbara, California 93106, United States*

Joya A. Cooley − *Department of Chemistry and Biochemistry California State University, Fullerton, California 92831, United States;* orcid.org/0000-0001-7187-3261

Complete contact information is available at: https://pubs.acs.org/10.1021/acs.chemmater.0c03496

Author Contributions

#K.E.W and D.D.R. are contributed equally to this work.

Notes

The authors declare no competing financial interest.

■ ACKNOWLEDGMENTS

This work was supported as part of the Center for Synthetic Control Across Length scales for Advancing Rechargeables (SCALAR), an Energy Frontier Research Center funded by the U.S. Department of Energy, Office of Science, Basic Energy Sciences under Award DE-SC0019381. The research reported here made use of shared facilities of the UC Santa Barbara Materials Research Science and Engineering Center (MRSEC, NSF DMR 1720256), a member of the Materials Research Facilities Network (www.mrfn.org). We acknowledge the use of the shared computing facilities of the Center for Scientific Computing at UC Santa Barbara, supported by NSF CNS-1725797, and the NSF MRSEC at UC Santa Barbara, NSF DMR-1720256. D.R. has been supported by the National Science Foundation Graduate Research Fellowship Program under DGE-1650604 and DGE-2034835. S.M.L.T. has been supported by the National Science Foundation Graduate Research Fellowship Program under DGE-1650114. Any opinions, findings, and conclusions or recommendations expressed in this material are those of the authors and do not necessarily reflect the views of the National Science Foundation. It is a pleasure to thank Miguel Zepeda of the UC Santa Barbara Materials Research Laboratory for the help with operando XRD.

■ REFERENCES

(1) Dunn, B.; Kamath, H.; Tarascon, J.-M. Electrical Energy Storage for the Grid: A Battery of Choices. *Science* **2011**, *334*, 928−935.

(2) Lukatskaya, M. R.; Dunn, B.; Gogotsi, Y. Multidimensional materials and device architectures for future hybrid energy storage. *Nat. Commun.* **2016**, *7*, 12647.

(3) Goodenough, J. B.; Park, K.-S. The Li-Ion Rechargeable Battery: A Perspective. *J. Am. Chem. Soc.* **2013**, *135*, 1167−1176.

(4) Wang, Y.; Cao, G. Developments in Nanostructured Cathode Materials for High-Performance Lithium-Ion Batteries. *Adv. Mater.* **2008**, *20*, 2251−2269.

(5) Mukherjee, R.; Krishnan, R.; Lu, T.-M.; Koratkar, N. Nanostructured Electrodes for High-Power Lithium Ion Batteries. *Nano Energy* **2012**, *1*, 518−533.

(6) Kim, D.-H.; Kim, J. Synthesis of $LiFePO_4$ Nanoparticles in Polyol Medium and Their Electrochemical Properties. *Electrochem. Solid-State Lett.* **2006**, *9*, A439−A442.

(7) Yang, Z.; Choi, D.; Kerisit, S.; Rosso, K. M.; Wang, D.; Zhang, J.; Graff, G.; Liu, J. Nanostructures and lithium electrochemical reactivity of lithium titanites and titanium oxides: A review. *J. Power Sources* **2009**, *192*, 588−598.

(8) Palacín, M. R.; Simon, P.; Tarascon, J. M. Nanomaterials for Electrochemical Energy Storage: The Good and the Bad. *Acta Chim. Slov.* **2016**, *63*, 417−423.

(9) Cook, J. B.; Lin, T. C.; Kim, H.-S.; Siordia, A.; Dunn, B. S.; Tolbert, S. H. Suppression of Electrochemically Driven Phase Transitions in Nanostructured MoS_2 Pseudocapacitors Probed Using Operando X-ray Diffraction. *ACS Nano* **2019**, *13*, 1223−1231.

(10) Doeff, M. M.; Wilcox, J. D.; Kostecki, R.; Lau, G. Optimization of Carbon Coatings on $LiFePO_4$. *J. Power Sources* **2006**, *163*, 180−184.

(11) Shin, H. C.; Cho, W. I.; Jang, H. Electrochemical Properties of Carbon-Coated $LiFePO_4$ Cathode Using Graphite, Carbon Black, and acetylene black. *Electrochim. Acta* **2006**, *52*, 1472−1476.

(12) Jiang, J.; Dahn, J. R. Dependence of the Heat of Reaction of $Li_{0.81}C_6$ (0.1 V), $Li_7Ti_5O_{12}$ (1.55 V), and $Li_{0.5}VO_2$ (2.45 V) Reacting with Nonaqueous Solvents or Electrolytes on the Average Potential of the Electrode Material. *J. Electrochem. Soc.* **2006**, *153*, A310−A315.

(13) Downie, L. E.; Krause, L. J.; Burns, J. C.; Jensen, L. D.; Chevrier, V. L.; Dahn, J. R. In Situ Detection of Lithium Plating on Graphite Electrodes by Electrochemical Calorimetry. *J. Electrochem. Soc.* **2013**, *160*, A588−A594.

(14) Burns, J. C.; Stevens, D. A.; Dahn, J. R. In Situ Detection of Lithium Plating Using High Precision Coulometry. *J. Electrochem. Soc.* **2015**, *162*, A959−A964.

(15) Ribière, P.; Grugeon, S.; Morcrette, M.; Boyanov, S.; Laruelle, S.; Marlair, G. Investigation on the fire-induced hazards of Li-ion battery cells by fire calorimetry. *Energy Environ. Sci.* **2012**, *5*, 5271−5280.
(16) Zhao, K.; Pharr, M.; Vlassak, J. J.; Suo, Z. Fracture of Electrodes in Lithium-Ion Batteries Caused by Fast Charging. *J. Appl. Phys.* **2010**, *108*, 073517.
(17) Odziomek, M.; Chaput, F.; Rutkowska, A.; Świerczek, K.; Olszewska, D.; Sitarz, M.; Lerouge, F.; Parola, S. Hierarchically Structured Lithium Titanate for Ultrafast Charging in Long-Life High Capacity Batteries. *Nat. Commun.* **2017**, *8*, 15636.
(18) Hayner, C. M.; Zhao, X.; Kung, H. H. Materials for Rechargeable Lithium-Ion Batteries. *Annu. Rev. Chem. Biomol. Eng.* **2012**, *3*, 445−471.
(19) Magnéli, A.; Hofman-Bang, N.; Gjertsen, P. The Crystal Structures of Mo_90_{26} (β'-Molybdenum Oxide) and Mo_80_{23} (β-Molybdenum Oxide). *Acta Chem. Scand.* **1948**, *2*, 501−517.
(20) Roth, R. S.; Wadsley, A. D. Multiple Phase Formation in the Binary system Nb_2O_5−WO_3. I. Preparation and Identification of Phases. *Acta Crystallogr.* **1965**, *19*, 26−32.
(21) Roth, R. S.; Wadsley, A. D.; Andersson, S. The Crystal Structure of PNb_9O_{25}, ($P_2O_5 \cdot 9Nb_2O_5$). *Acta Crystallogr.* **1965**, *18*, 643−647.
(22) Andersson, S.; Wadsley, A. D. Crystallographic Shear and Diffusion Paths in Certain Higher Oxides of Niobium, Tungsten, Molybdenum and Titanium. *Nature* **1966**, *211*, 581−583.
(23) Andersson, S. The description of non-stoichiometric transition metal oxides. A logical extension of inorganic crystallography. *Bull. Miner.* **1967**, *90*, 522−527.
(24) Cheetham, A. K.; Von Dreele, R. B. Cation Distributions in Niobium Oxide Block Structures. *Nat. Phys. Sci.* **1973**, *244*, 139−140.
(25) Dreele, R. V.; Cheetham, A. K. The structures of some titanium-niobium oxides by powder neutron diffraction. *Proc. R. Entomol. Soc. Lond. Ser. A Gen. Entomol.* **1974**, *338*, 311−326.
(26) Murphy, D. W.; Greenblatt, M.; Cava, R. J.; Zahurak, S. M. Topotactic Lithium Reactions with ReO_3 Related Shear Structures. *Solid State Ionics* **1981**, *5*, 327−329.
(27) Cava, R. J.; Kleinman, D. J.; Zahurak, S. M. $V_{3.2}W_{1.8}O_{13}$ and Studies of the V_2O_5−WO_3−VO_2 Ternary System. *Mater. Res. Bull.* **1983**, *18*, 869−873.
(28) Cava, R. J.; Murphy, D. W.; Zahurak, S. M. Lithium Insertion in Wadsley-Roth Phases Based on Niobium Oxide. *J. Electrochem. Soc.* **1983**, *130*, 2345−2351.
(29) Cava, R. J.; Santoro, A.; Murphy, D. W.; Zahurak, S. M.; Roth, R. S. The Structures of the Lithium Inserted Metal Oxides $Li_{0.2}ReO_3$ and $Li_{0.36}WO_3$. *J. Solid State Chem.* **1983**, *50*, 121−128.
(30) Cava, R.; Murphy, D.; Rietman, E.; Zahurak, S.; Barz, H. Lithium Insertion, Electrical Conductivity, and Chemical Substitution in Various Crystallographic Shear Structures. *Solid State Ionics* **1983**, *9-10*, 407−411.
(31) Han, J.-T.; Huang, Y.-H.; Goodenough, J. B. New Anode Framework for Rechargeable Lithium Batteries. *Chem. Mater.* **2011**, *23*, 2027−2029.
(32) Han, J.-T.; Goodenough, J. B. 3-V Full Cell Performance of Anode Framework $TiNb_2O_7$/Spinel $LiNi_{0.5}Mn_{1.5}O_4$. *Chem. Mater.* **2011**, *23*, 3404−3407.
(33) Saritha, D.; Pralong, V.; Varadaraju, U. V.; Raveau, B. Electrochemical Li Insertion Studies on $WNb_{12}O_{33}$ − A Shear ReO_3 Type Structure. *J. Solid State Chem.* **2010**, *183*, 988−993.
(34) Augustyn, V.; Come, J.; Lowe, M. A.; Kim, J. W.; Taberna, P.-L.; Tolbert, S. H.; Abruña, H. D.; Simon, P.; Dunn, B. High-rate electrochemical energy storage through Li^+ intercalation pseudocapacitance. *Nat. Mater.* **2013**, *12*, 518−522.
(35) Griffith, K. J.; Forse, A. C.; Griffin, J. M.; Grey, C. P. High-Rate Intercalation without Nanostructuring in Metastable Nb_2O_5 Bronze Phases. *J. Am. Chem. Soc.* **2016**, *138*, 8888−8899.
(36) Griffith, K. J.; Senyshyn, A.; Grey, C. P. Structural Stability from Crystallographic Shear in TiO_2-Nb_2O_5 Phases: Cation Ordering and Lithiation Behavior of $TiNb_{24}O_{62}$. *Inorg. Chem.* **2017**, *56*, 4002−4010.
(37) Griffith, K. J.; Wiaderek, K. M.; Cibin, G.; Marbella, L. E.; Grey, C. P. Niobium tungsten oxides for high-rate lithium-ion energy storage. *Nature* **2018**, *559*, 556−563.
(38) Griffith, K. J.; Seymour, I. D.; Hope, M. A.; Butala, M. M.; Lamontagne, L. K.; Preefer, M. B.; Koçer, C. P.; Henkelman, G.; Morris, A. J.; Cliffe, M. J.; Dutton, S. E.; Grey, C. P. Ionic and Electronic Conduction in $TiNb_2O_7$. *J. Am. Chem. Soc.* **2019**, *141*, 16706−16725.
(39) Zhu, X.; Xu, J.; Luo, Y.; Fu, Q.; Liang, G.; Luo, L.; Chen, Y.; Lin, C.; Zhao, X. S. $MoNb_{12}O_{33}$ as a new anode material for high-capacity, safe, rapid and durable Li^+ Storage: structural characteristics, electrochemical properties and working mechanisms. *J. Mater. Chem. A* **2019**, *7*, 6522−6532.
(40) Preefer, M. B.; Saber, M.; Wei, Q.; Bashian, N. H.; Bocarsly, J. D.; Zhang, W.; Lee, G.; Milam-Guerrero, J.; Howard, E. S.; Vincent, R. C.; Melot, B. C.; Van der Ven, A.; Seshadri, R.; Dunn, B. S. Multielectron Redox and Insulator-to-Metal Transition upon Lithium Insertion in the Fast-Charging, Wadsley-Roth Phase PNb9O25. *Chem. Mater.* **2020**, *32*, 4553−4563.
(41) Koçer, C. P.; Griffith, K. J.; Grey, C. P.; Morris, A. J. Cation Disorder and Lithium Insertion Mechanism of Wadsley-Roth Crystallographic Shear Phases from First Principles. *J. Am. Chem. Soc.* **2019**, *141*, 15121−15134.
(42) Bashian, N. H.; Zhou, S.; Zuba, M.; Ganose, A. M.; Stiles, J. W.; Ee, A.; Ashby, D. S.; Scanlon, D. O.; Piper, L. F. J.; Dunn, B.; Melot, B. C. Correlated Polyhedral Rotations in the Absence of Polarons during Electrochemical Insertion of Lithium in ReO_3. *ACS Energy Lett.* **2018**, *3*, 2513−2519.
(43) Griffith, K. J.; Grey, C. P. Superionic Lithium Intercalation through 2×2 nm^2 Columns in the Crystallographic Shear Phase $Nb_{18}W_8O_{69}$. *Chem. Mater.* **2020**, *32*, 3860−3868.
(44) Gaultois, M. W.; Sparks, T. D.; Borg, C. K. H.; Seshadri, R.; Bonificio, W. D.; Clarke, D. R. Data-Driven Review of Thermoelectric Materials: Performance and Resource Considerations. *Chem. Mater.* **2013**, *25*, 2911−2920.
(45) Darriet, J.; Galy, J. (W0.2V0.8)3O7: Synthese et Structure Cristalline. *J. Solid State Chem.* **1972**, *4*, 357−361.
(46) Zibrov, I. P.; Filonenko, V. P.; Sidorov, V. A.; Lyapin, S. G. V3.047O7, a New High-Pressure Oxide with the Simpsonite Structure. *Inorg. Mater.* **2016**, *52*, 902−908.
(47) Voskanyan, A. A.; Abramchuk, M.; Navrotsky, A. Entropy Stabilization of TiO_2−Nb_2O_5 Wadsley−Roth Shear Phases and Their Prospects for Lithium-Ion Battery Anode Materials. *Chem. Mater.* **2020**, *32*, 5301−5308.
(48) Coelho, A. A. TOPAS and TOPAS-Academic: An Optimization Program Integrating Computer Algebra and Crystallographic Objects Written in C++. *J. Appl. Crystallogr.* **2018**, *51*, 210−218.
(49) Momma, K.; Izumi, F. VESTA 3 For Three-Dimensional Visualization of Crystal, Volumetric and Morphology Data. *J. Appl. Crystallogr.* **2011**, *44*, 1272−1276.
(50) Stickel, J. J. Data Smoothing and Numerical Differentiation by a Regularization Method. *Comput. Chem. Eng.* **2010**, *34*, 467−475.
(51) Dedryvère, R.; Martinez, H.; Leroy, S.; Lemordant, D.; Bonhomme, F.; Biensan, P.; Gonbeau, D. Surface Film Formation on Electrodes in a $LiCoO_2$/Graphite cell: A Step by Step XPS Study. *J. Power Sources* **2007**, *174*, 462−468.
(52) Eshkenazi, V.; Peled, E.; Burstein, L.; Golodnitsky, D. XPS Analysis of the SEI Formed on Carbonaceous Materials. *Solid State Ionics* **2004**, *170*, 83−91.
(53) Verma, P.; Maire, P.; Novák, P. A Review of the Features and Analyses of the Solid Electrolyte Interphase in Li-ion Batteries. *Electrochim. Acta* **2010**, *55*, 6332−6341.
(54) Silversmit, G.; Depla, D.; Poelman, H.; Marin, G. B.; De Gryse, R. Determination of the V2p XPS Binding Energies for Different Vanadium Oxidation States (V5+ to V0+). *J. Electron Spectrosc. Relat. Phenom.* **2004**, *135*, 167−175.

(55) Kresse, G.; Hafner, J. Ab initio Molecular-Dynamics Simulation of the Liquid-Metal–Amorphous-Semiconductor Transition in Germanium. *Phys. Rev. B: Condens. Matter Mater. Phys.* **1994**, *49*, 14251–14269.
(56) Kresse, G.; Furthmüller, J. Efficient Iterative Schemes for ab initio Total-Energy Calculations Using a Plane-Wave Basis Set. *Phys. Rev. B: Condens. Matter Mater. Phys.* **1996**, *54*, 11169–11186.
(57) Kresse, G.; Furthmüller, J. Efficiency of Ab-Initio Total Energy Calculations for Metals and Semiconductors Using a Plane-Wave Basis Set. *Comput. Mater. Sci.* **1996**, *6*, 15–50.
(58) Blöchl, P. E. Projector Augmented-Wave Method. *Phys. Rev. B: Condens. Matter Mater. Phys.* **1994**, *50*, 17953–17979.
(59) Kresse, G.; Joubert, D. From Ultrasoft Pseudopotentials to the Projector Augmented-Wave Method. *Phys. Rev. B: Condens. Matter Mater. Phys.* **1999**, *59*, 1758–1775.
(60) Perdew, J. P.; Burke, K.; Ernzerhof, M. Generalized Gradient Approximation Made Simple. *Phys. Rev. Lett.* **1996**, *77*, 3865–3868.
(61) Sun, J.; Ruzsinszky, A.; Perdew, J. P. Strongly Constrained and Appropriately Normed Semilocal Density Functional. *Phys. Rev. Lett.* **2015**, *115*, 036402.
(62) Chakraborty, A.; Dixit, M.; Aurbach, D.; Major, D. T. Predicting Accurate Cathode properties of Layered Oxide Materials Using the SCAN Meta-GGA Density Functional. *npj Comput. Mater.* **2018**, *4*, 60.
(63) Dronskowski, R.; Bloechl, P. E. Crystal Orbital Hamilton Populations (COHP). Energy-Resolved Visualization of Chemical Bonding in Solids Based on Density-Functional Calculations. *J. Phys. Chem.* **1993**, *97*, 8617–8624.
(64) Deringer, V. L.; Tchougréeff, A. L.; Dronskowski, R. Crystal Orbital Hamilton Population (COHP) Analysis as Projected from Plane-Wave Basis Sets. *J. Phys. Chem. A* **2011**, *115*, 5461–5466.
(65) Maintz, S.; Deringer, V. L.; Tchougréeff, A. L.; Dronskowski, R. Analytic Projection From Plane-Wave and PAW Wavefunctions and Application to Chemical-Bonding Analysis in Solids. *J. Comput. Chem.* **2013**, *34*, 2557–2567.
(66) Maintz, S.; Deringer, V. L.; Tchougréeff, A. L.; Dronskowski, R. LOBSTER: A Tool to Extract Chemical Bonding from Plane-Wave Based DFT. *J. Comput. Chem.* **2016**, *37*, 1030–1035.
(67) Nishimura, S. PyAbstantia. 2017, https://shinichinishimura.github.io/pyabst/ (accessed Oct 11, 2019).
(68) Heurung, G.; Gruehn, R. High-Resolution Transmission Electron Microscopy – Investigation of Vanadium–Tungsten Oxides Prepared by Chemical Transport Reactions. *J. Solid State Chem.* **1984**, *55*, 337–343.
(69) Allpress, J. G.; Sanders, J. V.; Wadsley, A. D. Multiple Phase Formation in the Binary System Nb_2O_5–WO_3. VI. Electron Microscopic Observation and Evaluation of Non-Periodic Shear Structures. *Acta Crystallogr. B* **1969**, *25*, 1156–1164.
(70) See, K. A.; Lumley, M. A.; Stucky, G. D.; Grey, C. P.; Seshadri, R. Reversible Capacity of Conductive Carbon Additives at Low Potentials: Caveats for Testing Alternative Anode Materials for Li-Ion Batteries. *J. Electrochem. Soc.* **2017**, *164*, A327–A333.
(71) Augustyn, V.; Simon, P.; Dunn, B. Pseudocapacitive oxide materials for high-rate electrochemical energy storage. *Energy Environ. Sci.* **2014**, *7*, 1597–1614.
(72) Gopalakrishnan, J. Insertion/Extraction of Lithium and Sodium in Transition Metal Oxides and Chalcogenides. *Bull. Mater. Sci.* **1985**, *7*, 201–214.
(73) Xie, F. Y.; Gong, L.; Liu, X.; Tao, Y. T.; Zhang, W. H.; Chen, S. H.; Meng, H.; Chen, J. XPS Studies on Surface Reduction of Tungsten Oxide Nanowire Film by Ar^+ Bombardment. *J. Electron Spectrosc. Relat. Phenom.* **2012**, *185*, 112–118.
(74) Adams, S. From Bond Valence Maps to Energy Landscapes for Mobile Ions in Ion-Conducting Solids. *Solid State Ionics* **2006**, *177*, 1625–1630.
(75) Adams, S.; Rao, R. P. High Power Lithium Ion Battery Materials by Computational Design. *Phys. Status Solidi A* **2011**, *208*, 1746–1753.
(76) Brown, I. D. Recent Developments in the Methods and Applications of the Bond Valence Model. *Chem. Rev.* **2009**, *109*, 6858–6919.
(77) Koçer, C. P.; Griffith, K. J.; Grey, C. P.; Morris, A. J. First-Principles Study of Localized and Delocalized Electronic States in Crystallographic Shear Phases of Niobium Oxide. *Phys. Rev. B: Condens. Matter Mater. Phys.* **2019**, *99*, 075151.
(78) Parras, J. P.; Genreith-Schriever, A. R.; Zhang, H.; Elm, M. T.; Norby, T.; De Souza, R. A. Is ReO_3 A mixed Ionic–Electronic conductor? A DFT Study of Defect Formation and Migration in a $B^{VI}O_3$ Perovskite-Type Oxide. *Phys. Chem. Chem. Phys.* **2018**, *20*, 8008–8015.
(79) Heins, T. P.; Harms, N.; Schramm, L.-S.; Schröder, U. Development of a New Electrochemical Impedance Spectroscopy Approach for Monitoring the Solid Electrolyte Interphase Formation. *Energy Technol.* **2016**, *4*, 1509–1513.

APPENDIX A

Supporting information for Chapter 2:

Size-Dependent Suppression of Phase Transitions Leads to Fast-Charging in Nanoscale Li_xMoO_2

Table S1. Synthesis conditions for PMMA colloids with different sizes.

Avg. PMMA colloid size	APS	ALS	MMA	Water
60 nm	0.08 g	0.61 mL	12.56 mL	165 mL
150 – 200 nm	0.08 g	0.01 mL	10 mL	165 mL

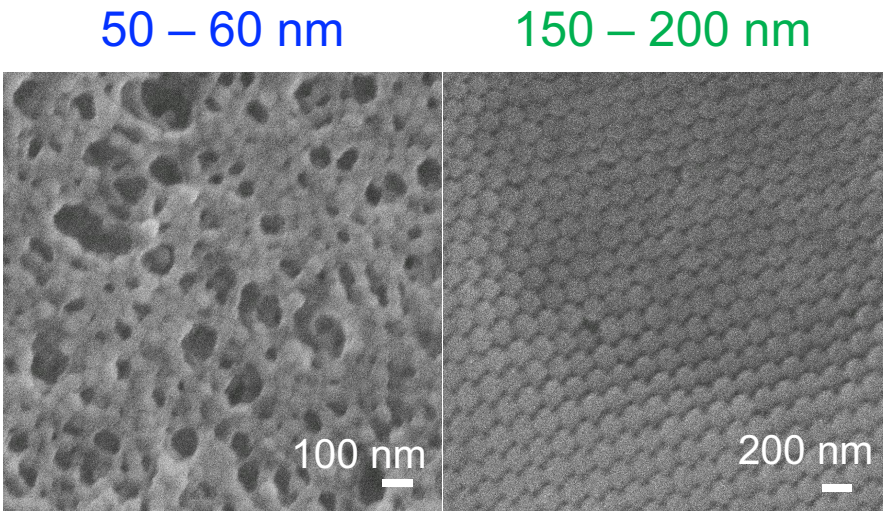

Figure S1. Scanning electron micrographs of PMMA colloids with different sizes. The 50 – 60 nm colloids (left) and 150 – 200 nm colloids (right) were used as templates for the small and large nanoporous MoO_2, respectively.

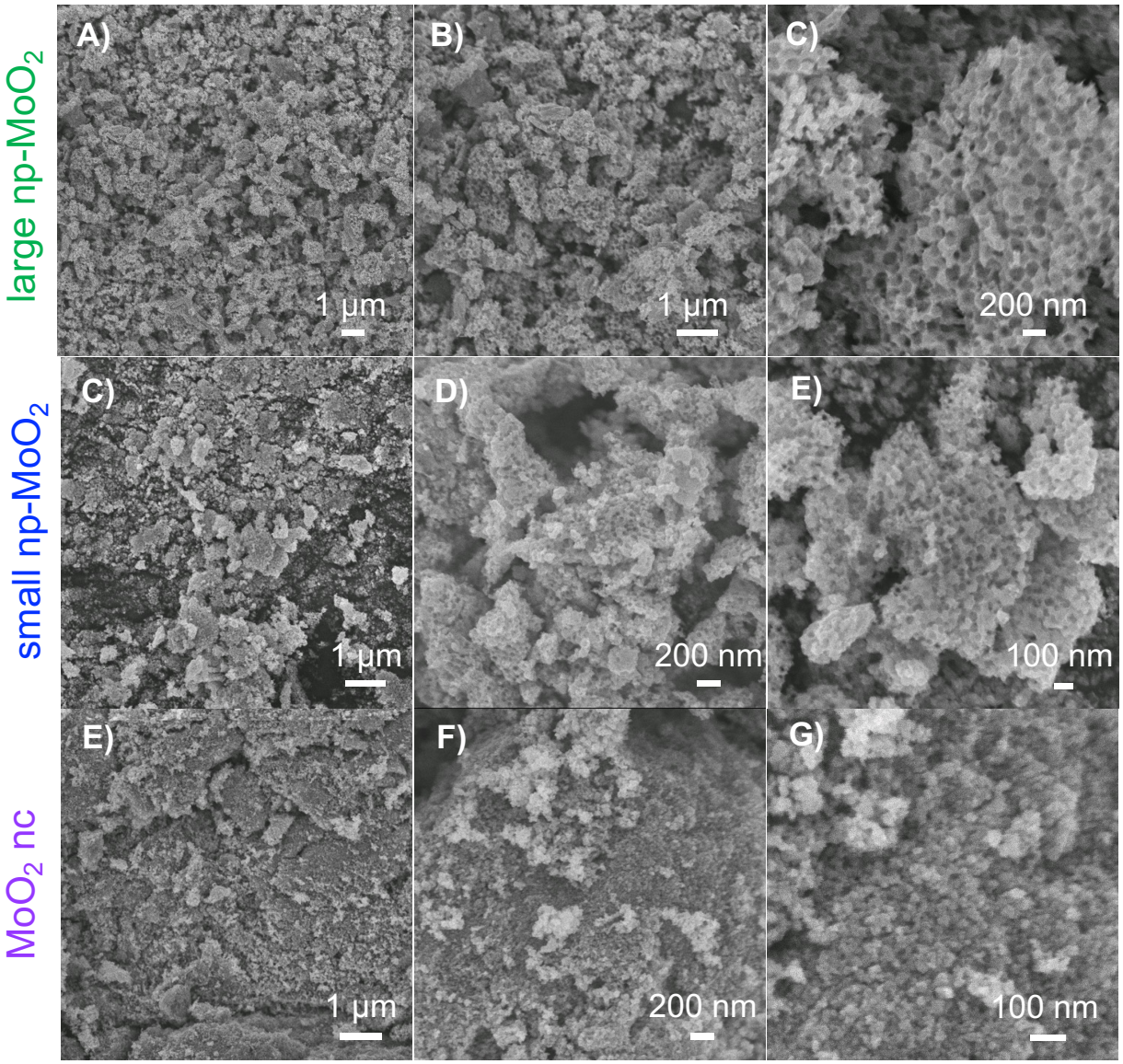

Figure S2. Additional scanning electron microscopy characterization of (**A** – **C**) large nanoporous MoO_2, (**C** – **E**) small nanoporous MoO_2, and (**E** – **G**) MoO_2 nanocrystals.

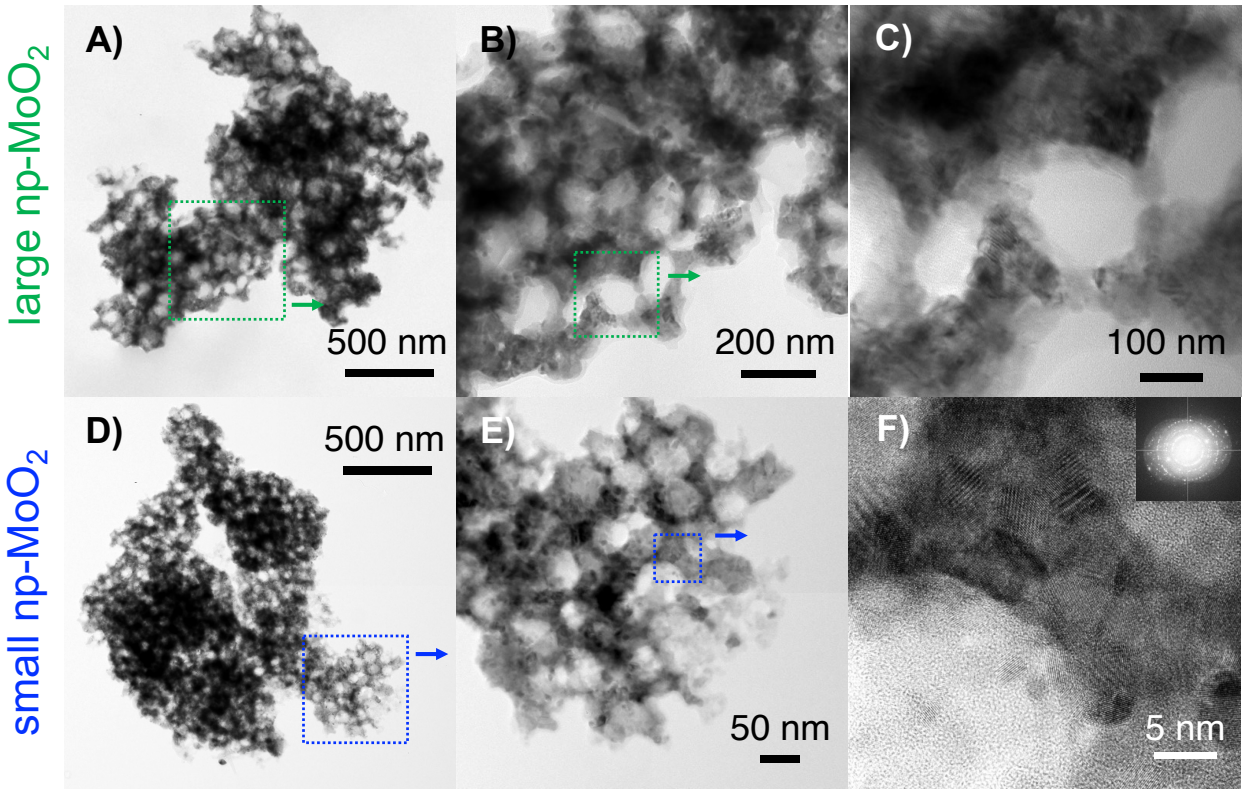

Figure S3. Additional high-resolution transmission electron microscopy (HRTEM) characterization of large (**A** – **C**) and small nanoporous MoO_2 (**D** – **F**). At low magnifications, entire micron-scale interconnected primary particles are shown with nanoscale porosity. At higher magnifications, individual nanoscale grains are shown throughout the pore walls. The inset in panel **F)** shows the fast Fourier transform of the image.

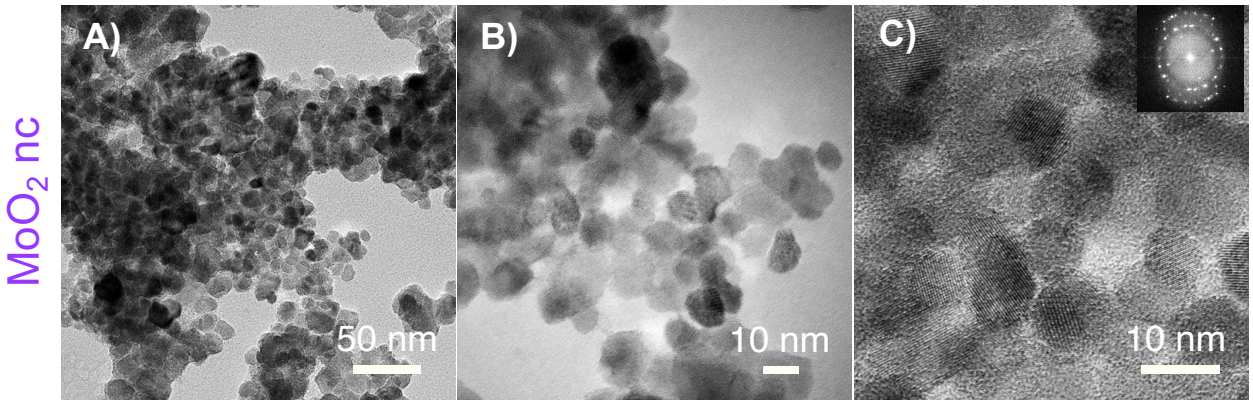

Figure S4. Additional HRTEM characterization of the MoO_2 nanocrystals shows mostly single-domain primary particles that agglomerate into larger secondary particles. The inset in panel C) shows the fast Fourier transform of the image.

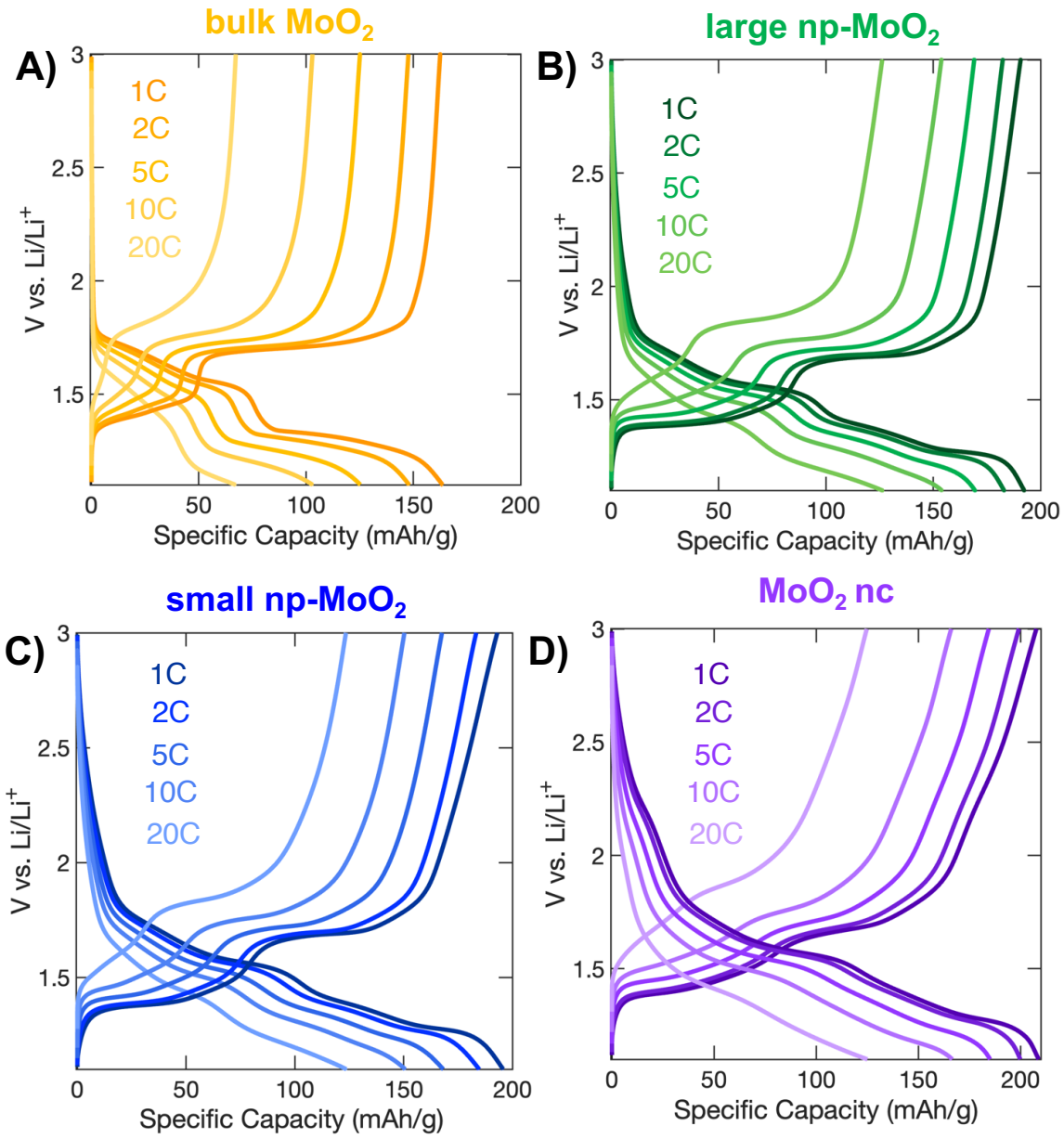

Figure S5. Rate-dependent galvanostatic profiles for each MoO_2 material.

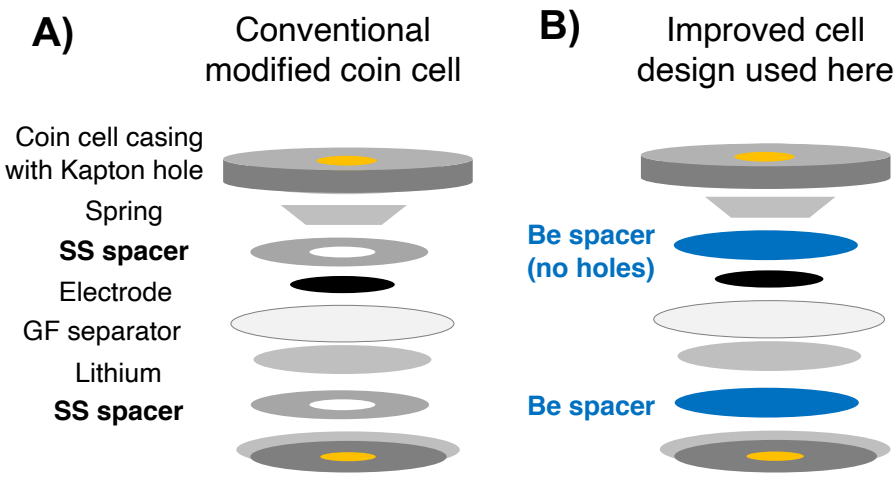

Figure S6. *Operando* SXRD cell design. **A)** Conventional modified coin cells use small holes in the cell casing and the spacers to provide X-ray transparency. However, the electrode area probed by the beam is subject to cycling artifacts due to decreased stack pressure and electrical contact. **B)** We circumvented these issues with an improved cell design, which uses Be spacers without holes. The Be spacers provide conductive windows sand ensure stack pressure over the probed area, but don't significantly attenuate the X-ray beam due to Be's low atomic number.

Advantages and disadvantages of *operando* cell design.

The small size and use of typical slurry electrodes in these modified beryllium coin cells provides some advantages compared to AMPIX cells, which use freestanding pellet electrodes that must cycle slowly and require high X-ray energy to penetrate the cell, but the smaller active mass and presence of a current collector in the modified Be coin cells lead to lower signal-to-noise and unavoidable background features. As such, we used the AMPIX cell for detailed refinement of the structure of bulk MoO_2 during cycling in **Figure 3** of the main text, and the modified beryllium coin cells in the rest of the experiments in Figure 4 of the main text to recreate the environment in a coin cell as accurately as possible. Notably, the two cell geometries show close similarities in the data for bulk MoO_2, which corroborates the validity of both methods.

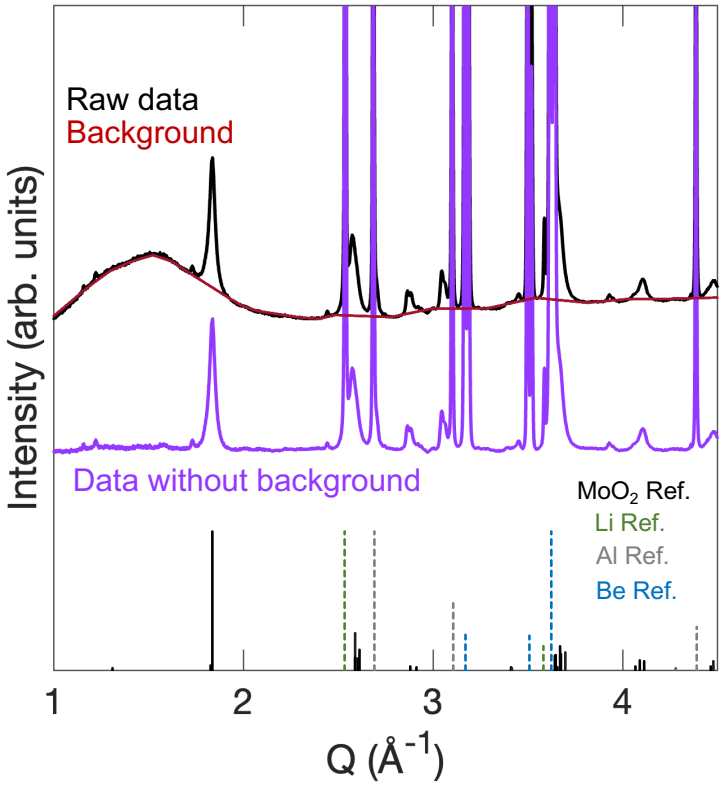

Figure S7. Representative background subtraction of *operando* SXRD data. A custom background was used to remove scattering from the electrolyte, which manifests as a broad feature in the region between Q = 1 – 2 $Å^{-1}$.

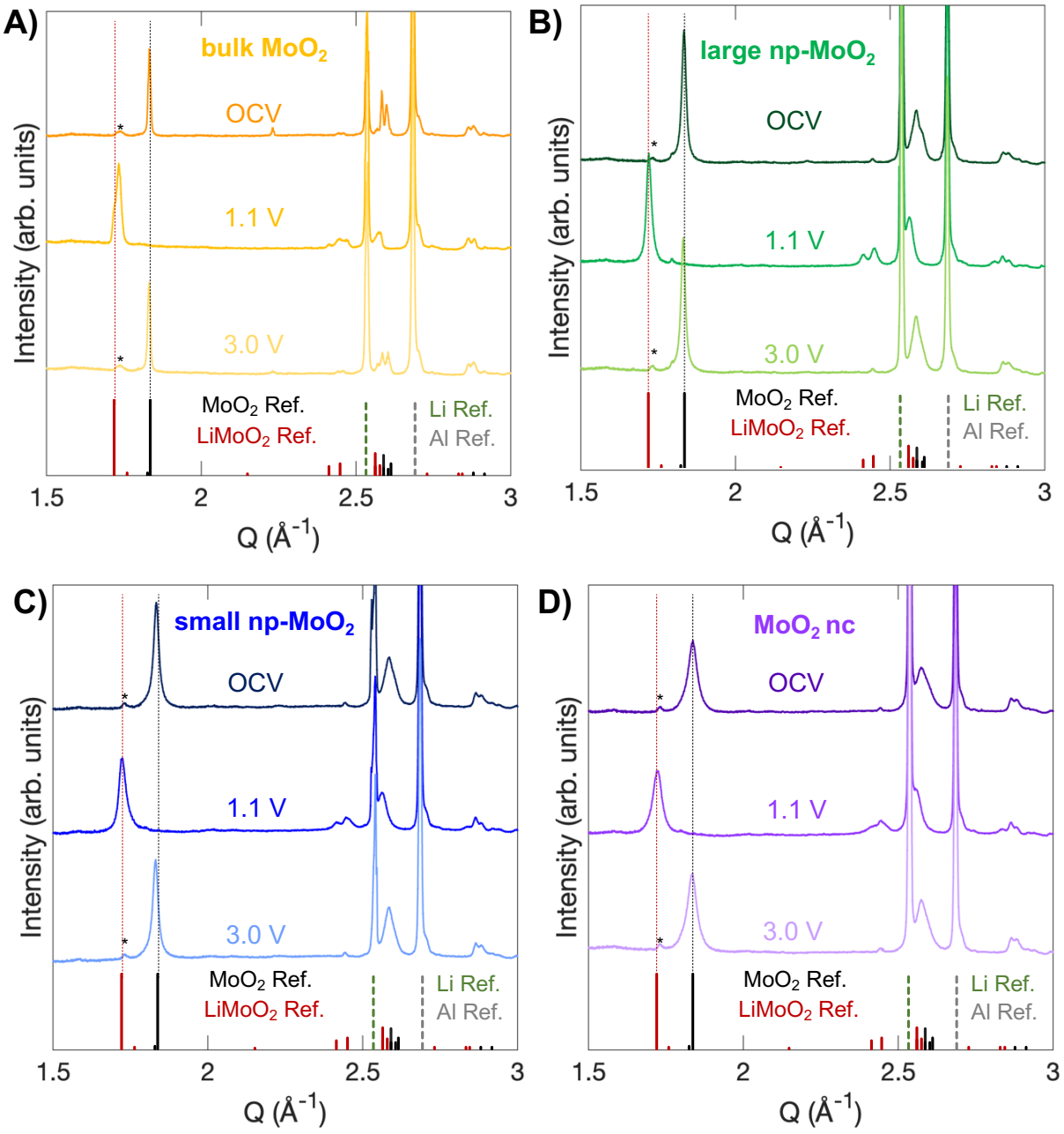

Figure S8. Selected patterns from the *operando* SXRD data in Figure 4 of the main text. For each MoO_2 material, patterns are shown in the pristine (OCV), fully lithiated (1.1 V), and fully delithiated (3.0 V) states. As seen from the data, the starting and ending peak positions are the same for all samples.

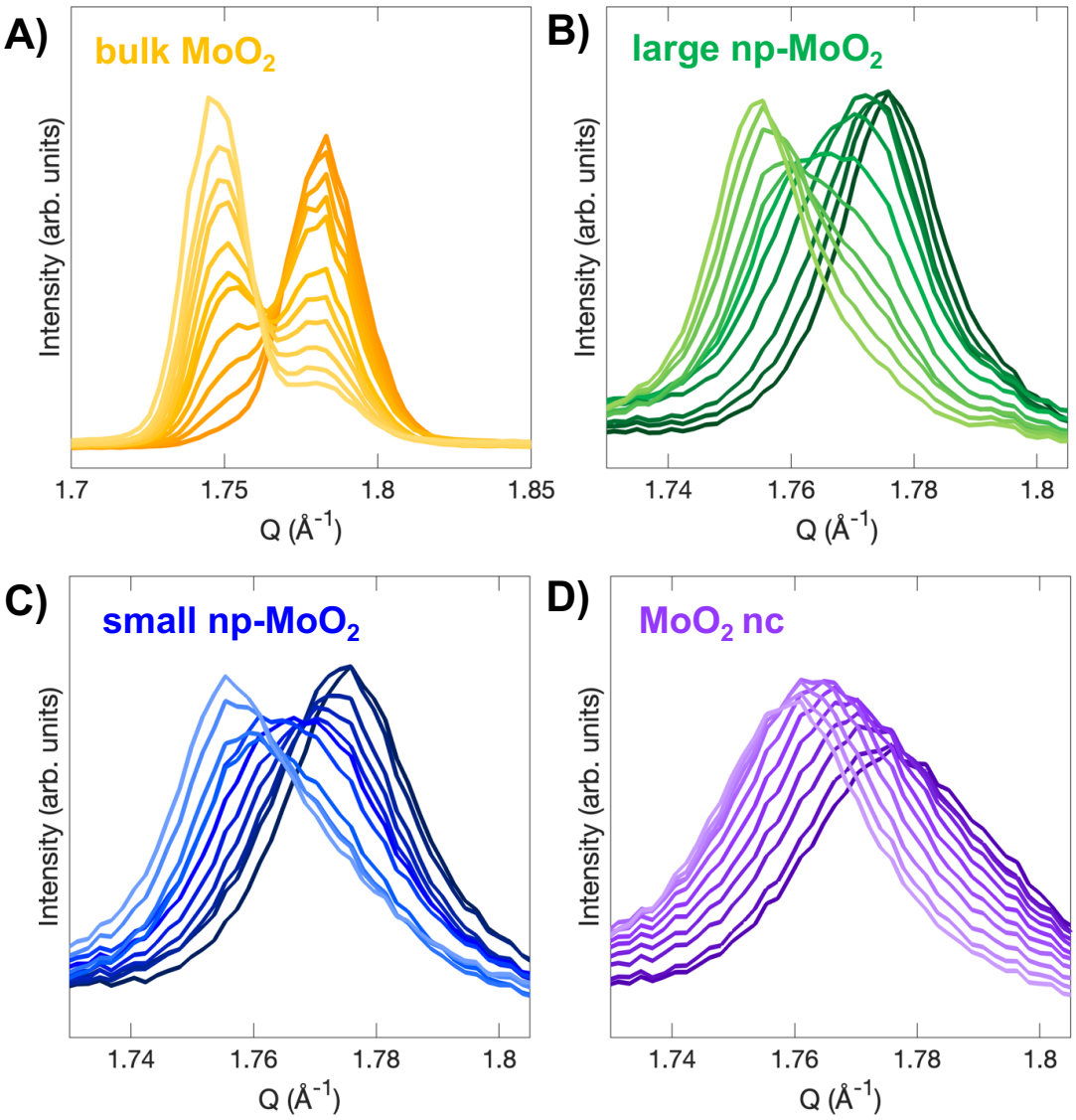

Figure S9. Detailed diffraction patterns upon lithiation from *operando* SXRD highlighting the most prominent two-phase region (CV peak 3). While bulk MoO_2 clearly shows a first-order phase transition, the two-phase coexistence in the nanoporous samples is less pronounced, but still clearly present. The MoO_2 nanocrystals show only a shift in the peak, with no two-phase coexistence.

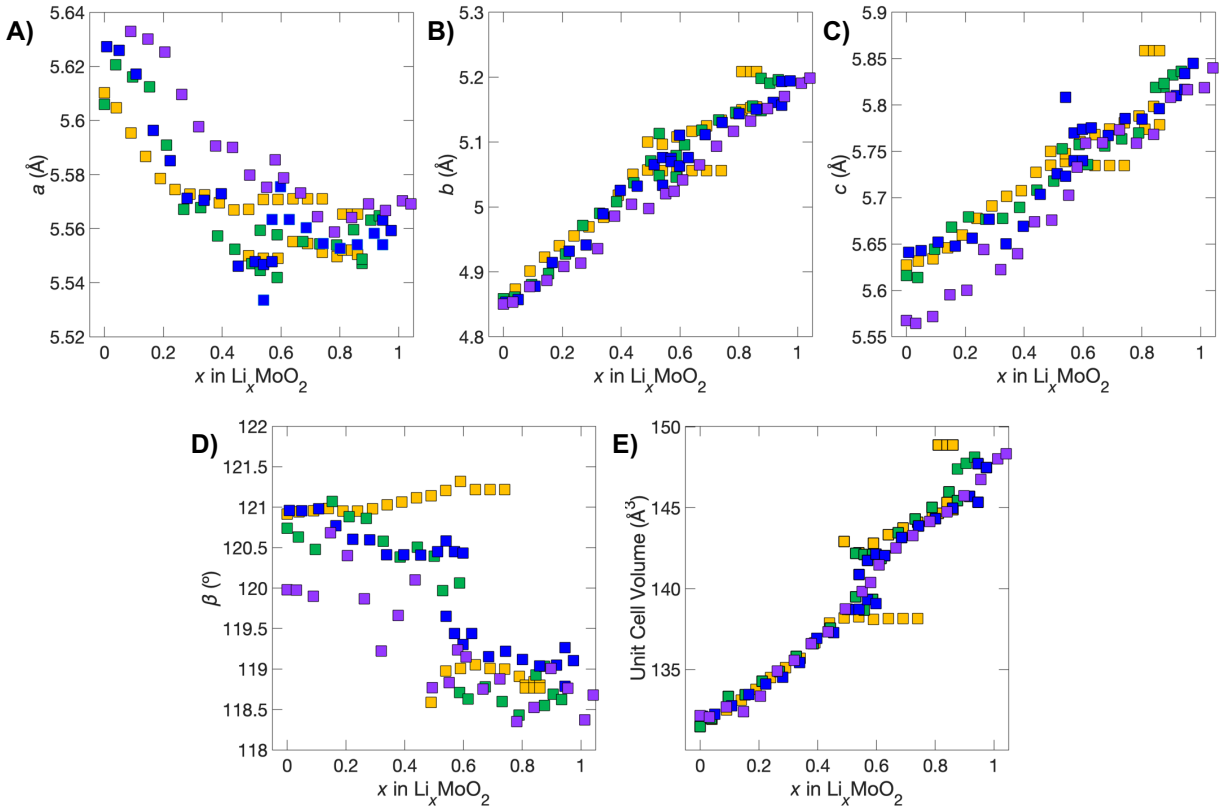

Figure S10. Detailed lattice parameters from Rietveld refinement of *operando* SXRD data. For this data, the bulk MoO_2 data is shown in yellow, the large nanoporous MoO_2 is shown in green, the small nanoporous MoO_2 is shown in blue, and the smallest MoO_2 nanocrystals are shown in purple. For all structural parameters, discontinuous shifts are seen in the bulk data, and those discontinuities decrease with decreasing domain size until completely continuous behavior is observed in the smallest MoO_2 nanocrystals.

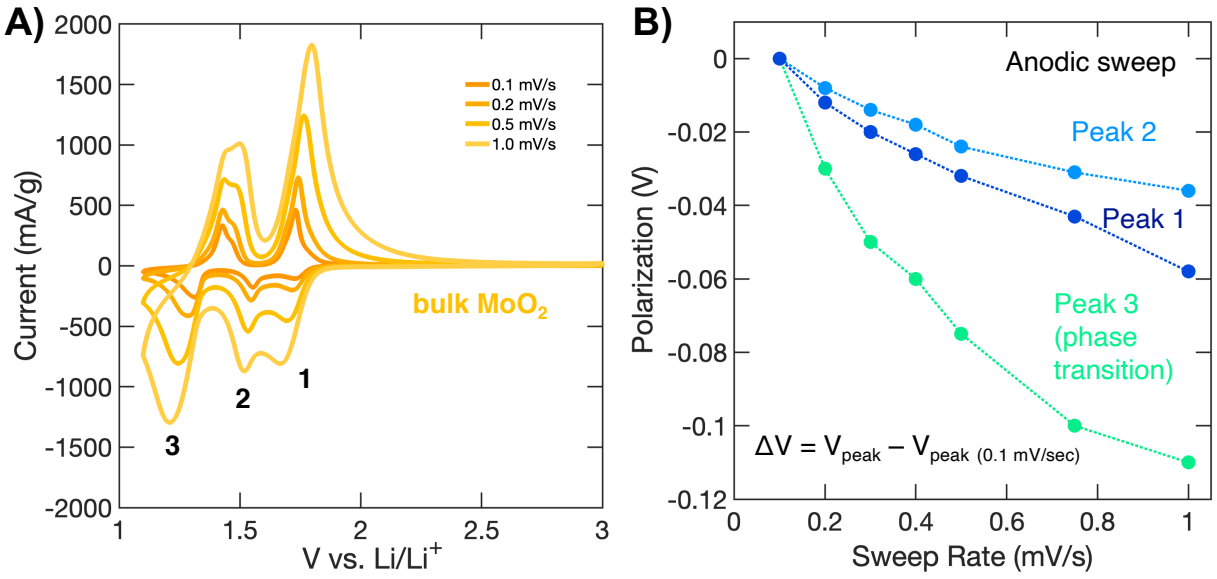

Figure S11. Relative polarization analysis for bulk MoO_2. For each labeled peak in the cyclic voltammogram in **A)**, the relative polarization for each sweep rate is shown in **B)**. Here, relative polarization was calculated by the shift in peak position at a given sweep rate from the original peak position at the slowest rate (0.1 mV/s).

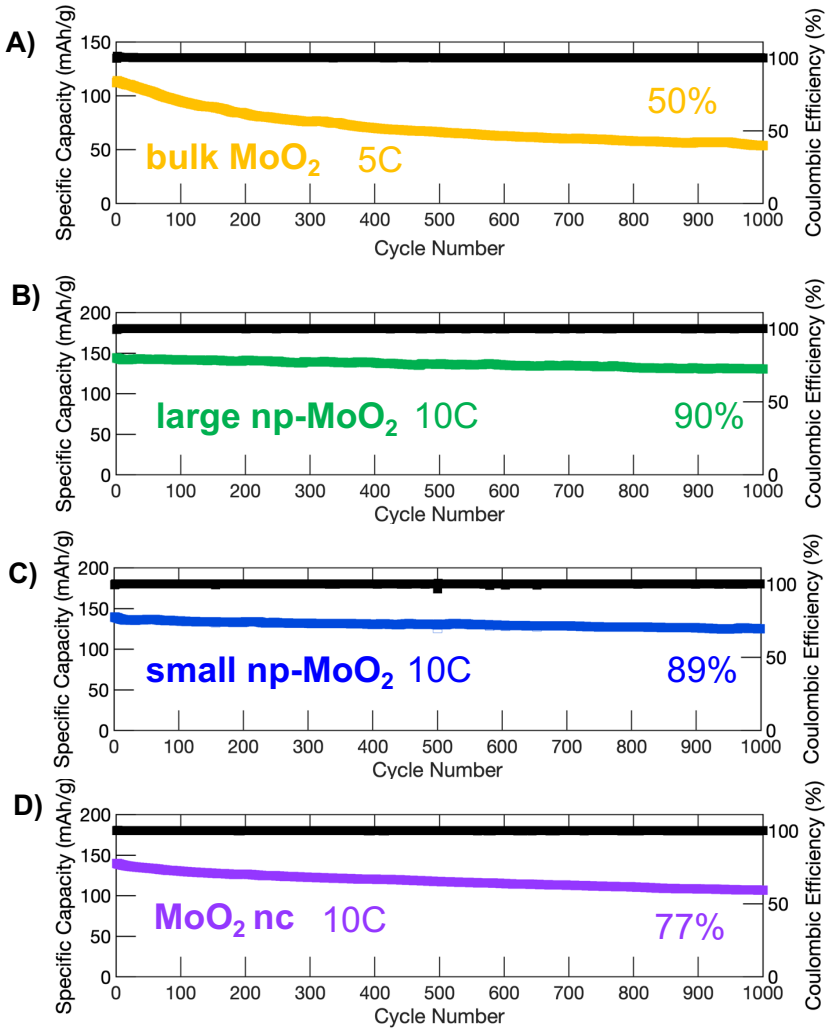

Figure S12. Individual long term cycling data for each of the MoO_2 materials, as shown in Figure 9A of the main text, with the coulombic efficiency plotted. For all of the materials, the coulombic efficiency remains at 100% throughout cycling.

APPENDIX B

Supporting Information for Chapter 3:

Analyzing How the Suppression of Phase Transitions Leads to Pseudocapacitive Properties in Li_xMoO_2 Using Electrochemical Impedance Spectroscopy

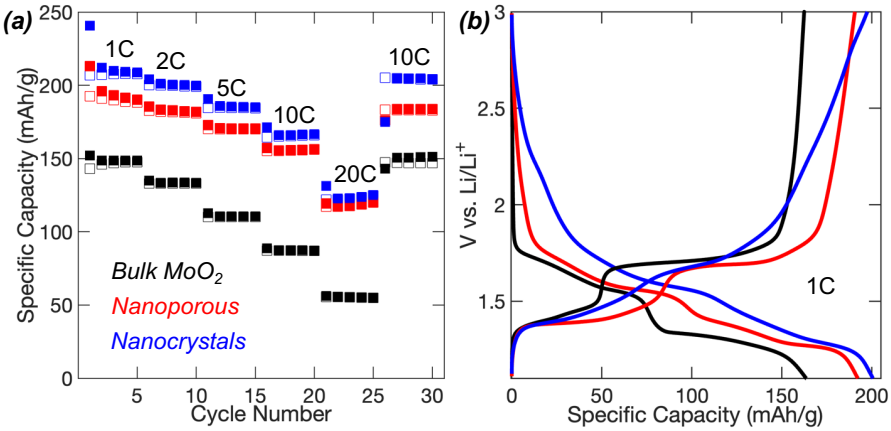

Figure S1. Galvanostatic cycling (a) rate performance and (b) profile for the three representative versions of MoO_2 in this study.

APPENDIX C

Supporting Information for Chapter 4:

Electrochemically-Formed Disordered Rock Salt ω-$V_9Mo_6O_{40}$ as a Fast-Charging Li-Ion Electrode Material

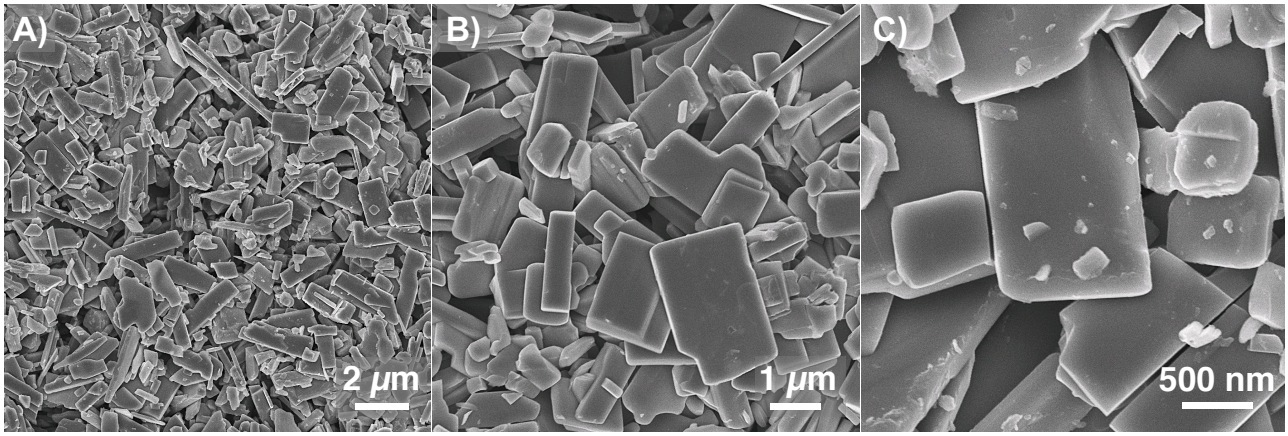

Figure S1. Additional scanning electron microscopy characterization of pristine bulk VMO.

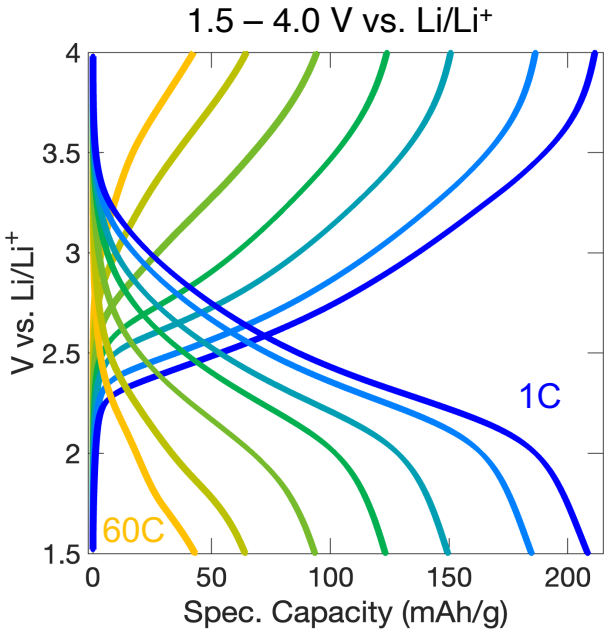

Figure S2. Rate-dependent galvanostatic profiles from cycling data for bulk VMO in Figure 2B of the main text with 4.0 V upper cutoff voltage.

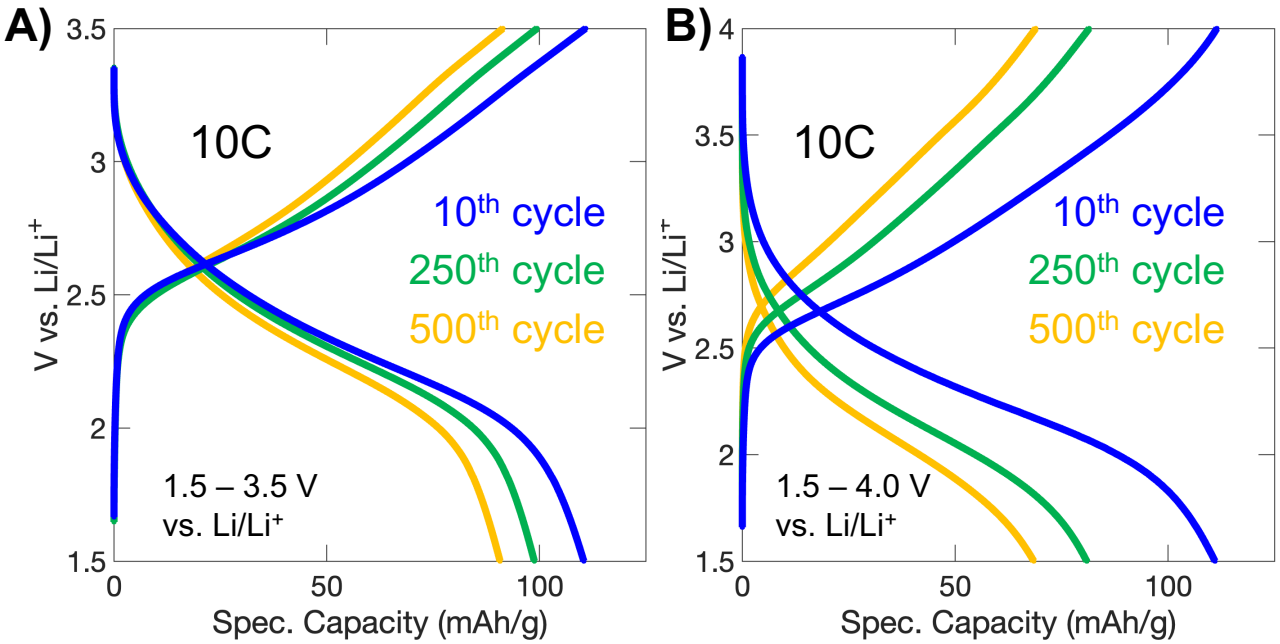

Figure S3. Galvanostatic profiles from long term cycling data in Figure 2C of the main text with **A)** 4.0 V upper cutoff voltage and **B)** 3.5 V upper cutoff voltage. The capacity decay occurs gradually and shows no major changes in the shape of the profile.

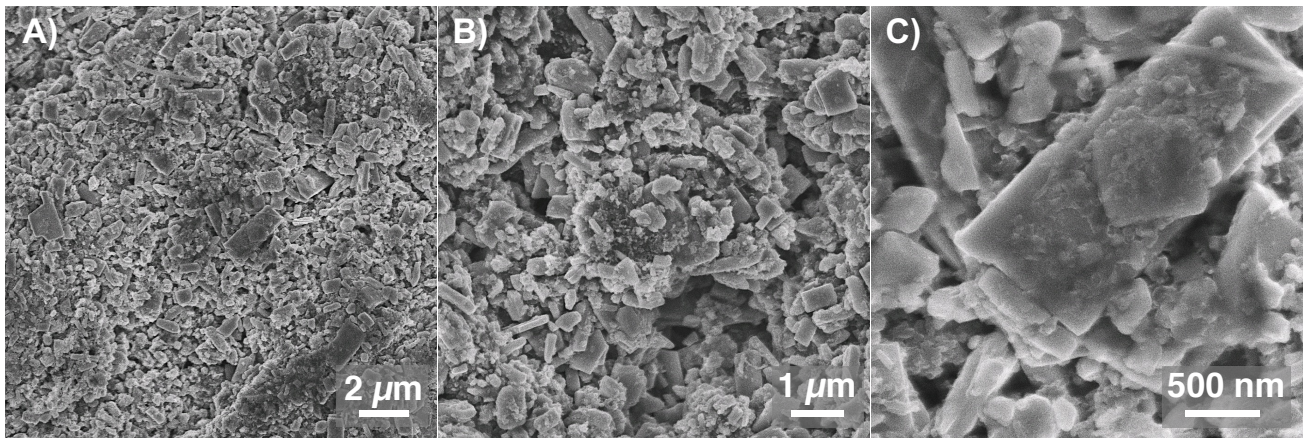

Figure S4. Additional scanning electron microscopy characterization of a cycled VMO electrode, showing retention of morphology after transformation to the disordered rock salt phase.

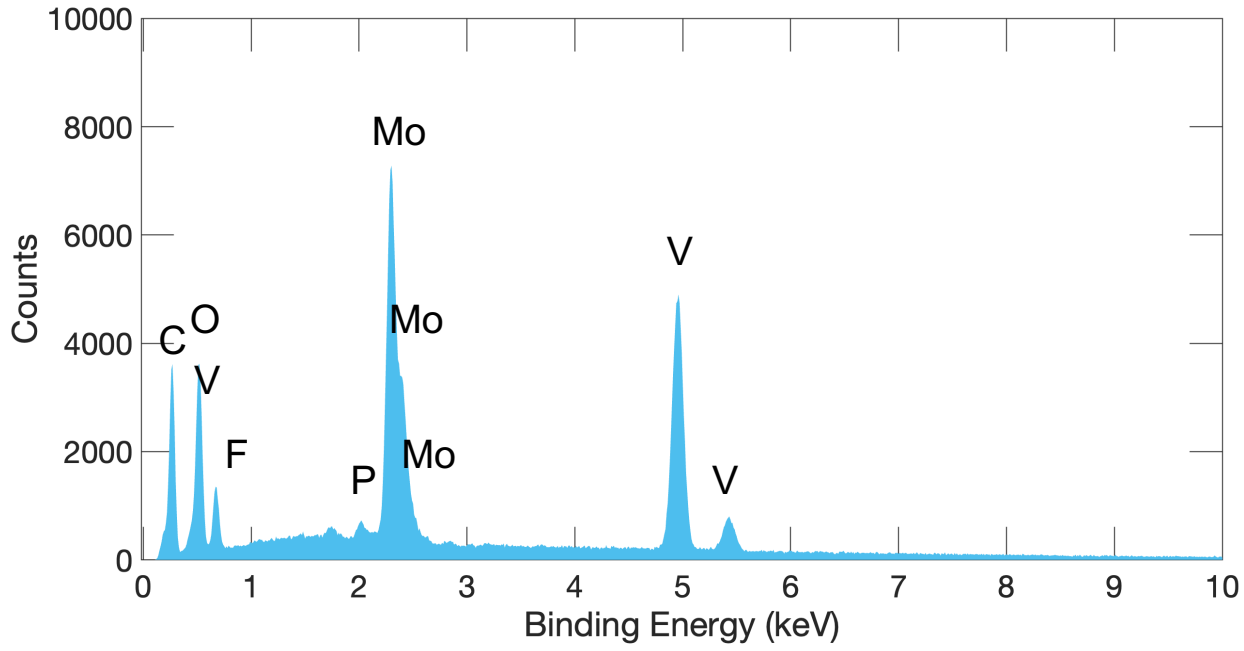

Figure S5. Energy dispersive spectroscopy (EDS) elemental characterization of a cycled VMO electrode, confirming the presence of both V and Mo in the disordered rock salt electrode.

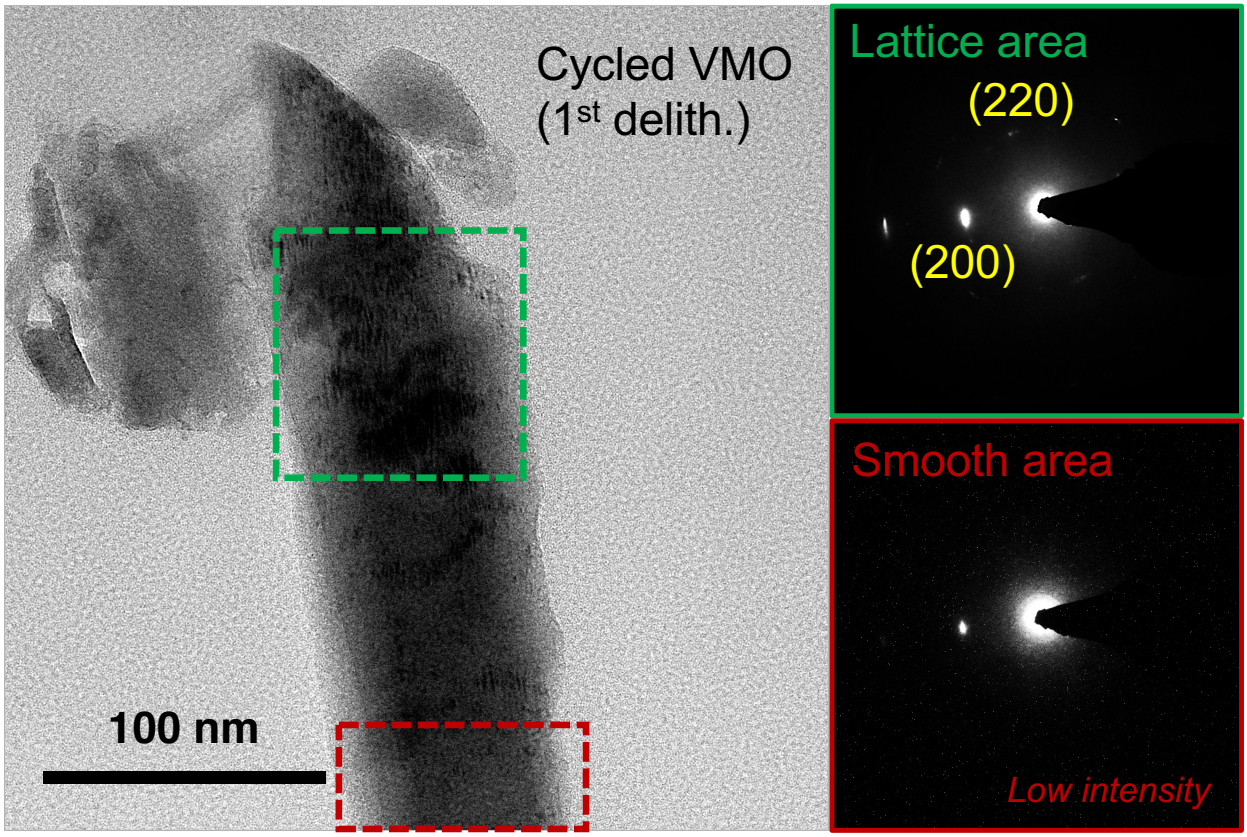

Figure S6. Electron diffraction of cycled VMO shows that the distorted, lamellar morphology corresponds to the rock salt structure.

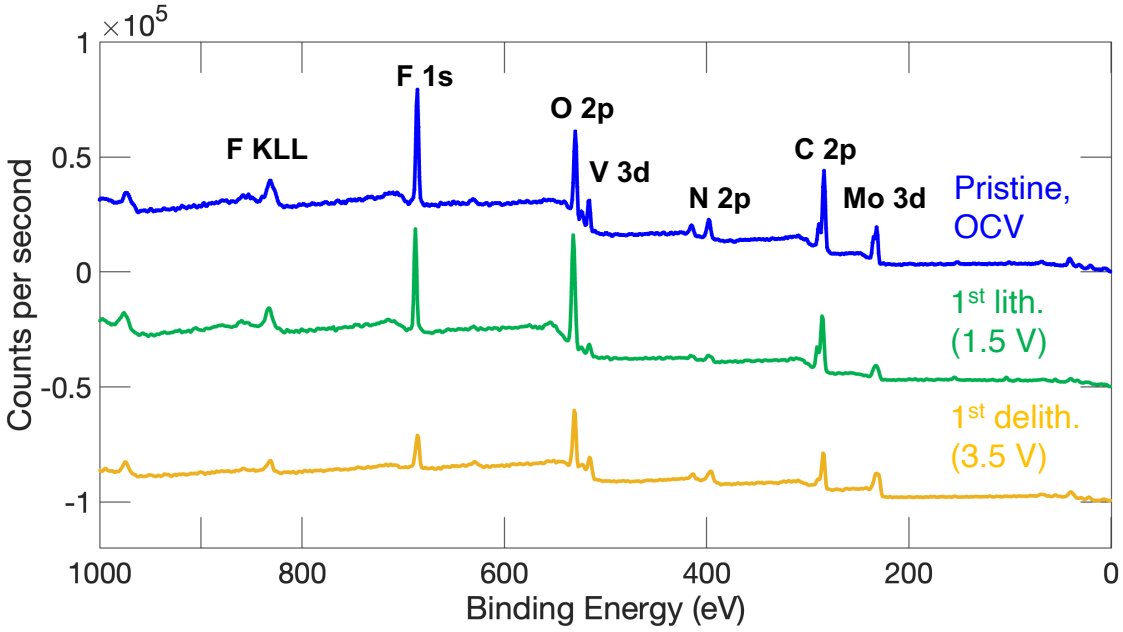

Figure S7. Full XPS survey scans from the high-resolution XPS data shown in Figure 6 of the main text.

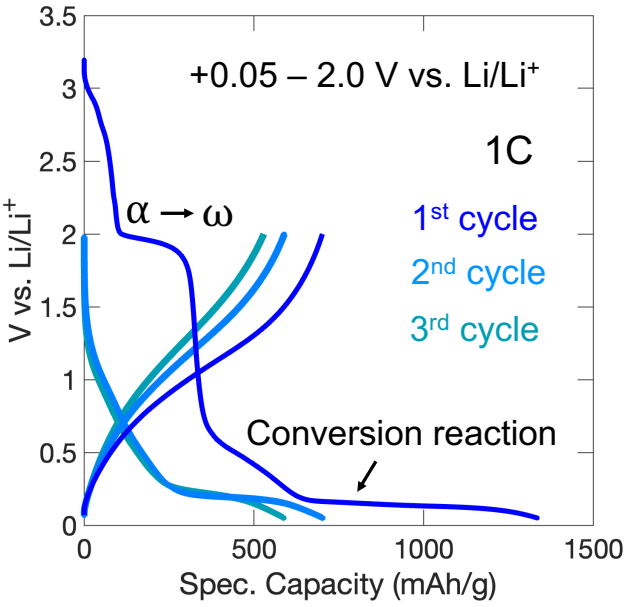

Figure S8. Low voltage cycling behavior of VMO electrode. V_2O_5, which also forms a disordered rock salt phase during electrochemical cycling, has been reported to undergo initial lithiation with high rate capability at low voltage. While VMO does have further lithiation at low voltage, it appears to be accompanied by the conversion reaction, where oxide is reduced to metal.

APPENDIX D

Supporting Information for Chapter 7:

High-Capacity Li^+ Storage through Multielectron Redox in the Fast-Charging Wadsley-Roth Phase $(W_{0.2}V_{0.8})_3O_7$

This appendix was reprinted from Wyckoff, K.E.; Robertson, D.D.; Preefer, M.B.; Teicher, S.M.; Bienz, J.; Kautzsch, L.; Mates, T.E.; Cooley, J.A.; Tolbert, S.H.; Seshadri, R. High-Capacity Li^+ Storage through Multielectron Redox in the Fast-Charging Wadsley–Roth Phase $(W_{0.2}V0_{.8})_3O_7$. *Chem. Mater.* **2020**, *32* (21), 9415-9424. Copyright 2020 American Chemical Society.

Supporting Information:

High Capacity Li^+ Storage through Multielectron Redox in the Fast-Charging Wadsley–Roth Phase $(W_{0.2}V_{0.8})_3O_7$

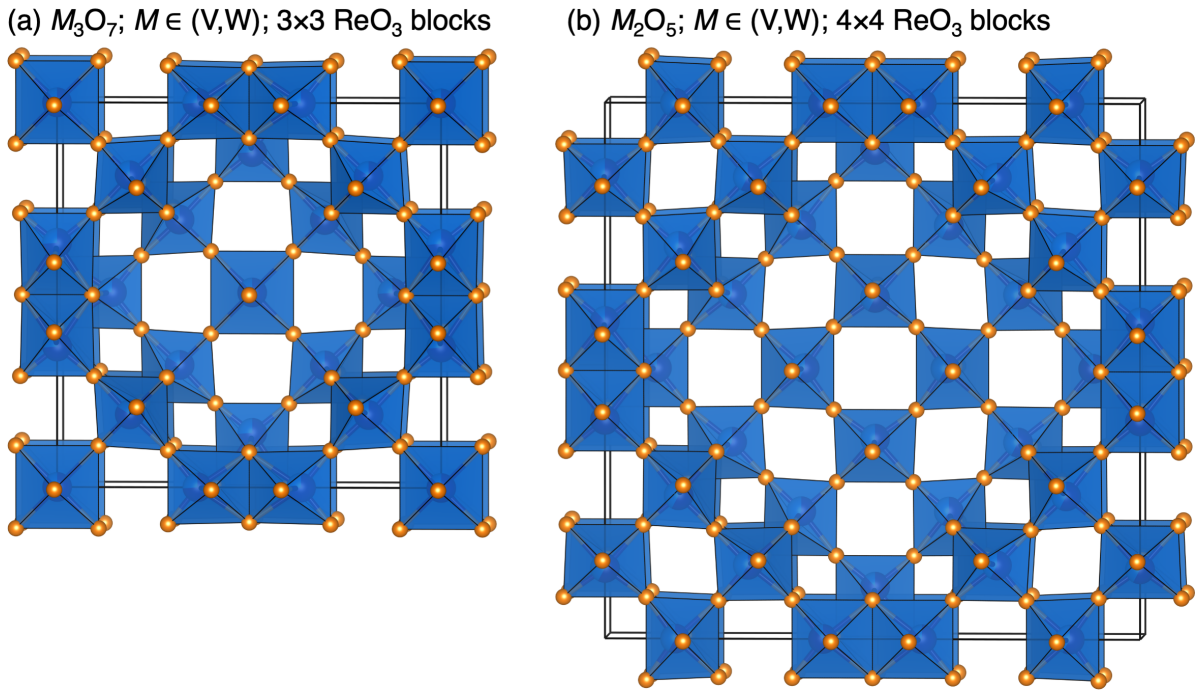

Figure 1: (a) The crystal structure of $(W_{0.2}V_{0.8})_3O_7$ is comprised of 3×3 blocks of octahedra, offset and connected through edge-sharing shear planes. The space group is $I4/mmm$. (b) The crystal structure of $(W_{0.35}V_{0.65})_2O_5$is comprised of 4×4 blocks of octahedra, offset and connected through edge-sharing shear planes. The space group is also $I4/mmm$.

Table 1: Summary of refinement parameters from Figure 2 in the main text for Conv. $(W_{0.2}V_{0.8})_3O_7$.

$(W_{0.2}V_{0.8})_3O_7$		$(W_{0.35}V_{0.65})_2O_5$	
parameter	value	parameter	value
lattice constant	a = 14.00277(3) Å c = 3.71467(2) Å	lattice constant	a = 19.55304(8) Å c = 3.70849(7) Å
space group	I_4/mmm	space group	I_4/mmm
block size	3×3	block size	4×4
percent	91%	percent	9%
R_{wp}	13.91		
R_{exp}	6.21		
GOF = R_{wp}/R_{exp}	2.24		

Table 2: Summary of refinement parameters from Figure 2 in the main text for FD $(W_{0.2}V_{0.8})_3O_7$.

$(W_{0.2}V_{0.8})_3O_7$	
parameter	value
lattice constant	a = 14.01155(5) Å c = 3.71502(9) Å
space group	I_4/mmm
block size	3×3
percent	100%
R_{wp}	12.30
R_{exp}	6.47
GOF = R_{wp}/R_{exp}	1.90

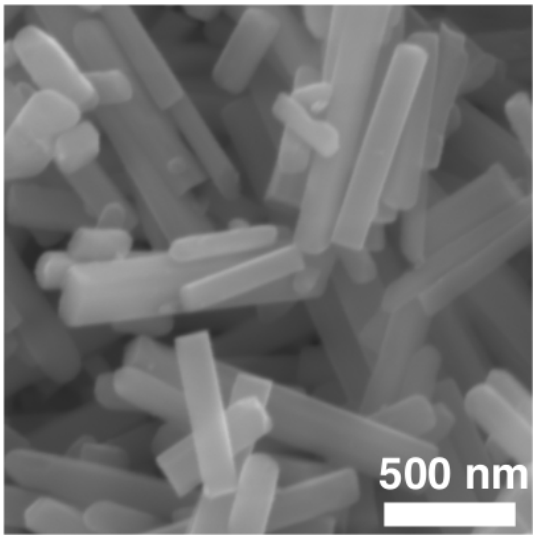

Figure 2: Higher magnification image of pristine FD material.

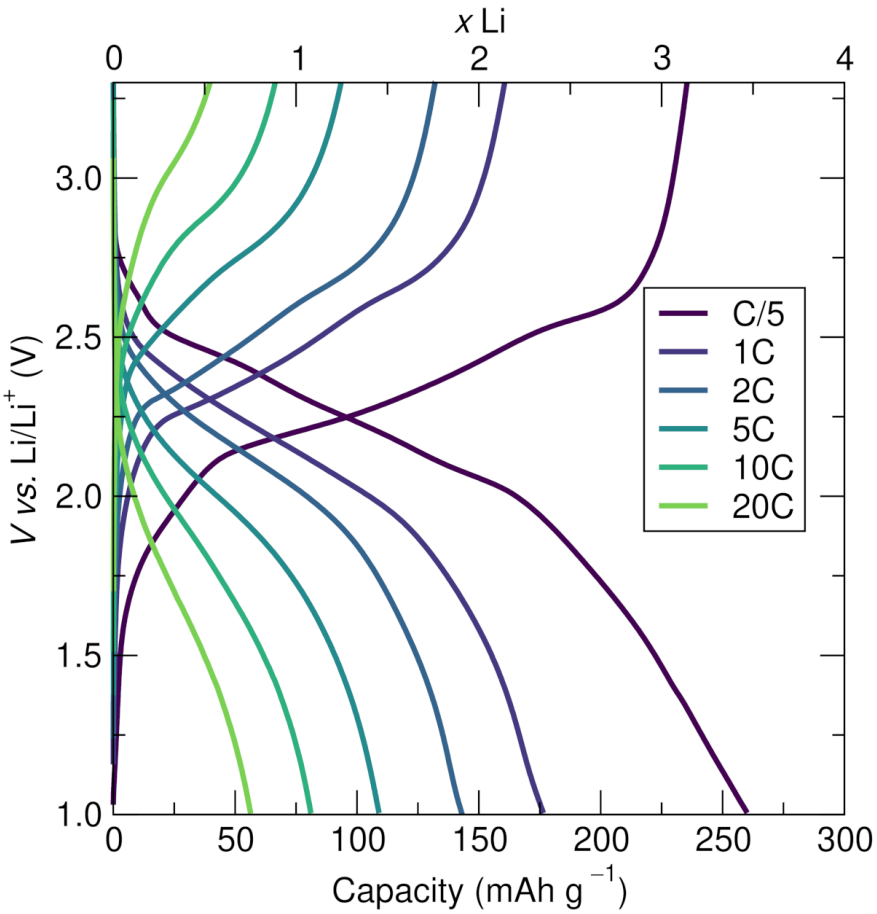

Figure 3: Galvanostatic cycling of Conv. $(W_{0.2}V_{0.8})_3O_7$ at rates from C/5 to 20C.

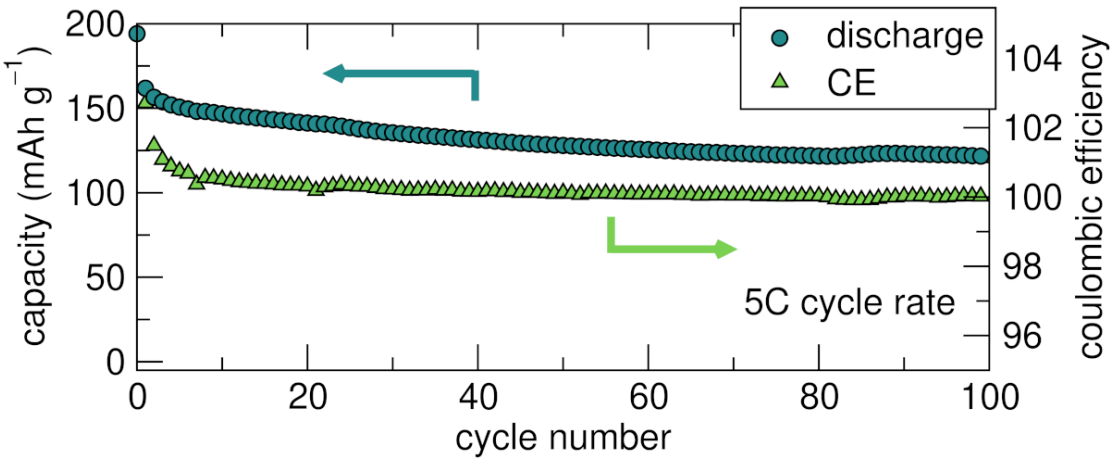

Figure 4: Extended cycling of Conv. $(W_{0.2}V_{0.8})_3O_7$ at a 5C rate.

Table 3: Summary of analysis of the exponent b from Figure 6 that shows the corresponding equations and coefficient of determination that fit the relationship between current and sweep rate for $(W_{0.2}V_{0.8})_3O_7$.

	avg.	b	$\mathbf{R}^2$
red	2.01 V	0.49	0.9975
	2.41 V	0.67	0.9963
ox	2.46 V	0.50	0.9968
	2.69 V	0.61	0.9975

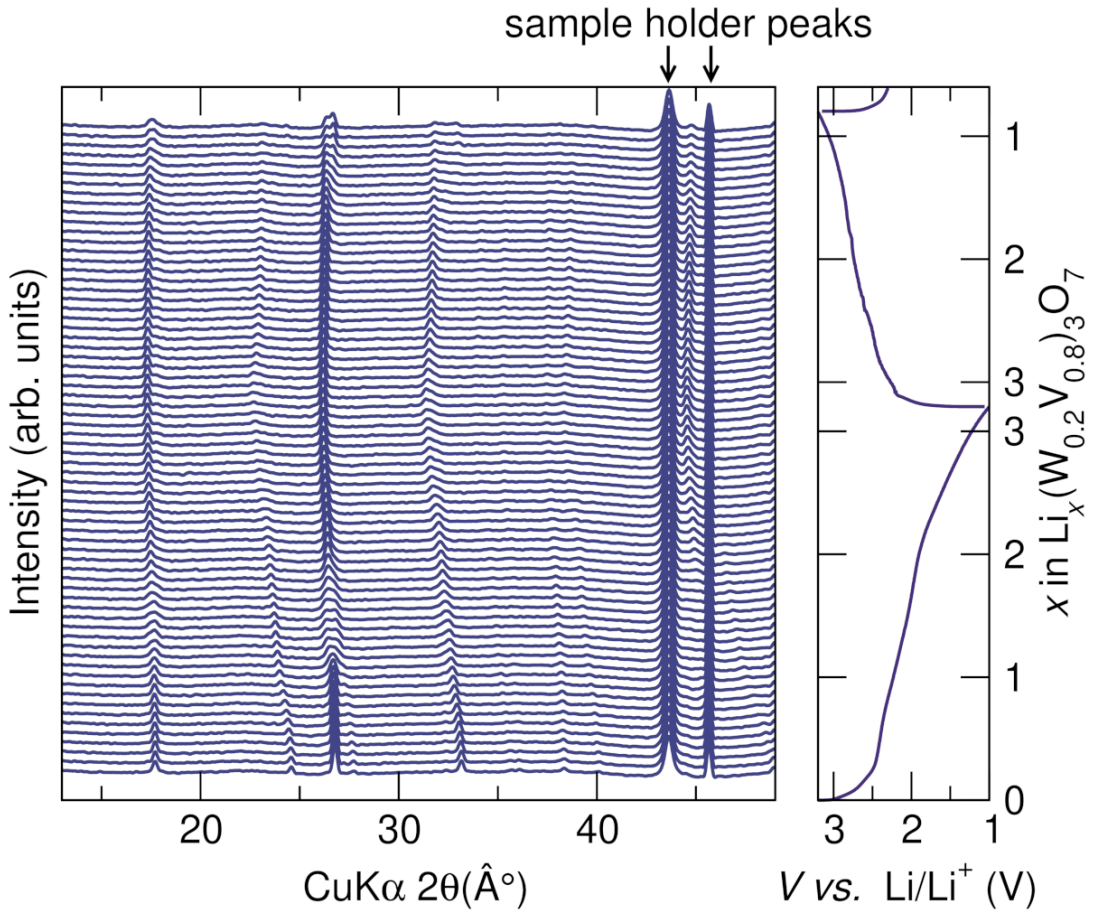

Figure 5: (left) Full *operando* diffraction range of FD $(W_{0.2}V_{0.8})_3O_7$ during the first galvanostatic cycle at a rate of C/10. Electrochemistry is shown on the right panel.

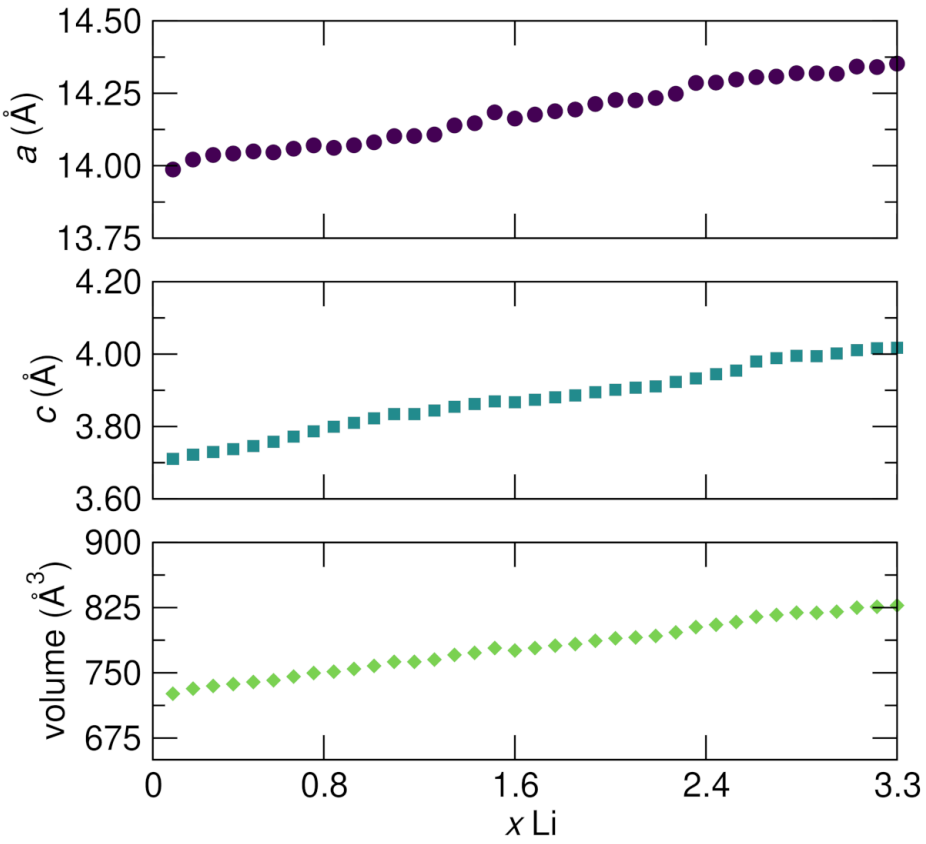

Figure 6: Variation of cell parameters and cell volume with lithiation of the principle 3×3 Wadley-Roth phase of FD $(W_{0.2}V_{0.8})_3O_7$ as a function of lithiation under conditions of *operando* diffraction. A moderate and nearly-linear increase in lattice parameters and cell volume is noted with increasing lithiation.

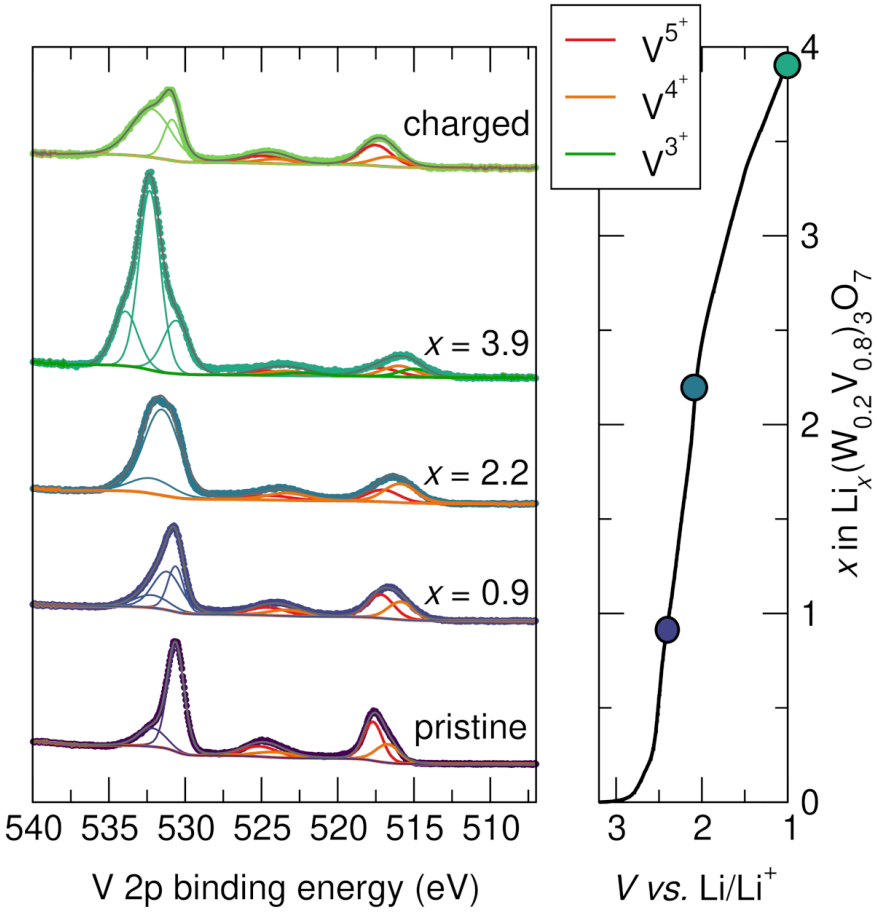

Figure 7: (left) Expanded view showing the full spectral regions for V $2p$ and O $1s$ from XPS. To improve accuracy, all states were fit together. The states of charge are mapped on the electrochemistry shown in the right panel.

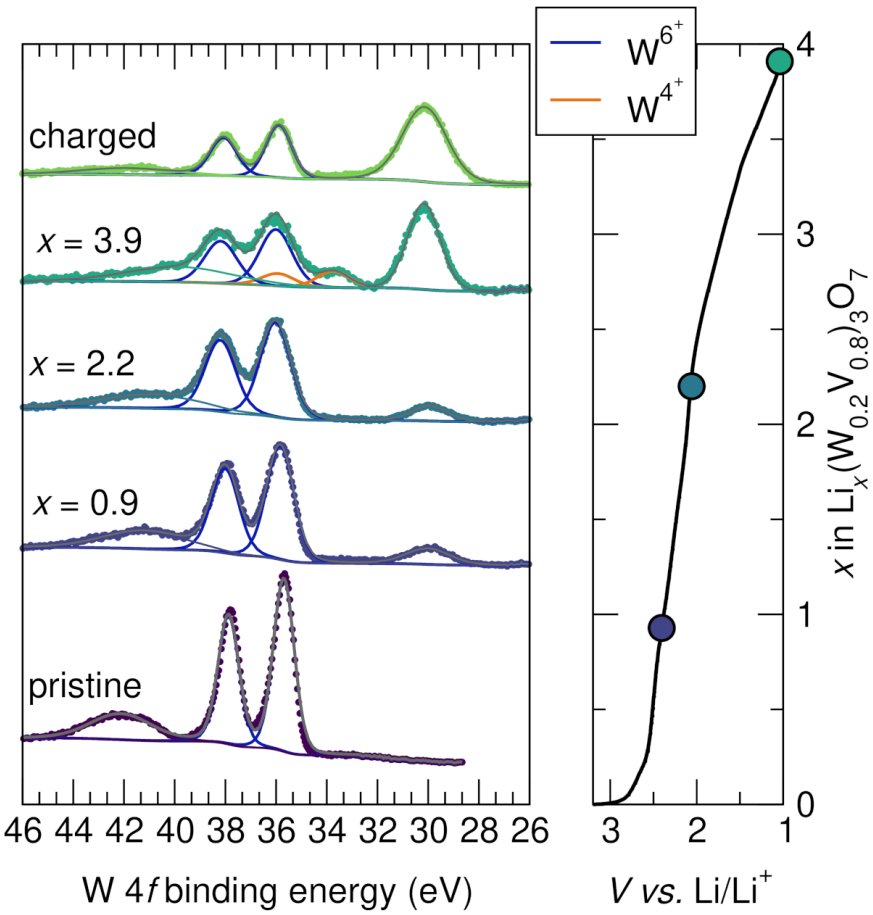

Figure 8: (left) Expanded view showing the full spectral regions for W $4f$ and F $1s$ from XPS. To improve accuracy, all states were fit together. The states of charge are mapped on the electrochemistry shown in the right panel.

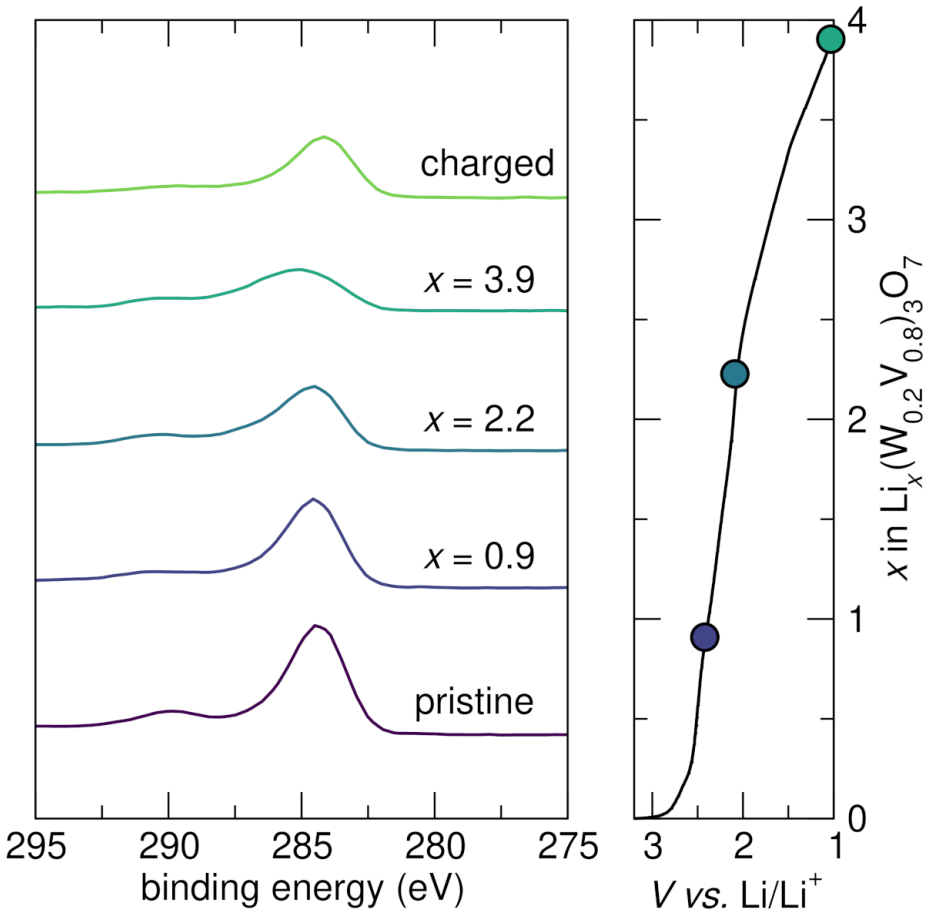

Figure 9: (left) XPS survey scans for each state of charge showing that the C 1s region lines up using the calibration method described in the main text. The states of charge are mapped on the electrochemistry shown in the right panel.

Table 4: Quantitative analysis of the evolution of oxidation states from fitting the high resolution spectra found in Figure 8 and Figure 9.

x in $Li_x(W_{0.2}V_{0.6})_3O_7$	% V^{5+}	% V^{4+}	% V^{3+}	% W^{6+}	% W^{4+}
0	63	37	0	100	0
0.91	57	43	0	100	0
2.15	39	61	0	100	0
3.94	35	38	27	77	23
charged	67	33	0	100	0

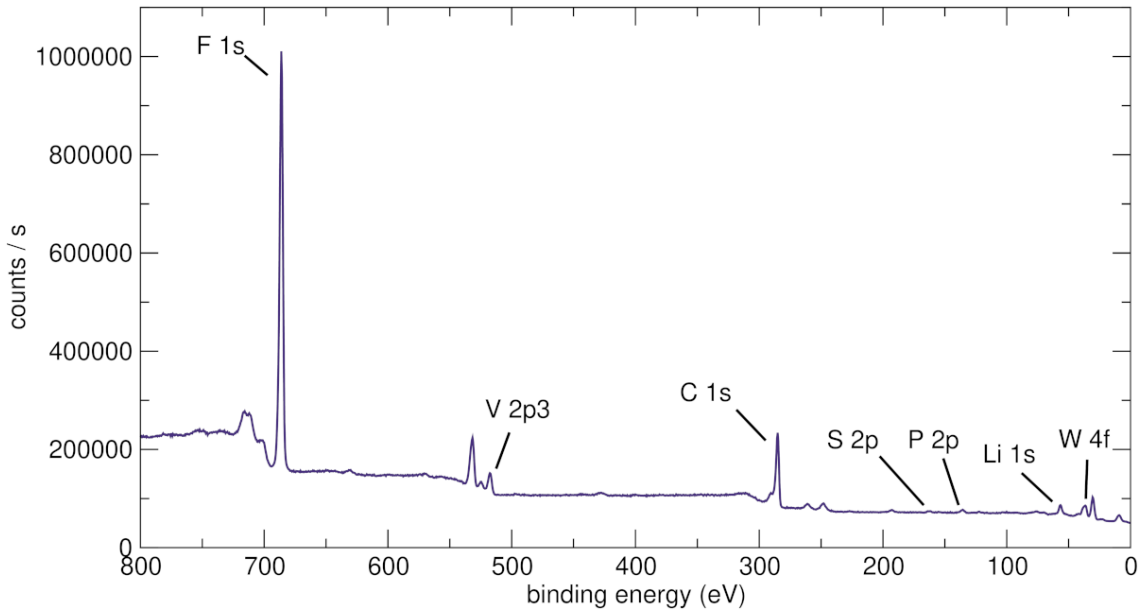

Figure 10: XPS survey scan of a fully discharged electrode shows signals from F $1s$, V $2p3$, C $1s$, S $2p$, P $2p$, Li $1s$, and W $4f$.

Table 5: Quantitative analysis of the elemental composition in an electrode from fitting the survey scan in Figure S10.

Peak	Peak binding energy (eV)	Atomic %
F 1s	685.97	39.64
V 2p3	517.21	1.06
C 1s	285.04	23.33
S 2p	162.00	0.27
P 2P	135.55	0.77
Li 1s	56.51	34.66
W 4f	36.55	0.27

	Expected	Measured
V:W ratio	4.0	3.93

Table 6: Quantitative analysis of the elemental composition from energy-dispersive X-ray spectroscopy in the pristine Conv. material.

Element	Expected atomic fraction	Measured atomic fraction
W	0.20	0.21
V	0.80	0.79